CLUSTERING OF HEAVY INERTIAL AEROSOLS IN SHEARED FLOWS

A Dissertation

Presented to the Faculty of the Graduate School

of Cornell University

in Partial Fulfillment of the Requirements for the Degree of

Doctor of Philosophy

by

Mohamed Houssem Kasbaoui

August 2017

CLUSTERING OF HEAVY INERTIAL AEROSOLS IN SHEARED FLOWS

Mohamed Houssem Kasbaoui, Ph.D.

Cornell University 2017

A wide range of technological and environmental applications rely on dispersed solid particles or droplets in a turbulent gas. These inertial aerosol particles achieve various properties such as mass and momentum transport;act as catalysts in reactive flows, or undergo chemical reaction themselves such as combustion. Predicting the dispersion of these aerosols by turbulence is a central problem rendered difficult by the complex interplay between the two phases. It has been documented that particles dispersed in a turbulent gas form large clusters that can strongly modulate the flow. The particle clusters span lengths several orders of magnitude larger than the particle diameter. Owing to their large density compared to that of the gas, $\rho_p/\rho_f = O(10^3)$, the particles can modulate the turbulence structure even at low volume fractions $10^{-5} \leqslant \phi \leqslant 10^{-3}$. Furthermore, the gravitational settling of these particles leads to anisotropic forcing of the turbulence.

This work reveals the mechanisms leading to the formation of particle clusters and the ways by which they alter the carrier flow in the semi-dilute regime (small volume fraction $\phi \ll 1$ but substantial mass loading $M = \rho_p/\rho_f\phi = O(1)$). It is found that (1) preferential concentration, the tendency of inertial particles to be expelled from vortical regions, leads to the formation of particle sheets in the high straining regions of the flow, (2) the dispersion induced by particle trajectory crossing controls the thickness of these sheets, (3) the shear-induced turning of the particle sheets towards the normal direction to gravity allows a Rayleigh-Taylor instability to grow and break the sheets in smaller clusters, and (4) the parti-

cles create flow perturbations predominantly in the downward gravity direction at scales 5 to 10 times larger than the viscous dissipation scale.

These conclusions are supported by the following studies. A linear stability analysis explores the activation of preferential concentration and the formation of particle density waves in homogeneous shear. Non-linear Euler-Euler and Euler-Lagrange simulations show that the waves steepen into particle sheets, characterize particle trajectory crossing, and reveal a transverse Rayleigh-Taylor instability that grows on the particle sheets. The simulations are made possible by a novel algorithm that emulates the unboundedness of homogeneous shear with shear-periodic boundary conditions and physical space forcing. This algorithm allows the unprecedented simulation of single phase homogeneously sheared turbulence until the establishment of the universal self-similar regime. Finally, Particle-laden homogeneously sheared turbulence is explored by means of a novel two-phase Rapid Distortion Theory that includes the effects of two-way coupling.

BIOGRAPHICAL SKETCH

Mohamed Houssem Kasbaoui was born on August 8th, 1989, in Tunis, Tunisia. He grew up going to the local science clubs, where he developed a keen interest for mechanics, chemistry, magnetism and rocketry. After graduating with the highest honors from Lyce Pilote Bourguiba in Tunis in 2008, he went on to pursue his studies in Paris, France. He studied engineering at Ecole Centrale Paris, and concomitantly physics at University Paris-Sud to broaden his scientific knowledge. He obtained a Diplôme d'Ingénieur from the former school and a Master of Science from the latter. While doing an internship at the division of experimental fluid mechanics of the Office National d'Etudes et Recherches Arospatiales in the Paris suburb, he developed a fascination for the fluid motion. In 2012, he joined the Sibley School of Mechanical and Aerospace Engineering Department at Cornell University for a PhD in Aerospace Engineering. His research aims at understanding the collective motion of heavy inertial aerosol particles in turbulence. These flows are of great importance to cloud formation and several energy applications. Using theoretical modeling in conjunction with high performance computing, he studied the role of cascading fundamental instabilities in creating particle clusters that significantly modulate flow turbulence.

ACKNOWLEDGEMENTS

During these last five years, I had the chance to evolve in an exceptional research environment at Cornell University working under the guidance of Prof. Donald Koch and Prof. Olivier Desjardins. This manuscript is the fruit of this work. It sits at the cross roads of three fields: fluid mechanics, theoretical modeling and high performance computing. There are many people that I need to acknowledge, without whom this work would not have been possible. On top of the list come my PhD advisors Prof. Donald L. Koch and Prof. Olivier Desjardins. Their high standards and mastery of the topics have been extremely inspirational. Prof. Koch introduced me to the art of theoretical analysis, linear stability analysis, multiple time scales, and modeling. His comprehensive knowledge of applied mathematics can only be paralleled by his acute physical intuition. At times when I would be excited about a piece of theory, he would remind me that the value of an analysis resides in the physical answers it provides rather than its complexity. I thank Prof. Desjardins for the hours spent at his office discussing theory and numerics. This work would not be the same without his availability and thrive for excellence and motivation. I have a deep appreciation for the ingenuity and far-reaching vision that make his research code NGA the powerful numerical package it is now. Starting out with no prior knowledge in scientific computing, I would not have been able to code physics-driven algorithms that tap so easily into the power of supercomputers if not for this computational platform. I am deeply grateful for the mentoring and support I received from them. I cannot imagine how hard it must have been to cope with my incomprehension and mistakes when I started out. I thank both of them for the many hours spent editing my papers, and for their patience when opinions diverge. The three-body problem could have been crippling but instead it proved to be a drive for original research. I also thank both

of them for giving me the freedom and trust to purse my own ideas, even though they ended up failing more often than not. Having both of them as mentors has been singularly enriching.

I would like to acknowledge the grateful support of Prof. Paul H. Steen whose availability and critical reading of my thesis contributed to the quality of this work. There are also a number of colleagues and students that I am grateful for: John Palmore, Jesse Capecelatro, Jeremy McCaslin, Sheng Wang, and Ravi Patel. Discussing my work with them and learning about their research helped me grow as a scientist. Sharing the fun and frustrating moments of research, meals, trips and sometimes even a bed at conferences made the whole experience much more enjoyable. I owe great thanks to Perry Schein, Himanshu Goyal, Lara Backer, Stephanie Firehammer, Jeremy Odent, Jihed Hadroug, Matt Kasemer, Bryan Peele and Nozomi Hitomi. Your presence made my time in Ithaca so much more pleasant. I also owe special gratitude to Sherry Zhang for being the amazing person she is. Her caring, generous and resourceful nature is a blessing. Finally, I would like to acknowledge my parents, Sana and Rafik, and my sister, Rania, for their unending support. Without the motivation and energy they provided me over the years, I never would have gotten to where I am today. I owe everything to them.

Financial support for this work was provided by the National Science Foundation grant (CBET-1233793).

TABLE OF CONTENTS

LIST OF TABLES

LIST OF FIGURES

CHAPTER 1

GENERAL INTRODUCTION

Among the most interesting problems in fluid mechanics are flows that contact a gas with solid particles or droplets. The applications are numerous and diverse. In environmental applications, substantial interest has been devoted to the dispersion of pollutants in the atmosphere (Shaw, 2003; Good *et al.*, 2014) and cloud formation (Gustavsson *et al.*, 2012; Falkovich *et al.*, 2002; Wilkinson *et al.*, 2006). Engineering applications that involve suspended particles include the pneumatic transport of solids, pulverized fuel combustors (Truelove, 1985), sprays (Fernando and Choi, 2007; Marmottant and Villermaux, 2004), fluidized beds and particle-laden jets (Longmire and Eaton, 1992). The suspended particles achieve various desired effects such as interphase heat and mass transfer, catalytic chemical reactions or combustion.

Aside from the technological relevance, the complex interplay between the two phases is of fundamental interest. The distribution of particles in turbulence can be strongly inhomogeneous. Particles with moderate inertia tend to be expelled from the vortical cores of the flow (Squires and Eaton, 1991; Eaton and Fessler, 1994). This mechanism, known as preferential concentration, causes the particles to wrap around vortices (Druzhinin, 1994; Moffatt, 1965; Longmire and Eaton, 1992) and accumulate in the low straining regions of the flow (Maxey, 1987; Squires and Eaton, 1991). Despite the incompressibility of the carrier gas, the ability of particles to accumulate in restricted regions of the flow attests of the strong compressibility of the dispersed phase. Hence, the dynamics of the overall flow are often different from single phase flows.

A primary reason why these flows are so complex is that the interaction between

the two phases leads to the formation of clusters in the particle phase that in turn modulate the carrier gas. These particle structures can span lengths several order of magnitude larger than the particle size (Squires and Eaton, 1991; Boivin *et al.*, 1998; Yang and Shy, 2005; Poelma *et al.*, 2007; Jenny *et al.*, 2012; Capecelatro *et al.*, 2015). The accumulation of particles into clusters causes the appearance of void bubbles, i.e., large regions depleted of particles. The structures can be large enough to have a significant impact on the dynamics of the carrier gas, even when individual particles are very small compared to the smallest scales of the flow. The modulation of turbulence by particle clusters leads to different energy and dissipation rate spectra from those predicted by the usual cascade of energy (Al Taweel and Landau, 1977; Druzhinin, 2001; Aliseda *et al.*, 2002; Pai and Subramaniam, 2012; Elghobashi and Truesdell, 1993). For heavy particles, the interaction of particles with the turbulence often leads to enhanced sedimentation rates. This mechanism often called "preferential sweeping" or "fast tracking" arises from the preferential sampling by particles of the downward moving fluid (i.e., in the direction of gravity) (Wang and Maxey, 1993; Yang and Lei, 1998; Good *et al.*, 2014; Aliseda *et al.*, 2002; Yang and Shy, 2005; Ireland *et al.*, 2016) and leads to settling speeds larger than those for an individual particle settling in a quiescent flow. When the particle volume fraction is large enough, the collective settling of particles leads to the anisotropic forcing of turbulence in the downward direction (Elghobashi and Truesdell, 1993).

The coupling between the two phases is strong in the semi-dilute regime where the volume fraction of the dispersed phase $\langle\phi\rangle$ is small enough (10^{-5} – 10^{-3}) but the mass loading $M = \rho_p/\rho_f\langle\phi\rangle$ is of appreciable magnitude ($O(1)$). This regime is widely abundant when the density ratio is large ($\rho_p/\rho_f = O(10^2) - O(10^3)$), particularly for micron-sized droplets and solid particles suspended in air. Owing

to the small volume fraction, inter-particle forces such as collisions are negligible. However, the local flow disturbances caused by the no-slip boundary condition at the particle surfaces collectively produce a substantial modification of the carrier fluid motion due to the large mass loading.

The design of flows in the semi-dilute regime requires the understanding of the fundamental mechanisms leading to clustering and modulation of the carrier flow. Part of the difficulty is due to the fact that computational methods for particle-laden flows are not as mature as for single phase flows. The two main simulation strategies suffer from various limitations. Simulations in the Euler-Lagrange formalism rely on solving the position and momentum of every discrete (Lagrangian) particle in addition to the fluid's Navier Stokes equations. This method is successful in capturing clustering in mesoscale simulations (Capecelatro *et al.*, 2015) but cannot realistically scale to match lab-scale experiments, let alone industrial flows, because the number of particles to track quickly diverges. An alternative formalism relies on an Eulerian description of the particle phase. Euler-Euler simulations rely on solving partial differential equations for the conserved particle quantities such as number density, momentum and energy. Efficient solvers allow better scaling of these methods, however these methods often lead to the formation of discontinuities in the particle phase that challenge the well-posedness and theoretical grounding of these methods (Fox, 2008). A more important factor may be that our basic physical understanding of single phase flows is built upon the study of a set of canonical hydrodynamic instabilities such as the Kelvin-Helmholtz and Rayleigh-Taylor instabilities, while there is a dearth of instability mechanisms highlighting the role of particle-gas interaction in destabilizing two-phase flows have been identified.

To address these challenges and understand the interplay between the two phases, we propose to study particle clustering in homogeneously sheared flows with a collection of theoretical and numerical approaches. Pure homogeneous shear retains the simplicity of linear flows but incorporates key elements of more complex anisotropic inhomogeneous flows. The balancing strain and rotation of the flow lead to vanishing preferential concentration effects. Yet, simulations show that as particles settle, clusters appear, elongate, break and reform. This motivated the four following studies.

1. **Understanding the onset of clustering with a linear stability analysis**: Results of this study are reported in chapter 2. It is found that the presence of sedimenting particles creates an unstable state driven by the preferential concentration mechanism. Sinusoidal perturbations traversing the homogeneously sheared suspension create periodic regions of dominant rotation and dominant strain, which cause particles to migrate and segregate breaking the homogeneity of the flow. The regions where particles accumulate force the flow in the direction of gravity more than the depleted regions do owing to the higher local number density. The overall behavior is unstable algebraically with a time scale equal to the inverse of the shear rate. The work exposes the onset of clustering in homogeneous shear flow based on a simplified Eulerian-Eulerian model first proposed by Maxey (1987) and then further developed by Druzhinin (1995); Ferry and Balachandar (2001) valid for heavy particles with small, but non-zero inertia. It is noteworthy that single phase homogeneous shear has long been known to be very robust to perturbations. In a seminal paper, Lord Kelvin proved that all velocity perturbations are suppressed by viscosity at a super-exponential rate ($\propto \exp(-\mu t^3)$). Hence, the instability presented in this chapter is strictly

two-phase in nature and the first of its kind in the semi-dilute regime.

2. **Developing a numerical procedure to simulate homogeneously sheared flows**: In chapter 3 we present an algorithm that enables solving the Navier-Stokes equations forced by large-scale homogeneous shear. The efficient and robust methodology facilitates understanding the effect of shear on complex flows such as turbulence and complex fluids such as particle-gas mixtures without the added complications of confining walls or shear rate inhomogeneities. The algorithm is based on a physical space implementation of shear forcing and an implementation of the so-called shear-periodic boundary conditions. Combined with an energy-conserving discretization tailored for turbulence simulations (Desjardins *et al.*, 2008a), the algorithm allows the unprecedented investigation of the single phase homogeneously sheared turbulence (HST) in the universal self-similar regime. Extensive comparisons with the experiments of Tavoularis and Corrsin (1981); Shen and Warhaft (2000); Isaza *et al.* (2009) show remarkable agreement with the available turbulence observables. It is noteworthy that the widely used shearing procedure of Rogallo (1981) and the one later proposed by Brucker *et al.* (2007) lead to sever dissipation of the kinetic energy in the former case and numerically unstable Gibbs oscillations in the latter one (Sukheswalla *et al.*, 2013), which prevent the establishment of the universal self-similar regime seen in experiments. This study sets up the stage for the simulation of particle-laden sheared flows.

3. **Exploring the clustering in homogeneous shear beyond the linear regime with Euler-Lagrange and Euler-Euler methods**: In chapter 5, we analyze the evolution of sinusoidal velocity perturbations traversing a homogeneously sheared suspension of randomly distributed particles. When

the perturbation is small, the simulations reproduce an evolution consistent with the findings of the linear stability analysis in chapter 2. Stronger perturbations lead to the manifestation of non-linearities that reveal the process by which clusters form: (1) the preferential concentration of inertial particles in the stretching regions of the flow leads to the formation of highly concentrated particle sheets, (2) the thickness of the latter is controlled by particle-trajectory crossing, which causes a local dispersion of particles, and (3) a transverse Rayleigh-Taylor instability, aided by the shear-induced rotation of the particle sheets towards the gravity normal direction, breaks the planar structure into smaller clusters. The simulations are conducted in the Euler-Lagrange and Euler-Euler formalisms with the shear methodology from chapter 3. Particle tracking and feed-back is based on the method of (Capecelatro and Desjardins, 2013b). In the Euler-Euler formalism, we use the Two-Fluid method (Druzhinin, 1995) and the Anisotropic Gaussian method (Vi *et al.*, 2015, 2016; Kong *et al.*, 2017). We find that the Two-Fluid method is unable to capture the particle dispersion due to particle-trajectory crossing and leads instead to the formation of discontinuities. These are removed with the Anisotropic Gaussian method which derives from a kinetic approach that provides a statistical description of particle-trajectory crossing.

4. **Understanding the modulation of rapidly sheared turbulence by particle clustering**: We conclude the study by a semi-analytical analysis of the modulation of turbulence scales by the dispersed particles. In chapter 5, we extend the single phase rapid distortion theory (RDT) (Townsend, 1970) to the two-way coupled particle-laden turbulence. The new theory explains the alteration of turbulence by the simultaneous effects of strong

large scale shear and the preferential concentration of particles in the low vorticity, high strain regions of the flow. The RDT equations are derived in the general two-way coupling setting and analyzed in the limits of vanishing particle-volume fraction, and vanishing mass loading.

CHAPTER 2

PREFERENTIAL CONCENTRATION DRIVEN INSTABILITY OF SHEARED GAS-SOLID SUSPENSIONS

2.1 Abstract

We examine the linear stability of a homogeneous gas-solid suspension of small Stokes number particles, with a moderate mass loading, subject to a simple shear flow. The modulation of the gravitational force exerted on the suspension, due to preferential concentration of particles in regions of low vorticity, in response to an imposed velocity perturbation, can lead to an algebraic instability. Since the fastest growing modes have wavelengths small compared with the characteristic length scale (U_g/Γ) and oscillate with frequencies large compared with Γ, U_g being the settling velocity and Γ the shear rate, we apply the WKB method, a multiple scale technique. This analysis reveals the existence of a number density mode which travels due to the settling of the particles and a momentum mode which travels due to the cross-streamline momentum transport caused by settling. These modes are coupled at a turning point which occurs when the wavevector is nearly horizontal and the most amplified perturbations are those in which a momentum wave upstream of the turning point creates a downstream number density wave. The particle number density perturbations reach a finite, but large amplitude that persists after the wave becomes aligned with the velocity gradient. The growth of the amplitude of particle concentration and fluid velocity disturbances is characterised as a function of the wavenumber and Reynolds number($Re = U_g^2/\Gamma\nu$) using both asymptotic theory and a numerical solution of the linearised equations.

2.2 Introduction

A striking feature of the dynamics of inertial particles in gas flows is the tendency of centripetal accelerations to expel the particles from vortical regions so that they preferentially concentrate in straining dominated regions of the flow (Squires and Eaton, 1991). It is natural to expect that the resulting fluctuations in the particle concentration and the forces the particles exert on the fluid will enhance the fluid velocity fluctuations. In this study, we investigate a mechanism by which preferential concentration of particles and the associated variations in the gravitational forces can lead to enhanced fluid velocity fluctuations in a unidirectional laminar flow. In particular, we consider the linear stability of an unbounded simple shear flow of a homogeneous dilute suspension of inertial particles in a gas, a scenario that allows for a rigorous analysis, but nevertheless extracts mechanisms of growth of concentration fluctuations that are generic and should apply to small wavelength perturbations in more complicated flow scenarios such as laminar shear mixing layers or turbulent flows. We show that preferential concentration and gravitational forces can lead to a large enhancement in the magnitude of particle concentration and fluid velocity waves as they rotate in the shear flow. The long-term growth of the fluctuations can then arise from the coupled effects of the new preferential concentration instability and the Rayleigh-Taylor instability of stratified particulate flows (Batchelor and Nitsche, 1991).

The qualitative physical understanding of the complex dynamics of single phase fluids is greatly enhanced by the study of a set of classical hydrodynamic instabilities. Our poorer understanding of dispersed multiphase and particulate flows may result then not only from their greater complexity but also from the limited supply of readily understandable instability mechanisms. Many of the classical instabil-

ities of particulate flows, such as the instability of fluidized beds to void fraction waves (Anderson *et al.*, 1995; Batchelor, 1988) and the clustering of particles in rapid granular flow (Wang *et al.*, 1996) involve dense flows with particle volume fraction ϕ of order one where the hydrodynamic and collisional interactions among the particles dominate the flow. At the other extreme very dilute flows with small particle mass loading M can be understood with reference to the hydrodynamic instabilities of the carrier fluid. Here, the mass loading is the ratio of the mass supplied by the particles to that supplied by the fluid, i.e., $M = nm/\rho_f$, where n is the number of particles per unit volume, m is the mass of a particle, and ρ_f is the density of the fluid. As an example, the dynamics of settling particles in two co-flowing gas streams with different velocities is controlled by the Kelvin-Helmholtz instability of the fluid (Tio *et al.*, 1993). Additionally, the classic approach of Saffman (1962) to the stability of such suspensions is to consider an effective fluid with a density adjusted to take in account the presence of particles.

The most challenging regime is a semi-dilute regime with small particle volume fractions $\phi \ll 1$ but moderate mass loadings $M = O(1)$. In such a regime, the particulate and gas phases play comparable roles in the suspension dynamics. Examples of these flows include the handling of particles in pneumatic conveying (Nishimura and Hunt, 2000), methods of contacting gas and solids such as circulating fluidized beds (Dasgupta *et al.*, 1994), and the suspension of particles in dust storms (Alfaro and Gomes, 2001). While these applications are influenced by particle-boundary interactions in addition to bulk gas-solid interactions, one can isolate the bulk gas-solid interactions studied here in more idealised experiments such as particle-seeded grid generated turbulent flows (Aliseda *et al.*, 2002) and studies of self-induced turbulence of sedimenting particles (Parthasarathy and Faeth, 1990).

In this paper, we analyse the stability of a homogeneous gas-solid suspension in an unbounded simple shear flow. When analysing the evolution of disturbances to unbounded simple shear flows in the form of Fourier modes, it is necessary to account for the turning of the wavevector of the disturbance mode by the imposed shear flow. Kelvin (1887) first analysed the linearised disturbances with turning wavevector, known as Kelvin modes, to the Navier-Stokes equations for unbounded simple shear flow. Interestingly, it has been noted by Craik and Criminale (1986) that each of these modes, due to its transverse nature, is also a solution to the full Navier-Stokes equations, although a collection of Kelvin modes is not. Lord Kelvin demonstrated that the momentum perturbations eventually decay at long times algebraically in the inviscid case and super-exponentially (exponential of a third order polynomial) for finite Reynolds numbers. Nevertheless, the modes experience a transient period of algebraic growth which has led to the postulate of the so-called bypass transition to turbulence for shearing flows by a mechanism that couples non-linear effects with the initial linear transient growth, referred to as "bootstrapping" (Trefethen *et al.*, 1993).

To analyse the stability of unbounded simple shear flow in the presence of a particulate phase, it is necessary to solve equations describing the state of the particulate phase along with mass, momentum and energy conservation equations. Such an analysis has been performed for rapidly sheared granular materials by Schmid and Kytomaa (1994) by solving momentum and kinetic energy conservation coupled with the constitutive equations for a granular material (Lun *et al.*, 1984). As in the case of the Navier-Stokes problem, it was found that disturbances in granular materials have a transient period of algebraic growth followed by decay of the disturbances at long times. The extent of the transient growth was much larger for granular materials than for Newtonian fluids leading to an increased

possibility that non-linear effects may arise during the transient period and sustain the disturbed state.

In the present study, we will analyse the coupled linearised dynamics associated with momentum conservation and particle number density conservation in a dilute gas-solid suspension. It will be seen that there is a large algebraic growth of disturbances in this system. In contrast to the cases of single phase Newtonian flow and granular flows, the number density disturbances in the dilute gas-solid system do not decay at long times but reach a steady amplitude, allowing an indefinite time period for the development of secondary instabilities.

The inertia of the particles, measured by the particle Stokes number $St = \Gamma\tau_p$, plays a critical role in the preferential concentration of particles that is crucial to the instability mechanism studied here. However, to facilitate an analytical development we will consider the case of small but non-zero Stokes number for which Ferry and Balachandar (2001, 2002) have developed a partial differential equation for particle concentration. Here Γ is the shear rate of the imposed flow, $\tau_p = m/(6\pi\mu a)$ is the particle response time, μ is the gas viscosity and a is the particle radius. In the dilute, low Stokes number regime, one can neglect the direct hydrodynamic and collisional interactions among the particles, although particles experience indirect interactions through the disturbances to the continuum solution for the fluid velocity induced by the forces exerted by other particles.

We will show that inertially induced preferential concentration of particles combined with their gravitational forcing can destabilise a sheared gas-solid suspension. Evidence that gravity and particle inertia are effective in creating hydrodynamic fluctuations can be gleaned from previous direct numerical simulation (DNS) and experimental studies of turbulent flows. For example, Elghobashi and Truesdell

(1993) used forcing to produce isotropic turbulence in a DNS and then introduced particles and observed the decaying turbulence. They found that particles that settle with velocities comparable with the root-mean-square fluid velocity enhance both the turbulent energy and turbulent dissipation rate more than particles experiencing no gravitational force. The enhancement was highest at small wavelengths where the larger scales of turbulence could be viewed as producing shearing flows. Some experimental evidence for particle enhanced hydrodynamic fluctuations comes from the study of particles in grid generated turbulence by Aliseda *et al.* (2002). It is known from DNS (Wang and Maxey, 1993) that particles settle faster in turbulence than in quiescent fluid because the particles are expelled from vortical up-welling regions. Aliseda *et al.* (2002) found that the sedimentation velocity increased with increasing mass loading suggesting that the particles increased the fluid velocity fluctuations and thereby enhanced their own sedimentation.

In this paper, we will analyse the linear stability of a uniformly sheared unbounded gas-solid suspension with a uniform number density. To account for particle inertia and particle-gas coupling we consider a small but finite Stokes number and a moderate mass loading. The particular case of horizontal shear will be investigated, since it is most relevant to flows such as wind driven dust flow and pneumatic conveying. In section 2, we derive the linearised equations for Fourier-mode velocity and concentration disturbances with wavevectors that turn in the imposed shear flow. From numerical integration of these equations, we observe that the solutions exhibit multiple time scales when the wavelength is much smaller than the characteristic distance $L = U_g/\Gamma$ over which a particle settles during the shearing time $1/\Gamma$, where U_g is the particle settling velocity. In this case the number density and velocity waves undergo many periods of oscilla-

tion due to settling of particles and transport of momentum by particle settling in the time it takes the waves to turn in the shear flow. Since these high wavenumber disturbances have the largest growth, they are analyzed in more detail using the WKB method of multiple time scale analysis. The WKB analysis for inviscid and viscous solutions is presented in sections 3 and 4, respectively. The analysis reveals the existence of two perturbation modes, which we term the momentum and number density modes. These modes evolve independently for most of their existence. However, the coupling of the two modes in the vicinity of a turning point, when the wavevector is nearly vertical, plays a crucial role in determining the amplitude of the final number density disturbance created by an initial fluid velocity disturbance. A concluding perspective on the study is given in section 5.

2.3 Derivation of the governing equations

2.3.1 Derivation of the non-linear equations

We assume that the particles are small enough that they experience a hydrodynamic force that equals the Stokes drag force as well as a gravitational force. For a solid-gas suspension, the Basset history force and the lift force can be neglected due to the large density ratio. The particle equation of motion is then:

$$\frac{d\mathbf{v}}{dt} = \frac{\mathbf{u} - \mathbf{v}}{\tau_p} + \mathbf{g} \tag{2.1}$$

where $\mathbf{v}$ is the particle velocity and $\mathbf{u}$ is the fluid velocity. Because we consider small volume fractions, particle-particle collisions are also neglected. The particles act on an incompressible Newtonian fluid through a body force term equal to the number of particles per unit volume times the particle-fluid interaction force

(Druzhinin, 1995; Ferry and Balachandar, 2001). The resulting governing equations for the fluid are:

$$\frac{\partial \mathbf{u}}{\partial t} + \mathbf{u} \cdot \nabla \mathbf{u} = -\frac{1}{\rho_f} \nabla p + \nu \nabla^2 \mathbf{u} + \frac{mn}{\rho_f} \frac{\mathbf{v} - \mathbf{u}}{\tau_p} \tag{2.2}$$

$$\nabla \cdot \mathbf{u} = 0 \tag{2.3}$$

In the case of an unbounded shear flow, for which we write the velocity gradient tensor as $\nabla \mathbf{u}_b = \Gamma \mathbf{e_2} \mathbf{e}_1$, the only characteristic length in the problem is $L = U_g/\Gamma$ where $\mathbf{U}_g = \tau_p \mathbf{g}$ refers to the settling velocity of the particles. Note that L represents the distance settled by the particles during the characteristic shearing time. An appropriate Reynolds number for the suspension is then $Re = U_g L/\nu = U_g^2/(\Gamma \nu)$.

While a range of methods can be used to model particles and their interaction with the fluid, Eulerian methods have the advantage of considering the net effect of the particles through spatial fields such as the number density field without requiring the tracking of each individual particle. The number density conservation equation is given by:

$$\frac{\partial n}{\partial t} + \nabla \cdot (\mathbf{v} n) = 0 \tag{2.4}$$

Equation (2.4) does not include particle diffusion. The diameter of particles large enough to have non-zero Stokes numbers precludes the importance of Brownian diffusion. The suspension is sufficiently dilute to neglect particle collisions and near-field hydrodynamic interactions. Furthermore, the equations already capture the net force exerted by the particles on the fluid so that hydrodynamic diffusion due to point particles would be described by equations (2.2) and (2.4) provided that the number density fluctuations associated with randomly distributed particles were included in the initial conditions for the number density field.

Starting from the Maxey and Riley (1983) equations of motion for a rigid

sphere, Ferry and Balachandar (2001) derived an asymptotic expansion for the particles' velocity in the limit of small Stokes number $St = \Gamma\tau_p \ll 1$. We treat the settling velocity as a leading order contribution to this expansion since U_g is the characteristic velocity scale in the problem. Thus, the expansion up to first order in the particle response time is:

$$\mathbf{v} = \mathbf{u} + \mathbf{U}_g - \tau_p(\frac{\partial \mathbf{u}}{\partial t} + (\mathbf{u} + \mathbf{U}_g) \cdot \nabla \mathbf{u}) + O(\tau_p^2) \tag{2.5}$$

The expansion (2.5) is given in dimensional form. When non-dimensionalised by the settling velocity magnitude U_g, the characteristic distance L and the shearing time $1/\Gamma$, it becomes

$$\mathbf{v} = \mathbf{u} + \mathbf{1}_g - St(\frac{\partial \mathbf{u}}{\partial t} + (\mathbf{u} + \mathbf{1}_g) \cdot \nabla \mathbf{u}) + O(St^2) \tag{2.6}$$

where $\mathbf{1}_g = \mathbf{U}_g/U_g$ is a unit vector parallel to gravity. This low Stokes number formulation has the advantage that the particle velocity can be related to the local fluid velocity and its derivatives, whereas the flow history along individual particle trajectories must be accounted for at finite Stokes numbers. Note that when $St = 0$, the particles move with the fluid velocity, acting as tracers. For small but finite Stokes numbers, the particles deviate from the fluid motion because of the fluid acceleration in a reference frame that translates with the sum of the fluid and settling velocities. It has been shown in (Ferry and Balachandar, 2002) that the above expression is in excellent agreement with a Lagrangian treatment of particles in a turbulent channel flow. The particle concentration equation coupled with the particles' velocity field (2.5) was solved by Rani and Balachandar (2003) in isotropic, homogeneous turbulence and found to be in good agreement with results from Lagrangian particle tracking.

Using the expression (2.5) in the governing equations, we derive the fluid equations of motion and number density conservation equation. Non-dimensionalised

by the length scale $L = U_g/\Gamma$, velocity scale U_g, base state number density n_0 and shearing time scale $1/\Gamma$, the equations are :

$$\nabla \cdot \mathbf{u} = 0 \tag{2.7}$$

$$(1 + Mn)\left(\frac{\partial \mathbf{u}}{\partial t} + \mathbf{u}.\nabla\mathbf{u}\right) = -\nabla p + \frac{1}{Re}\nabla^2\mathbf{u} + \frac{Mn}{St}\mathbf{1}_g \cdot (\mathbf{I} - St\nabla\mathbf{u}) \tag{2.8}$$

$$\frac{\partial n}{\partial t} + \left(\mathbf{u} + \mathbf{1}_g - St\left(\frac{\partial \mathbf{u}}{\partial t} + (\mathbf{u} + \mathbf{1}_g).\nabla\mathbf{u}\right)\right) \cdot \nabla n = St\ n\nabla\mathbf{u} : \nabla\mathbf{u} \tag{2.9}$$

where $\mathbf{I}$ is the identity tensor. Note that the suspension appears to have an effective density $\rho_f(1 + Mn)$ equal to the sum of the mass densities of the gas and particulate phases. Another striking feature of the momentum equation (2.8) is that in addition to the gravitational force, the particles exert a body force proportional to $-\mathbf{1}_g \cdot \nabla\mathbf{u}$. This term arises from the convection of momentum across fluid streamlines by the settling of the particles.

The number density field in (2.9) is convected by the approximate particle velocity field and can change along particle paths as a result of the compressibility of the particle velocity field. The divergence of the particle velocity is $-St\nabla\mathbf{u} : \nabla\mathbf{u} = -St(S^2 - \Omega^2)$ with $S^2 = \mathbf{S} : \mathbf{S}$ and $\Omega^2 = \mathbf{R} : \mathbf{R}$ being the second invariants of the fluid strain $\mathbf{S} = 1/2(\nabla\mathbf{u} + \nabla\mathbf{u}^\mathsf{T})$ and rotation tensors $\mathbf{R} = 1/2(\nabla\mathbf{u} - \nabla\mathbf{u}^\mathsf{T})$. A homogeneous shear flow base state does not contribute to the particle density modulation since $\nabla\mathbf{u}_b : \nabla\mathbf{u}_b = 0$. This is because a simple shear flow has equal portions of straining and rotational motion. It is through a perturbation to the simple shear and the resulting local imbalance between vorticity and extension that one will obtain a non zero term in the right-hand side of (2.9). In particular, regions of higher vorticity ($\nabla\mathbf{u} : \nabla\mathbf{u} = S^2 - \Omega^2 < 0$) will lead to a depletion of particles, while particles aggregate in regions of higher strain ($\nabla\mathbf{u} : \nabla\mathbf{u} = S^2 - \Omega^2 > 0$). This process is known as preferential concentration.

The preferential concentration term is order $O(St)$ in (2.9), because to leading

order the particle velocity is equal to the sum of the fluid velocity and settling velocity both of which are divergence free. It follows that a uniform number density is unaltered by the $O(1)$ particle velocity field and number density fluctuations arise only at $O(St)$. Thus, we can write $n = 1 + St\ n'$. In terms of the scaled number density fluctuations n', the conservation equations (2.8) and (2.9) at $O(St)$ become:

$$(1+M)\left(\frac{\partial \mathbf{u}}{\partial t} + \mathbf{u}.\nabla\mathbf{u}\right) = -\nabla p' + \frac{1}{Re}\nabla^2\mathbf{u} - M\mathbf{1}_g \cdot \nabla\mathbf{u} + Mn'\mathbf{1}_g \tag{2.10}$$

$$\frac{\partial n'}{\partial t} + (\mathbf{u} + \mathbf{1}_g)\cdot\nabla n' = \nabla\mathbf{u} : \nabla\mathbf{u} \tag{2.11}$$

where $p' = p - \frac{M}{St}\mathbf{1}_g \cdot \mathbf{r}$ is a reduced pressure adjusted to remove the gravitational forcing of a uniform particle suspension.

2.3.2 Linear stability analysis

Next, we assume that the fluid velocity includes a small perturbation to the base simple shear flow such that $\mathbf{u} = \mathbf{r}\cdot\nabla\mathbf{u}_b + \mathbf{u}'$, with the base velocity gradient tensor constant and proportional to the shear rate as defined above. Hence the momentum perturbation satisfies:

$$\begin{aligned}\frac{\partial \mathbf{u}'}{\partial t} + \mathbf{r}\cdot\nabla\mathbf{u}_b\cdot\nabla\mathbf{u}' \ &+\ \mathbf{u}'\cdot\nabla\mathbf{u}_b + \frac{M}{1+M}\mathbf{1}_g\cdot\nabla\mathbf{u}' = \\ &-\ \frac{1}{1+M}\nabla p' + \frac{1}{1+M}\frac{1}{Re}\nabla^2\mathbf{u}' + \frac{M}{1+M}\mathbf{1}_g n'\end{aligned} \tag{2.12}$$

$$\nabla\cdot\mathbf{u}' = 0 \tag{2.13}$$

and the number density equation becomes:

$$\frac{\partial n'}{\partial t} + \mathbf{r}\cdot\nabla\mathbf{u}_b\cdot\nabla n' + \mathbf{1}_g\nabla n' = 2\nabla\mathbf{u}_b : \nabla u' \tag{2.14}$$

An arbitrary small perturbation of the number density and fluid velocity fields

can be decomposed into spatial Fourier modes and so we define the Fourier transform as:

$$\hat{n}(t,\mathbf{k}) = \frac{1}{(2\pi)^{3/2}} \int_{\mathbf{r}\in\mathbb{R}^3} n'(t,\mathbf{r}) \exp(-i\mathbf{k}\cdot\mathbf{r}) d\mathbf{r} \tag{2.15}$$

$$\tag{2.16}$$

and the inverse transforms as

$$n'(t,\mathbf{r}) = \frac{1}{(2\pi)^{3/2}} \int_{\mathbf{k}\in\mathbb{R}^3} \hat{n}(t,\mathbf{k}) \exp(i\mathbf{k}\cdot\mathbf{r}) d\mathbf{k} \tag{2.17}$$

$$\tag{2.18}$$

The disturbance equations (2.12) and (2.14) become in Fourier space:

$$\frac{\partial \hat{n}}{\partial t} - \mathbf{k}\cdot\nabla\mathbf{u}_b^{\mathsf{T}}\cdot\nabla_k\hat{n} + i\mathbf{1}_g\cdot\mathbf{k}\hat{n} = i2\nabla\mathbf{u}_b : \mathbf{k}\hat{\mathbf{u}} \tag{2.19}$$

$$\frac{\partial \hat{\mathbf{u}}}{\partial t} - \mathbf{k}\cdot\nabla\mathbf{u}_b^{\mathsf{T}}\cdot\nabla_k\hat{\mathbf{u}} + \hat{\mathbf{u}}\cdot\nabla\mathbf{u}_b + i\frac{M}{1+M}\mathbf{1}_g\cdot\mathbf{k}\hat{\mathbf{u}} = -i\frac{1}{1+M}\mathbf{k}\hat{p} - \frac{1}{1+M}\frac{k^2}{Re}\hat{\mathbf{u}} + \frac{M}{1+M}\mathbf{1}_g\hat{n} \tag{2.20}$$

For an incompressible fluid, pressure balances the component of the force field along the $\mathbf{k}$ direction. The residual force field drives the flow. The operation $\mathbf{I}-\mathbf{kk}$ projects equation (2.20) along the direction parallel to the wave front. The resulting momentum balance in the transverse direction is:

$$\begin{aligned}\frac{\partial \hat{\mathbf{u}}}{\partial t} - \mathbf{k}\cdot\nabla\mathbf{u}_b^{\mathsf{T}}\cdot\nabla_k\hat{\mathbf{u}} = &-(\mathbf{I}-2\frac{\mathbf{kk}}{k^2})\nabla\mathbf{u}_b^{\mathsf{T}}\cdot\hat{\mathbf{u}} - i\frac{M}{1+M}\mathbf{1}_g\cdot\mathbf{k}\hat{\mathbf{u}} \\ &-\frac{1}{1+M}\frac{k^2}{Re}\hat{\mathbf{u}} + (\mathbf{I}-\frac{\mathbf{kk}}{k^2})\frac{M}{1+M}\mathbf{1}_g\hat{n}\end{aligned} \tag{2.21}$$

Applying the method of characteristics, the conservation equations can be converted to ordinary differential equations with respect to time along the characteristics defined by:

$$\frac{d\mathbf{k}}{dt} = -\nabla\mathbf{u}_b\cdot\mathbf{k} \tag{2.22}$$

The conservation equations along the characteristics with a turning wavevector given by (2.22) are:

$$\frac{d\hat{n}}{dt} + i\mathbf{1}_g \cdot \mathbf{k}\hat{n} = i2\nabla\mathbf{u}_b : \mathbf{k}\hat{\mathbf{u}} \tag{2.23}$$

$$\frac{d\hat{\mathbf{u}}}{dt} = -(\mathbf{I}-2\frac{\mathbf{kk}}{k^2})\nabla\mathbf{u}_b^{\mathsf{T}}\cdot\hat{\mathbf{u}} - i\frac{M}{1+M}\mathbf{1}_g\cdot\mathbf{k}\hat{\mathbf{u}} - \frac{1}{1+M}\frac{k^2}{Re}\hat{\mathbf{u}} + (\mathbf{I}-\frac{\mathbf{kk}}{k^2})\frac{M}{1+M}\mathbf{1}_g\hat{n} \tag{2.24}$$

The condition (2.22) reflects the fact that a wave of arbitrary initial orientation rotates under the action of the shearing and its wavelength evolves as the wave is stretched and compressed by the straining component of the imposed flow. As a result of the turning wavevector, these plane-wave disturbances exhibit a non-separable dependence on space and time. A classical approach in stability analysis is to write the disturbance equations in the form

$$\frac{d\mathbf{x}}{dt} = \mathbf{A}\mathbf{x} \tag{2.25}$$

where $\mathbf{x}$ is a multidimensional vector that represents the unknowns of the problem and $\mathbf{A}$ is an operator that contains the governing equations. When $\mathbf{A}$ is constant in time, the solution to (2.25) is :

$$\mathbf{x}(t) = \exp(t\mathbf{A})\mathbf{x}(t=0) \tag{2.26}$$

The usual procedure is then to analyse the spectrum of the operator $\mathbf{A}$. However, this method fails in the case we are considering, because $\mathbf{A}$ is now time dependent. Integrating (2.25) becomes challenging both conceptually and numerically. Dyson (1949) has proposed a formal solution that makes use of a time-ordering operator $\mathcal{T}$

$$\mathbf{x}(t) = \mathcal{T}\left\{\exp\left(\int_0^t \mathbf{A}(\tau)d\tau\right)\right\}\mathbf{x}(t=0) \tag{2.27}$$

that is not practical for computational purposes. A numerically tractable expansion found in (Bellman, 1997)

$$\mathbf{x}(t) = \lim_{n\to\infty} \left\{ \mathbf{I} + \int_0^t dt_n \int_0^{t_n} dt_{n-1} \cdots \int_0^{t_1} dt_0 \mathbf{A}(t_0)\mathbf{A}(t_1)\cdots\mathbf{A}(t_n) \right\} \mathbf{x}(t=0) \quad (2.28)$$

was used by Schmid and Kytomaa (1994) in the context of granular flow in unbounded homogeneous shear. Alternatively, Magnus (1954)'s method provides a representation based on an exponential of a series of operators. The common denominator to these different approaches, is the high degree of complexity of the form of solution and the difficulty of implementation. In contrast, we shall demonstrate, in our case, that for the large wavenumbers, which give the largest perturbation growth, one can obtain simpler analytical approximate solutions to the equations (2.23) and (2.24) using the WKB method.

In the following, we will investigate the particular case in which gravity is aligned with the velocity gradient of the imposed shear flow, so that $\mathbf{1}_g = -\mathbf{e_2}$ and $\nabla \mathbf{u}_b = \mathbf{e}_2\mathbf{e}_1$. In this configuration, the number density equation (2.23) is:

$$\frac{d\hat{n}}{dt} = ik_2\hat{n} + i2k_1\hat{u}_2 \quad (2.29)$$

and the momentum equation (2.24) along the $\mathbf{e}_2$ axis is:

$$\frac{d\hat{u}_2}{dt} = 2\frac{k_2k_1}{k^2}\hat{u}_2 + \frac{M}{1+M}ik_2\hat{u}_2 - \frac{M}{1+M}(1-\frac{k_2^2}{k^2})\hat{n} - \frac{1}{1+M}\frac{k^2}{Re}\hat{u}_2 \quad (2.30)$$

The velocity component along $\mathbf{e_1}$, that is $\hat{u}_1$, can be easily obtained with the continuity equation. From the relation (2.22), the two components of the wavevector along directions $\mathbf{e}_1$ and $\mathbf{e}_3$ have constant values, while along $\mathbf{e}_2$ the component is $k_2 = -k_1 t$ where we choose the origin of time such that k_2 becomes zero at $t = 0$. Thus, for negative values of time, the wavevector is pointing upstream ($k_2 > 0$) while, for positive values of time, it is pointing downstream ($k_2 < 0$) as illustrated in figure 2.1. We will consider initial times t_0 that may be positive or negative

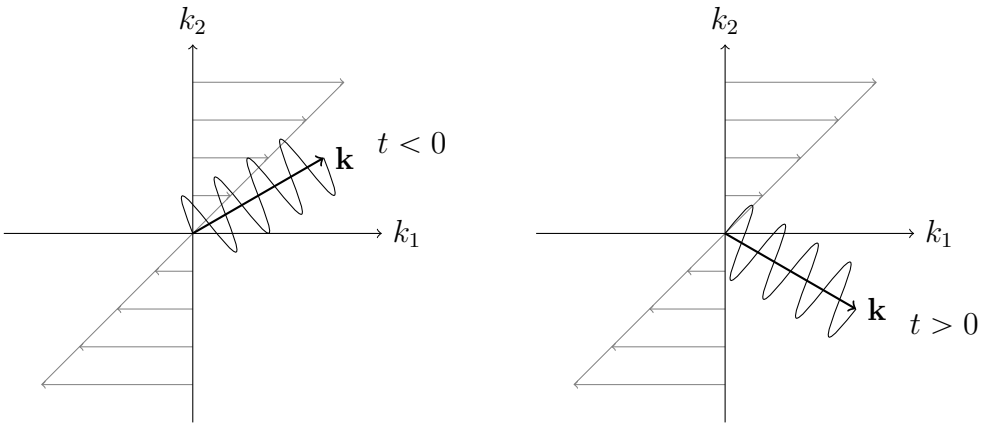

(a) Upstream configuration (b) Downstream configuration

Figure 2.1: As the wave rotates, it goes from an upstream configuration corresponding to negative times, to a downstream configuration corresponding to positive times.

according to the desired initial orientation of the wavevector. We constrain the analysis to perturbations for which $k_3 = 0$. The 3-component of the wavenumber makes no qualitative difference in the dynamics of the system.

2.3.3 Numerical investigation

To understand the dynamics of coupled particle number density and fluid momentum perturbations in a sheared gas-solid suspension we begin by examining numerical solutions to (2.29) and (2.30) for the inviscid case $Re \to \infty$ with a moderate mass loading $M = 0.5$. Figure 2.2 illustrates the response of the number density perturbation and the vertical component of the fluid velocity perturbation to an initial disturbance of the fluid momentum scaled with an arbitrary small amplitude ϵ of ($\hat{n} = 0$, $\hat{u}_2 = 1$). Note that since the initial scaled amplitude is unity, the later scaled amplitude is also equal to the relative amplification of the wave. A comparison of figure 2.2 (a,b) to (c,d) illustrates the effect of increasing

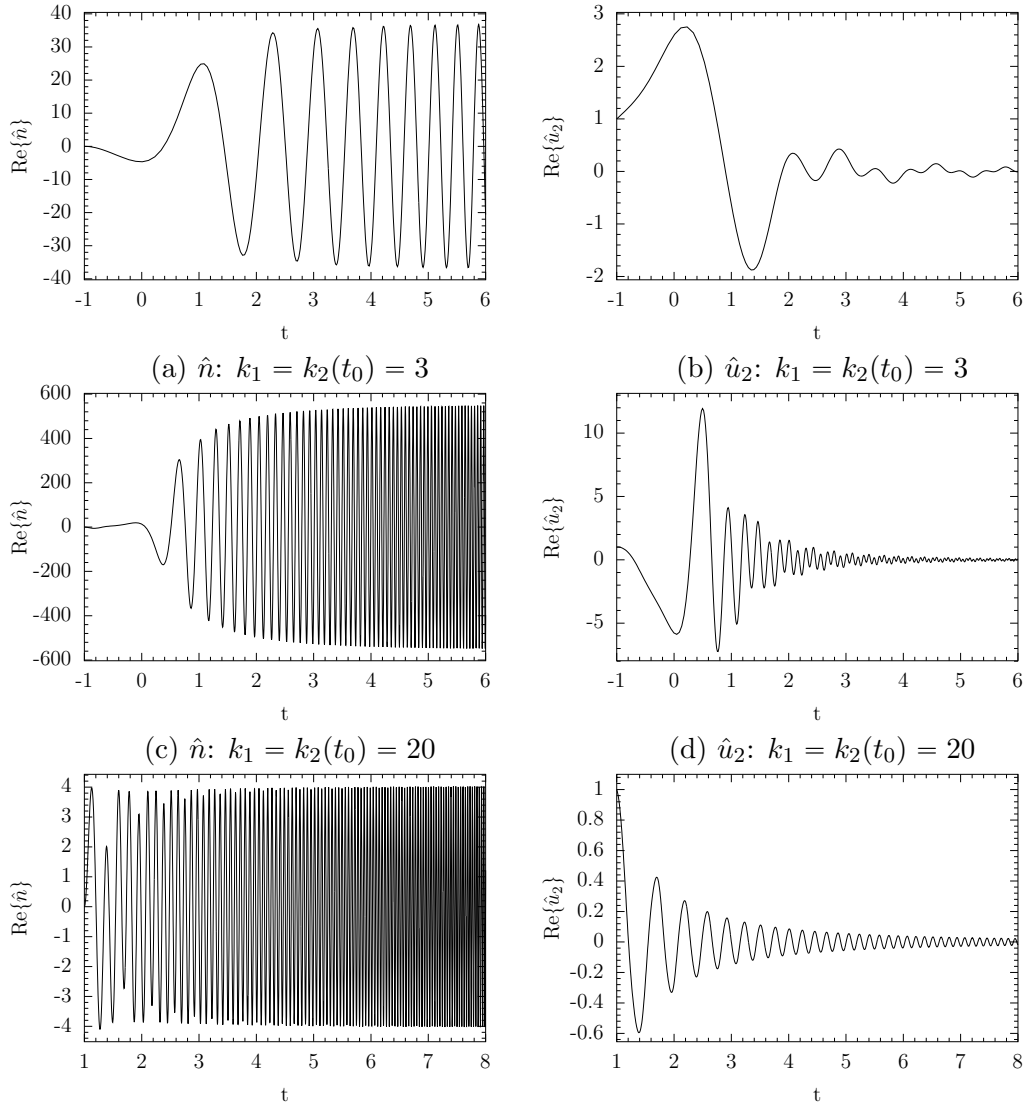

(a) $\hat{n}$: $k_1 = k_2(t_0) = 3$

(b) $\hat{u}_2$: $k_1 = k_2(t_0) = 3$

(c) $\hat{n}$: $k_1 = k_2(t_0) = 20$

(d) $\hat{u}_2$: $k_1 = k_2(t_0) = 20$

(e) $\hat{n}$: $k_1 = 20$, $k_2(t_0) = -20$

(f) $\hat{u}_2$: $k_1 = 20$, $k_2(t_0) = -20$

Figure 2.2: Real part of the number density and vertical fluid velocity for the initial conditions $\hat{n} = 0$, $\hat{u}_2 = 1$. Different orientations and magnitudes of the wavevector are considered. The initial time is t_0. The Reynolds number is taken to be infinitely large and the mass loading is $M = 0.5$.

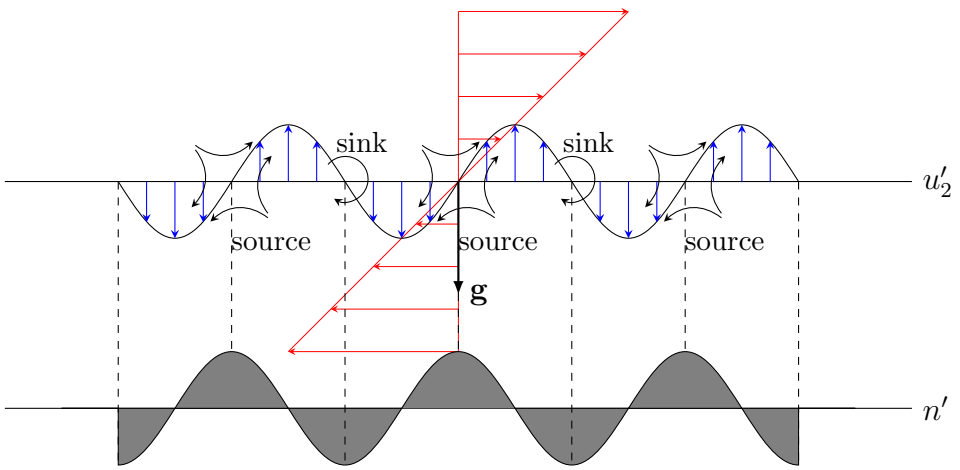

Figure 2.3: Mechanism of instability of a particle laden simple shear flow: a disturbance to the fluid flow (arrows) leads through preferential concentration to variations in particle number density (grey). The particle concentration variations create a fluctuating gravitational force which enhances the fluid velocity disturbance.

the wavenumber of the perturbation, while a comparison of figure 2.2 (c,d) to (e,f) indicates the effect of changing from an initially upstream to downstream wavevector orientation. We can see in figure 2.2(d) that the momentum disturbance for an upstream wavevector grows significantly in amplitude as the wavevector approaches a horizontal orientation and decays with time thereafter. This behaviour is qualitatively similar to that observed in Kelvin waves in a single phase fluid although the transient growth is stronger in the presence of inertial particles. The number density perturbation (figure 2.2(c)) remains small while the wavevector is upstream of the horizontal orientation and grows rapidly as the wavevector passes downstream of horizontal eventually saturating with an amplification of about 500. While this behavior does not represent an exponential growth of a small perturbation as can occur in a linearly unstable unsheared system, growth by more than two orders of magnitude can potentially lead to non-linear effects or secondary instabilities for a relatively modest finite amplitude of the initial disturbance.

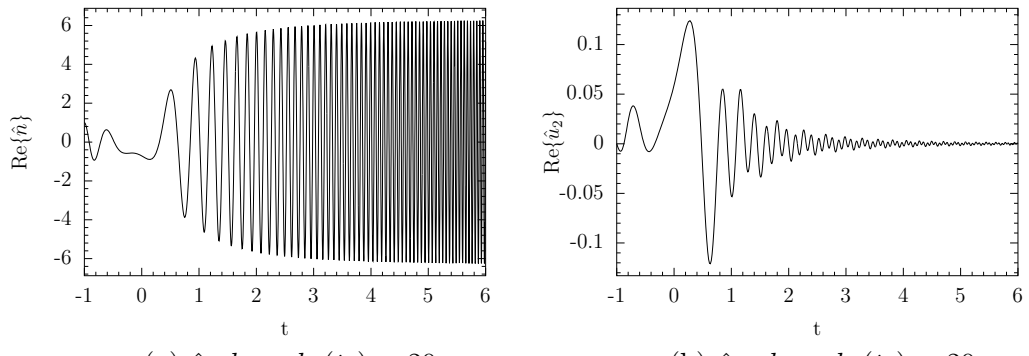

(a) $\hat{n}$: $k_1 = k_2(t_0) = 20$

(b) $\hat{u}_2$: $k_1 = k_2(t_0) = 20$

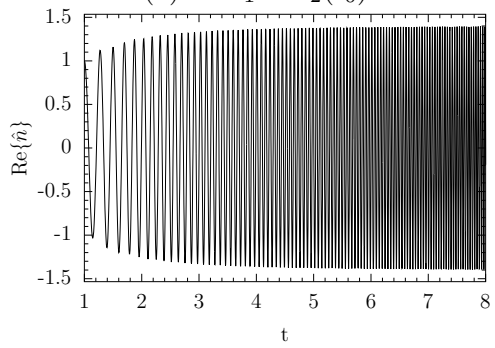

(c) $\hat{n}$: $k_1 = 20$, $k_2(t_0) = -20$

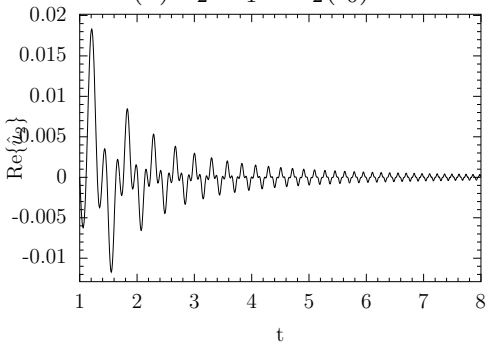

(d) $\hat{u}_2$: $k_1 = 20$, $k_2(t_0) = -20$

Figure 2.4: Real part of the number density and vertical fluid velocity for the initial conditions $\hat{n} = 1$, $\hat{u}_2 = 0$. Different orientations and magnitudes of the wavevector are considered. The initial time is t_0. The Reynolds number is taken to be infinitely large and the mass loading is $M = 0.5$.

Comparing figure 2.2 (a,b) to (c,d), we see that increasing the wavenumber of the perturbation increases both the amplitude and frequency of the resulting number density and momentum perturbations. This suggests that high wavenumber perturbations are most amplified at least in the inviscid limit. Assuming that a non-linear mechanism exists by which number density perturbations can create sustained momentum perturbations this observation would be consistent with the observation of Elghobashi and Truesdell (1993) that turbulence enhancement by settling particles is most pronounced at high wavenumbers. The number density perturbations in figure 2.2 (c) oscillate with a high frequency while changing amplitude at a slower rate, indicating that the dynamics are represented by mul-

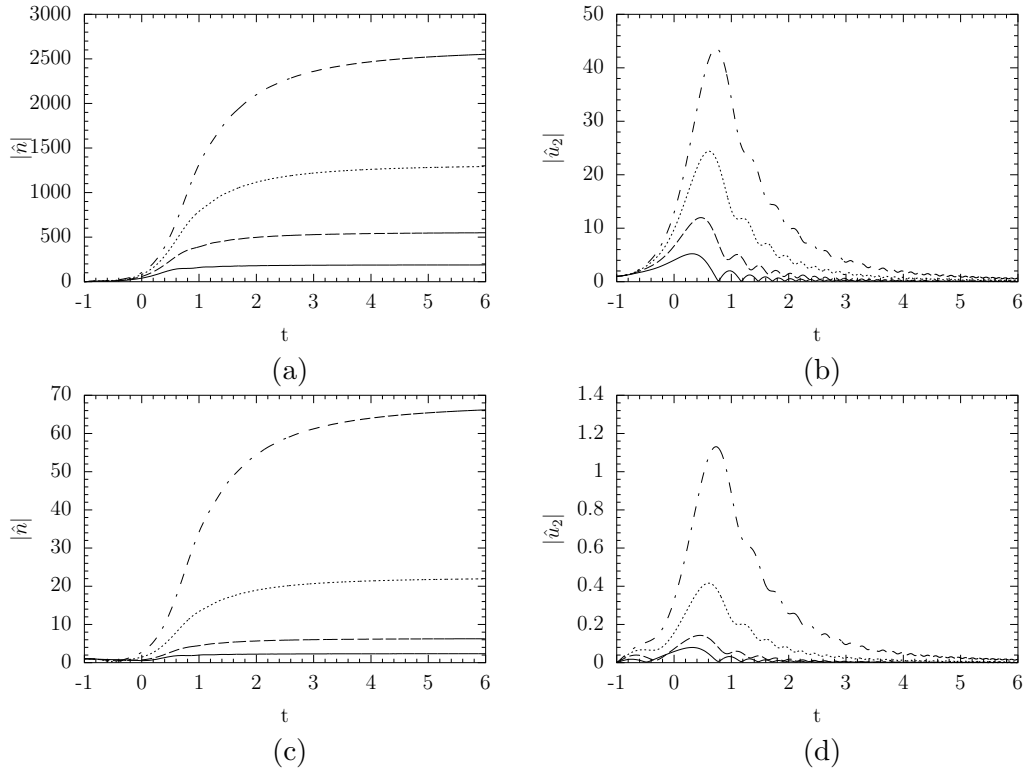

Figure 2.5: Amplitude of the number density and the vertical fluid velocity due to a momentum disturbance $\hat{n} = 0$, $\hat{u}_2 = 1$ (a,b) and a number density disturbance $\hat{n} = 0$, $\hat{u}_2 = 1$ (c,d) for an inviscid flow with $k_1 = k_2(t_0) = 20$. The mass loading is $M = 0.25$ (—), 0.5 (−−), 0.75 $(\cdots)$, 1 $(\cdot-)$.

tiple time scales in the limit $k_1 \gg 1$. An examination of the behavior at different wavenumbers indicates that the oscillations for values of t not too close to zero occur with a period of order $1/k_1$, while the amplitude varies over an $O(1)$ time scale. The period of the oscillations grows at $t \to 0$ and the period and time scale of amplitude variation are of the same order as t when $t = O(k_1^{1/2})$. These observations suggest that a multiple time scale asymptotic analysis is applicable for $k_1 \gg 1$, the limit in which the largest growth of the perturbation is observed. The behavior near $t = 0$ does not show a distinctive time scale separation, something that is indicative of a so called turning point, a point in time around which the different time scales collapse into one. These findings motivate the use of the

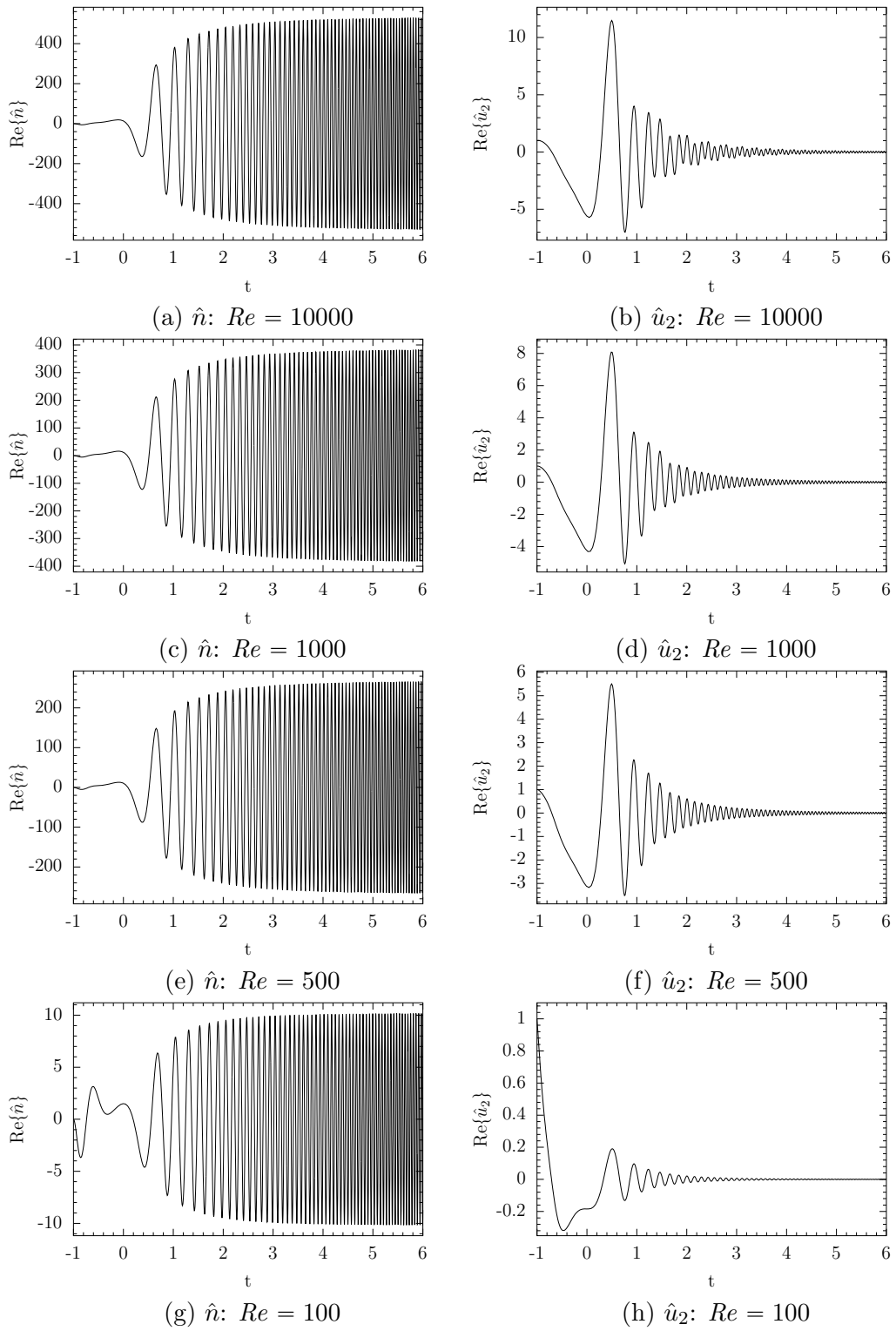

(a) $\hat{n}$: $Re = 10000$ (b) $\hat{u}_2$: $Re = 10000$

(c) $\hat{n}$: $Re = 1000$ (d) $\hat{u}_2$: $Re = 1000$

(e) $\hat{n}$: $Re = 500$ (f) $\hat{u}_2$: $Re = 500$

(g) $\hat{n}$: $Re = 100$ (h) $\hat{u}_2$: $Re = 100$

Figure 2.6: Number density and vertical fluid velocity for $Re = 10000,\ 1000,\ 500$ and 100. The initial conditions are a momentum perturbation and a wavevector such that $k_1 = k_2(t_0) = 20$. The mass loading is $M = 0.5$.

WKB asymptotic method, a method that addresses the separate time scales and connects them through the turning point.

Further evidence of the importance of the turning point at $t = 0$ can be seen by comparing the response to an initially upstream wave ($k_2(t_0) > 0$) in figure 2.2(c,d) and an initially downstream wave ($k_2(t_0) < 0$) in figure 2.2 (e,f). While a substantial growth of the disturbance occurs for an upstream wave, the downstream wave exhibits no growth of the number density disturbance and a monotonic decay in the amplitude of the momentum disturbance. From this comparison, we see that the turning point at $t = 0$ plays a crucial role in creating a large growth of the disturbance.

The mechanism of the instability is illustrated in figure 2.3. The divergence of the particle velocity field, which results in preferential concentration of particles, is proportional to the difference between the mean-squared strain rate and rotation rate (2.22). The base state simple shear flow has equal portions of strain and rotation and results in no preferential concentration. However, a sinusoidally varying fluid velocity perturbation alternately reinforces and attenuates the vorticity due to the imposed flow leading to regions where the number density is decreased and increased. This number density wave illustrated in grey in the figure is directly out of phase with the momentum disturbance. Nonetheless, the gravity force acting on the perturbed number density field (third term in the right-hand side of (2.30)) can reinforce the momentum wave if the two waves propagate relative to one another. This propagation does occur and is facilitated by the particles' inertia, the transient effects due to the shear-induced rotation of the wave and the sedimentation of the particles relative to the wave when the wavevector is not horizontal.

Now, consider an initial number density perturbation ($\hat{n} = 1$, $\hat{u}_2 = 0$). The

simulations reported in figure 2.4 show the same features at high k_1 (time scale separation, sharp transient at $t = 0$) as for a momentum perturbation. The final number density disturbance is again larger when the initial disturbance has a larger wavenumber. However, amplification of the number density disturbance created by an initial disturbance to the fluid velocity (figure 2.2 (c)) is much larger than that due to an initial number density disturbance (figure 2.4 (a)).

Figure 2.5 illustrates the effect that mass loading has on the growth in amplitude of the number density and fluid velocity due to an initial momentum disturbance (a,b) and an initial number density disturbance (c,d). It can be seen that saturation amplitude of the number density wave and the transient peak of the fluid velocity disturbance both grow significantly with increasing mass loading and this growth occurs for both initial number density and momentum disturbances.

The inviscid numerics indicate that the largest growth in the amplitude of disturbances occurs at the highest dimensionless wavenumbers, making the inviscid analysis ill posed. However, it may be expected that viscous effects will reduce the growth rate when the dimensional wavelength becomes smaller than $\sqrt{\nu/\Gamma}$ the distance over which viscous diffusion can damp fluid velocity variations during the $O(1/\Gamma)$ time required for shear induced rotation of the wave. We will see that this leads to a finite growth rate at an intermediate wavenumber in the well posed viscous problem.

The effect of finite Reynolds number on an initial momentum perturbation with $k_1 = 20$ is illustrated in figure 2.6, where the Reynolds number is varied from 10000 to 1000, 500 and 100. The $Re = 10000$ results in figure 2.6 (a,b) are very close to the corresponding inviscid results in figure 2.2 (c,d). In the range $Re = 1000$ to 500, the saturation amplitude of the number density wave begins to decreases and

by Re = 100 it is reduced over fifty-fold compared with the inviscid result. These results indicate that the large amplification of the disturbance that was seen in the inviscid numeric can be retained at large but finite Reynolds numbers.

We have suggested based on the inviscid numeric that an asymptotic analysis based on $k_1 \gg 1$ would be fruitful since the instability is most amplified in this limit. One might raise the concern, however, that viscous effects become increasingly important at higher wavenumber and might make high wavenumber disturbances less amplified in viscous gases. To explore this issue, we plot the saturation amplitude of the number density wave due to an initial upstream momentum disturbance as a function of wavenumber in figure 2.7 for two viscous cases with $Re = 1500$ and $Re = 2500$. At moderate values of the wavenumber, the saturation amplitude grows with amplitude similarly to the inviscid simulations. The amplitude then passes through a maximum and decreases at high wavenumbers. The optimal wavenumber is $k_1 \approx 35$ and $k_1 \approx 50$ at $Re = 1500$ and $Re = 2500$, respectively, and further analysis shows that the optimum wavenumber scales as $k_1 \sim Re^{1/2}$. The dimensional wavelength of the optimum perturbation is $(\nu/\Gamma)^{1/2}$. As one might expect, this is the wavelength at which viscous diffusion of momentum can propagate across the wavelength attenuating the momentum disturbance within the time it takes the wave to turn toward the horizontal and amplify. Smaller wavelength disturbances are damped by viscous diffusion while larger wavelengths experience less amplification as indicated by the inviscid numerics.

We have seen that the optimum wavenumber remains asymptotically large in a viscous fluid when the Reynolds number is asymptotically large. With this observation in mind, we will employ a WKB asymptotic analysis for $k_1 \gg 1$ to obtain more insight and analytical predictions for the growth of the disturbances,

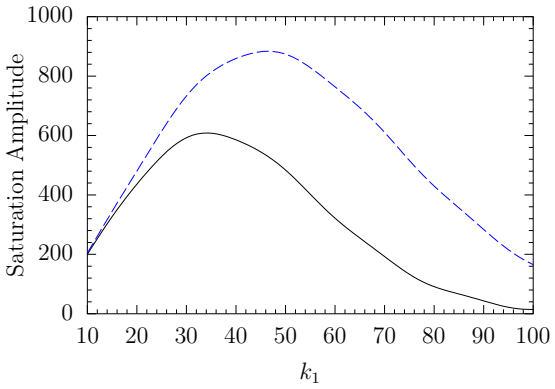

Figure 2.7: Saturation amplitude generated by a momentum perturbation at $t_0 = -1$ for a mass loading $M = 0.5$. The solid curve corresponds to $Re = 1500$ and the dashed curve to $Re = 2500$.

exploring the inviscid case in Section 3 and the viscous case in Section 4.

2.4 Asymptotic analysis for large wavenumber using WKB method: Inviscid analysis

2.4.1 Outer region

In this section, we apply a WKB multiple time scale asymptotic analysis valid for $k_1 \gg 1$ to the inviscid equations for the velocity and number density fluctuations. An in-depth explanation of the WKB method (sometimes referred to as WKBJ after Wentzel-Kramer-Brillouin-Jeffreys) has been provided in Hinch (1991) and Bender and Orszag (1999). The WKB approach is often used for analysing the behaviour of a wave in an inhomogeneous medium (or a potential barrier) with properties that might undergo a sharp transition. This transition layer would then connect the wave properties on either side. In the present context, the analysis we present is adapted for turning waves with a wavevector that varies with time. One

might consider then that the velocity and number density perturbations experience varying effects of gravity, preferential concentration, and particle inertia as they rotate and dilate.

It is most convenient to perform the WKB method on a single ordinary differential equation obtained by combining (2.29) and (2.30) as

$$\frac{d^2\hat{n}}{dt^2} + A(t)\frac{d\hat{n}}{dt} + B(t)\hat{n} = 0 \tag{2.31}$$

Making use of $k_2 = -k_1 t$ and dropping viscous terms, we can express the two coefficient functions A and B as:

$$\begin{aligned} A(t) &= k_1\left(i\frac{1+2M}{1+M}t + \frac{1}{k_1}\frac{2t}{1+t^2}\right) \\ &= k_1\left(a_0(t) + \frac{1}{k_1}a_1(t)\right) \qquad (2.32) \\ B(t) &= ik_1^2\left(i\frac{M}{1+M}t^2 + \frac{1}{k_1}\left(\frac{2}{1+M}\frac{t^2}{1+t^2} + \frac{1+3M}{1+M}\right)\right) \\ &= k_1^2\left(b_0(t) + \frac{1}{k_1}b_1(t)\right) \qquad (2.33) \end{aligned}$$

We begin by developing approximate solutions to (2.31) with (2.32) and (2.33) valid for times that are not close to zero, i.e., times at which the wavevector is either significantly upstream ($t < 0$) or downstream ($t > 0$) of the horizontal orientation. From the numerical solution in figure 2.2 (c), we expect that the number density field oscillates with an $O(k_1)$ frequency and that the frequency and amplitude of the wave vary over $O(1)$ time scales. The standard form of the solution sought by the WKB method involves an exponential of an expansion in k_1 of the form:

$$\hat{n}(t) = \exp\left(k_1\sum_{n=0}^{\infty}\left(\frac{1}{k_1}\right)^n S_n(t)\right) \tag{2.34}$$

where the first term with an imaginary $S_0(t)$ provides the $O(k_1)$ frequency that varies over $O(1)$ time periods and S_1 provides a modulation of the amplitude over

$O(1)$ time scales. It is generally expected that this form will provide an accurate representation of the solution for most times outside a short interval around a point in time referred to as a turning point. The exponential form is valid as long as $(1/k^n)\ S_n \ll (1/k^{n+1})\, S_{n+1}$ is satisfied. It can be seen from (2.33) that this outer solution will break down when $b_0(t) \sim b_1(t)/k_1$, corresponding to times $t \sim 1/\sqrt{k_1}$. An inner solution valid for such small times when the wavevector is nearly horizontal will be developed later. Substituting this expansion in the number density equation yields a series of ODEs:

$$\begin{cases} O(k_1) & {S'}_0^2 + a_0 {S'}_0 + b_0 = 0 \\ O(1) & (2{S'}_0 + a_0){S'}_1 + {S''}_0 + a_1 {S'}_0 + b_1 = 0 \\ O(\frac{1}{k_1^{n-1}}) & (2{S'}_0 + a_0){S'}_n + {S''}_{n-1} + \sum_{j=1}^{n-1} {S'}_j {S'}_{n-j} + a_1 {S'}_{n-1} = 0 \quad \forall n \geqslant 2 \end{cases} \tag{2.35}$$

The order $O(k_1)$ equation is a quadratic equation for S'_0 and yields a pair of solutions:

$${S'}_0 = \frac{-a_0 \pm (a_0^2 - 4b_0)^{1/2}}{2} \tag{2.36}$$

Each of the higher (nth) order equations provides a linear equation for ${S'}_n$ in terms of known results from the previous orders. In particular, the first order solution is

$${S'}_1 = -\frac{{S''}_0 + b_1 + a_1 {S'}_0}{2{S'}_0 + a_0} \tag{2.37}$$

giving one solution for each of the solutions for S_0. As in most applications of the WKB method, zeroth and first order terms in the expansion provide an adequate approximation of the outer solutions by specifying the time varying frequency and amplitude, respectively. To understand the physical nature of the two solutions, it is useful to express a_0 and b_0 as functions of terms appearing in the conservation

equations:

$$a_0 = \frac{1}{k_1}\left(\frac{M}{1+M}\frac{FT[\mathbf{1}_g \cdot \nabla u_2]}{FT[u_2]} + \frac{FT[\mathbf{1}_g \cdot \nabla n]}{FT[n]}\right) \tag{2.38}$$

$$b_0 = \frac{1}{k_1^2}\frac{M}{1+M}\frac{FT[\mathbf{1}_g \cdot \nabla u_2]}{FT[u_2]}\ \frac{FT[\mathbf{1}_g \cdot \nabla n]}{FT[n]} \tag{2.39}$$

where FT denotes the Fourier transform operator. The two solution for the zeroth order are:

$$k_1 S_0{}^{\mathtt{M}} = \int_0^t \frac{M}{1+M}\frac{FT[\mathbf{1}_g \cdot \nabla u_2]}{FT[u_2]}dt' = -i\frac{M}{1+M}k_1\frac{t^2}{2} \tag{2.40}$$

$$k_1 S_0{}^{\mathtt{N}} = \int_0^t \frac{FT[\mathbf{1}_g \cdot \nabla n]}{FT[n]}dt' = -ik_1\frac{t^2}{2} \tag{2.41}$$

We will refer to $S_0{}^{\mathtt{N}}$ as the number density mode (or `N` mode) since its frequency arises from the rate of convection of particle number density by sedimentation as it appears in the number density conservation equation. $S_0{}^{\mathtt{M}}$ will be called the momentum mode (`M` mode), because its frequency arises from the convection of momentum by particle sedimentation as it appears in the momentum conservation equation. The propagation of momentum differs from the settling speed by a factor of $M/(1+M)$ because momentum is transported only by the particles (M) but is stored by both particle and gas ($1+M$). The reader is referred to section 2.4.2 for further explanations of this choice of nomenclature.

The amplitudes of the modes are determined by $S_1{}^{\mathtt{M}}$ and $S_1{}^{\mathtt{N}}$ and Equation (2.37) which governs these quantities can be written as:

$$S_1' = -\frac{a_1}{2} - \frac{1}{4}\frac{u'}{u} \pm \frac{1}{2}\frac{a_0' + a_1 a_0 - 2b_1}{u^{1/2}} \tag{2.42}$$

where $u = a_0^2 - 4b_0$. We can integrate the equation to find the first order term:

$$S_1{}^{\mathtt{M}}(t) = -(1+2M)\ln(|t|) - (1-M)\ln(1+t^2) \tag{2.43}$$

$$S_1{}^{\mathtt{N}}(t) = 2M\ln(|t|) - M\ln(1+t^2) \tag{2.44}$$

Therefore the two modes are :

$$\hat{n}^{\mathtt{M}}(t) = \frac{1}{|t|^{1+2M}} \frac{1}{(1+t^2)^{1-M}} \exp\left(-ik_1 \frac{M}{1+M} \frac{t^2}{2}\right) \tag{2.45}$$

$$\hat{n}^{\mathtt{N}}(t) = \left(\frac{t^2}{1+t^2}\right)^M \exp\left(-ik_1 \frac{t^2}{2}\right) \tag{2.46}$$

Here it becomes clear that $k_1 S_0$ constitutes the phase, while S_1 controls the amplitude. Notice that the two modes are waves with effective angular frequencies $\omega^{\mathtt{M}}(t) = \frac{k_1}{2}\frac{M}{1+M}t$ for the momentum mode and $\omega^{\mathtt{N}}(t) = \frac{k_1}{2}t$ for the number density mode. These frequencies depend on time and increase as $|t|$ increases and the wavevector is aligned with gravity. The increase in frequency with $|t|$ is readily apparent in figure 2.2 (c,d) and it results from the fact that the wavelength of the disturbance decreases as $1/t$ as $|t| \to \infty$ so that the time required for particles or momentum to traverse the wave decreases. It is interesting to note that the amplitude of the momentum mode grows when the wavevector is upstream of the horizontal ($t < 0$) and decays with time downstream ($t > 0$). This behavior might be expected as the case $M = 0$ corresponding to a single phase fluid recovers Kelvin modes, which are known to undergo transient amplification. In contrast the number density mode decreases in amplitude for $t < 0$ and grows for $t > 0$. It will be seen that the turning point near $t = 0$ allows a transformation of disturbance amplitude between the two modes. Thus, an upstream momentum mode that triggers a downstream number density mode can be expected to lead to the largest growth of perturbations.

To obtain more insight into the nature of the modes it is useful to consider their fluid velocity disturbances, which can be obtained from (2.29) as

$$\hat{u}_2^{\mathtt{M}}(t) = \left(\frac{1}{2}\frac{t}{1+M} + i\frac{1}{2k_1}\left[\frac{1+2M}{t} + (1-M)\frac{2t}{1+t^2}\right]\right)\hat{n}^{\mathtt{M}}(t) \tag{2.47}$$

$$\hat{u}_2^{\mathtt{N}}(t) = -i\frac{M}{k_1}\left(\frac{1}{t} - \frac{t}{1+t^2}\right)\hat{n}^{\mathtt{N}}(t) \tag{2.48}$$

As suggested by its name, the number density mode has a fluid velocity that is $O(1/k_1)$ smaller than its number density. The momentum mode has comparable fluid velocity and number density disturbances.

The general solution is a linear combination of the two modes

$$\hat{n}(t) = \Lambda_{\mathtt{M}}\hat{n}^{\mathtt{M}}(t) + \Lambda_{\mathtt{N}}\hat{n}^{\mathtt{N}}(t) \tag{2.49}$$

$$\hat{u}_2(t) = \Lambda_{\mathtt{M}}\hat{u}_2^{\mathtt{M}}(t) + \Lambda_{\mathtt{N}}\hat{u}_2^{\mathtt{N}}(t) \tag{2.50}$$

in which the coefficients $\Lambda_{\mathtt{M}}$ and $\Lambda_{\mathtt{N}}$ depend on the choice of initial conditions. For a fluid velocity perturbation with no initial number density disturbance, one obtains a momentum and a number density mode with comparable magnitudes $\Lambda_{\mathtt{M}} \sim \Lambda_{\mathtt{N}}$. However, the subsequent fluid velocity field is produced primarily by the momentum mode since $\hat{u}_2^{\mathtt{N}} \ll \hat{u}_2^{\mathtt{M}}$. An initial perturbation to the number density field produces primarily a number density mode with a much smaller momentum mode $\Lambda_{\mathtt{M}} \sim \Lambda_{\mathtt{N}}/k_1$. These observations along with our previous discussion of the temporal dynamics of the modes help to explain why the fluid velocity disturbances in figure 2.2 (c,d) produced much larger growth than the number density disturbances in figure 2.4 (a,b). The velocity initial condition produces an $O(1)$ momentum mode that grows up to the turning point and then induces a number density mode that grows downstream of the turning point. On the other hand, the number density initial condition primarily induces a number density mode whose amplitude declines in the upstream orientations and a much smaller momentum mode that grows in the upstream region.

2.4.2 Mechanisms leading to time variation of the amplitudes of the modes in the outer region

In the previous discussion, we solved systematically for S_0 and S_1 in the exponential ansatz and obtained the N and M modes, two waves with effective angular frequencies $\omega^{\mathtt{M}}(t) = \frac{k_1}{2}\frac{M}{1+M}t$ and $\omega^{\mathtt{N}}(t) = \frac{k_1}{2}t$ and respective amplitudes $(\tilde{u}_2^{\mathtt{N}}, \tilde{n}^{\mathtt{N}})$ and $(\tilde{u}_2^{\mathtt{M}}, \tilde{n}^{\mathtt{M}})$. Thus, for example, the number density and fluid velocity in the number density mode can be written in terms of the frequency and amplitudes as:

$$\begin{aligned}
\hat{n}^{\mathtt{N}}(t) &= \tilde{n}^{\mathtt{N}} \exp\left(i\omega^{\mathtt{N}}(t)t\right) \\
&= \left(\frac{t^2}{1+t^2}\right)^M \exp\left(-ik_1\frac{t^2}{2}\right) \\
\hat{u}_2^{\mathtt{N}}(t) &= \tilde{u}_2^{\mathtt{N}} \exp(i\omega^{\mathtt{N}}(t)t) \\
&= -i\frac{M}{k_1}\left(\frac{1}{t} - \frac{t}{1+t^2}\right)\hat{n}^{\mathtt{N}}(t)
\end{aligned}$$

Substituting $\hat{n}^{\mathtt{N}}(t) = \tilde{n}^{\mathtt{N}} \exp(i\omega^{\mathtt{N}}(t)t)$ and $\hat{u}_2^{\mathtt{N}}(t) = \tilde{u}_2^{\mathtt{N}} \exp(i\omega^{\mathtt{N}}(t)t)$ into (2.29) and (2.30), yields the following equations for the time variation of the amplitudes for the N mode:

$$\frac{d\tilde{n}^{\mathtt{N}}}{dt} = 2ik_1\tilde{u}_2^{\mathtt{N}} \tag{2.51}$$

$$\frac{d\tilde{u}_2^{\mathtt{N}}}{dt} = -\frac{ik_2}{1+M}\tilde{u}_2^{\mathtt{N}} + \frac{2k_2k_1}{k^2}\tilde{u}_2^{\mathtt{N}} - \frac{M}{1+M}\frac{k_1^2}{k^2}\tilde{n}^{\mathtt{N}} \tag{2.52}$$

Thus, in a reference frame of a wave that rotates with the shear flow and translates with the settling velocity, the amplitude of the number density in (2.51) changes solely due to preferential concentration. The three terms on the right-hand side of (2.52) indicate that the velocity evolves due to the propagation of momentum by settling, a shear-induced amplification upstream and diminution downstream of the horizontal orientation, and the gravitational forcing by the particles, respectively. Recalling that the fluid velocity associated with the N mode is $O(1/k_1)$ smaller than

the number density, i.e., $\tilde{u}_2^{\mathtt{N}} \sim \tilde{n}^{\mathtt{N}}/k_1$, the leading order solution of (2.52) involves a quasi-steady balance of the production of momentum due to the gravitational forcing and its transport by settling induced momentum flux, i.e.,

$$\frac{ik_2}{1+M}\tilde{u}_2^{\mathtt{N}} = -\frac{M}{1+M}\frac{k_1^2}{k^2}\tilde{n}^{\mathtt{N}} \tag{2.53}$$

which, when using $k_2 = -k_1 t$, becomes

$$\hat{u}_2^N = -i\frac{M}{k_1}\frac{1}{t(1+t^2)}\hat{n}^N \tag{2.54}$$

The fluid velocity induced by the gravitational forcing decays as $1/(t(1+t^2))$ with increasing t because the smaller wavelength at large time increases the rate of momentum transport across the wave and the alignment of the wavevector toward the vertical direction reduces the portion of the gravitational forcing that drives a fluid velocity rather than a hydrostatic pressure field. Inserting the quasi-static approximation for the fluid velocity field (2.53) into the number density equation (2.51), we see that

$$t\frac{d\tilde{n}^{\mathtt{N}}}{dt} - \frac{2M}{1+t^2}\tilde{n}^{\mathtt{N}} = 0 \tag{2.55}$$

which integrates to

$$\tilde{n}^{\mathtt{N}} = (t^2/(1+t^2))^M. \tag{2.56}$$

The mechanism for the decay (in the upstream region) and growth (in the downstream region) is illustrated in figure 2.8. The number density field creates a wave of fluid motion that moves downward in regions of high concentration and upward in regions of low concentration (dashed lines). However, the momentum disturbance is shifted upward because the inertia of the gas causes momentum to move upward relative to the settling particles resulting in the momentum disturbance illustrated by the solid line. This momentum disturbance through preferential concentration attenuates the number density field in the upstream region and reinforces it in the downstream region.

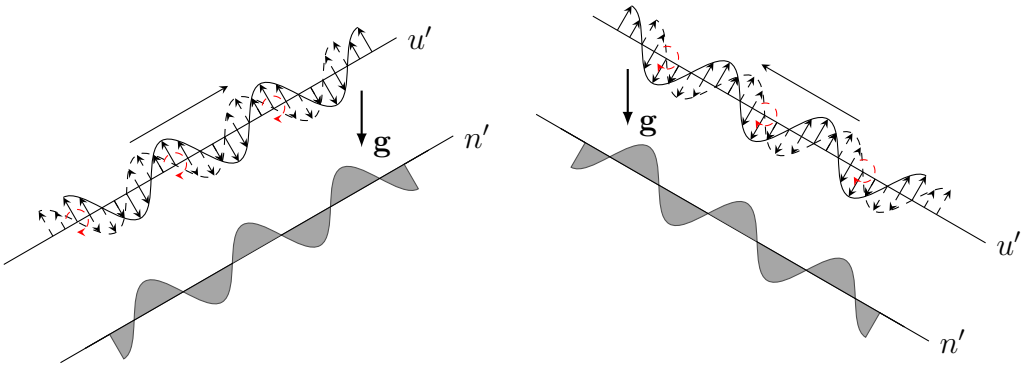

(a) N mode in the upstream region (b) N mode in the downstream region

Figure 2.8: Mechanism leading to growth of the N mode in the upstream region and attenuation of the N mode in the downstream region. Waves are illustrated in the reference frame of the number density field.

Proceeding to analyze the M mode in a similar manner, we consider the ansatz $\hat{n}^{\mathtt{M}}(t) = \tilde{n}^{\mathtt{M}} \exp(i\omega^{\mathtt{M}}(t)t)$ and $\hat{u}_2^{\mathtt{M}}(t) = \tilde{u}_2^{\mathtt{M}} \exp(i\omega^{\mathtt{M}}(t)t)$ and substitute in (2.29) and (2.30),

$$\frac{d\tilde{n}^{\mathtt{M}}}{dt} = \frac{ik_2}{1+M}\tilde{n}^{\mathtt{M}} + 2ik_1\tilde{u}_2^{\mathtt{M}} \tag{2.57}$$

$$\frac{d\tilde{u}_2^{\mathtt{M}}}{dt} = 2\frac{k_2k_1}{k^2}\tilde{u}_2^{\mathtt{M}} - \frac{M}{1+M}\frac{k_1^2}{k^2}\tilde{n}^{\mathtt{M}} \tag{2.58}$$

The M mode wave travels due to the momentum propagation caused by the settling velocity. In this reference frame, the wave at high wavenumber satisfies

$$0 = \frac{ik_2}{1+M}\tilde{n}^{\mathtt{M}} + 2ik_1\tilde{u}_2^{\mathtt{M}} \tag{2.59}$$

$$\frac{d\tilde{u}_2^{\mathtt{M}}}{dt} = 2\frac{k_2k_1}{k^2}\tilde{u}_2^{\mathtt{M}} - \frac{M}{1+M}\frac{k_1^2}{k^2}\tilde{n}^{\mathtt{M}} \tag{2.60}$$

It consists of a quasi-steady number density field resulting from a balance of preferential concentration and the settling of the particles downward relative to the wave, and a momentum field whose dynamic response is driven by the convection of the base state shear flow momentum across streamlines by the disturbance (first

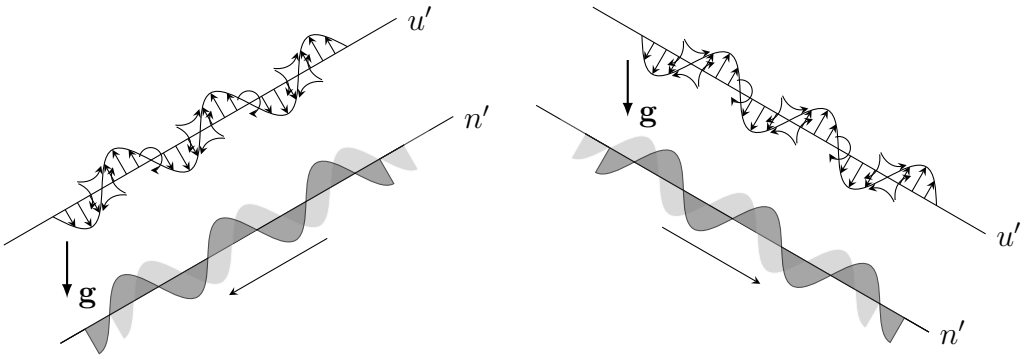

(a) M mode in the upstream region (b) M mode in the downstream region

Figure 2.9: Preferential concentration mechanism for the amplification of the M mode in the upstream region and attenuation of the M mode in the downstream region. The waves are illustrated in the reference frame of the fluid velocity field.

term on the right-hand side of (2.60)) and the gravitational forcing of the particles (second term on the right-hand side). Both these mechanisms lead to an upstream growth and downstream decay of the amplitude of the momentum wave. The upstream growth and downstream decay due to the first term was derived by Lord Kelvin. The mechanism leading to the upstream growth and downstream decay due to the gravitational forcing is illustrated in figure 2.9. The fluid velocity field creates a number density field (light grey) due to preferential concentration which is shifted downward relative to the wave by sedimentation (dark grey) so that its gravitational force reinforces the wave in the upstream and attenuates it in the downstream region.

2.4.3 Inner region

As noted earlier, the outer solutions obtained in the previous section break down for times near $t = 0$ corresponding to wavevector orientations that are nearly perpendicular to the gravity and velocity gradient direction. We now seek an

inner solution valid in the turning point near $t = 0$. To facilitate the analysis we first transform equation (2.31) into the so called canonical form (Hinch, 1991). Using the transformation:

$$x(t) = \hat{n}(t) \exp\left(\frac{1}{2}\int^t A(t')dt'\right) \tag{2.61}$$

the number density equation becomes:

$$\frac{1}{k_1^2}\frac{d^2x}{dt^2} + g(t)x = 0 \tag{2.62}$$

where

$$\begin{aligned} g(t) &= \frac{1}{k_1^2}\left[B(t) - \frac{1}{2}\frac{dA}{dt}(t) - \frac{1}{4}A^2(t)\right] \\ &= -\frac{1}{4}\left(\frac{2i\pi t}{1+M}\right)^2 + \frac{1}{k_1}\left(i\pi\frac{1+4M}{1+M} + 2i\pi\frac{1-2M}{1+M}\frac{t^2}{1+t^2}\right) - \frac{1}{k_1^2}\frac{1}{1+t^2} \\ &= g_0(t) + \frac{1}{k_1}g_1(t) + \frac{1}{k_1^2}g_2(t) \end{aligned}$$

This equation takes the form of a wave equation with a time dependent frequency. The small parameter $1/k_1^2$ multiplying the highest order is a classical feature of equations necessitating a multiple time scales approach. When $t = O(1)$, $g = O(1)$ and the frequency is $O(k_1)$ as assumed in the outer solution. However, as $t \to 0$, $g_0 \to 0$ and the exponential expansion (2.34) breaks down when $g_0(t) \sim (1/k_1)\, g_1(t)$, corresponding to $t = O(1/\sqrt{k_1})$. Thus, the inner region time scale is $\tau = t\sqrt{k_1} = O(1)$. We verify that the third term can be neglected by noting that $g_0(\tau) \sim (1/k_1)\, g_1(\tau) = O(1/k_1)$ while $(1/k_1^2)g_2(\tau) = O(1/k_1^2)$. In terms of the inner region time scale, equation (2.62) becomes:

$$\frac{d^2x}{d\tau^2} + \left(\frac{1}{4}\frac{\tau^2}{(1+M)^2} + i\frac{1+4M}{2(1+M)}\right)x = 0 \tag{2.63}$$

This equation is a parabolic cylinder equation and can be placed in a standard form by defining a time variable $T = \tau/\sqrt{2(1+M)}$, so that

$$\frac{d^2x}{dT^2} + (T^2 + \lambda)x = 0 \tag{2.64}$$

where $\lambda = i(1+4M)$. The two solutions of this equation are parabolic cylinder functions $D_{-\frac{1+i\lambda}{2}}[\pm(1+i)T]$ as defined by Gradshteyn *et al.* (2000).

To summarise, solutions for the number density disturbance have been obtained in terms of an outer solution for the upstream wavevectors ($t<0$), an inner solution for the turning point region when the wavevector is nearly horizontal ($t\to 0$), and an outer solution for the downstream wavevector region ($t>0$) and are given by:

$$\hat{n}(t) = \begin{cases} \overline{\Lambda}_{\mathtt{N}}\hat{n}^{\mathtt{N}} + \overline{\Lambda}_{\mathtt{M}}\hat{n}^{\mathtt{M}} & t = O(1)\ t<0 \\ \left(\Lambda_+ D_{2M}[\frac{(1+i)\sqrt{k_1}t}{\sqrt{2(1+M)}}] + \Lambda_- D_{2M}[-\frac{(1+i)\sqrt{k_1}t}{\sqrt{2(1+M)}}]\right) & \\ \qquad \times \exp(\frac{i}{4}\frac{1+2M}{1+M}k_1\frac{t^2}{2}) & t = O(\frac{1}{\sqrt{k_1}}) \\ \underline{\Lambda}_{\mathtt{N}}\hat{n}^{\mathtt{N}} + \underline{\Lambda}_{\mathtt{M}}\hat{n}^{\mathtt{M}} & t = O(1)\ t>0 \end{cases} \tag{2.65}$$

While the solutions in both outer regions, upstream and downstream, are linear combinations of M and N modes, the coefficients of the modes will differ in the two regions. For this reason, we used over-lines for the pair $\{\Lambda_{\mathtt{M}}, \Lambda_{\mathtt{N}}\}$ in the upstream region, and under-lines in the downstream region. The number density and momentum modes, $\hat{n}^{\mathtt{N}}$ and $\hat{n}^{\mathtt{M}}$, are given by (2.45) and (2.46).

The behavior of Parabolic Cylinder functions in the matching region ($|t| \gg 1/\sqrt{k_1}$), is similar to a combination of N and M modes. This makes it possible to directly match the coefficients in the upstream region with the ones in the downstream region, yielding

$$\begin{cases} \underline{\Lambda}_{\mathtt{N}} = & -\frac{i\sqrt{i}}{M\Gamma(2M)}\sqrt{\frac{\pi}{2}}\left(\frac{k_1}{1+M}\right)^{1/2+2M} e^{-i\pi M}\overline{\Lambda}_{\mathtt{M}} + e^{-2\pi i M}\overline{\Lambda}_{\mathtt{N}} \\ \underline{\Lambda}_{\mathtt{M}} = & -e^{-2\pi i M}\overline{\Lambda}_{\mathtt{M}} - i\sqrt{i}\sqrt{\frac{2}{\pi}}2M\sin(2M\pi)\Gamma(2M)e^{-i\pi M}(\frac{1+M}{k_1})^{1/2+2M}\overline{\Lambda}_{\mathtt{N}} \end{cases} \tag{2.66}$$

The mathematical details of the matching procedure can be found in appendix A.

The matching provides a mixing of modes as one crosses the turning point. In fact, one can see from (2.66) that each of the upstream modes generate both N and

M modes in the downstream region. A closer examination shows that an incoming N mode creates a downstream N mode whose coefficient differs from that for the upstream mode only by a phase shift as well as a momentum mode whose coefficient is smaller by a factor $k_1^{-1/2-2M}$ than that of the incoming N mode. The latter small contribution decays further with time for $t > 0$. An upstream M mode is much more effective in creating downstream disturbances. It induces a downstream M mode with a phase shift relative to the upstream mode. More importantly, it generates a downstream N mode whose coefficient is $k_1^{1/2+2M}$ larger than the upstream M mode coefficient. The growth of the number density and velocity disturbances does not occur primarily within the turning point since $|\overline{\Lambda}_{\mathtt{M}}\hat{n}^{\mathtt{M}}(t = -1/\sqrt{k_1})| \sim |\underline{\Lambda}_{\mathtt{N}}\hat{n}^{\mathtt{N}}(t = 1/\sqrt{k_1})|$. However, by transforming these disturbances from an N mode to an M mode, the disturbance is able to grow in both the upstream and downstream regions. This observation explains the previous numerical results (figures 2.2 and 2.4) that an initial condition corresponding to an upstream fluid velocity disturbance which primarily excites the M mode leads to a much larger downstream number density disturbance than is created by an initial disturbance of the number density field.

To demonstrate the validity of the WKB analysis presented above, we present in figure 2.10 a comparison between the WKB analytical predictions for the upstream and downstream outer regions and results obtained by numerically integrating the original ordinary differential equations. The downstream WKB results make use of the relationships (2.66) between upstream and downstream mode coefficients obtained by matching with the inner region. The oscillations in the amplitudes (more visible for the velocity), which are also reproduced by the theoretical solution, come from the interferences between the two complex modes. The figure proves the validity of the matching relations (2.66) and validates the treatment of

the inner region.

To provide a succinct measure of the growth of the number density fluctuations due to an initial perturbation, we define two growth functions, G_1 corresponding to an initial number density perturbation, ($\hat{n}|_{t_0} = 1$ and $\hat{u}_2|_{t_0} = 0$) and G_2 to for a momentum perturbation ($\hat{n}|_{t_0} = 1$ and $\hat{u}_2|_{t_0} = 0$), in terms of the ratio :

$$G_i(k_1, M, t_0) = \lim_{t\to+\infty} \frac{||\mathbf{x}(t)||}{||\mathbf{x}(t_0)||} \quad i \in \{1, 2\} \tag{2.67}$$

where the vector $\mathbf{x} = (\hat{n}, \hat{u}_2)$ is a generalised representation of the solution, and $||\mathbf{x}|| = \sqrt{\hat{n}^2 + \hat{u}_2^2}$ the 2-norm. The index i represents the type of initial condition considered: by definition $i = 1$ refers to a number density perturbation and $i = 2$ refers to a momentum perturbation. Note that in both cases $||\mathbf{x}(t_0)|| = 1$, and because u_2 decays at long times, the growth functions G_1 and G_2 represent the saturation amplitude of the number density due to a unity perturbation of each of the two types, i.e.,

$$G_i(k_1, M, t_0) = \lim_{t\to+\infty} |\hat{n}(t)| \quad i \in \{1, 2\} \tag{2.68}$$

Figure 2.11a shows the growth function G_1 for different values of the mass loading M. The initial time has been set to $t_0 = -1$ which means that the wave is initiated in an upstream configuration with a 45 angle from the horizontal axis ($k_2 = k_1$). We observe good agreement between the theory (dashed lines) and the simulations (solid lines) as we increase k_1. The growth for $M = 0.25$ shows a weak dependence on k_1. This can be explained simply by looking at the form G_1 takes using the theoretical expressions derived so far:

$$
\begin{aligned}
G_1^{Th}(k_1, M) &= \lim_{t\to} |\hat{n}(t)| = |\underline{\Lambda}_{\mathtt{N}}| \\
&= \left| e^{-2\pi i M}\overline{\Lambda}_{\mathtt{N}} - \frac{i\sqrt{i}}{M\Gamma(2M)}\sqrt{\frac{\pi}{2}}\left(\frac{k_1}{1+M}\right)^{1/2+2M} e^{-i\pi M}\overline{\Lambda}_{\mathtt{M}} \right| \quad (2.69)
\end{aligned}
$$

The theoretical growth G_1^{Th} is a sum (weighted by some constants) of $\overline{\Lambda}_{\mathtt{N}}$ and $k_1^{1/2+2M}\overline{\Lambda}_{\mathtt{M}}$. Now, at the initial time t_0, which was taken to be $|t_0| \sim 1$, the modes scale as ($\hat{n}^{\mathtt{N}}|_{t_0} \sim 1$, $\hat{u}_2^{\mathtt{N}}|_{t_0} \sim 1/k_1$) and ($\hat{n}^{\mathtt{M}}|_{t_0} \sim 1$, $\hat{u}_2^{\mathtt{M}}|_{t_0} \sim 1$). In order to satisfy the initial conditions, $\overline{\Lambda}_{\mathtt{N}}\hat{n}^{\mathtt{N}}|_{t_0} + \overline{\Lambda}_{\mathtt{M}}\hat{n}^{\mathtt{M}}|_{t_0} = 1$ and $\overline{\Lambda}_{\mathtt{N}}\hat{u}_2^{\mathtt{N}}|_{t_0} + \overline{\Lambda}_{\mathtt{M}}\hat{u}_2^{\mathtt{M}}|_{t_0} = 0$ the coefficients $\overline{\Lambda}_{\mathtt{N}}$ and $\overline{\Lambda}_{\mathtt{M}}$ scale as $\overline{\Lambda}_{\mathtt{N}} \sim 1$ and $\overline{\Lambda}_{\mathtt{M}} \sim 1/k_1$. Hence the growth is a sum of a function of order 1 and a function $k_1^{1/2+2M}\overline{\Lambda}_{\mathtt{M}}$ that varies as $k_1^{-1/2+2M}$, which explains the absence of dependence on k_1 for $M = 0.25$.

In figure 2.11b , we plot the evolution of the growth function G_2 as defined in the case ($\hat{n}|_{t_0} = 0$, $\hat{u}_2|_{t_0} = 1$) for different values of the mass loading. Contrary to the previous case, we do not observe a plateau for $M = 0.25$. Despite, G_2 having the same expression as G_1, i.e.,

$$
\begin{aligned}
G_2^{Th}(k_1, M) &= |\underline{\Lambda}_{\mathtt{N}}| \\
&= \left| e^{-2\pi i M}\overline{\Lambda}_{\mathtt{N}} - \frac{i\sqrt{i}}{M\Gamma(2M)}\sqrt{\frac{\pi}{2}}\left(\frac{k_1}{1+M}\right)^{1/2+2M} e^{-i\pi M}\overline{\Lambda}_{\mathtt{M}} \right| \quad (2.70)
\end{aligned}
$$

the initial conditions in the momentum perturbation case lead to $\overline{\Lambda}_{\mathtt{N}} \sim \overline{\Lambda}_{\mathtt{M}} \sim 1$, making the second term in the growth a function of $k_1^{1/2+2M}$.

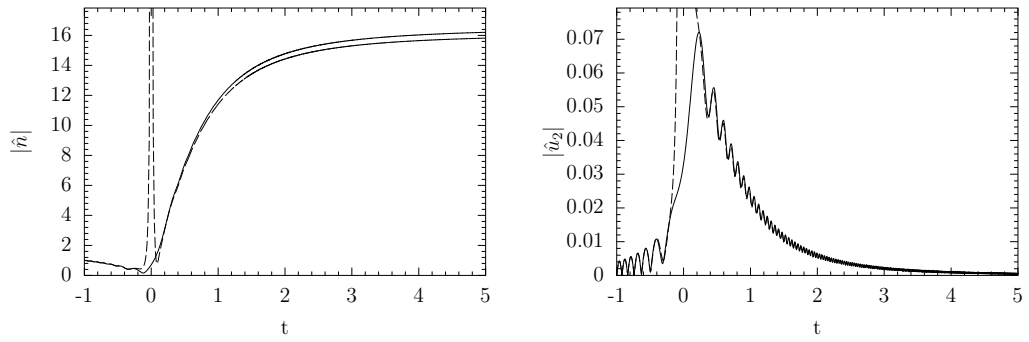

(a) (b)

Figure 2.10: Comparison of the amplitude of number density (a) and velocity (b) predicted by numerical solution of the ordinary differential equations (solid line) and the outer WKB analytical solutions (dashed line). The initial conditions are for a number density $\hat{n} = 1$, $\hat{u}_2 = 0$ perturbation with an initial wavevector $k_1 = k_2(t_0) = 125$. The Reynolds number is infinitely large and the mass loading $M = 0.5$.

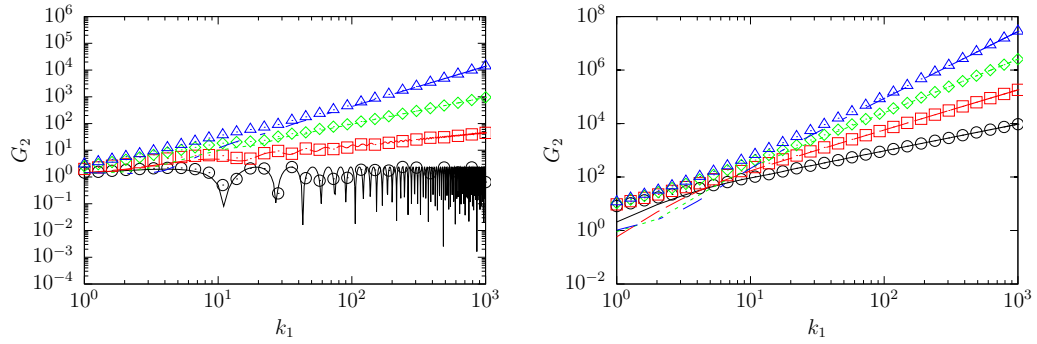

(a) (b)

Figure 2.11: Amplitude growth G_1 and G_2 as a function of k_1. The initial configuration is $k_2(t_0) = k_1$, i.e., $t_0 = -1$. Symbols represent simulations while lines represent theory. Four mass loadings are considered: $M = 0.25$ (—/⊙), 0.5 (− −/▫), 0.75 ($\cdots$/◇), 1 ($\cdot -$/ △).

2.5 WKB analysis for viscous gases

2.5.1 Weakly viscous regime $Re \sim k_1^2$

For simplicity, we presented the WKB analysis in the previous section for an inviscid gas. Since the growth of the perturbation obtained in the inviscid analysis increases with increasing wavenumber, it is important to assess the role of viscous effects in limiting the growth and establishing a most amplified perturbation. Thus, we will now generalise the analysis for finite Reynolds numbers. In the outer regions,the number density satisfies (2.31) with the coefficients :

$$\begin{aligned} A(t) &= -2\frac{k_2 k_1}{k_2} - \frac{1+2M}{1+M} i k_2 + \frac{k^2}{(1+M)Re} \\ &= k_1 \left(i\frac{1+2M}{1+M} t + \frac{1}{k_1}\frac{2t}{1+t^2} + \frac{k_1}{Re}\frac{1+t^2}{1+M} \right) \\ &= k_1 \left(a_0(t) + \frac{1}{k_1} a_1(t) + \frac{k_1}{Re} a_{Re}(t) \right) \end{aligned} \tag{2.71}$$

$$\begin{aligned} B(t) &= i\left(\frac{1+3M}{1+M} k_1 + \frac{2}{1+M}\frac{k_2^2 k_1}{k^2} + \frac{M}{1+M} i k_2^2 - \frac{k^2 k_2}{(1+M)Re} \right) \\ &= i k_1^2 \left(i\frac{M}{1+M} t^2 + \frac{1}{k_1}\left(\frac{2}{1+M}\frac{t^2}{1+t^2} + \frac{1+3M}{1+M} \right) + \frac{k_1}{Re}\frac{t(1+t^2)}{1+M} \right) \\ &= k_1^2 \left(b_0(t) + \frac{1}{k_1} b_1(t) + \frac{k_1}{Re} b_{Re}(t) \right) \end{aligned} \tag{2.72}$$

It is clear that the magnitude of k_1/Re controls the order at which the functions a_{Re} and b_{Re} enter the WKB expansion. When $k_1/Re = O(1/k_1^n)$ with $n \geqslant 2$, the viscous effects are too small to impact the first two orders S_0 and S_1. In such cases, the inviscid analysis presented earlier is accurate. On the other hand, a Reynolds number such that $k_1/Re = O(1/k_1)$, is small enough to change the equation for S_1, but leaves S_0 unchanged. For this case, which we term weakly viscous, the viscous damping influences the amplitude of the outer solution while leaving the frequency

unchanged. The weakly viscous case, $Re = O(k_1^2)$ corresponds to a dimensional wavelength in the outer region on the order of the distance, $(\nu/\Gamma)^{1/2}$, that viscous diffusion of momentum occurs during the turning of the wave by the shear in the outer region. The equations for the WKB expansion are now (2.36) and

$$S''_0 + 2S'_0 S'_1 + a_0 S'_1 + \left(a_1 + \frac{k_1^2}{Re} a_{Re}\right) S'_0 + b_1 + \frac{k_1^2}{Re} b_{Re} = 0 \quad (2.73)$$

Proceeding as in the previous analysis, we derive two modes which now account for the viscous terms:

$$\hat{n}^{\mathtt{M}}(t) = \frac{1}{|t|^{2M+1}} \frac{1}{(1+t^2)^{1-M}} \exp\left(-i\frac{M}{1+M} k_1 \frac{t^2}{2}\right) \times \exp\left(-\frac{k_1^2}{Re(1+M)} t\left(1 + \frac{t^2}{3}\right)\right) \quad (2.74)$$

$$\hat{n}^{\mathtt{N}}(t) = \left(\frac{t^2}{1+t^2}\right)^M \exp\left(-ik_1 \frac{t^2}{2}\right) \quad (2.75)$$

The number density mode is not influenced by the Reynolds number and remains the same as that in the inviscid analysis. The momentum mode has the same form as that for the inviscid analysis except for the final term giving viscous damping in terms of an exponential function of k_1, Re, M and t. The damping is more rapid when the wavevector is nearly vertical (large $|t|$) and becomes asymptotically small as one approaches the turning point $|t| \sim O(1/k_1^{1/2})$, because the wavelength over which viscous diffusion must occur becomes smaller as $|t| \to \infty$ and larger as $|t| \to 0$. The lack of damping of the number density mode indicates that even in a viscous gas, the disturbance does not decay at long times and one is left with a finite long time number density fluctuation. Since it has been found that the most amplified perturbations are those in which an initial momentum perturbation triggers a number density wave in the turning point, the damping of the `M` mode will play an important role in limiting the maximum growth that can be achieved.

Consistent with our observation that damping of the outer solution becomes

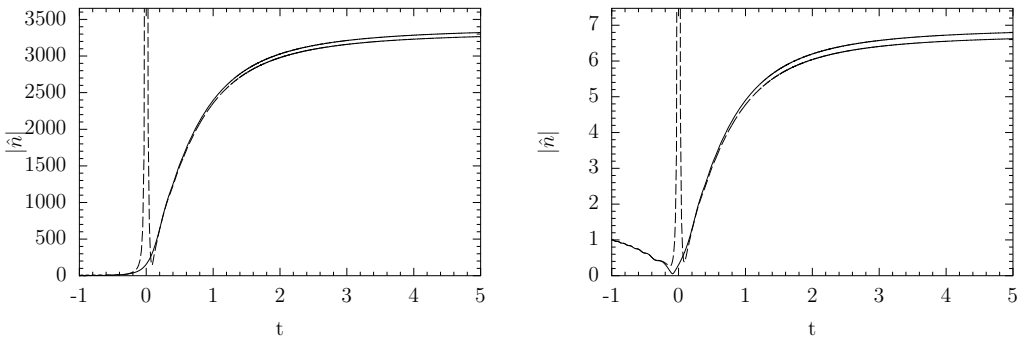

(a) $\hat{n}(t = t_0) = 0, \hat{u}_2(t = t_0) = 1$ (b) $\hat{n}(t = t_0) = 1, \hat{u}_2(t = t_0) = 0$

Figure 2.12: Comparison between theory (dashed line) and simulation (solid line) for the parameters $k_1 = 125$, $k_2 = k_1 = 125$, $M = 0.5$, $Re = k_1^2 = 15625$ and different initial conditions. The initial configuration is $k_2(t_0) = k_1$. Only the two outer WKB solutions are represented.

negligible as one approaches the inner region $|t| \sim O(1/k_1^{1/2})$ in the weakly viscous limit $Re = O(k_1^2)$, we will see that the inner solution remains unaltered from the inviscid analysis in section 2.4.3 for this case. Thus, one can still use the matching relations (2.66) to relate the coefficients of the upstream and downstream outer region modes. In figures 2.12a and 2.12b, we show a comparison of the weakly viscous outer solution with the numerical solution for examples within the weakly viscous regime corresponding to initial velocity and number density perturbations, respectively. The theory yields an accurate prediction of the variation of the amplitude with time.

2.5.2 Moderately viscous regime, $Re \sim k_1^{3/2}$

At a sufficiently small Reynolds number, viscous effects will begin to influence the solution even during the relatively short time period of the turning point. To examine these viscous effects we repeat the procedure for deriving the turning point approximation by transforming (2.31) to (2.62) using the transformation

(2.61), and doing a Taylor series expansion of g, keeping in mind that time scales as $t = O(1/\sqrt{k_1})$ in the inner region. It is found that no viscous terms arise when $Re = O(k_1^2)$. However, if we perform this analysis for a Reynolds number that scales as $Re = O(k_1^{3/2})$, we obtain:

$$g(\tau) = \frac{1}{k_1}\left\{\frac{1}{4(1+M)^2}\left(\tau + \frac{ik_1^{3/2}}{Re}\right)^2 + i\frac{1+4M}{2(1+M)} + O\left(\frac{1}{k_1}\right)\right\} \quad (2.76)$$

where $\tau = tk_1^{1/2}$. The resulting equation takes the form of a parabolic cylinder equation in terms of a complex shifted time variable:

$$\frac{d^2x}{dT^{*2}} + (T^{*2} + \lambda)x = 0 \quad (2.77)$$

where $T^* = \sqrt{\frac{k_1}{2(1+M)}}t^*$, $t^* = t + ik_1/Re$, and $\lambda = i(1+4M)$. Viscous effects would not alter the matching the coefficients of the waves in the upstream and downstream outer regions because, in the matching region corresponding to $|t| \gg 1/\sqrt{k_1}$, the complex shift can be neglected and $t^* \simeq t$. However, viscous effects in the inner region do alter the response to a wave produced by a momentum initial condition within the inner region. We may then expect viscous effects to scale with $Re/k_1^{3/2}$ for an initial fluid velocity disturbance whose wavevector is horizontal. This prediction of the analysis is corroborated by the numerical solution presented in figure 2.13.

To summarise, viscosity affects the results in three different parameter regimes. For very high Reynolds number Re and moderate wavenumbers such that $k_1 \ll Re^{1/2}$, viscosity plays no role and the dynamics can be described by the inviscid equations. The growth of the disturbance for this range of wavenumbers is a power law of k_1. The weakly viscous case occurs for higher wavenumbers such that $k_1 \sim Re^{1/2}$ and $k_1 \ll Re^{2/3}$. Damping of the `M` mode, for these waves, happens in the outer regions only, but the `N` mode is unaffected by viscosity. Since the

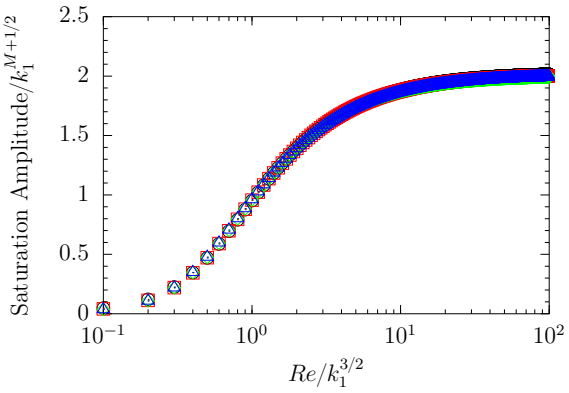

Figure 2.13: Saturation amplitude of number density for initially horizontal waves with initial conditions $\hat{n} = 0$, $\hat{u}_2 = 1$. The mass loading is $M = 0.5$. The amplitudes are obtained numerically with the symbols referring to $k_1 = 50$ ($\odot$), 75 ($\square$), 100 ($\Diamond$), 125 ($\triangle$).

inner region creates the `N` mode responsible for the long term saturation from an incoming `M` mode, waves that start far enough upstream for some amplification of the incoming `M` mode but without too much viscous damping lead to the largest growth. Next, viscous effects cause strong damping of the `M` mode in the outer region and begin to have an effect even in the inner region for wavenumbers of order $Re^{2/3}$. In this case, the largest growth is seen for initial conditions with nearly horizontal wavenumbers, although this growth is much smaller than for the weakly viscous case. Finally, if $k_1 \gg Re^{2/3}$ viscosity dominates in both the inner and outer regions and only the `N` mode survives providing a disturbance that neither grows nor decays with time.

2.5.3 Growth of the perturbations at finite Re

To assess quantitatively the growth at finite Reynolds numbers, we consider again the growth functions G_1, due to a number density perturbation initial condition, and G_2, due to a momentum perturbation initial condition, defined in (2.67). The

theoretical growth based on the solutions we found is given in (2.69) and (2.70). For the sake of clarity, we reproduce the equality below

$$\begin{aligned} G_i^{Th}(k_1, M, Re, t_0) &= |\underline{\Lambda}_{\mathtt{N}}| \\ &= \left| e^{-2\pi i M} \overline{\Lambda}_{\mathtt{N}} - \frac{e^{-i\pi M} i\sqrt{i\pi/2}}{M\Gamma(2M)} \left(\frac{k_1}{1+M}\right)^{1/2+2M} \overline{\Lambda}_{\mathtt{M}} \right| \end{aligned} \quad (2.78)$$

The coefficients $\overline{\Lambda}_{\mathtt{M}}$ and $\overline{\Lambda}_{\mathtt{N}}$ for the initial conditions ($\hat{n}|_{t_0} = 1$ and $\hat{u}_2|_{t_0} = 0$) are found to be :

$$\begin{cases} \overline{\Lambda}_{\mathtt{N}} \simeq \frac{1}{\hat{n}_{\mathtt{N}}(t_0)} \\ \overline{\Lambda}_{\mathtt{M}} \simeq \frac{i2M(1+M)}{k_1 t_0^2(1+t_0^2)} \frac{1}{\hat{n}_{\mathtt{M}}(t_0)} \end{cases} \quad (2.79)$$

Note that $|\hat{n}_{\mathtt{M}}(t_0)| \sim \exp(k_1^2/Re(1+M))$ for $t_0 < 0$ and $|t_0| = O(1)$ which can be very large if Re/k_1^2 is small. The expressions above show that the growth has a contribution $|\overline{\Lambda}_{\mathtt{N}}|$ that comes from the N mode prior to the turning point and that depends on Re/k_1^2 only. An additional contribution comes from the M mode prior to the turning point, $|k_1^{1/2+2M}\overline{\Lambda}_{\mathtt{M}}|$ that varies like $k_1^{-1/2+2M}$ times a function of Re/k_1^2. In figure 2.14a, we compare the simulated and predicted growth normalised by $k_1^{-1/2+2M}$ as a function of Re/k_1^2 . This scaling collapses the results partially but not completely because the N mode contribution plays comparable role to the M mode contribution for the wavenumbers considered and does not scale as $k_1^{-1/2+2M}$.

The second set of initial conditions ($\hat{n}|_{t_0} = 0$ and $\hat{u}_2|_{t_0} = 1$) yields

$$\begin{cases} \overline{\Lambda}_{\mathtt{N}} \simeq -\frac{2(1+M)}{t_0} \frac{1}{\hat{n}_{\mathtt{N}}(t_0)} \\ \overline{\Lambda}_{\mathtt{M}} \simeq \frac{2(1+M)}{t_0} \frac{1}{\hat{n}_{\mathtt{M}}(t_0)} \end{cases} \quad (2.80)$$

In this case the N mode contribution is negligible and the results are dominated by M mode contribution that scales as $k_1^{1/2+2M} \exp(k_1^2/Re(1+M))$ for a $t_0 < 0$ and $|t_0| = O(1)$. We test this scaling in figure 2.14b where we reported $G_2(k_1, M, Re, t_0)/k_1^{1/2+2M}$ for different values of k_1 as a function of Re/k_1^2 and for

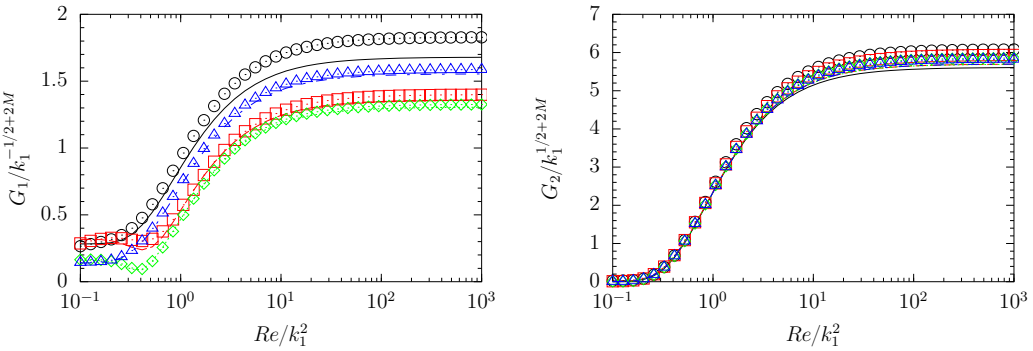

Figure 2.14: Growth functions G_1 and G_2 normalised based on the theoretical predictions for the given initial conditions versus Re/k_1^2, for a mass loading $M = 0.5$. Symbols correspond to simulations and lines to theoretical values. The wavevector is initially at an angle 45^o upstream ($t_0 = -1$), with $k_1 = 25$ (—/⊙), 50 ($--$/▫), 75 ($\cdots$/◇), 100 ($\cdot-$/△).

$t_0 = -1$. We observe that for all values of k_1, the curves collapse proving, that the growth normalised by $k_1^{1/2+2M}$ varies solely with the ratio Re/k_1^2 for high k_1 and fixed mass loading M and initial time t_0.

Generally, the initial wavevector of the perturbations can have any direction. In the inviscid case $Re = \infty$, the growth can take arbitrary large values as $|t_0| = |k_2/k_1|$ increases for $t_0 < 0$. A finite Reynolds number will, however, set a limit to the growth and will damp `M` modes with sufficiently large values of $|t_0|$ before they reach the turning point where they can induce an `N` mode. The optimal starting configuration leading to the most growth will then depend on the mass loading, Reynolds number, and the horizontal component of the wavenumber. The corresponding optimal growth for a set of parameters is given by

$$\sup_{t_0} G_i(k_1, M, Re) \tag{2.81}$$

and is met for an ideal initial configuration $-t_0^{\text{opt}} = (k_2/k_1)^{\text{opt}}$.

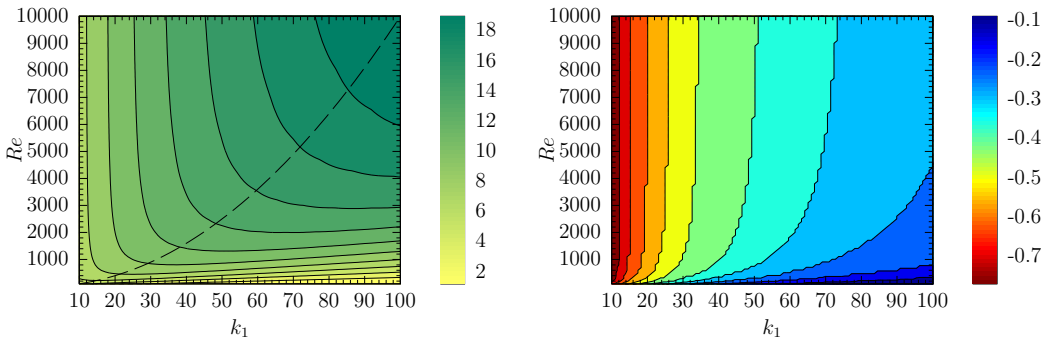

(a) $\sup_{t_0} G_1$ for $M = 0.5$ (b) t^{opt} for $M = 0.5$

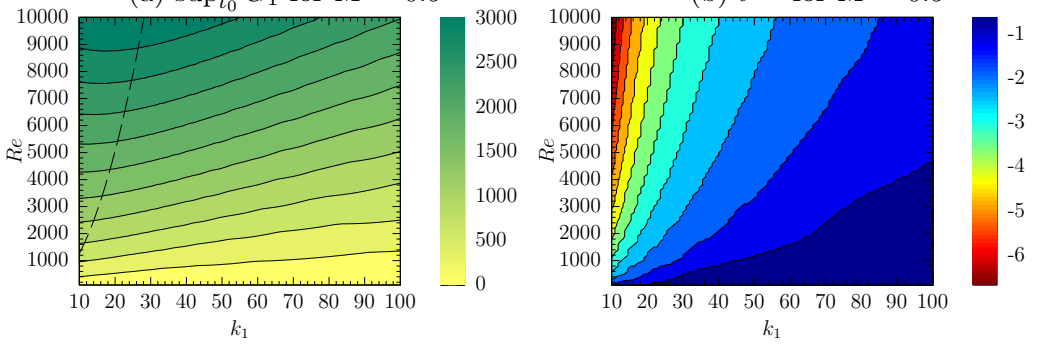

(c) $\sup_{t_0} G_2$ for $M = 0.5$ (d) t^{opt} for $M = 0.5$

Figure 2.15: Iso-contours of the growth functions in (k_1, Re) space. The dashed line is $Re = k_1^2$ in (a) and $Re = 12.6k_1^2$ in (c)

The iso-contours of $\sup G_1$ and $\sup G_2$ in (k_1, Re) space obtained from numerical solution of the differential equations are presented in figure 2.15 for a mass loading $M = 0.5$ along with the corresponding plot of the optimal $|t_0|$. As suggested by the previous discussion, the plots show that k_2/k_1 tends to zero, i.e., towards the inner region, as the Reynolds number goes to zero. The locations of the most amplified wavenumbers follow roughly the $Re \sim k_1^2$ scaling for $\sup G_1$ and $Re \sim 12.6k_1^2$ for $\sup G_2$ that one would expect based on the weakly viscous analysis.

To obtain theoretical predictions for the most amplified mode for a given Re and M, one can solve $\partial G_i/\partial k_1 = \partial G_i/\partial t_0 = 0$. We focus on the case of an initial momentum disturbance, since it leads to the highest growth. For $k_1 \gg 1$, one can use the approximate expression G_2^{Th} given in (2.70) (we neglect the N

mode contribution as justified previously) combined with the expressions for the coefficient $\Lambda_{\mathtt{N}}$ in (2.80). Maximizing the growth leads to an optimal initial time satisfying

$$\left(2M - \frac{5}{6}\right) t_0^4 + \left(\frac{8}{3}M - 3\right) t_0^2 + \frac{1}{2} - 2M = 0 \tag{2.82}$$

and a corresponding optimal k_1^{opt} given by the relation

$$Re = -\frac{4t_0(1 + t_0^2/3)}{(1 + 4M)(1 + M)} k_1^2 \tag{2.83}$$

For mass loadings larger than 5/12, the optimum time given by (2.82) can be written as

$$t_0^{\text{opt}} = -\sqrt{\frac{8/3M - 3 - 4/3\sqrt{13M^2 - 15M + 6}}{5/3 - 4M}} \tag{2.84}$$

In the case of mass loading $M = 0.5$, this time is $t^{\text{opt}} = -3.2$. Using the relation (2.83) we obtain $Re = 12.63k_1^2$ in agreement with the numerical solutions.

For mass loadings smaller than 5/12, the most amplified mode is obtained when $t_0 \to -\infty$ and $k_1 \to 0$. For such small wavenumbers, the expression (2.70) is no longer valid and one can only conclude that small wavenumbers, not captured by the WKB method, can lead to higher growth than the larger wavenumbers. Figure 2.16 demonstrates that the relations (2.83) and (2.84) are able to predict the optimal wavenumber and initial orientation for mass loadings $M = 1$, 1.25 and 1.5. Note that the growth is very large for these cases which might have implications on the development of non-linearities. Figure 2.17 shows that for the mass loadings smaller than $5/12 \sim 0.46$ (here $M = 0.125$, 0.25, 0.3 and 0.46) the most amplified wavenumber at a given Reynolds number is below $k_1 = 10$, corroborating our theoretical argument that small wavenumbers are most amplified for such small mass loadings.

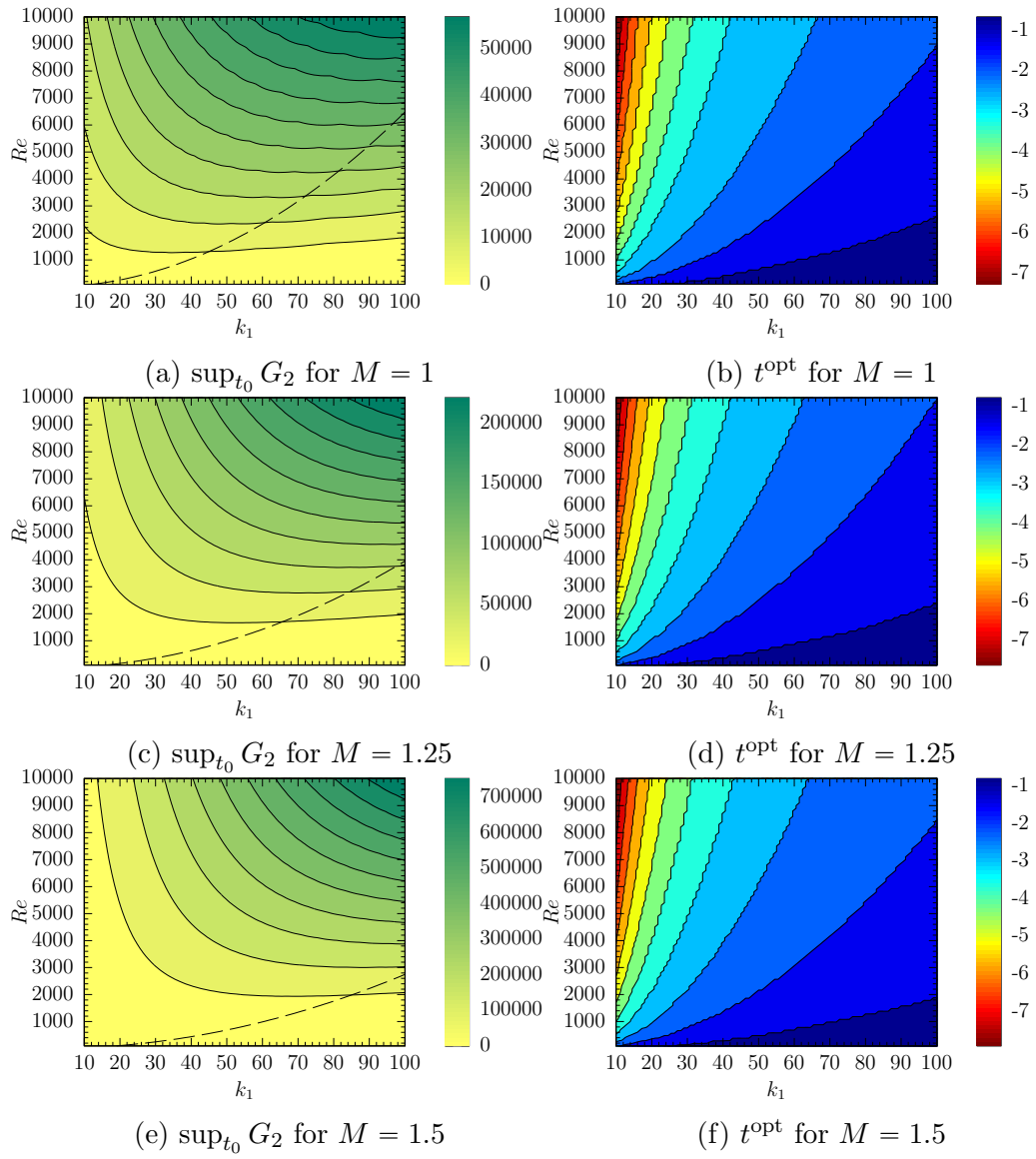

(a) $\sup_{t_0} G_2$ for $M = 1$

(b) t^{opt} for $M = 1$

(c) $\sup_{t_0} G_2$ for $M = 1.25$

(d) t^{opt} for $M = 1.25$

(e) $\sup_{t_0} G_2$ for $M = 1.5$

(f) t^{opt} for $M = 1.5$

Figure 2.16: Iso-contours of $\sup_{t_0} G_2$ in (k_1, Re) space with the corresponding t_0^{opt} obtained from simulations. The dashed line represent the most amplified wavenumbers obtained using (2.84) and (2.83)

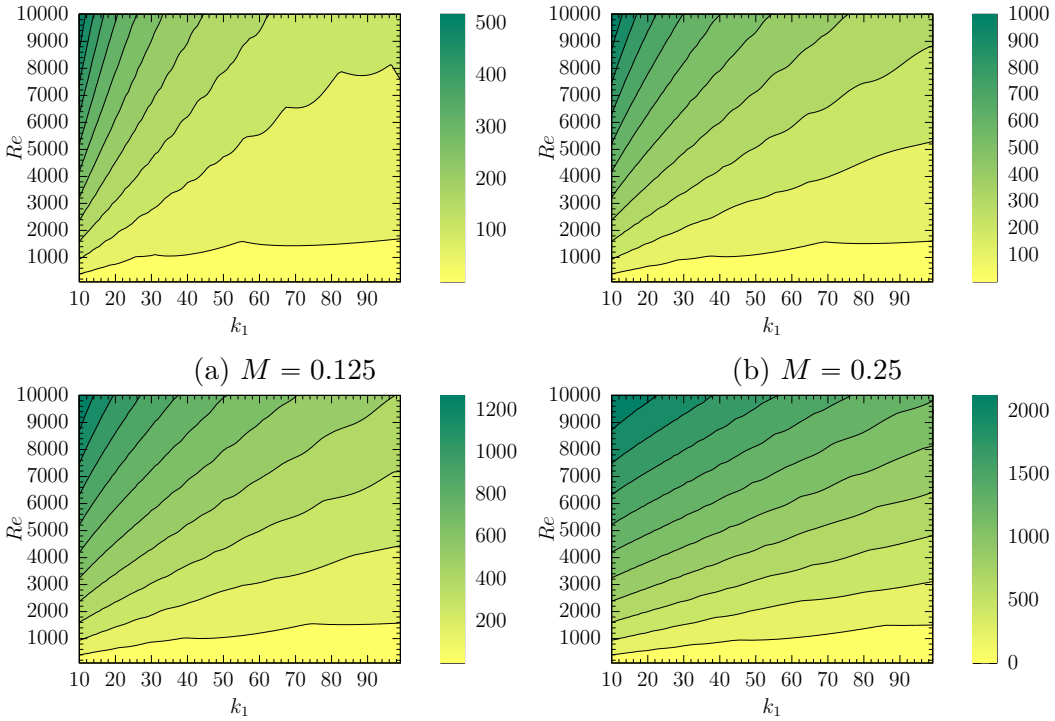

(a) $M = 0.125$ (b) $M = 0.25$

(c) $M = 0.3$ (d) $M = 0.46$

Figure 2.17: $\sup_{t_0} G_2$ for four different mass loadings smaller than $5/12 \sim 0.466$. The iso-contours are obtained from simulations.

2.6 Conclusion

The stability of a gas-solid suspension with small but nonzero Stokes numbers subject to a homogeneous shear has been investigated with a linear stability analysis. The complete description of rotating wave like perturbations, analogous to the Kelvin modes for single phase flow, has been detailed. A WKB asymptotic analysis yielded analytical results for cases where the initial wavelength of the perturbation is smaller than the characteristic particle settling distance in a shear time scale: $L = U_g/\Gamma$, the case that was shown to yield the largest growth for mass loadings $M > \frac{5}{12}$. The theory is applicable for order one mass loadings for which analytical solutions were shown to replicate numerical simulations with excellent agreement. The instability presented in this paper can be considered as one of the

few building-block instabilities available to enhance our qualitative understanding of the mechanics of dispersed multiphase flows.

To model the gas-solid suspension, a small Stokes approximation of the particle velocity field (2.5) was used in addition to a momentum coupling between the two phases as described for dilute suspensions in (Druzhinin, 1995) (2.2). The resulting number density equation features preferential concentration, a term that acts as a sink in high vorticity regions of the flow and as a source in high stretching regions (2.9). The feed back of the particles on the fluid momentum is via a gravitational forcing term in (2.8) that depends on the effective local suspension density $\rho_{\text{eff}} = \rho_f + m_p n$. This coupled action is critical to the maintenance and growth of a perturbation. The latter is chosen as a rotating wave, a class of perturbations relevant to the study of unbounded homogeneous shear, and first introduced in (Kelvin, 1887). Such a perturbation is characterised by its initial wavevector which for two-dimensional perturbations is $(k_1, k_2(t))$. This wavevector evolves with time and eventually aligns along the mean velocity gradient (2.22).

For the case when gravity is parallel to the velocity gradient, we have used the WKB analysis valid for $k_1 \gg U_g/\Gamma$ two identify two solutions, which are termed the number density (`N`) mode and the momentum (`M`) mode. Analytical expressions for the modes are given by (2.45, 2.46, 2.48, 2.47, 2.75 and 2.74). Any small perturbation can be expressed as a linear combination of the two modes, when the wavevector has an orientation far from the horizontal with $|k_2| \gg \sqrt{k_1\Gamma/U_g}$. As the wave rotates under the base shear, and goes from an upstream configuration $k_2(t)/k_1 > 0$ to a downstream configuration $k_2(t)/k_1 < 0$, there is a very narrow range of configurations $|k_2| = O(\sqrt{k_1\Gamma/U_g})$, referred to as the inner region, where the solution is given in terms of Parabolic Cylinder functions. As the wave passes

across this inner region the upstream N and M mode can each produce both a downstream N and M mode . This particular point is critical to the growth of perturbations.

The sketch in figure 2.18 shows the evolution of disturbances produced by an initial momentum mode (figure 2.18 a) and an initial number density mode (figure 2.18 b). In section 2.4.2, we discussed the manner in which preferential concentration, gravitational forcing and the relative propagation of momentum and number density disturbances due to settling lead an N mode to decay upstream and grow downstream of the turning point, while an M mode grows upstream and decays downstream of the turning point (see figures 2.8 and 2.9). As shown in figure 2.18b, an initial N mode decays until reaching the turning point and produces at the turning point an N that manages to return to the initial amplitude and a small M that decays. In contrast the initial M mode illustrated in figure 2.18a grows in the upstream region and produces at the turning point a downstream N mode that grows further and saturates at a large finite amplitude as $t \to \infty$. As a result the largest growth occurs due to initial fluid velocity disturbances which produce large number density disturbances as the wave turns.

The inviscid analysis in section 2.4 shows that an initial velocity disturbance leads to a downstream N mode with an amplification factor of $(U_g k_1/\Gamma)^{1/2+2M}$ that grows algebraically with decreasing wavelength when the wavelength is much smaller than the distance U_g/Γ that particles settle during the shearing time scale, i.e., $k_1 \gg \Gamma/U_g$. However, when viscous diffusion can transfer momentum across the wavelength during the shearing time, i.e., $\nu k_1^2/\Gamma = O(1)$, viscous effects begin to damp the M mode as shown in section 2.5. As a result the maximum amplification occurs at a wavenumber $k_1 = O\left((\Gamma/\nu)^{1/2}\right)$ and a wave orientation $k_2/k_1 = O(1)$

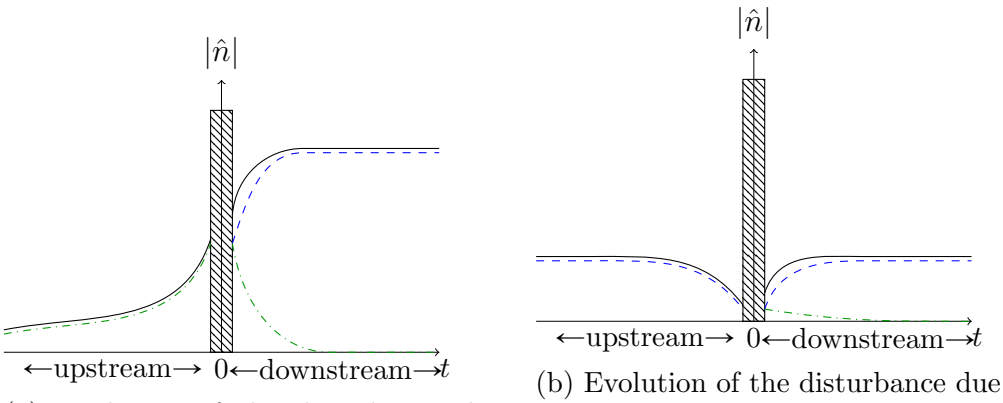

(a) Evolution of the disturbance due to an upstream `M` mode: the mode grows until it reaches the inner region, which results in the generation of a `N` mode in the downstream region. The latter grows to a saturation amplitude $k_1^{1/2+2M}$ times higher than the upstream mode that created it. The downstream `M` mode vanishes with time.

(b) Evolution of the disturbance due to an upstream `N` mode: the mode decays until it reaches the inner region, which results in the generation of a small `M` mode in the downstream region. The latter decays and the downstream `N` reaches a saturation amplitude similar to the starting one. There is no overall amplification due to an upstream `N` mode.

Figure 2.18: Two schematics depicting the evolution of the `N` (dashed/blue) and `M` (dash-dotted/green) modes from upstream to downstream. The solid black curve represents the total perturbation, which is a linear combination of the two modes.

which is determined as a function of the mass loading in equation (2.84). The optimal wavelength is small compared with the settling distance U_g/Γ and the WKB analysis predicts the maximum growth wavevector analytically provided that $M > 5/12$. For smaller mass loading, the optimal wavelength is $O(U_g/\Gamma)$ and a numerical solution of the linearized equations is required to determine it value. Large wavenumber momentum disturbances with $k_1 \gg (\Gamma/\nu)^{1/2}$ are greatly damped before reaching the turning point. At these wavenumbers, the most amplified wavevector orientation is near the horizontal in the turning point region. Initial disturbances with horizontal wavenumbers are finally damped at a still higher wavenumber $k_1 = O((\Gamma U_g)^{1/3}\nu^{2/3})$ for which viscous effects become important in the turning point region, cf. figure 2.13. Nonetheless, the largest growth occurs

for disturbances with $k_1 = O\left((\Gamma/\nu)^{1/2}\right)$ and $k_2/k_1 = O(1)$ as given by equations (2.84) and (2.83).

It would be natural to expect that an instability involving preferential concentration of particles and their gravitational forcing of the gas flow might lead to an enhancement of the particle settling rate. While the extent to which this ultimately occurs depends on the non-linear evolution of the number density and velocity perturbations, some indication of the initial change in settling velocity for small perturbations can be gleaned from the linear stability analysis. The phase-average vertical particle velocity is

$$\langle v_2 \rangle = \mathbf{e}_2 \cdot \frac{\int_0^{2\pi} \mathrm{Re}\{n(\mathbf{x},t)\}\mathrm{Re}\{\mathbf{v}(\mathbf{x},t)\}d\xi}{\int_0^{2\pi} n_0 d\xi} \tag{2.85}$$

$$\tag{2.86}$$

where $\xi = \mathbf{k} \cdot \mathbf{x}$ is a spatial coordinate parallel to the wavevector and Re{ } is the real part of a complex number. In presence of the perturbations the average particle velocity differs from $-U_g$ by

$$\Delta\langle v_2 \rangle = \langle v_2 \rangle - (-U_g) = \frac{St}{2\pi}\mathrm{Re}\left\{\hat{u}_2 \hat{n}^*\right\} \tag{2.87}$$

The star here denotes the complex conjugate. The scaled change in the particle velocity is plotted as a function of time in figure 2.19. The change of the particle velocity averaged over a period of oscillation is zero in the outer region ($|\sqrt{Lk_1}\Gamma t| \gg 1$). However, in the inner region ($|\sqrt{Lk_1}\Gamma t| \leqslant 10$), i.e., when the number density streaks are vertical and the coupling between the velocity perturbation and particle phase is strongest, there is a net enhancement of the settling rate. In the absence of a secondary instability, the increase of the settling velocity is transient and one can characterize its effects in terms of the net extra displacement a particle experiences as the wave vector passes through the turning point. This extra displacement for

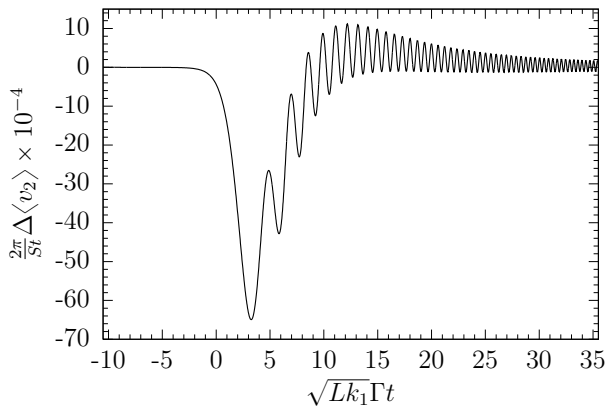

Figure 2.19: Change in the particle velocity due to perturbations with the scaled initial conditions $\hat{u}_2 = 1$, $\hat{n} = 0$ for the parameters $U_g k_1/\Gamma = 100$, $M = 1, and\ Re = \infty$. The change is scaled with the small amplitude of the initial perturbation.

the parameters considered in figure 2.19 is

$$\Delta\langle r_2\rangle_{t_0} = \int_{-1}^{\infty} \Delta\langle v_2\rangle \frac{1}{\Gamma} d\,(\Gamma t) \quad \sim \quad -2.7\ 10^4 u'\tau_p \tag{2.88}$$

in which u' is the magnitude of the initial velocity perturbation, which should be small compared to U_g in the context of linear theory. Thus, the instability leads to a downward displacement that is by many orders of magnitude larger than the displacement an inertial particle might experience to the initial perturbation due to its relaxation time τ_p.

Despite its algebraic nature, the instability presented in this paper can amplify disturbances by a significant amount. To illustrate this, consider the example of a suspension of $80\mu m$ diameter silica particles in sheared air at standard pressure and temperature with $\Gamma = 1.5 s^{-1}$. The particle Stokes number is $St = 0.07$. With a volume fraction $\phi = 4.6\ 10^{-4}$, the suspension mass loading is $M = 1$. The Reynolds number is $Re = U_g^2/(\Gamma\nu) = 11690$. Under these conditions, an initial perturbation to the velocity field with a wavelength $\lambda = 1.1 cm$ oriented 56^o upstream leads to an amplification of 4 orders of magnitude (7.4×10^4) despite some viscous effects

$(Re/(Lk_1)^2 \sim 1)$.

It has long been hypothesised that transient linear growth can explain the transition to turbulence in flows that are otherwise unconditionally stable from the stand point of traditional linear analysis, such as flows in circular pipe. Several research groups wave worked on means of identifying optimal transient perturbations (Trefethen *et al.*, 1993; Trefethen, 1997; Schmid, 2007), and it has been shown by Baggett and Trefethen (1997) that an optimal transient mode that achieves a growth of 1.5 to 2 orders of magnitude can trigger non-linearities leading to significantly higher magnifications. This effect is known as bootstrapping. The instability presented in this paper, although of finite amplitude, is able to achieve a growth of 4 orders of magnitude and more, which makes us believe that it might achieve even higher growth by bootstrapping.

In the present mechanism the large finite amplitude disturbance that is created is not transient but persists at long times allowing even more opportunity for the onset of secondary instabilities than in cases such as single-phase pipe flow. Once a wave is amplified and turned by the shear, the final state is a periodic number density stratified vertically. Such a configuration is subject to a Rayleigh Taylor instability as described in (Batchelor and Nitsche, 1991). While the shear mechanism converts, for the most part, a momentum perturbation into a number density perturbation, a secondary Rayleigh Taylor instability converts a number density perturbation back to a momentum one while resetting the wave orientation to a direction that is not parallel to gravity. A second cycle of shear and Rayleigh Taylor instability may then be expected to take place to further reinforce the perturbation. Whether, these two instabilities take place simultaneously or sequentially will depend on the size of the initial disturbance and their respective

growth rates.

While we have considered the idealized case of the instability of a homogeneously sheared gas-solid suspension, this analysis will be applicable to disturbances that are small in comparison with the distance over which the shear rate varies in a more complex flow. As an example, consider a mixing layer in which two fluid streams with velocity difference ΔU have interacted long enough to develop a shear layer of thickness δ. The shear rate in this layer will be $\Gamma = O(\Delta U/\delta)$ and the Reynolds number of the shear layer is $\mathrm{Re}_{\mathrm{SL}} = \Delta U\delta/\nu = \Gamma\delta^2/\nu$. The current analysis predicts that, in the presence of particles settling across this mixing layer, a fluid velocity disturbance will lead to a large growth of particle concentration fluctuations with an optimal wavelength $\lambda = 2\pi/k_1 = O((\nu/\Gamma)^{1/2})$. This optimal wavelength is much smaller than the shear layer thickness $\delta = (\nu/\Gamma)^{1/2}\mathrm{Re}_{\mathrm{SL}}^{1/2}$ for any high Reynolds number shear layer. Thus, the dominance of small wavelength disturbances that justifies the use of the WKB analysis makes the analysis applicable to the consideration of local disturbances in many complex flows.

Acknowledgement

This work was supported by NSF grant CBET-1233793.

CHAPTER 3

AN ALGORITHM FOR SOLVING THE NAVIER-STOKES EQUATIONS WITH SHEAR-PERIODIC BOUNDARY CONDITIONS AND ITS APPLICATION TO HOMOGENEOUSLY SHEARED TURBULENCE

3.1 Abstract

The simulation of homogeneously sheared turbulence (HST) is conducted until a universal self-similar state is established at the long non-dimensional time $\Gamma t = 20$, where Γ is the shear rate. The simulations are enabled by a new robust and discretely conservative algorithm. The method solves the governing equations in physical space using the so-called shear-periodic boundary conditions. Convection by the mean homogeneous shear flow is treated implicitly in a split step approach. A semi-iterative Crank-Nicolson time integrator is chosen for robustness and stability. The numerical strategy captures without distortion the Kelvin modes, rotating waves that are fundamental to homogeneously sheared flows and are at the core of rapid distortion theory. Three direct numerical simulations of HST with the initial Taylor scale Reynolds number $Re_{\lambda 0} = 29$ and shear numbers $S_0^* = \Gamma q^2/\epsilon = 3$,15, and 27 are performed on a $2048 \times 1024 \times 1024$ grid. The long integration time considered allows the establishment of a self-similar state observed in experiments but often absent from simulations conducted over shorter times. The asymptotic state appears universal with a long time production to dissipation rate $\mathcal{P}/\epsilon \sim 1.5$ and shear number $S^* \sim 10$ in agreement with experiments. While the small scales exhibit strong anisotropy increasing with initial shear number, the skewness of the transverse velocity derivative decreases with increasing Reynolds number.

3.2 Introduction

Designing efficient and robust algorithms for the simulation of homogeneously sheared flows is valuable for understanding the effect of shear on complex flows such as turbulence and complex fluids such as particle suspensions without the added complications of confining walls or shear rate inhomogeneities. In particular, homogeneously sheared turbulence (HST) has been widely studied as a flow intermediate in complexity between homogeneous, isotropic turbulence and inhomogeneous and wall-bounded flows. HST allows consideration of anisotropy arising due to a mean flow and the production of turbulent kinetic energy by the mean shear. In this paper, we build upon the method for calculating HST using shear-periodic boundary conditions in real space proposed by Gerz *et al.* (1989) and create a new algorithm that is shown to yield stable, energy conserving, and accurate simulation of HST for long time periods. We present a thorough comparison of the simulations with HST experiments and discuss the universality of the long time behavior of HST.

A step towards elucidating the mechanisms that arise in complex flows with complex geometries consists in the analysis of HST. This flow presents an intermediate complexity between isotropic, homogeneous turbulence and fully inhomogeneous turbulent flows of interest in the design of engineering systems. The work done by the mean shear produces turbulent kinetic energy and the shear deformation contributes to the complexity of the flow structures. For example, Rogers and Moin (1987) showed that HST can produce hairpin vortices usually observed in near-wall turbulent flow. Sweep and ejection mechanisms similar to those present in turbulent boundary layers were also shown to exist in HST (Pumir and Shraiman, 1995). Without bounding walls, HST can provide a simpler view

of the effects of shear on turbulence.

Particular interest has been devoted to the long time behavior of HST. Most experiments point to the existence of a self-similar state (Shen and Warhaft, 2000; Garg and Warhaft, 1998; Tavoularis and Karnik, 1989; Tavoularis and Corrsin, 1981; Isaza *et al.*, 2009), a state controlled by a single time scale and most notably displaying exponential growth of the kinetic energy. However, the experimental literature dealing with the sensitivity of the asymptotic state to the initial conditions is scarce (Isaza and Collins, 2011). The existence of a self-similar state is less clear from the direct-number simulation (DNS) literature. Part of the ambiguity arises because many simulations stop too early leaving no time for the flow to re-organize from the artificial initial turbulence to a self-similar state. The simulations of Sukheswalla *et al.* (2013) suggest that an unambiguous self-similar state can be reached by $\Gamma t = 20$. But the question of the universality of the asymptotic state for various initial conditions remains open.

The simulation of HST (see figure 3.1 for a sketch of the geometry) and other homogeneously sheared cases requires the deployment of a special class of algorithms. The workhorse of most HST simulations is a pseudo-spectral algorithm developed by Rogallo (1981). In this approach the governing equations are solved on a mesh that deforms with the mean flow (see figure 3.2a). This method is widely popular due to the ease of implementation (Shotorban and Balachandar, 2006; Chung and Matheou, 2012; Salhi *et al.*, 2014; Jacobitz *et al.*, 2016, 2008, 2010; Rogers and Moin, 1987; Lee *et al.*, 1990; Adrian and Moin, 1988; Gualtieri *et al.*, 2007a; Holt *et al.*, 1992; Ishihara *et al.*, 2002). Challenges arising from different mean velocities at the two boundaries in the direction of the shear are circumvented by the use of simple periodic boundary conditions in the deforming

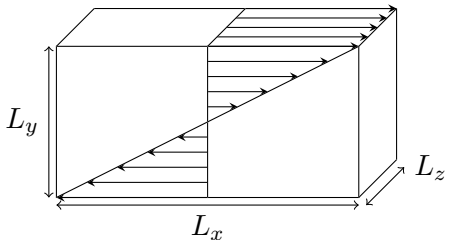

Figure 3.1: Geometrical configuration. The velocity vectors illustrate the mean shear given by $(\Gamma y, 0, 0)$.

Figure 3.2: In Rogallo's method (3.2a) the governing equations are solved on a deforming mesh allowing for normal periodicity in all directions. Baron's method (4.3) solves the equations on a straight mesh using the shear-periodic boundary conditions to account for the displacement of the computational domain in the shear direction (Baron, 1982).

mesh reference frame. Past a certain level of deformation, the solution is interpolated to a straightened mesh to restore the aspect ratio of the computational cells. The cost of remeshing can be severely penalizing and leads to discontinuous turbulence statistics. Brucker *et al.* (2007) estimate that up to 40% of the turbulent kinetic energy can be lost over the long term depending on the shear rate. They propose another pseudo-spectral method that replaces the remeshing of the physical grid by a shift of wavenumber space at every iteration of the algorithm. The method achieves continuous statistics but the long time behavior is plagued by Gibbs oscillations coming from the fine vortical structures in HST and requires the use of numerical dissipation for stabilization (Sukheswalla *et al.*, 2013).

Another method was introduced by Baron (1982) and later improved by Schumann and coworkers (Schumann, 1985; Schumann *et al.*, 1986; Gerz *et al.*, 1989).

This method solves the equations in physical space without the need of remeshing as in Rogallo's method. To do so, it relies on two key elements. First, the so-called shear-periodic boundary conditions are employed (see figure 4.3). For a quantity of interest f, these boundary conditions apply in the following way

$$f(x, L_y, z) = f(x - \Gamma t L_y, 0, z) \tag{3.1}$$

where Γ is the shear rate and L_y is the domain size in the shear direction y. Second, an operator splitting is used when solving the momentum equation leaving out the convection by mean shear to a separate step. The authors conducted a series of tests on stably stratified HST (Gerz *et al.*, 1989; Kaltenbach *et al.*, 1994; Schumann, 1996) and showed promising results. However, the complex interplay between the operator splitting, the boundary conditions and interpolation method has not been fully unveiled. Additionally, it is stated in (Schumann *et al.*, 1986) that the method is unstable, and particularly so at higher resolutions, longer simulation times and for unstratified HST, which is less numerically stable than the stratified situation.

To understand the issues with the method in (Gerz *et al.*, 1989), we consider rotating waves, a class of solutions fundamental to homogeneously sheared flows. In addition to being relevant to a variety of problems (single phase flows (Thomson, 1887), particle-laden flows (Kasbaoui *et al.*, 2015), granular flows (Schmid and Kytomaa, 1994), accretion disks (Goldreich and Tremaine, 1978; Johnson and Gammie, 2005; Salhi *et al.*, 2014), etc.), rotating waves have a direct application to HST. The Rapid Distortion Theory (RDT) (Moffatt, 1965; Townsend, 1970; Maxey, 1982; Rogers, 1991; Pope, 2001; Isaza and Collins, 2009), applicable when the mean deformation greatly exceeds the non-linear effects, shows that the fluctuating velocity $\mathbf{u}$ defined as the deviation from the mean shear can be expressed

as a series of "rotating" Fourier modes

$$\mathbf{u}(\mathbf{x},t) = \int\int\int \left\{ \mathbf{A}(\mathbf{k}_0,t)\hat{\mathbf{u}}_0 e^{-\nu t\left(k^2 - k_{x,0}k_{y,0}\Gamma t + \frac{(k_{x,0}\Gamma t)^2}{3}\right)} \exp\left(i\mathbf{k}(t)\cdot\mathbf{x}\right) \right\} d\mathbf{k}_0 \quad (3.2)$$

with $\mathbf{A}$ being the RDT matrix (Maxey, 1982; Isaza and Collins, 2009), defined in Appendix B, and $\hat{\mathbf{u}}_0$ the amplitude of the mode $\mathbf{k}_0 = (k_{x,0}, k_{y,0}, k_{z,0})$ at a chosen time origin. The evolution of the wavevector (and thus the orientation and wavelength of the mode) results from the shear: $d\mathbf{k}/dt = \Gamma \mathbf{e}_y \mathbf{e}_x \cdot \mathbf{k}$. We find that the method proposed by Gerz *et al.* (1989) cannot maintain the normal structure of these waves. This deficiency is likely the reason for its lack of robustness. We resolve these issues by adopting a semi-implicit Crank-Nicolson for the time integration, careful execution of the operator splitting and timing of the shear-periodic boundary conditions.

The improved method combined with an energy-conserving discretization tailored for turbulence simulations (Desjardins *et al.*, 2008a) allows us to produce statistics of HST for long times ($\Gamma t = 20$) without artificial stabilization. Direct numerical simulations (DNS) of HST suffer from a loss of resolution at large times caused by the continuous production of finer turbulent structures by the shear straining. Simulations found in the literature run typically until $\Gamma t \sim 10$ (Isaza and Collins, 2009; Brucker *et al.*, 2007; Isaza and Collins, 2011; Lee *et al.*, 1990). The extension of the time window is critical to determining the nature of HST at long time.

With the ability to simulate for this long, we are in a position to compare our results to experiments and assess the sensitivity of the self-similar state to the initial conditions. The anisotropy of HST is also of interest and will be discussed.

This paper is organized as follows. Section 2 presents the governing equations. Section 3 goes into the details of the numerical approach. Rotating modes are used

to understand the shortcomings of the method introduced in (Gerz *et al.*, 1989). A fix is proposed and is verified to faithfully capture the rotating modes. In section 4, we use the algorithm to simulate HST. We present an extensive comparison with available experiments. A self-similar state, only weakly sensitive to the initial conditions, is found. Agreement with RDT is shown to hold until $\Gamma t \sim 5$. We finally look into measures of local anisotropy in section 5.

3.3 Governing equations

The governing equations for an incompressible Newtonian fluid are

$$\frac{\partial \mathbf{U}}{\partial t} + \mathbf{U} \cdot \nabla \mathbf{U} = -\frac{1}{\rho}\nabla p + \nu \nabla^2 \mathbf{U} \tag{3.3}$$

$$\nabla \cdot \mathbf{U} = 0 \tag{3.4}$$

where $\mathbf{U}$, p, ρ, ν are the fluid velocity, pressure, density and kinematic viscosity respectively. The flow is subject to a mean shear wherein the flow is in the x direction and varies in the y direction with a shear rate Γ (see figure 3.1) given by $(\Gamma y, 0, 0)$. In the study of homogeneously sheared flow, a first step consists in separating the velocity fluctuations $\mathbf{u}$ from the mean shear motion

$$\mathbf{U} = \Gamma y \mathbf{e}_x + \mathbf{u} \tag{3.5}$$

Introducing the shear decomposition (3.5) in the governing equations (3.3) and (3.4) yields the evolution equations of the fluctuating part of the velocity field

$$\frac{\partial \mathbf{u}}{\partial t} + \mathbf{u} \cdot \nabla \mathbf{u} = -\frac{1}{\rho}\nabla p + \nu \nabla^2 \mathbf{u} - \Gamma y \frac{\partial \mathbf{u}}{\partial x} - \Gamma u_y \mathbf{e}_x \tag{3.6}$$

$$\nabla \cdot \mathbf{u} = 0 \tag{3.7}$$

Two new terms appear in the momentum equation for the fluctuating velocity. The $\Gamma u_y \mathbf{e}_x$ term is a production of streamwise momentum caused by the convection of

mean shear by the fluctuating velocity. The second term $\Gamma y(\partial \mathbf{u}/\partial x)$ arises due to the convection of fluctuations by the mean shear. As we explain below, it is this term that requires a careful implementation.

3.4 Numerical strategy

The approach discussed by Gerz *et al.* (1989) solves the equations (3.6) and (3.7) in physical space in the reference frame of the laboratory. These equations are completed by the shear-periodic boundary conditions (4.26) in the shear direction y, and periodic boundary conditions in the other two directions. As recognized by Gerz *et al.* (1989), special handling of the convection by homogeneous shear term is required.

In a finite volume code, direct implementation of $\Gamma y(\partial \mathbf{u}/\partial x)$ as a source term is problematic. Errors associated with the discretization of the derivative are further magnified by the inhomogeneous coordinate y multiplying the term. A severe consequence for HST simulations is the breaking of the homogeneity of the fluctuating velocity field. To circumvent this, Gerz *et al.* (1989) propose a solution that relies on operator splitting and spectral interpolations for the shear-periodic boundary conditions. The method was tested on stratified homogeneously sheared turbulence (Kaltenbach *et al.*, 1994; Schumann, 1996) and proved to be superior to the classic Rogallo algorithm (Rogallo, 1981). However, the method is recognized to be "weakly unstable" (Schumann, 1985) and we will show that it fails to capture the analytical Kelvin modes.

To understand how these issues can be addressed, we start by summarizing the key ideas from (Gerz *et al.*, 1989). The first step towards finding $\mathbf{u}^{n+1}$ consists in

updating the velocity with an Adam-Bashforth scheme using the previous solutions $\mathbf{u}^n$ and $\mathbf{u}^{n-1}$,i.e.,

$$\tilde{\mathbf{u}} = \mathbf{u}^n + \Delta t \left(\frac{3}{2} \mathcal{M}\left(\mathbf{u}^n\right) - \frac{1}{2} \mathcal{M}\left(\mathbf{u}^{n-1}\right) \right) \tag{3.8}$$

where $\mathcal{M}$ is the momentum operator from which the shear convection term is omitted

$$\mathcal{M}\left(\mathbf{u}\right) = \nu \nabla^2 \mathbf{u} - \nabla \cdot (\mathbf{u}\mathbf{u}) - \Gamma u_y \mathbf{e}_x \tag{3.9}$$

Next, the convection by shear is included using

$$\check{\mathbf{u}}(\mathbf{x}) = \tilde{\mathbf{u}}\left(\mathbf{x} - \Delta t \Gamma y \mathbf{e}_x\right) \tag{3.10}$$

This is equivalent to solving the equation of pure convection by homogeneous shear

$$\frac{\partial \mathbf{u}}{\partial t} + \Gamma y \mathbf{e}_x \cdot \frac{\partial \mathbf{u}}{\partial x} = 0 \tag{3.11}$$

using the method of characteristics over a time interval Δt. We term step (3.10) the "shear-remapping" operation because it maps local values to upstream ones. The boundary conditions (4.26) are then applied at time $n+1$. Finally, the pressure-Poisson equation is solved and the velocity updated

$$\nabla^2 p^{n+1} = \frac{1}{\Delta t} \nabla \cdot \check{\mathbf{u}} \tag{3.12}$$

$$\mathbf{u}^{n+1} = \check{\mathbf{u}} - \frac{\Delta t}{\rho} \nabla p^{n+1} \tag{3.13}$$

This is efficiently done with a spectral pre-conditioner in the x and z directions. A linear system is solved for the direction y with a careful implementation of the boundary conditions. Further details can be found in Schumann (1985).

In most cases in the literature, validation of codes dealing with homogeneously sheared flows has been conducted on HST with the goal to obtain statistics that are

in accordance with experiments or turbulence theories (Pope, 2001). In such complex flows, it is easy to miss numerical errors. A stronger test case is a comparison against the analytical Kelvin modes. These are the individual modes appearing in the RDT expansion (3.2). In 2D ($k_z = 0$), a Kelvin mode reads

$$u_y^K(\mathbf{x},t) = \left(\frac{k_0}{k}\right)^2 e^{-\nu t\left(k^2 - k_x k_{y,0}\Gamma t + \frac{(k_x \Gamma t)^2}{3}\right)} u_{y,0} \exp\left(i\mathbf{k}\cdot\mathbf{x}\right) \tag{3.14}$$

$$u_x^K(\mathbf{x},t) = -\frac{k_y(t)}{k_x} u_y^K(\mathbf{x},t) \tag{3.15}$$

$$k_y = k_{y,0} - k_x \Gamma t \tag{3.16}$$

In the above, $\mathbf{k}(t) = (k_x, k_y)$ is the rotating wavevector of the Kelvin mode, the magnitude of which is $k = \sqrt{k_x^2 + k_y^2}$ (i.e, the wavenumber). According to (3.16), the orientation of the wave changes over time to align with the shear direction $\mathbf{e}_y$. The wavelength increases when the wavevector is in the stretching quadrant of the homogeneous shear ($k_x k_y > 0$), and decreases in the compressive quadrant ($k_x k_y < 0$). The Kelvin mode is a solution to the full Navier-Stokes equations and decays in a super exponential fashion. These attributes make it an excellent way of validating numerical codes. A desirable feature of any algorithm is the ability to keep the level of numerical errors below the magnitude of the mode, even as it decays. The simulation of Kelvin modes has potential to quickly expose numerical artifacts due to the very fast decay of the solution.

We performed simulations with the method above on a 2D square domain. The algorithm is implemented in the CFD code NGA (Desjardins *et al.*, 2008a), on a staggered mesh, and with a second order discretization. The simulation parameters are listed in table 3.1. The initial wavevector is 45^o upstream of the gradient direction with 4 periods in the domain. Figure 3.3 reports the time evolution of the velocity amplitudes of the Kelvin mode based on the analytical expressions (3.14), (3.15) and (3.16). Notice that these quantities decay exponentially, and

Parameters	Expression	Value
Grid	$n_x \times n_y \times n_z$	$128 \times 128 \times 1$
Box size	$L_x = L_y$	2π
Wavenumber	k_x	4
Orientation	$k_{y,0}/k_x$	1
Reynolds number	$\Gamma\lambda^2/\nu$	208
Amplitude	$u_{y,0}/(\Gamma L_y)$	0.25
CFL_b	$(\Gamma L_y)\Delta t/\Delta x$	0.25

Table 3.1: Parameters for simulating the Kelvin modes given in non-dimensional form. The Reynolds number is defined using the perturbation wavelength $\lambda = \sqrt{(2\pi/k_x)^2 + (2\pi/k_{y,0})^2}$ and base shear flow seen by the perturbation ($\Gamma\lambda$). The base Courant-Friedrichs-Lewy number CFL_b is associated to the base shear flow in the simulation domain (ΓL_y).

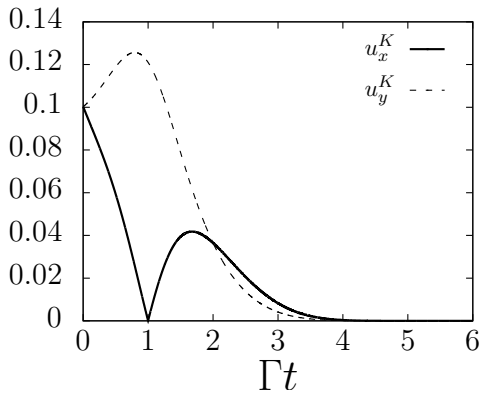

Figure 3.3: Magnitude of the theoretical Kelvin mode with the parameters from table 3.1.

that at $\Gamma t = 1$, $\hat{u}_x^K$ vanishes because the wavector becomes horizontal. Snapshots of the simulation with the method of Gerz *et al.* (1989) are given in figure 3.4 (a-d) for non-dimensional time Γt going from 0 to 5. The figure shows isocontours of the horizontal component of velocity u_x. While we do observe the rotation of the wave, the horizontal velocity does not vanish to machine precision at $\Gamma t = 1$. Furthermore, numerical errors eventually dominate the solution with errors being largest near the top and bottom boundaries $y = \pm L_y/2$. A look at the relative error of the y component in figure 3.7 also shows that errors dominate the solution after $\Gamma t \sim 4$.

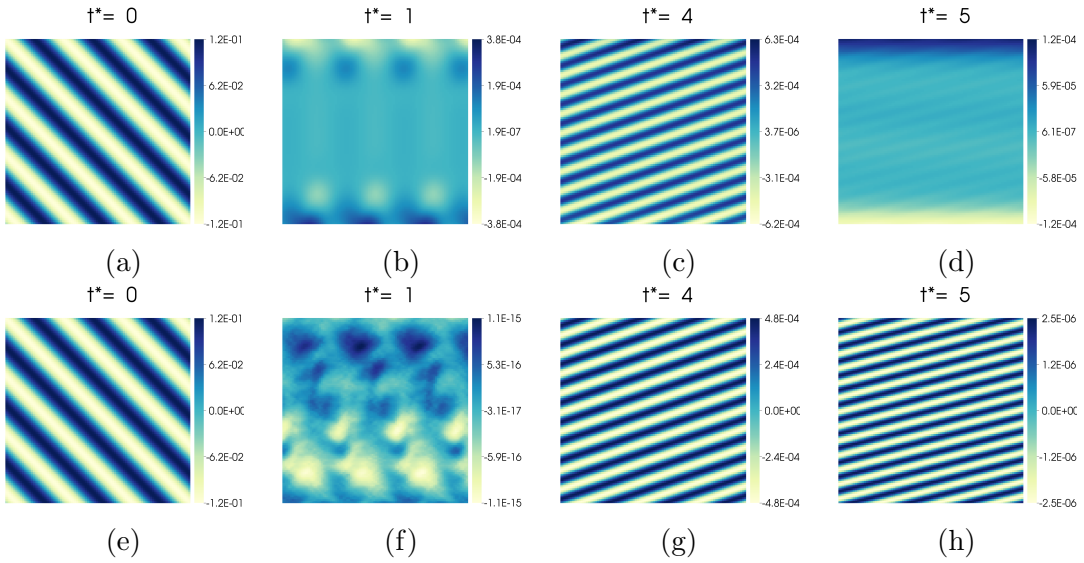

Figure 3.4: Snapshots of a Kelvin mode perturbation at the non-dimensional times $t^\star = \Gamma t$ =0, 1, 4 and 5 using Gerz *et al.* (1989)'s approach (a-d) and the new method (e-h). The new algorithm maintains the normal structure of the wave perturbation as it is turned and dissipated at all times. The original method described by Gerz *et al.* (1989) does not preserve the structure of a wave. The errors are most visible when the horizontal perturbation vanishes at $\Gamma t = 1$ and when the wave is quickly dissipated by viscosity ($\Gamma t > 4$).

The problem with the algorithm of Gerz *et al.* (1989) is the incompatibility between the time discretization and the operator splitting. These two need to work hand in hand because the shear-periodic boundary conditions are time-dependent. In particular, the Adam-Bashforth time integrator is ill advised here because it convolves waves with different orientations ($\mathbf{u}^n$ and $\mathbf{u}^{n-1}$).

To understand why this an issue, let us consider the simpler equation parametrized by a constant $A > 0$

$$\frac{\partial u}{\partial t} + \Gamma y \frac{\partial u}{\partial x} = Au \tag{3.17}$$

Despite being radically simpler than the Navier-Stokes equation and unbounded, this equation still captures some of the physics of homogeneously sheared flows. In fact, the turbulent kinetic energy in the self-similar regime of HST (discussed

in the following section) displays exponential growth that obeys equation (3.17) above. Solutions of the form of turning waves $u = \hat{u}(t)\exp(i\mathbf{k}\cdot\mathbf{x})$ must satisfy

$$\frac{d\mathbf{k}}{dt}\cdot\mathbf{x} = -\Gamma y\mathbf{k}\cdot\mathbf{e}_x \tag{3.18}$$

$$\frac{d\hat{u}}{dt} = A\hat{u} \tag{3.19}$$

Hence, we find that $u = u(0)\exp(At)\exp\left(i\left(k_x x + (k_{y,0} - k_x\Gamma t)y\right)\right)$ is a solution to (3.17). The numerical solution is well behaved when any perturbations are of the same form, i.e., rotating waves as not to break the normal structure of the wave. In this case, the perturbations grow slowly and are not amplified in a relative sense. The discretization error ϵ, that is the difference between the numerical and analytical solutions, evolves according to the same equation (3.17). Now, suppose these errors at the time steps n and $n-1$ are waves of amplitude $\hat{\epsilon}^n$ and $\hat{\epsilon}^{n-1}$ and wavevectors $\mathbf{k}^n$ and $\mathbf{k}^{n-1}$. For clarity, the error at the n-th time steps reads

$$\epsilon^n = \hat{\epsilon}^n\exp(i\mathbf{k}^n\cdot\mathbf{x}) \tag{3.20}$$

At the next time step, the new error needs to retain the form (3.20) with a new wavevector and amplitude, $\mathbf{k}^{n+1}$, $\hat{\epsilon}^{n+1}$, that are discrete solutions to the ordinary differential equations (3.18) and (3.19).

With the algorithm above, the Adam-Bashforth integration yields an intermediary error

$$\bar{\epsilon}^{n+1} = \epsilon^n + \Delta tA\left(\frac{3}{2}\hat{\epsilon}^n\exp(i\mathbf{k}^n\cdot\mathbf{x}) - \frac{1}{2}\hat{\epsilon}^{n-1}\exp\left(i\mathbf{k}^{n-1}\cdot\mathbf{x}\right)\right) \tag{3.21}$$

$$= \left(\hat{\epsilon}^n + \Delta tA\left(\frac{3}{2}\hat{\epsilon}^n - \frac{1}{2}\hat{\epsilon}^{n-1}\exp(-i\Delta\mathbf{k}\cdot\mathbf{x})\right)\right)\exp(i\mathbf{k}^n\cdot\mathbf{x}) \tag{3.22}$$

where $\Delta\mathbf{k} = \mathbf{k}^n - \mathbf{k}^{n-1}$. The application of the "shear-remapping" step yields the

error at $n+1$

$$\epsilon^{n+1} = \overbrace{\left(\hat{\epsilon}^n + \Delta t A \left(\frac{3}{2}\hat{\epsilon}^n - \frac{1}{2}\hat{\epsilon}^{n-1}\exp\left(-i\Delta\mathbf{k}\cdot(\mathbf{x}-\Delta t\Gamma y\mathbf{e}_x)\right)\right)\right)}^{\hat{\epsilon}^{n+1}} \times \exp\underbrace{\left(i\mathbf{k}^n\cdot(\mathbf{x}-\Delta t\Gamma y\mathbf{e}_x)\right)}_{i\mathbf{k}^{n+1}\cdot\mathbf{x}} \tag{3.23}$$

Let us examine if this update preserves the structure of a wave. First, the phase of the update (3.23) can be recast with a new wavevector $\mathbf{k}^{n+1}$ in the following way

$$\mathbf{k}^n\cdot(\mathbf{x}-\Delta t\Gamma y\mathbf{e}_x) = \mathbf{k}^{n+1}\cdot\mathbf{x} \tag{3.24}$$

Further reorganization of the result above shows that the new wavevector is indeed solution to (3.18)

$$\frac{\mathbf{k}^{n+1}-\mathbf{k}^n}{\Delta t}\cdot\mathbf{x} = -\Gamma y\mathbf{k}^n\cdot\mathbf{e}_x \tag{3.25}$$

This is actually an exact solution of (3.18) because the wavevector is a linear function of time.

The amplitude $\hat{\epsilon}^{n+1}$ in the update (3.23) is, however, not a valid one and does not satisfy the condition (3.19). The failure is caused by the presence of spatial coordinates in its expression, and precisely because of the different orientations ($\Delta\mathbf{k}\neq 0$) of the right hand side between $n-1$ and n. The problematic term can be simplified as the following

$$\exp\left(-i\Delta\mathbf{k}\cdot(\mathbf{r}-\Delta t\Gamma y\mathbf{e}_x)\right) = \exp\left(-ik_x\Gamma y\Delta t\right) \sim 1 - ik_x\Gamma y\Delta t \tag{3.26}$$

showing that the errors will be larger at the top and bottom of the domain. This is consistent with previous observations.

In addition to distorting the wave, numerical errors grow faster than the analytical solution. The error amplitude can be cast in the form $\hat{\epsilon}^n = e^{\alpha(y)n\Delta t}$, similarly

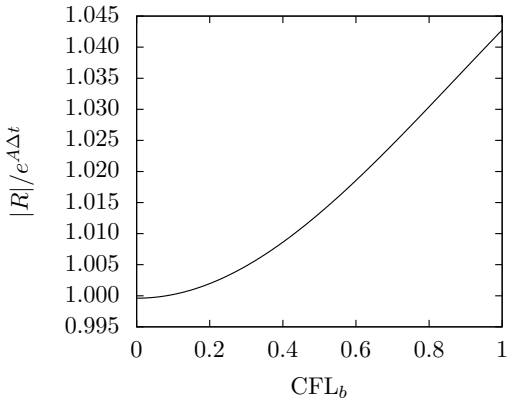

Figure 3.5: Ratio of the error amplification between n and $n+1$ to the amplification of the analytical solution. The value is given for the highest wavenumber admissible in the simulation grid $k_x = \pi n_x / L_x$ and at position $y = L_y/2$. Cell to cell numerical oscillations are expected for a ratio larger than one.

to the analytical amplitude but with a growth rate that depends on y. From equation (3.23), the relative amplification $R = e^{\alpha(y)\Delta t}$ between step n and $n-1$ satisfies

$$R^2(y) - \left(1 + \frac{3}{2} A\Delta t\right) R(y) + \frac{A\Delta t C(y)}{2} = 0 \tag{3.27}$$

where $C(y) = \exp(ik_x \Gamma y \Delta t)$. Because we expect the scheme to fare the worst at the top and bottom boundaries, let us work directly at $y = L_y/2$ and consider the highest wavenumber, $k_x = \pi n_x / L_x$. We see that for these parameters, $C = \exp(i\pi \mathrm{CFL}_b/2)$, where $\mathrm{CFL}_b = \Gamma L_y \Delta t / \Delta x$ is the convective Courant-Friedrichs-Lewy number for the base shear. With a reasonable time step $A\Delta t = 0.1$ and $\mathrm{CFL}_b = 0.9$, we find that $|R| / e^{A\Delta t} \sim 1.036$. This indicates that distortions and cell to cell numerical instabilities are likely to occur near the boundaries of the domain. Figure 3.5 shows that the relative amplification of the error becomes lower than that of the analytical solutions only for prohibitively small CFL_b numbers.

We now propose an approach that builds on the method of Gerz *et al.* (1989) to ensure stability, robustness and adequate simulation of rotating waves. Figure 3.6 presents an overview of the algorithm. Coming from the realization that we

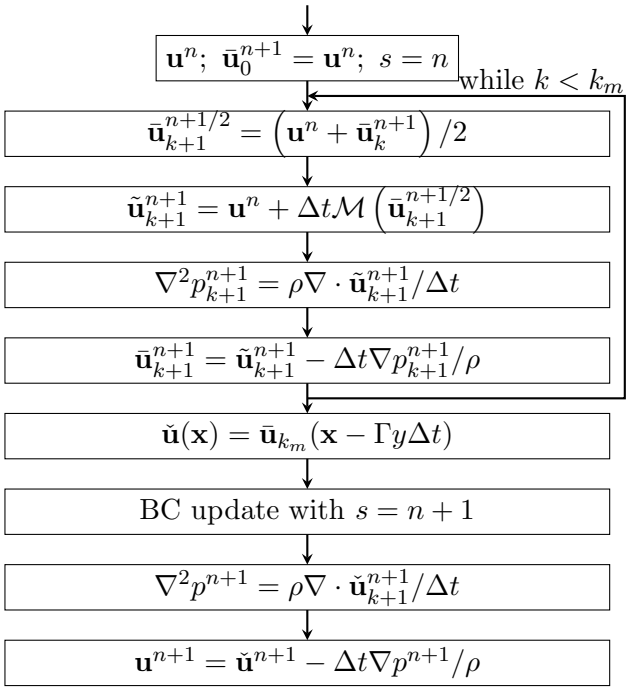

Figure 3.6: Summary of the algorithm with Crank-Nicolson time integration and operator splitting.

cannot use solutions from previous time steps, we replace the Adam-Bashforth time integration with a semi-implicit Crank-Nicolson method.

Let us focus on the $(k+1)$-th sub-iteration: to find the update $\bar{\mathbf{u}}_{k+1}^{n+1}$ at the end of sub-iteration $k+1$, we start by estimating the quantities at mid-step, i.e.,

$$\bar{\mathbf{u}}_{k+1}^{n+1/2} = \frac{\mathbf{u}^n + \bar{\mathbf{u}}_k^{n+1}}{2} \tag{3.28}$$

We will also keep track of a counter s, corresponding to the time at which the boundary conditions are applied. At the start of the sub-iteration, we have $s = n$. Next, we solve the momentum equation without the convection by shear term

$$\tilde{\mathbf{u}}_{k+1}^{n+1} = \mathbf{u}^n + \Delta t \mathcal{M}\left(\bar{\mathbf{u}}_{k+1}^{n+1/2}\right) \tag{3.29}$$

The pressure-Poisson equation is then solved, and the solenoidal condition enforced

$$\nabla^2 p_{k+1}^{n+1} = \rho \frac{\nabla \cdot \tilde{\mathbf{u}}_{k+1}^{n+1}}{\Delta t} \tag{3.30}$$

$$\bar{\mathbf{u}}_{k+1}^{n+1} = \tilde{\mathbf{u}}_{k+1}^{n+1} - \frac{\Delta t}{\rho} \nabla p_{k+1}^{n+1} \tag{3.31}$$

Notice that the necessary boundary conditions update before the pressure-Poisson step are still applied with the time of step n. At this point, we loop through these steps for a maximum number of sub-iterations k_m. The next steps consist in applying the shear-remapping, updating the shear timer s, solving a new pressure-Poisson system and reinforcing the solenoidal condition

$$\breve{\mathbf{u}}^{n+1}(\mathbf{x}) = \bar{\mathbf{u}}_{k_m}^{n+1}(\mathbf{x} - \Gamma y \Delta t) \tag{3.32}$$

$$s = n + 1 \tag{3.33}$$

$$\nabla^2 p^{n+1} = \frac{\nabla \cdot \breve{\mathbf{u}}^{n+1}}{\Delta t} \tag{3.34}$$

$$\mathbf{u}^{n+1} = \breve{\mathbf{u}}^{n+1} - \frac{\Delta t}{\rho} \nabla p^{n+1} \tag{3.35}$$

It is important that the shear counter is updated right after the shear-remapping step and that all subsequent boundary conditions are applied with the new time. Additional information on the pressure solver can be found in Schumann (1985). The velocity field evaluations required for the shear-remapping step and the shear-periodic boundary conditions are obtained using discrete Fourier interpolations (Schumann *et al.*, 1986).

The operator splitting proposed in (Gerz *et al.*, 1989) and adopted here carries a splitting penalty that is first order in time. This is similar in principle to the widely accepted pressure correction approach for incompressible flows (referring to the decoupling of steps (3.29), (3.30) and (3.31)), which is in essence a first order

operator splitting (Chorin, 1968; Temam, 1968). Later studies (Akselvoll, 1995; Dukowicz and Dvinsky, 1992; Wall *et al.*, 2002), show that nesting the advection-correction steps within the semi-implicit Crank-Nicolson loop, achieves formal second order accuracy with $k_m = 2$ sub-iterations. In practice, 2 or 3 sub-iterations are sufficient to fully converge the algorithm (Pierce, 2001). Note that in contrast to Pierce (2001) and Akselvoll (1995) we do not calculate and inverse a jacobian of the Navier-Stokes equations at each sub-iteration of the Crank-Nicolson algorithm since all the time scales are properly resolved in our simulations. The reader interested in the detailed numerical properties of this family of schemes is refered to (Gresho, 1990; Orszag *et al.*, 1986; Kim and Moin, 1985; Akselvoll, 1995; Dukowicz and Dvinsky, 1992; Wall *et al.*, 2002; Pierce and Moin, 2004; Pierce, 2001). To improve the time accuracy associated with the additional shear-remapping step, it would be tempting to perform this inside the Crank-Nicolson loop. However, the present analysis aims to show that this is not as trivial as it may seem. As we have shown with the Von Neumann analysis of the errors above, the interpolation (3.28) would lead to a mid-step velocity $\bar{\mathbf{u}}_{k+1}^{n+1/2}$ that does not preserve the normality of the rotating waves, because $\bar{\mathbf{u}}_{k}^{n+1}$ would be "shear-remapped" one more time than $\mathbf{u}^n$. This causes the solver to be numerically unstable. For robusteness, it is crucial to leave the shear-remapping outside of the Crank-Nicolson loop.

Other time integration procedures can be used to replace the Crank-Nicolson as long as all time interpolations are based on states with the same degree of "shear-remapping". For instance, a Von Neumann analysis of equation (3.17) would show that a second order Runge-Kutta integration scheme could be employed without breaking the normal structure of the rotating waves. Unlike the Adam-Bashforth which mixes states at n and $n-1$, the Runge-Kutta scheme uses a mid-step state that is a linear combination of states at n only. We rely on the iterative Crank-

Nicolson for the reasons explained above.

For the test problem (3.17), this algorithm yields an error at $n+1$ of the form

$$\epsilon^{n+1} = \hat{\epsilon}^n \left(\sum_{k=0}^{k_m} \frac{(\Delta t A)^k}{k!} \right) \exp\left(i \mathbf{k}^{n+1} \cdot \mathbf{r} \right) \tag{3.36}$$

Because the amplitude of the error at $n+1$ is independent of the inhomogeneous coordinate y, the structure of the wave is preserved. Additionally, the rate of growth of errors $R = \epsilon^{n+1}/\epsilon^n$ is strictly smaller than the rate of growth of the analytical solution $e^{A\Delta t}$. When tested on the Kelvin modes, the relative errors, shown in figure 3.7, are significantly lower than previously found with the method of Gerz *et al.* (1989). Snapshots of the horizontal velocity isocontours, figure 3.4 (e-h), show that the structure of the rotating wave remains intact even as it rotates and dissipates.

Contrary to the methods of Rogallo (1981) and Gerz *et al.* (1989) there is no CFL_b restriction with this approach. This property derives from the characteristic method employed in the shear-remapping step. The semi-implicit Crank-Nicolson is second order in time. Combined with NGA's arbitrarily high order spatial discretization on a staggered mesh (Desjardins *et al.*, 2008a), the implementation conserves mass, momentum and kinetic energy in a discrete sense. We primarily use a second order discretization for the simulation of HST, although fourth and sixth order discretizations are also considered.

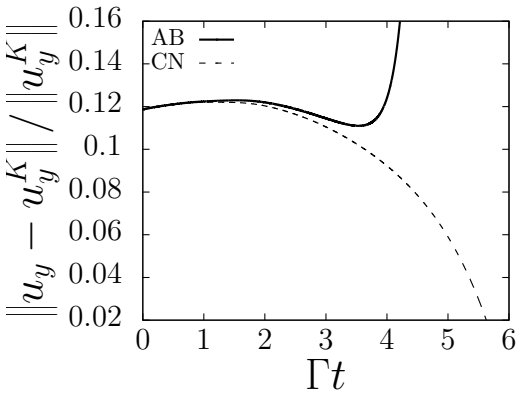

Figure 3.7: Relative error from the simulations of Kelvin modes using Gerz *et al.* (1989) approach and the one presented here. When the perturbation starts dissipating ($\Gamma t > 3$), numerical errors quickly dominate in the original approach of Gerz *et al.* (1989).

3.5 Direct numerical simulation of homogeneously sheared turbulence

In this section, we seek to further validate the numerical approach and explore the physics of homogeneous shear turbulence. The analysis of the long time statistics is undertaken to test the universality of the self-similar regime. We provide comparisons with experimental data and predictions from rapid distortion theory. To understand whether the flow achieves local isotropy, we consider the statistics of the transverse velocity derivative.

The flow is initialized with the turbulence spectrum provided in Isaza and Collins (2009) (IC)

$$E_0(k) = C_k \epsilon_0^{2/3} \kappa_0^{-5/3} \begin{cases} (k/\kappa_0)^2 & k < \kappa_0 \\ (k/\kappa_0)^{-5/3} & \kappa_0 \leqslant k \leqslant \kappa_\eta \\ 0 & k > \kappa_\eta \end{cases} \tag{3.37}$$

where ϵ_0 is the initial dissipation rate, κ_0 is the spectrum peak wavenumber and

$C_k = 1.5$ is a constant. The largest wavenumber κ_η follows

$$\kappa_\eta = \kappa_0 \left[\frac{2\epsilon_0^{1/3}}{3\nu C_k \kappa_0^{4/3}} + \frac{11}{15} \right] \tag{3.38}$$

This flow is characterized by two non-dimensional numbers, the Taylor micro-scale Reynolds number $Re_\lambda = \lambda(q^2/3)^{1/2}/\nu$, based on the micro-scale $\lambda = \sqrt{15\nu q^2/(3\epsilon)}$, and the shear number $S^* = \Gamma q^2/\epsilon$, where q^2 is twice the kinetic energy. In HST, Re_λ and S^* are dynamic quantities varying with increasing total strain Γt. We denote the initial values with a subscript 0. Note that alternative definitions of Re_λ can be found in the literature. For instance a number of experimental studies report results in terms of the longitudinal Taylor micro-scale $\lambda_{xx} = \sqrt{\langle u_x^2 \rangle / \langle (\partial u_x/\partial x)^2 \rangle}$ and the corresponding Reynolds number $Re_{\lambda_{xx}} = \langle u_x^2 \rangle^{1/2} \lambda_{xx}/\nu$. Brackets in these expressions denote spatial averaging. The two Taylor micro-scales can be found from one another using $\epsilon = 5\nu q^2/\lambda^2 = 15\nu \langle u_x^2 \rangle / \lambda_{xx}^2$, which requires knowledge of the second moment of the velocity. When only two velocity components are measured, we estimate $q^2 = (1+\alpha)(\langle u_x^2 \rangle + \langle u_y^2 \rangle)$. The quantity $\alpha = \langle u_z^2 \rangle / (\langle u_x^2 \rangle + \langle u_y^2 \rangle)$ is estimated at 0.43 by Isaza *et al.* (2009), in agreement with prior experimental measurements.

There has been much debate in the literature about whether this flow reaches a self-similar state. According to Pope (2001) and George and Gibson (1992), this is a state attained once the flow is controlled by a single time scale. This regime is observed when the following features apply:

1. The kinetic energy q^2 grows exponentially, taking the form $q^2/q_0^2 \propto \exp(\sigma \Gamma t)$, where σ is the growth rate.
2. Statistics normalized by the shear rate Γ and kinetic energy become independent of time. These include: the ratio of production rate $\mathcal{P} = -\Gamma \langle u_x u_y \rangle$

to dissipation rate ϵ, shear number S^* and anisotropic Reynolds stress tensor $b_{ij} = \langle u_i u_j \rangle / q^2 - \delta_{ij}/3$.

3. The integral length scale $L_{11} = \int_0^\infty u_x(x,y,z)u_x(x+r,y,z)dr/\langle u_x^2 \rangle$ when scaled by q/Γ reaches a constant.

Virtually all experiments indicate the existence of a self-similar state. Experiments from Tavoularis and Corrsin (1981) (TC), Tavoularis and Karnik (1989) (TK), Shen and Warhaft (2000) (SW), Rohr *et al.* (1988) and Isaza *et al.* (2009) (ICW) find asymptotic states consistent with the requirement of self-similarity. On the other hand, DNS studies offer a more uncertain view of the long time state. The simulations of Lee *et al.* (1990) (based on Rogallo's method) do not achieve a self-similar state, whereas the DNS of Isaza and Collins (2009) (IC) and Sukheswalla *et al.* (2013) (SC) (both based on the pseudo-spectral method of Brucker *et al.* (2007)) indicate the opposite. Table 3.2 reports a compilation of data from the literature.

In the self-similar regime, the dependence of the asymptotic values on the initial conditions is still an open question. In the case of a self-similar regime independent of S_0^* and $Re_{\lambda,0}$, the long time values of $\mathcal{P}/\epsilon$, S^*, and b_{ij} would be universal quantities. The experimental evidence for the universality of the long-time state with different initial conditions is not clear cut. SW and TC find comparable asymptotic values (see table 3.2) despite the different facilities, Reynolds number and shear rates considered. In both cases, the asymptotic shear number S^* and ratio of $\mathcal{P}/\epsilon$ were found close to 12 and 1.6 respectively. This is further confirmed by ICW in their lower initial shear number experiment (ICW6). Nonetheless, the latter group finds a higher pair $(S^*, \mathcal{P}/\epsilon)$ in their larger initial shear number experiment (ICW12). They also report that the variation of $Re_{\lambda,0}$ leads to no

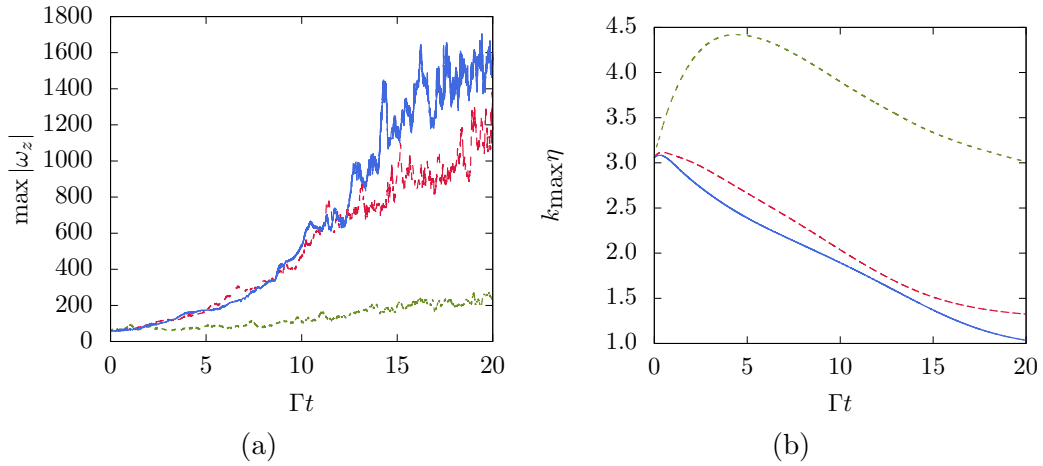

Figure 3.8: Evolution of the maximum vorticity in the z direction (a) and product of the largest resolved wavenumber with the Kolmogorov length scale (b) for the three cases considered: —, S27; −−, S15; $\cdots$, S03. The bounded evolution of the vorticity shows the stability of the numerics. The small scales of the turbulence are well resolved when $k_{\max}\eta > 1$.

change in the asymptotic values. The conclusion we draw from these experiments is that the asymptotic state is likely independent of $Re_{\lambda,0}$ but the dependence on S_0^* is unresolved. As we explain later, we find from our simulations little sensitivity to the initial shear number in the self similar regime.

In this study, we performed three runs termed S03, S15, and S27 corresponding to the initial shear numbers $S_0^* = 3,\ 15,\ 27$ respectively, and initial Reynolds number $Re_{\lambda 0} = 29$ for all three cases. The choice of three distinct shear numbers allows the analysis of the sensitivity of the long time state to this quantity. In addition, cases S15 and S27 have sufficiently high shear numbers to allow for comparisons with RDT.

Details of the simulation setup are given in table 3.3. The choice of parameters follows the DNS of SC and is based on a thorough discussion in IC. It is argued that the correct resolution of all scales is of paramount importance to achieving a self-similar state. The challenge in HST is that the large scales grow and the

small scales decrease as the simulation progresses. For a given mesh, the loss of resolution is inevitable. The integration time window can be extended by the choice of a finer grid at greater computational cost. We perform our simulations with 2 billion grid cells and limit the integration to the dimensionless time $\Gamma t = 20$. Figure 3.8b shows that adequate resolution of the small scales is achieved for all cases by maintaining $k_{\max}\eta \geqslant 1$ where $k_{\max}$ is the largest resolved wavenumber and $\eta = (\nu^3/\epsilon)^{1/4}$ is the Kolmogorov length. Note that the nearly monotonic decrease of η is in agreement with the experimental findings of Tavoularis and Corrsin (1981) as well as Rohr *et al.* (1988). The computational box remains amply larger than the largest turbulence scales. The integral length scale L_{11}, a measure of these scales, remains $< 0.07L_x$ at all times for the three simulations.

We note that a subset of the literature considered integration times significantly longer than $\Gamma t = 20$ but at significantly lower resolutions. Pumir and Shraiman (1995) employ Rogallo's method, which is stable to very long times but with a loss of kinetic energy due to remeshing (Brucker *et al.*, 2007), to run simulations until $\Gamma t = 210$ at the resolution 144^3. More recently, Gualtieri *et al.* (2007a) ran simulations until $\Gamma t = 870$ at the resolution $256 \times 256 \times 128$. Other similar approaches include (Pumir, 1996; Schumacher and Eckhardt, 2000; Schumacher, 2001; Gualtieri *et al.*, 2002; Schumacher, 2004). These simulations are, *by design*, confined by the numerical box. The goal of these studies is generally to achieve statistical stationarity where the production rate balances the dissipation rate, and the small scales are bound by the mesh resolution. While confinement by the box may have its own purposes (see (Gualtieri *et al.*, 2007a)), these settings do not allow the manifestation of the self-similar regime, a state of significant imbalance between production and dissipation and continuously decreasing small scales.

3.5.1 Numerical robustness

Before considering the physics of these flows, we address a note on the numerical feasibility of the simulations. Figure 3.8a reports the maximum vorticity in the z direction for all three runs. The signal is noisy (as for any instantaneous quantity in a turbulent field) but remains bounded nevertheless. In SC simulations, this quantity diverges around $\Gamma t \sim 10$ and is believed to be the root of the instability of the simulations. The remedy proposed consisted in damping the small scale features with a spectral filter every few time steps. This fix stabilizes the method of Brucker *et al.* (2007) at the expense of making it more dissipative. Detailed study of the effects of the filter in SC shows that the dissipation rate is strongly affected by the filtration procedure and cannot be faithfully captured by this approach (Sukheswalla *et al.*, 2013). Our attempts to run these cases with the original method of Gerz *et al.* (1989) also failed quite rapidly (around $\Gamma t \sim 2$). We ran these cases using the numerical method described in section 3.4 without the input of any artificial viscosity or dissipation processes, retaining the most accurate numerical properties.

To test the effect of the spatial discretization, we run case S15 with second, fourth, and sixth order discretizations. The production and dissipation rates are shown in figure 3.9. The discretization order affects primarily the small scales through the dissipation rate. Differences manifest towards the end of the simulation $\Gamma t \sim 20$ but are very small given the ample resolution. We conclude that the second order scheme is sufficient.

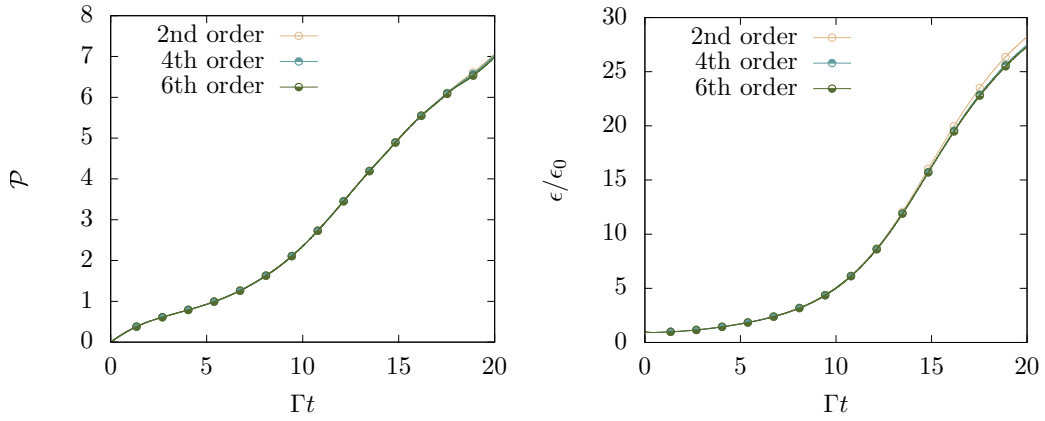

(a) Production rate (b) Normalized dissipation rate

Figure 3.9: Effect of the spatial discretization on the large (production rate) and small scale (dissipation rate) statistics.

	DNS					Experiment			
Parameters	S03	S15	S27	SC	IC	ICW6	ICW12	TC	SW
S_0^*	3	15	27	15	15	6	12	-	-
S^*	9.19	10.33	11.85	-	19.6	11.6	16.02	12.15	12.48
$Re_{\lambda 0}$	29	29	29	50	26	-	-	-	-
Re_λ	91	107	111	-	-	-	-	160	663
$Re_{\lambda_{11,0}}$	-	-	-	-	-	100	100	-	-
$Re_{\lambda_{11}}$	-	-	-	-	-	-	-	266	974
$\mathcal{P}/\epsilon$	1.34	1.46	1.69	-	2.8	1.61	1.9	1.72	1.51
$-\rho_{xy}$	0.45	0.44	0.44	0.59	0.55	0.44	0.38	0.45	0.38
b_{xx}	0.14	0.15	0.16	0.31	0.29	-	-	0.2	0.15
b_{yy}	-0.11	-0.12	-0.12	-0.19	-0.20	-	-	-0.15	-0.12
b_{zz}	-0.03	-0.03	-0.04	-0.12	-0.09	-	-	-0.05	-0.03
b_{xy}	-0.15	-0.14	-0.14	-0.17	-0.16	-0.14	-0.12	-0.14	-0.12
σ	0.10	0.15	0.17	0.14	0.20	0.10	0.27	0.12	0.08
$\Gamma L_{11,1}/q$	1.12	0.94	1.00	2.47	-	1.64	2.31	2.33	-

Table 3.2: Comparisons of the present asymptotic DNS statistics (S03, S15, S27) with previous DNS and experiments. SC: Sukheswalla *et al.* (2013); IC: Isaza and Collins (2009); ICW: Isaza *et al.* (2009); TC: Tavoularis and Corrsin (1981); SW: Shen and Warhaft (2000). When the kinetic energy is not reported in experiments, it is estimated with $q^2 = 1.43(\langle u_x^2 \rangle + \langle u_y^2 \rangle)$ preferably or with $q^2 = 2\langle u_x^2 \rangle$.

Run	L_x	L_y	L_z	n_x	n_y	n_z	ϵ_0	κ_0	ν	S_0^*	$Re_{\lambda 0}$
S03	4π	2π	2π	2048	1024	1024	0.1754	14	6×10^{-4}	3	29
S15	4π	2π	2π	2048	1024	1024	0.1754	14	6×10^{-4}	15	29
S27	4π	2π	2π	2048	1024	1024	0.1754	14	6×10^{-4}	27	29

Table 3.3: Parameters for the three runs considered in this study.

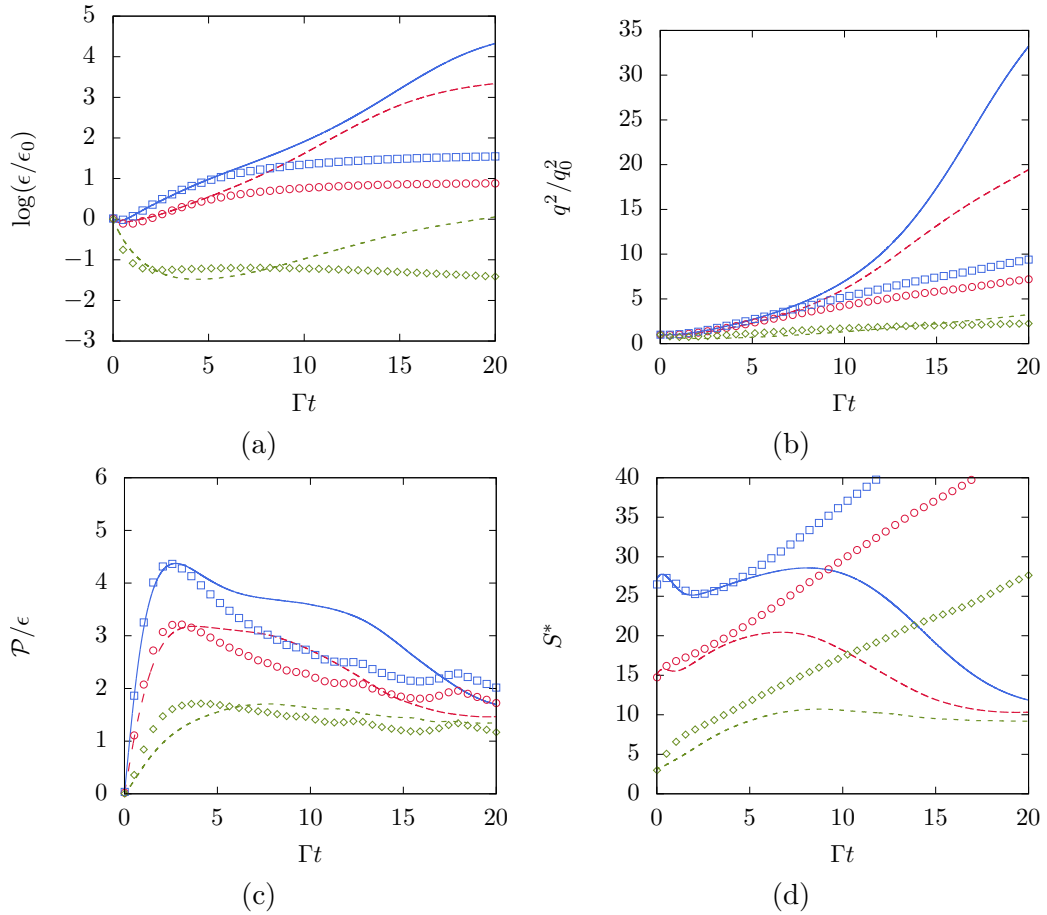

Figure 3.10: Some turbulence statistics: normalized dissipation rate (a) normalized kinetic energy (b) ratio of production rate to dissipation rate (c) and shear number (d). The DNS (lines) show a self-similar regime weakly sensitive to the initial shear number. The viscous RDT (symbols) shows agreement for total strains $\Gamma t \leqslant 5$. DNS: —, S27; −−, S15; $\cdots$, S03. νRDT: □, S27; ○, S15; ◇, S03.

3.5.2 Analysis of the self-similar regime

The temporal evolution of the normalized dissipation rate ϵ/ϵ_0, normalized kinetic energy q^2/q_0^2, the ratio of production to dissipation rates $\mathcal{P}/\epsilon$ and shear number S^* are presented in figure 3.10. Both the dissipation rate and kinetic energy are seen to grow exponentially after $\Gamma t \sim 5$. This is consistent with previous DNS and experiments as well as the requirement for a self similar state. The growth rate σ of the kinetic energy depends on the initial shear number S_0^*. A fit to the DNS data for times $4 \leqslant \Gamma t \leqslant 20$, yields $\sigma = 0.10$ for the medium shearing case S03 and $\sigma = 0.15$ and 0.17 for the high shearing case S15 and S27 respectively. These values are close to the ones reported by SC (0.12, 0.14 and 0.13 for their simulations with initial shear number 3, 15 and 27 respectively, and $Re_{\lambda 0} = 50$). However, unlike SC, we observe a monotonic increase in σ with increasing shear number. One might expect a monotonic increase in σ with increasing S_0^* based on previous observations in the experimental and theoretical literature. It is known from Tavoularis (1985) that the growth rate is function of the shear number and initial length scale of the flow. The theoretical analysis in George and Gibson (1992) of the self-similar state points towards a growth rate that increases with increasing shear rate Γ for similar initial turbulence spectra. Furthermore, the experiments of Isaza *et al.* (2009) of (ICW6 and ICW12) hint towards positive correlations between these two quantities (see table 3.2). Definitive conclusions would require the study of more than just two shear numbers. Experiments from TK report the growth rate for a large number of experiments but the shear number is varied at the same time as other parameters. It can be noted that a fit over the time window $4 \leqslant \Gamma t \leqslant 9$, as done in IC, yields values substantially close to those found in that study: $\sigma = 0.12,\ 0.20,\ 0.20$ from our runs S03/S15/S27 and $\sigma = 0.10,\ 0.20,\ 0.18$ from theirs. This seems to indicate the total integration time

in IC was not sufficiently long to attain a self-similar state. The experiments of TC and SW do not report the growth rate σ. However, indirect comparisons can be made by considering the turbulent kinetic energy balance under the assumption of exponential growth (Tavoularis, 1985)

$$\sigma = \frac{1}{\Gamma q^2}\frac{dq^2}{dt} \quad = \quad 2b_{xy}\left(\frac{\epsilon}{\mathcal{P}} - 1\right) \tag{3.39}$$

Using this approach, we find $\sigma = 0.12$ and $\sigma = 0.08$ for TC and SW experiments respectively. These values are in approximate agreement with our findings.

At long times, the ratio of production to dissipation (figure 3.10c) and shear number (figure 3.10d) tend to collapse to S_0^*-independent asymptotic values for all three cases that are close to to the ones reported by SW, TC and ICW. At the end of the simulations $\Gamma t = 20$, $\mathcal{P}/\epsilon = 1.34$, 1.51 and 1.63 and $S^* = 9.18$, 10.47 and 11.44 for S03, S15 and S27 respectively. For comparison, in their respective experiments, SW measure $(\mathcal{P}/\epsilon, S^*)$=(1.51,12.22), TC $(\mathcal{P}/\epsilon, S^*)$=(1.72,12.15), and ICW $(\mathcal{P}/\epsilon, S^*)$=(1.61,11.6) in their lower initial shear number case. The latter group reports different plateaus in their high S_0^* experiment , but it is worth mentioning that this experiment relied on an active shear generator unlike the passive one used in their lower S_0^* experiment and by SW and TC. The constancy of $\mathcal{P}/\epsilon$ and S^* in our simulations further corroborates the self-similarity of the flow. It is interesting to note that the asymptotic values seem to collapse despite the widely different initial shear numbers. Previous DNS find different trends. While Rogers (1986) finds asymptotic states insensitive to the initial conditions, the DNS of Rogallo (1981), Lee *et al.* (1990), Isaza and Collins (2009), and Sukheswalla *et al.* (2013) indicate the opposite behavior.

The anisotropic Reynolds stresses seen in figure 3.11 reach asymptotes independent of the initial shear number. These values are in good agreement with TC and

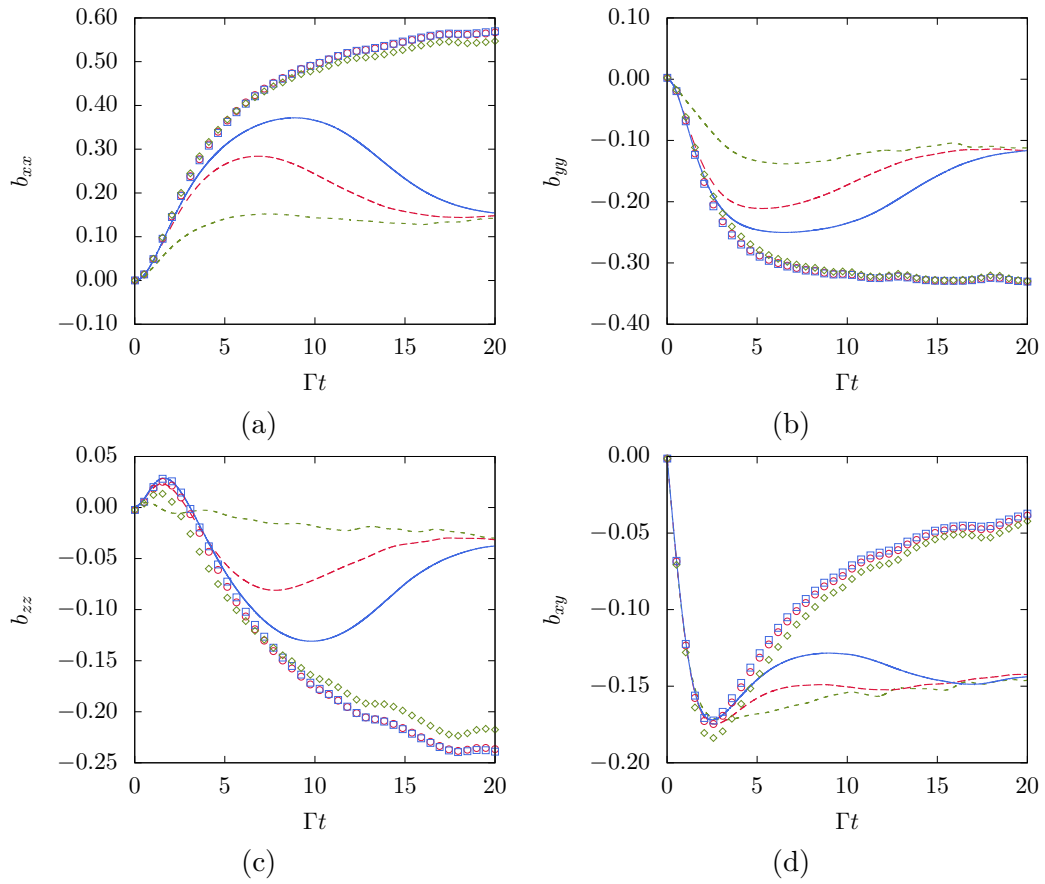

Figure 3.11: Anisotropic stress tensor components. Lines and symbols as in figure 3.10.

SW experiments. The early evolution of b_{xx}, b_{yy}, b_{zz}, and b_{xy} also show very little sensitivity to the shear number. In the experiments of Isaza *et al.* (2009), doubling the shear number led to no appreciable variation of b_{xy}, which was found to be equal to -0.12. It is possible that the asymptotic values might be controlled solely by the initial Reynolds number $Re_{\lambda 0}$. The cross correlation $\rho_{xy} = \langle u_x u_y \rangle / \sqrt{\langle u_x^2 \rangle \langle u_y^2 \rangle}$ from our simulations reaches a value -0.45 in agreement with most experiments. In contrast, most DNS studies, including the ones shown in table 3.2, find values in the range -0.5 to -0.6 (Sukheswalla *et al.*, 2013).

To complete the analysis of the self-similar state, we graph the normalized integral length scale $\Gamma L_{11}/q$ in figure 3.12. Rogallo (1981) explains that this quantity

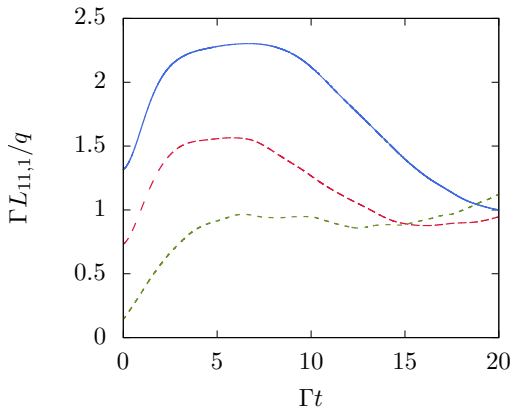

Figure 3.12: Integral lengthscale normalized by the characteristic large scale length q/Γ. Lines as in figure 3.10.

must reach a non-zero plateau. On one hand, if $\Gamma L_{11}/q$ were to diverge, then the distortion terms would dominate at large times leading to the ultimate decay of kinetic energy predicted by RDT (Rogallo, 1981; Rogers, 1991). On the other hand, vanishing $\Gamma L_{11}/q$ implies a return to isotropoy of the flow and decay of the kinetic energy as well. Consequently, the self-similar regime is characterized by constant $\Gamma L_{11}/q$. Figure 3.12 suggests that this plateau is established around ~ 1 for all three case S03, S15 and S27.

3.5.3 Comparisons with viscous RDT

Here, we compare the short and long term turbulence statistics with predictions from viscous RDT. Previous researchers have also compared results with RDT. Rogers (1991) provides early time expansions of the inviscid RDT solution, valid until $\Gamma t \sim 1$ at very high shear rates. IC extended these expansions to the viscous case. They show a dependence on shear number of the turbulence statistics that was absent from inviscid RDT. Comparisons with their DNS data was limited to the ratio $\mathcal{P}/\epsilon$ and showed qualitative agreement. DNS based on Rogallo's method

without remeshing by Lee *et al.* (1990) shows agreement with the inviscid linear theory at the high shear number $S_0^* = 33.5$ until $\Gamma t = 12$. Here we systematically compare the statistics discussed above to viscous RDT (νRDT) introduced in IC. The Reynolds stresses $R_{ij} = \langle u_i u_j \rangle$ and dissipation rate ϵ from νRDT are retrieved by computing the following integrals

$$R_{ij}(t) = \int\int\int e^{-2\nu t\left(k^2 - k_{x,0}k_{y,0}\Gamma t + \frac{(k_{x,0}\Gamma t)^2}{3}\right)} A_{ip}A_{jq}\phi^0_{pq}(\mathbf{k}_0)d\mathbf{k}_0 \tag{3.40}$$

$$\epsilon(t) = \nu\int\int\int k^2 e^{-2\nu t\left(k^2 - k_{x,0}k_{y,0}\Gamma t + \frac{(k_{x,0}\Gamma t)^2}{3}\right)} A_{ip}A_{iq}\phi^0_{pq}(\mathbf{k}_0)d\mathbf{k}_0 \tag{3.41}$$

where $\mathbf{A}$ is the RDT matrix defined in appendix B and ϕ^0_{ij} is the initial velocity spectrum

$$\phi^0_{ij}(\mathbf{k}_0) = \frac{E_0(k_0)}{4\pi k^2}\left(\delta_{ij} - \frac{k_{i,0}k_{j,0}}{k_0^2}\right) \tag{3.42}$$

We evaluate the triple integral in spherical coordinates. The integral over wavenumber space, which is finite given the energy spectrum (3.37), is performed analytically to greatly reduce the computational cost. The integral over the azimuthal and polar angles is evaluated with a mid-point rule. All quantities presented here are computed on a mesh on the unit sphere refined until convergence. Notice that a non-dimensionalization of time in the term $\exp\left(-2\nu t\left(\cdots\right)\right)$ appearing in (3.40) and (3.41) reveals a factor $S^* q^2/Re^2$. This, with the realization that the shear number does not appear in the RDT matrix, shows that only a viscous RDT approach accounts for differences arising from different shear numbers.

Figure 3.10 shows statistics computed from νRDT along side the DNS statistics for the medium shear number case S03 and the high shear number cases S15 and S27. We note first that the inclusion of viscous effects allows νRDT to predict distinct evolution for the two cases considered. We observe that νRDT matches closely the DNS data until $\Gamma t \sim 5$. As expected, νRDT matches the DNS data the best for the highest shear number with the agreement for S03 being only

qualitative. The viscous RDT matches the peak $\mathcal{P}/\epsilon$ and early transient in S^*. The anisotropic stresses b_{xx}, b_{yy}, b_{zz} and b_{xy} from νRDT, seen in figure 3.11, appear to have a similar time window of agreement with DNS, i.e., $0 < \Gamma t < 5$. The evolution of these quantities predicted by νRDT is marginally sensitive to the shear number.

The quality of the agreement for later times $\Gamma t > 5$ quickly deteriorates for all cases and quantities considered. The anomalous behavior of the long time turbulence statistics from νRDT is caused by the absence of non-linear effects in the RDT model. It results in an approach that does not support the existence of a self-similar state as found in most experiments and as we find in our DNS. The kinetic energy from νRDT grows linearly at large times (3.10b) contrary to the exponential growth expected. Rogers (1991), using asymptotic expansion of inviscid RDT, already showed linear growth of the kinetic energy at long times. The breakdown of the approach is further seen from the anisotropic stresses that tend towards $b_{xx} = 2/3$, $b_{yy} = b_{zz} = -1/3$ and $b_{xy} = 0$, corresponding to a mono-component flow field ($u_y/u_x = u_z/u_x = 0$) (Lee *et al.*, 1990).

IC suggest that the inclusion of a nonlinear model for the pressure-strain might alleviate this issue. In the absence of such a solution, we find that νRDT and our DNS at high shear numbers display satisfactory agreement until $\Gamma t \sim 5$. Note that the short time expansion in IC were found to give acceptable results only until $\Gamma t \sim 1$. Computing the full νRDT integrals allowed the extension of this time range.

3.5.4 The transverse velocity derivative statistics $\partial u_x/\partial y$

Homogeneous sheared turbulence HST has been central in the testing of one of the most celebrated turbulence theories. Kolmogorov's theory of local isotropic turbulence is most famously known for the -5/3 scaling of the energy spectrum with wave number. The postulate states that the small scales become statistically homogeneous and isotropic when the Reynolds number is high enough. The theory is so successful that it has constituted the basis of a number of turbulence models and numerical methods. For instance, large eddy simulations leverage the universality of the small scales to simplify the calculation to a numerical evaluation of the large scales only reducing considerably the computational cost.

How large exactly this Reynolds number needs to be to achieve the isotropization of the small scales has been at the core of many experiments. It is argued that HST is particularly suited to test the local isotropy postulate. First, the widely studied homogeneous isotropic turbulence DNS and grid turbulence (nearly isotropic) are of limited use here. Second, general inhomogeneous flows (wake turbulence, turbulent jets, channel flows) studied at laboratory conditions or with DNS hardly achieve the stringent high Reynolds number required for true local isotropy. The absence of wall effects allow HST in theory to achieve izotropization of the small scales at lower Re_λ.

A consequence of the local isotropy postulate is that the odd moments of the transverse velocity derivative need to be zero in the limit of infinite Reynolds number ($Re_\lambda \to \infty$). Garg and Warhaft (1998), SW and Ferchichi and Tavoularis (2000) investigated experimentally the effect of Reynolds number on kurtosis and skewness of the transverse velocity derivative $\partial u_x/\partial y$ in homogeneously sheared turbulence. Garg and Warhaft (1998) considered longitudinal Taylor micro-scale

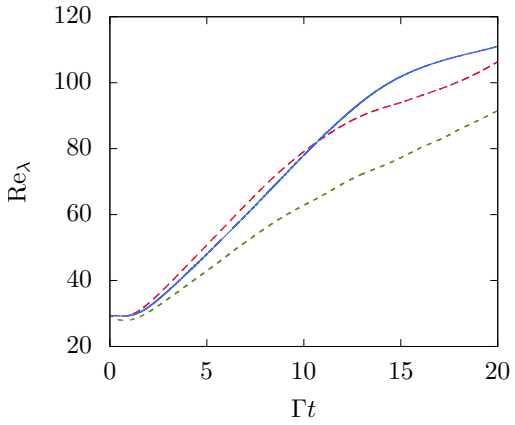

Figure 3.13: Evolution of the Taylor-microscale Reynolds number. Lines as in figure 3.10.

Reynolds numbers in the range $156 \leqslant Re_{\lambda_{xx}} \leqslant 390$ ($\sim 112 \leqslant Re_\lambda \leqslant 280$). Ferchichi and Tavoularis (2000) widened the range of Reynolds numbers studied to $140 \leqslant Re_{\lambda_{xx}} \leqslant 660$ while SW were able to achieve the highest $Re_{\lambda_{xx}} = 1100$. The numerical study in Isaza and Collins (2011) explored the effects of initial shear number S_0^* on the moments of the velocity derivative over the range $22 \leqslant Re_\lambda \leqslant 68$. In (Boris *et al.*, 2004; Biferale and Procaccia, 2005; Casciola *et al.*, 2005; Gualtieri *et al.*, 2007b), the anisotropy of scales is analyzed by decomposing the longitudinal structure function on the group of rotations SO(3). All of the past references concluded that, even at the highest Re_λ they considered, the flow still exhibited local anisotropy.

DNS of HST for Re_λ of $O(10^3)$ is unachievable with current computational resources and the resolution requirements discussed above. Figure 3.13 shows the evolution of the Reynolds number for cases S03, S15 and S27. The maximum Reynolds number achieved was $Re_\lambda = 111$ for S27, followed by $Re_\lambda = 107$ for S15. Notice that the Reynolds number grows at a similar rate for the high shear number cases S15 and S27 and a slower rate for S03. The upper bound of Re_λ in our simulations corresponds to the lower bound in the experiments cited above.

Nevertheless, this allows us to compare S15 and S27 with SW data at $Re_{\lambda_{xx}} = 158$ ($Re_\lambda \sim 107$) and establish preliminary trends at low Reynolds numbers. The simulations also allow the analysis of the effect of initial shear number.

Figure 3.14a shows the probability density function (pdf) of the normalized transverse velocity derivative

$$\xi = \frac{\partial u_x/\partial y}{\langle (\partial u_x/\partial y)^2 \rangle^{1/2}} \tag{3.43}$$

at $Re_\lambda = 107$. The two runs, S15 and S27, are reported alongside SW measurements. The pdfs are highly non-Gaussian and asymmetric. We observe a sharp peak shifted towards negative values and exponential tails. At this Reynolds number, cases S15 and S27 are essentially the same universal self-similar flow. They both yield great agreement with SW data with S27 displaying a little more asymmetry of the pdf and shorter tails. These small variations are likely to be caused by the slightly higher asymptotic shear number attained by S27 (see table 3.2).

The integrand of the expressions for the moments of the pdf of the normalized transverse velocity derivative, $\xi^n \mathrm{pdf}(\xi)$, are reported in figure 3.14 for $n = 3$ to 7. Qualitatively the agreement between SW data and DNS holds well for all 7 moments. The integral of the odd orders $n = 3$, 5 and 7 from $-\infty$ to $+\infty$ correspond to the skewness S_{3y}, super-skewness S_{5y} and hyper-skewness S_{7y} of the transverse velocity derivative $\partial u_x/\partial y$. The integral of the even orders $n = 4$ and 6 are the kurtosis K_{4y} and super-kurtosis K_{6y}. Due to experimental constraints, SW were able to measure only 18 standard deviations of the pdf of ξ, resulting in insufficient sampling for the computation of K_{6y} and S_{7y}. This is not an issue for DNS and shows how computational approaches might complete the information provided by experiments.

Figure 3.15a and 3.15b show the evolution with Re_λ of the odd and even mo-

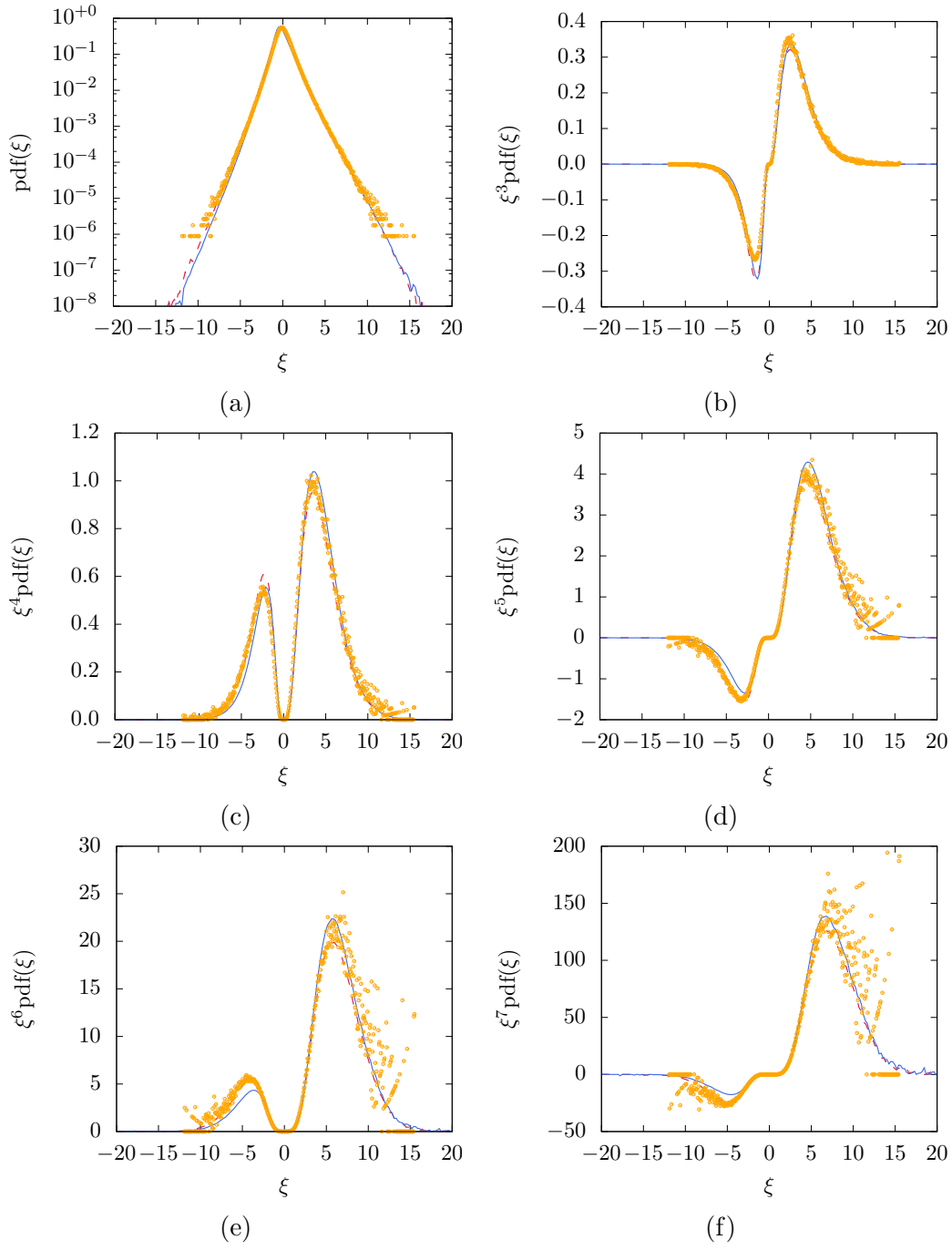

Figure 3.14: Probability density function of the normalized transverse velocity derivative $\xi = (\partial u_x/\partial y)/\langle(\partial u_x/\partial y)^2\rangle^{1/2}$ and the integrand for computing the moments of ξ at $Re_\lambda = 107$. Lines as in figure 3.10. Symbol $\odot$ from figure 9 in SW.

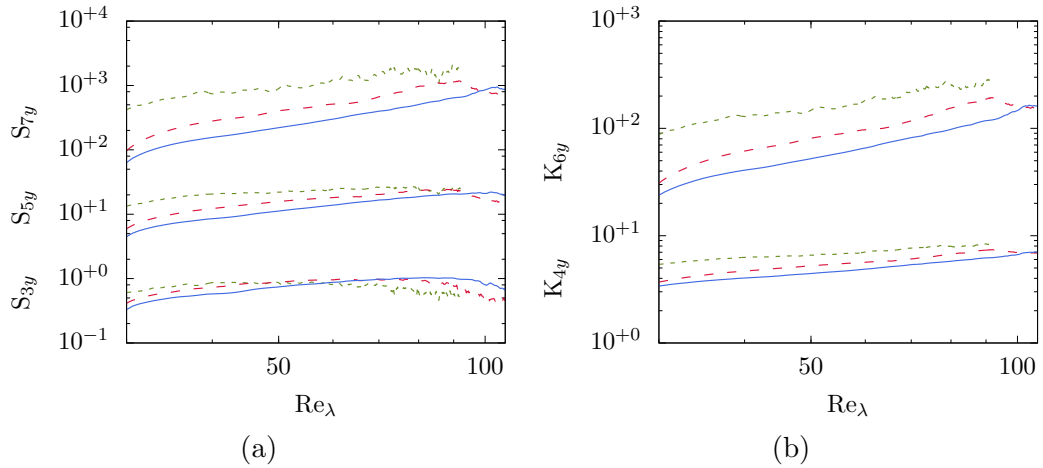

Figure 3.15: Transverse velocity derivative moments. Figure (a) reports the skewness (bottom), super-skewness (middle) and hyper-skewness (top). Figure (b) shows the kurtosis (bottom) and super-kurtosis (top). Lines as in figure 3.10.

ments respectively. In particular, at $Re_\lambda = 107$, we find $S_{3y} = 0.62$, $S_{5y} = 18.9$, $S_{7y} = 840$, $K_{4y} = 6.97$ and $K_{6y} = 149$ from S27, $S_{3y} = 0.46$, $S_{5y} = 15.5$, $S_{7y} = 716$, $K_{4y} = 6.88$ and $K_{6y} = 153$ from S1. SW data yields $S_{3y} = 0.6$, $S_{5y} = 16$, $S_{7y} = 860$, $K_{4y} = 7.2$ and $K_{6y} = 175$. Note that the experimental uncertainty for the hyper-skewness and super-kurtosis is larger due to the under-sampling discusser above. In light of this, the DNS displays close agreement with the experiment.

To test Kolmogorov's postulate, it is customary to perform a fit of the data to a power law ARe_λ^n. Under Kolmogorov's postulate of local isotropy, n is negative for the odd moments (n_{3y}, n_{5y}, n_{7y}) and positive for the even moments (n_{4y} and n_{6y}). To minimize the effects of the isotropic initial conditions, we perform the fit on our data for $Re_\lambda > 50$. The exponents from our simulations and previous studies are reported in 3.4.

The skewness S_{3y} decreases for all three runs S03 and S15 and S27, although only slightly for the latter one. The differences in decay rate come from the initial period of growth of S_{3y} due to the artificial initial conditions. The larger the

Parameters	n_{3y}	n_{5y}	n_{7y}	n_{4y}	n_{6y}
S03	-0.92	0.07	1.07	0.40	1.07
S15	-1.02	0.05	1.10	0.46	1.11
S27	-0.09	0.82	1.96	0.62	1.56
SW	-0.52	-0.02	0.63	0.25	0.7
FT1	-0.77	-0.69	-	0.10	0.25
FT2	-1.00	-0.98	-	0.05	0.08

Table 3.4: Exponent in the power fit Re_λ^n of the transverse velocity derivative moments. Experiments: SW, (Shen and Warhaft, 2000); FT1 & FT2, (Ferchichi and Tavoularis, 2000). DNS.

initial shear number, the more the moments are affected by the initial conditions. We note that the super-skewness and hyper-skewness have positive exponents in contradiction with the local isotropy postulate. However, SW report similar trends: decaying S_{3y}, stagnating S_{5y} and increasing S_{7y}. The kurtosis and super-kurtosis grow with increasing Re_λ as in Kolomogorov's theory, albeit with stronger rates than in experiments.

3.6 Conclusion

The development of algorithms capable of simulating homogeneously sheared flows enables the exploration of many physical questions. In this paper, we improve on the algorithm presented in (Gerz *et al.*, 1989) and apply it to homogeneously sheared turbulence. The algorithm is based on a physical space formulation in the reference frame of the laboratory. This is in contrast with the formulation of Brucker *et al.* (2007) in Fourier space and the formulation of Rogallo (1981) in a moving reference frame. The former approach is subject to Gibbs oscillations at large total strains and the latter suffers from interpolation errors due to frequent remeshing and the degradation of the cells aspect ratio. The method presented is

stable and accurate and does not suffer from these problems.

Issues in the original method (Schumann, 1985; Schumann *et al.*, 1986; Gerz *et al.*, 1989) have been addressed. The use of a semi-implicit Crank-Nicolson in conjunction with operator splitting for convection by the base shear term (see figure 3.6) allows the correct simulation of Kelvin modes (a "rotating" wave that is a solution to the full Navier-Stokes equations) and stable simulations of HST. We present a Von Neumann analysis that explains why the use of an Adam-Bashforth integrator (1) distorts Kelvin modes and (2) leads to fast growing errors near the top and bottom boundaries $y = \pm L_y/2$.

We use the improved algorithm presented to simulate HST until a self-similar state is attained. For the initial Reynolds number $Re_{\lambda 0} = 29$ and three different initial shear numbers $S_0^* = 3$, 15 and 27, we simulate until $\Gamma t = 20$ on a $2048 \times 1024 \times 1024$ mesh. The large resolution is necessary to capture the smallest scales of the flow at all times as they keep decreasing due to the mean shear motion. The simulation until $\Gamma t = 20$ allows the observation of a self-similar state, reported in most experiments and characterized by: (1) exponentially growing turbulent kinetic energy; (2) plateauing of the turbulence statistics when non-dimensionalized by the shear rate (shear number S^*, ratio of production to dissipation $\mathcal{P}/\epsilon$, anisotropic Reynolds stresses b_{ij}); and (3) plateauing of the integral length scale non-dimensionalized by the shear rate and kinetic energy. Comparisons to the experiments of Shen and Warhaft (2000) and Tavoularis and Corrsin (1981) show excellent agreement.

The three runs show that the self-similar states achieved are almost independent of the initial shear number S_0^*. Most notably, we find the asymptotic values $S^* \sim 10$, $\mathcal{P}/\epsilon \sim 1.5$ and $b_{xy} \sim -0.14$. Experiments under different operating conditions

(table 3.2) report values close to the ones we find. This suggests that the self-similar state is universal and is independent of the initial shear number and Reynolds number.

Comparisons with viscous rapid distortion theory νRDT (Isaza and Collins, 2009) show good agreement until $\Gamma t \sim 5$. As expected from this linear theory, the agreement deteriorates with diminishing initial shear number. The long time statistics of RDT ($\Gamma t > 5$) differ significantly from those found in simulations and experiments because of the absence of all non-linearities. These terms have a cumulative effect that lead to the exponential growth of kinetic energy and the appearance of a self-similar state. In contrast, RDT displays linear growth of the kinetic energy and long time statistics that depend sensitively on the initial shear number.

For the initial non-dimensional numbers considered, the small scales display significant anisotropy. The probability density function of the transverse velocity derivative $\partial u_x/\partial y$ shows qualitative and quantitative agreement with the one measured by (Shen and Warhaft, 2000) at $Re_\lambda = 107$. The evolution of the third, fifth and seventh moments S_{3y}, S_{5y} and S_{7y} indicate that local isotropization of scales, if it occurs at all, requires significantly higher Reynolds numbers than the one considered $29 \leqslant Re_\lambda \leqslant 111$. Despite growing super and hyper skewnesses with Reynolds number, the skeweness S_{3y} is seen to decrease. This trend is similar to what is reported in experiments. We also find that the degree of anisotropy increases with increasing initial shear number.

CHAPTER 4

CLUSTERING IN UNBOUNDED HOMOGENEOUS PARTICLE-LADEN SHEAR IN EULER-EULER AND EULER-LAGRANGE SIMULATIONS

4.1 Abstract

Particle-laden flows of sedimenting solid particles or droplets in a carrier gas have strong inter-phase coupling. Even at low particle volume fractions, the two-way coupling can be significant due to the large particle to gas density ratio. In this semi-dilute regime, the slip velocity between phases leads to sustained clustering that strongly modulates the overall flow. The analysis of perturbations in homogeneous shear reveals the process by which clusters form: (1) the preferential concentration of inertial particles in the stretching regions of the flow leads to the formation of highly concentrated particle sheets, (2) the thickness of the latter is controlled by particle-trajectory crossing, which causes a local dispersion of particles, (3) a transverse Rayleigh-Taylor instability, aided by the shear-induced rotation of the particle sheets towards the gravity normal direction, breaks the planar structure into smaller clusters. Simulations in the Euler-Lagrange formalism are compared to Euler-Euler simulations with the Two-Fluid and Anisotropic Gaussian methods. It is found that the Two-Fluid method is unable to capture the particle dispersion due to particle-trajectory crossing and leads instead to the formation of discontinuities. These are removed with the Anisotropic Gaussian method which derives from a kinetic approach with particle-trajectory crossing in mind.

4.2 Introduction

Suspended particles in a carrier fluid can promote heat and mass transfer, catalytic chemical reactions or combustion. The dynamics of such flows are significantly more complex than single phase flows and it is challenging to obtain a physical understanding of the phenomena at play. A particular feature of particle-laden gas flows is the tendency of inertial particles to form clusters many times larger than the particle size. To understand the mechanisms leading to clustering in semi-dilute (low volume fraction but moderate mass loading) suspensions of heavy particles in a gas, we study the case of homogeneously sheared flow. In this configuration, elongated particle clusters are continuously formed and broken down under the combined action of shear, gravity and the preferential concentration of particles in high strain and low vorticity regions of the flow. Kasbaoui *et al.* (2015) previously addressed the onset of clustering of heavy particles with small but non-zero inertia with a linear stability analysis. The non-linear regime is addressed in this paper and reveals a route to clustering in which preferential concentration, flow modulation, particle-trajectory crossing and the Rayleigh-Taylor instability appear successively.

Semi-dilute particle-ladens flow pose special challenges to physical understanding. The interplay between the two phases leads to behaviors distinctly different from purely hydrodynamic or granular flows. Most prominently, the interaction between the two phases leads to the formation of clusters in the particle phase (Squires and Eaton, 1991; Boivin *et al.*, 1998; Yang and Shy, 2005; Poelma *et al.*, 2007; Jenny *et al.*, 2012; Meyer, 2012; Capecelatro *et al.*, 2015). The aggregates of particles modulate the carrier phase on scales larger than a single particle. In turbulence, the inter-phase coupling leads to deviations of the energy and dissipation rate spectra from those predicted by the usual cascade of energy from large to

small scales (Al Taweel and Landau, 1977; Druzhinin, 2001; Aliseda *et al.*, 2002; Pai and Subramaniam, 2012). For heavy particles in a carrier gas, this altered energy cascade occurs even in semi-dilute suspensions and is promoted by gravity (Elghobashi and Truesdell, 1993). Instabilities that lead to clustering of sedimenting particles could provide a mechanism by which gravitational potential energy is transformed into fluid and particle kinetic energy at length scales governed by the two-phase dynamics.

The analysis of clustering in unbounded homogeneous shear reveals mechanisms that can be hard to detect in turbulent flows. This flow retains the simplicity of linear flows but incorporates key elements of more complex anisotropic inhomogeneous flows. The seemingly simple flow exhibits singularly rich behaviors when perturbed sinusoidally and forced by gravity. In the absence of particles, Lord Kelvin (Thomson, 1887) showed that these perturbations are diffused by the fluid's viscosity yielding an exponentially stable state. Recently, we showed by means of a linear stability analysis (LSA) that the addition of particles creates an unstable state through the preferential concentration mechanism (Kasbaoui *et al.*, 2015). The sinusoidal perturbations create periodic regions of dominant rotation and dominant strain, which cause particles to migrate and segregate breaking the homogeneity of the flow. The regions where particles accumulate force the flow in the direction of gravity more than the depleted regions do owing to the higher local number density. The overall behavior is unstable algebraically with a time scale equal to the inverse of the shear rate. The work exposes the onset of clustering in homogeneous shear flow based on a simplified Eulerian-Eulerian model first proposed by Maxey (1987) and then further developed by Druzhinin (1995) and Ferry and Balachandar (2001) valid for heavy particles with small, but non-zero inertia. Characterization of the full clustering route requires analysis of the flow

with large perturbations out of the reach of LSA.

Experimental investigations of clustering in unbounded homogeneous shear are rendered difficult by the size of parameter space to be explored and flow geometry. In addition to the usual Reynolds number Re, the mass loading M (ratio of the masses of the two phases), Stokes number St (product of shear rate and particle characteristic time) and average particle volume fraction $\langle\phi\rangle$ are parameters that critically dictate the working regime of particle-laden flows. Moreover, experiments are often hard to conduct because of the two phases obstructing each other (Modarress *et al.*, 1984; Shuen *et al.*, 1985; Mostafa *et al.*, 1989; Hardalupas *et al.*, 1989; Prevost *et al.*, 1996; Gillandt *et al.*, 2001; Yang and Shy, 2005; Poelma *et al.*, 2007; Lau and Nathan, 2014). These difficulties make numerical approaches particularly appealing in this context.

Numerical endeavors start by a choice of governing equations to be solved. There are two dominant paradigms for treating the two phases, each with their own conceptual difficulties. Euler-Lagrange (EL) simulations rely on solving the position and momentum of every discrete (Lagrangian) particle in addition to the fluid's Navier-Stokes equations. This method is successful in capturing clustering in mesoscale simulations but cannot realistically scale to match lab-scale experiments, let alone industrial flows, because the number of particles to track quickly becomes intractable. An alternative formalism relies on an Eulerian description of the particle phase. Euler-Euler (EE) approaches are usually more computationally efficient and easier to scale. However, the analysis of clustering with these methods is challenging. One challenge is the conceptual difficulties in the derivation of partial differential equations (PDE) for the particle volume fraction and momentum that lead to limits to their applicability. The particle phase is highly

compressible and as such particles are allowed to accumulate in restricted regions of space. The compressibility of the particle phase leads to strong volume fraction gradients, shocks, and void bubbles, i.e., depleted regions where the volume fraction approaches zero. According to Ferrante and Elghobashi (2007) this results in particle velocity fields that contain "holes" indicating a topology change. Moreover, the dynamics of the particle often lead to local folds in phase space resulting in caustics (Gustavsson *et al.*, 2012; Ravichandran and Govindarajan, 2015; Falkovich *et al.*, 2002; Wilkinson *et al.*, 2006). The ability of particles to cross one another's trajectories leads to local multiplicity in the particle velocity (Fox, 2008). This prompted the development of kinetic models (Koch, 1990) and other approaches inspired by rarefied gas flows (Desjardins *et al.*, 2008b; Fox, 2008; Simonin *et al.*, 2002; McGraw, 1997). In this exploratory work, we use leading EE and EL methods to expose similarities and differences across the methodologies.

Building on the linear analysis, we propose to revisit the instability in the light of the EL methodology (Capecelatro and Desjardins, 2013b) and two EE approaches: the low volume fraction Two-Fluid method (TF) (Druzhinin, 1994; Elghobashi and AbouArab, 1983) and the Anisotropic Gaussian method (AG) (Vi *et al.*, 2015). In section 4.5, we present the governing equations and outlines of the instability. Section 4.4 presents the numerical strategies. Careful attention is given to the forcing by the homogeneous shear and the shear-periodic boundary conditions. In section 4.5, the numerical results are compared to the linear stability analysis in the small amplitude regime. This shows agreement across all methods when the particle distribution inhomogeneities are small. In section 4.6, we probe the flow with strong perturbations that trigger non-linear effects. This leads to strong clustering in EL and EE simulations, aided by a secondary Rayleigh-Taylor instability and particle trajectory crossing. The differences noted in the three

computational approaches expose the importance of particle-trajectory crossing in removing discontinuities arising in TF simulations. Concluding remarks are reported in section 4.7.

4.3 Particle-laden homogeneous shear

4.3.1 Governing equations and particle phase methods

Consider a dilute monodisperse cloud of particles suspended in an incompressible Newtonian gas. The carrier phase has a density ρ_f and viscosity μ_f and satisfies the Navier Stokes equations

$$\nabla \cdot \mathbf{U} = 0 \tag{4.1}$$

$$\rho_f \frac{\partial \mathbf{U}}{\partial t} + \rho_f \mathbf{U} \cdot \nabla \mathbf{U} = -\nabla p + \mu_f \nabla^2 \mathbf{U} + \rho_f \mathbf{g} - \mathbf{F} \tag{4.2}$$

where $\mathbf{U}$ is the fluid velocity, p is the pressure, $\mathbf{g}$ is the gravitational acceleration and $\mathbf{F}$ is the momentum coupling force with the dispersed phase. For dilute small solid particles of density ρ_p, diameter d_p, velocity $\mathbf{V}$ and relaxation time $\tau_p = \rho_p d_p^2/(18\mu_f)$, this coupling is captured by the Stokes drag

$$\mathbf{F} = \rho_p \phi \frac{\mathbf{U} - \mathbf{V}}{\tau_p} \tag{4.3}$$

where ϕ is the local volume fraction. Other forces such as lift and Basset history force are negligible when the density ratio is large.

It is important to note that semi-dilute suspensions for which the average volume fraction $\langle \phi \rangle$ is small can still have a strong coupling between the two phases. Owing to the large density ratio ρ_p/ρ_f of solid particles in gaseous flows, the mass

loading $M = \langle\phi\rangle\rho_p/\rho_f$, a measure of the coupling between the phases, can be of order unity. This means ensembles of particles can collectively modulate the flow on a level on par with the mean fluid velocity.

When treating homogeneous shear flows, it is customary to do a decomposition that isolates the perturbations from the mean homogeneous shear motion

$$\mathbf{U} = \Gamma y \mathbf{e}_x + \mathbf{u} \tag{4.4}$$

$$\mathbf{V} = \Gamma y \mathbf{e}_x + \mathbf{v} \tag{4.5}$$

Here $\mathbf{u}$ and $\mathbf{v}$ are the fluctuating fluid and particle velocities, Γ is the shear rate, $\mathbf{e}_x$ is the streamwise direction and y is the coordinate along the cross direction $\mathbf{e}_y = -\mathbf{g}/g$ which is also parallel to gravity. The fluid fluctuations are given by the following governing equations

$$\nabla \cdot \mathbf{u} = 0 \tag{4.6}$$

$$\rho_f \frac{\partial \mathbf{u}}{\partial t} + \rho_f \mathbf{u} \cdot \nabla \mathbf{u} = -\nabla p + \mu_f \nabla^2 \mathbf{U} + \rho_f \mathbf{g} - \mathbf{F} - \rho_f \Gamma u_y \mathbf{e}_x - \rho_f \Gamma y \frac{\partial \mathbf{u}}{\partial x} \tag{4.7}$$

In the absence of particles, the homogeneous shear flow contains only two intrinsic scales: the shear characteristic time $\tau_f = \Gamma^{-1}$, and the shear viscous dissipation length scale $L_\mu = \sqrt{\mu_f/(\rho_f \Gamma)}$. The unboundedness of the flow removes any other scale. New scales arise in particle-laden shear subject to gravity. The particle settling velocity $V_g = \tau_p g$ and settling distance in one shear time, $L_g = V_g/\Gamma$, are the two-phase flow characteristic velocity and length scales. This enables us to define a total of four independent dimensionless numbers: the mass loading M, average volume fraction $\langle\phi\rangle$, Stokes number $St = \Gamma\tau_p$, and Reynolds number $Re = \rho_f V_g L_g/\mu_f = (L_g/L_\mu)^2$.

The Stokes number is a measure of the particle inertia in shear. When not identically zero, a slip velocity exists between the two phases that is proportional

to the local fluid acceleration as seen from (4.3). Large Stokes particles exhibit a weak response to local fluid variations (Saffman, 1962). Small Stokes particles, on the other hand, adapt quickly to flow changes resulting in trajectories that follow closely the fluid streamlines, although not exactly.

In this context, the Reynolds number is a measure of the relative strength of inertial accelerations due to gravity at the scale of a particle to the viscous dissipation. It also shows that fluid perturbations induced by slow settling particles are suppressed by viscosity. It is noteworthy that, while shear reinforces preferential concentration (Kasbaoui *et al.*, 2015), it can also lead to reduced flow modulation by strengthening the dissipation compared to the gravitational effects ($Re = (L_g/L_\mu)^2 \propto 1/\Gamma$).

A complete description of particle-laden flows requires governing equations for the particle phase. Below we examine three approaches used in the present study

Euler-Lagrange method (EL): Based on Maxey and Riley (1983) work, the equation of motion of particle "i" in homogeneous shear is given by

$$\frac{d\mathbf{x}^i}{dt} = \mathbf{v}^i + \Gamma y^i \mathbf{e}_x \tag{4.8}$$

$$\frac{d\mathbf{v}^i}{dt} = \frac{\mathbf{u}\left(\mathbf{x}^i, t\right) - \mathbf{v}^i}{\tau_p} + \mathbf{g} \tag{4.9}$$

where $\mathbf{x}^i$ and $\mathbf{v}^i$ are respectively the position and fluctuating velocity of this particle. Only Stokes drag is retained here for the same reasons as in (4.3).

Euler-Lagrange approaches rely on solving these equations for all N discrete particles in the flow. The Eulerian particle velocity at the location $\mathbf{x}$ is computed from the Lagrangian velocities in the following way

$$\mathbf{v}(\mathbf{x}, t) = \frac{1}{N} \sum_i^N v^i(t) q\left(||\mathbf{x} - \mathbf{x}^i||\right) \tag{4.10}$$

where q is a filter kernel with width equal to the grid spacing Δx. The particle volume fraction ϕ is obtained in a similar way. The construction of these Eulerian quantities allow the evaluation of the forcing term (4.3) exerted by the particles on the gas.

Two-Fluid Euler-Euler method (TF): Euler-Euler formulations derive from the observation that on scales significantly larger than the particle diameter but smaller than the confining apparatus, the particle phase bears a coherent, organized, fluid-like motion. In these approaches the Eulerian particle velocity $\mathbf{v}$ becomes the subject of models and equations to be solved. The discrete particulate view is lost in favor of a continuum description in terms of number density $n = \phi\pi d_p^3/6$ and particle velocity field $\mathbf{v}$.

In two fluid methods for semi-dilute suspensions, the population balance is dictated by pure advection by the particle velocity field. The latter is found by taking the derivative in equation (4.9) along the particle trajectory $d/dt = \partial/\partial t + \mathbf{v}\cdot\nabla$. The governing equations for the dispersed phase have the following conservative form

$$\frac{\partial(\rho_p n)}{\partial t} + \nabla\cdot(\rho_p n\mathbf{v}) = -\Gamma y\frac{\partial(\rho_p n)}{\partial x} \tag{4.11}$$

$$\frac{\partial(\rho_p n\mathbf{v})}{\partial t} + \nabla\cdot(\rho_p n\mathbf{v}\mathbf{v}) = \rho_p n\mathbf{g} + \rho_p n\frac{\mathbf{u}-\mathbf{v}}{\tau_p} - \rho_p n\Gamma v_y\mathbf{e}_x - \Gamma y\frac{\partial(\rho_p n\mathbf{v})}{\partial x} \tag{4.12}$$

The shear decomposition is assumed in the equations above. Together with the fluid's mass and momentum conservation equations, equations (4.11), (4.12), (4.1) and (4.2) provide a complete set of equations to describe semi-dilute gas-solid flows. This formulation assumes that particles interact only through their effect on the mean fluid velocity.

Anisotropic-Gaussian Euler-Euler method (AG): Equation (4.12) relies on the fundamental hypothesis that the particle velocity field is single-valued. This is not always true for gas-solid flows. In fact, a feature of inertial particulate flows is the ability of trajectories of particles with different histories to cross leading to multiple particle velocities at a single point. Kinetic based methods recognize this as a limitation and borrow from the rarefied-flow community to handle the crossing characteristics. The idea is to allow the particle velocity field to take multiple values, by solving a probabilistic equation governing the number density probability density function (pdf) $f(t, \mathbf{x}, \mathbf{v})$. Following Williams (1958), the equation in phase space for the pdf of a dilute system of collision-less particles interacting only through the mean fluid velocity is given by

$$\frac{\partial f}{\partial t} + \mathbf{c} \cdot \nabla_x f + \nabla_c \cdot \left(f \left(\frac{\mathbf{u} - \mathbf{v}}{\tau_p} + \mathbf{g} \right) \right) = 0 \tag{4.13}$$

Because of the larger space of variables, equation (4.13) is vastly more complicated to solve. To make this method computationally tractable, many methods rely on solving for a finite number of moments instead of the full pdf f. Since the transport of every moment relies on the next order moment, the difficulty resides in finding a closure to the high order ones. One approach is to formulate closures in the form of constitutive relations linking high order moments to low order ones given in physical space. These are usually applicable for a limited range of Stokes number. See Simonin *et al.* (2002); Kaufmann *et al.* (2008); Fvrier *et al.* (2005) for small Stokes number closures, and Masi and Simonin (2014) for large Stokes number ones. Another approach is based on postulating a form of the number density pdf itself. With a choice of pdf using only low order moments, the high order moments can be found from direct integration of the pdf, hence, providing closure to the moment transport equations (Desjardins *et al.*, 2008b; Fox, 2008). This is the method we follow in this paper.

In this work, we focus on the Anisotropic Gaussian closure, originally proposed for rarefied gases (Levermore and Morokoff, 1998) and later extended to particle-laden flows (Vi *et al.*, 2015). In this method, the number density pdf is approximated by

$$f(\mathbf{c}) = \frac{\rho_p n}{\left(2\pi \left|\mathbf{P}_p\right|\right)^{2/3}} \exp\left(-\frac{1}{2}\left(\mathbf{c}-\mathbf{v}\right)\cdot \mathbf{P}_p^{-1}\left(\mathbf{c}-\mathbf{v}\right)\right) \tag{4.14}$$

where $\mathbf{v} = (\rho_p n)^{-1}\int \mathbf{c} f d\mathbf{c}$ is the Eulerian particle velocity (first order moment) and $\mathbf{P}_p$ is the particle pressure tensor derived from the energy tensor (second order moment) $\mathbf{E} = \int \mathbf{cc} f d\mathbf{c} = \rho_p n\left(\mathbf{P}_p + \mathbf{vv}\right)$. It is clear that moments up to the second order need to be solved in order to build the presumed AG pdf. Using the shear decomposition, these read

$$\frac{\partial \rho_p n}{\partial t} + \nabla\cdot\left(\rho_p n \mathbf{v}\right) = -\Gamma y \frac{\partial \rho_p n}{\partial x} \tag{4.15}$$

$$\frac{\partial\left(\rho_p n \mathbf{v}\right)}{\partial t} + \nabla\cdot\mathbf{E} = \rho_p n \mathbf{g} + \frac{\rho_p n \mathbf{u} - \left(\rho_p n \mathbf{v}\right)}{\tau_p} - \rho_p n \Gamma v_y \mathbf{e}_x - \Gamma y \frac{\partial\left(\rho_p n \mathbf{v}\right)}{\partial x} \tag{4.16}$$

$$\begin{aligned}\frac{\partial \mathbf{E}}{\partial t} + \nabla\cdot\mathbf{Q} &= \mathbf{g}(\rho_p n\mathbf{v}) + (\rho_p n\mathbf{v})\mathbf{g} + \frac{(\rho_p n\mathbf{v})\mathbf{u} + \mathbf{u}(\rho_p n\mathbf{v}) - 2\mathbf{E}}{\tau_p} \\ &- \Gamma\left(\mathbf{E}\cdot\mathbf{e_y}\right)\mathbf{e}_x - \Gamma \mathbf{e}_x\left(\mathbf{e}_y\cdot\mathbf{E}\right) - \Gamma y \frac{\partial \mathbf{E}}{\partial x}\end{aligned} \tag{4.17}$$

where $\mathbf{Q}$ is the particle heat flux third order tensor, a third order moment that requires closure. The reconstruction of the AG distribution provides closure by allowing the direct computation of this moment from the presumed pdf $\mathbf{Q} = \int \mathbf{ccc} f d\mathbf{c}$.

Sabat *et al.* (2016) show that the AG method reproduces the same level of clustering found in Euler-Lagrange simulations of one-way coupled decaying homogeneous isotropic turbulence. The agreement holds across the whole range of Stokes number in contrast with the TF method which leads to excessive clustering for moderate and large Stokes numbers. The success of this approach stems from its ability to capture the particle dispersion due to particle-trajectory crossing. It is also argued to be the most likely distribution, in the sense of entropy

maximization, given the moments of f up to the second order (Vi *et al.*, 2015).

Note that the AG method can be considered as an extension of the TF method. In the limit of infinitely small Stokes number, the particle pressure tensor vanishes and the AG distribution collapses onto the mono-kinetic distribution $f(t, \mathbf{x}, \mathbf{c}) = n(t, \mathbf{x})\delta\left(\mathbf{c} - \mathbf{v}(t, \mathbf{x})\right)$. Integrating the moments of the population balance equation (4.13) with this distribution yields the TF equations (4.11) and (4.12).

To conclude this section, we shall note that many (Druzhinin, 1995; Ferry and Balachandar, 2001; Vi *et al.*, 2015) have argued, based on one-way coupling studies, that particle trajectory crossing for flows with small volume fraction and small Stokes number is negligible. However, this has not been verified in the two-way coupled semi-dilute regime. In the following, the granular temperature $\Theta = \mathrm{Tr}\left(\mathbf{P}_p\right)/3$ from the AG and EL methods will serve as a measure of the presence of trajectory crossing as this quantity is identically zero in the TF method.

4.3.2 An Algebraic Instability

The instability of particle-laden shear is the result of two concomitant effects: preferential concentration and an inertial acceleration or gravity. It is possible to show that preferential concentration is directly related to the extreme compressibility of the particle phase (Maxey, 1987). For particles with small inertia, the rate of volumetric expansion and contraction is given by

$$\nabla \cdot \mathbf{v} \simeq \tau_p \left(S - R\right) + O\left(\tau_p^2\right) \tag{4.18}$$

where $S = 1/2\left(\nabla\mathbf{u} + \nabla\mathbf{u}^T\right) : 1/2\left(\nabla\mathbf{u} + \nabla\mathbf{u}^T\right)$ and $R = 1/2\left(\nabla\mathbf{u} - \nabla\mathbf{u}^T\right) : 1/2\left(\nabla\mathbf{u} - \nabla\mathbf{u}^T\right)$ denote the second invariants of the fluid strain and rotation tensors (Squires and Eaton, 1991). When the local strain exceeds the local rotation

particles accumulate. In the opposite scenario of local rotation dominating over strain, the particles are expelled. In pure particle-laden homogeneous shear, strain and rotation perfectly balance each other $S = R = \Gamma/2$ leading to no preferential concentration. Additionally, a cloud of homogeneously distributed particles exerts a uniform gravitational loading on the fluid, the effect of which is an increased hydrostatic pressure. This state is possible but not tenable as minute perturbations quickly alter these balances.

Figure 4.1 illustrates the way sinusoidal perturbations grow. First, a perturbation to the fluid velocity disturbs the balance of strain and rotation. The perturbation creates alternating regions of dominant strain and dominant rotation. Preferential concentration acts to expel particles from the rotational regions to the straining ones. The migration of the particles results in reinforced gravitational loading exerted on the fluid in the regions with excess particles, and lower loading in the depleted ones. The turning of the wave in the shear flow and the translation of the particles relative to the fluid due to sedimentation allow this inhomogeneous forcing to have components in phase with the initial fluid velocity perturbation. As a result the inhomogeneous gravitational forcing strengthens the initial fluid velocity perturbation.

Most hydrodynamic instabilities, such as Kelvin-Helmholtz and Rayleigh-Taylor instabilities are said to be normal and exhibit an exponential unbounded growth. On the contrary, in the homogeneous shear instability, perturbations initially grow algebraically with time and reach a finite amplitude at long times. It broadly falls under the category of nonmodal instabilities (Schmid, 2007). The homogeneous shear pumps energy into the perturbation helping it grow but also has a stabilizing effect over sinusoidal perturbations. A wave of any initial arbitrary

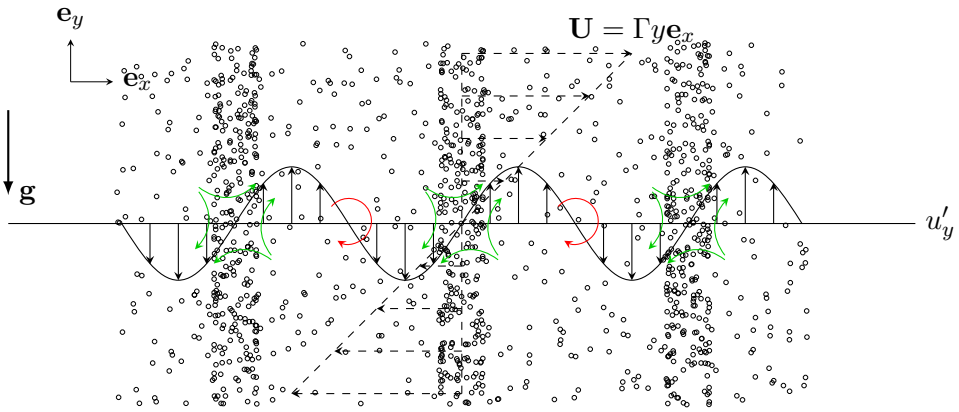

Figure 4.1: A sinusoidal velocity perturbation alters the balance of strain and rotation in homogeneous shear. Regions with excess straining accumulate particles by the preferential concentration mechanism while regions with excess rotation expel particles. As the particle volume fraction turns in the shear flow and translates due to sedimentation, the resulting particle distribution perturbation feeds back to the gas due to the stronger gravitational forcing exerted by the heavier loaded regions of the perturbation.

orientation, i.e., wavevector $\mathbf{k} = (k_x, k_y)$, is rotated by the shear in a few shear times $\tau_f = \Gamma^{-1}$ such that the final orientation is parallel to the shear gradient as illustrated in figure 4.2. Formally, this is described by

$$\frac{d\mathbf{k}}{dt} = \nabla \left(\Gamma y \mathbf{e}_x\right) \cdot \mathbf{k} \rightarrow k_y(t) = k_{y,0} - k_x \Gamma t \tag{4.19}$$

When the velocity gradient direction is parallel to gravity, the behavior depicted in figure 4.1 and explained above might or might not be sampled depending on the initial orientation of the perturbations. Waves that are initially oriented upstream ($k_x k_y > 0$) sample the normal orientation ($k_x k_y = 0$) for a brief time before the shear further turn them downstream ($k_x k_y < 0$). The normal orientation is a configuration of maximum coupling between the two phases and strongest growth. Downstream waves do not sample this configuration and hence do not grow substantially. Once the wavector is nearly parallel to both shear gradient and gravity, the result is nearly vertically stacked layers of higher and lower number density. The particle phase cannot drive fluid velocity perturbations anymore and

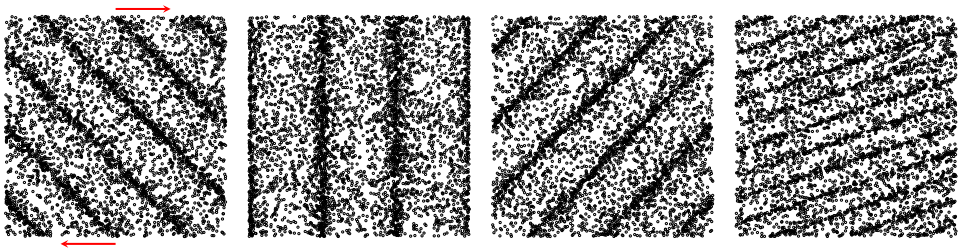

Figure 4.2: The homogeneous shear causes the turning of wave perturbations and the contraction of length scales. The sketch shows an initial upstream sinusoidal perturbation in the particle distribution strained at $\Gamma t = 0, 1, 2$ and 4 (left to right).

growth ceases completely in the linear regime. The activation of non-linear states will depend on the magnitude of the initial perturbation.

The growth and saturation of the number density has been studied with a linear stability analysis by Kasbaoui *et al.* (2015) for small heavy inertial solid particles in a gas. To make the derivation analytically tractable, an asymptotic solution to equation (4.12) was used in the LSA. Proposed by Ferry and Balachandar (2001), the expansion is valid in the limit of small Stokes numbers ($St \ll 1$) and leads to a relationship between the particle velocity and the local fluid velocity given by

$$\mathbf{v} = \mathbf{u} + \mathbf{V}_g - \tau_p \left(\frac{\partial \mathbf{u}}{\partial t} + (\mathbf{u} + \mathbf{V}_g) \cdot \nabla \mathbf{u} + \Gamma y \frac{\partial \mathbf{u}}{\partial x} + \Gamma u_y \mathbf{e}_x \right) + O\left(\tau_p^2\right) \qquad (4.20)$$

This expansion greatly reduces the difficulty of the problem. One needs only to solve the number density transport equation (4.11) with the evaluated particle velocity to completely describe the flow. The expansion simplifies the analytical analysis while also retaining important physical features such as particle sedimentation, preferential concentration and turbophoresis. For asymptotically small Stokes number particles, other solutions might exist but Balachandar and co-workers argue that they will converge towards the expansion exponentially fast with a time of scale equal to the particle response time.

In the LSA, the algebraic, non-modal growth of the instability was demonstrated with sinusoidal disturbances of the form

$$n(\mathbf{x},t) = \langle n\rangle + St\hat{n}(t)\exp\left(i\left(k_x x + k_y(t)y\right)\right) \tag{4.21}$$

$$\mathbf{u}(\mathbf{x},t) = \hat{\mathbf{u}}(t)\exp\left(i\left(k_x x + k_y(t)y\right)\right) \tag{4.22}$$

where the wavevector obeys (4.19), $\langle n\rangle = \langle\phi\rangle\pi d_p^3/6$ is the mean number density and $\hat{n}$ and $\hat{\mathbf{u}}$ are the wave amplitudes. The linearized evolution of the latter quantities is given by the coupled ordinary differential equations

$$\frac{d\hat{n}}{dt} = -i\mathbf{V}_g\cdot\mathbf{k}\hat{n} + \frac{\langle n\rangle}{\Gamma}i2\nabla\mathbf{u}_b : \mathbf{k}\hat{\mathbf{u}} \tag{4.23}$$

$$\begin{aligned}\frac{d\hat{\mathbf{u}}}{dt} &= -\left(i\frac{M}{1+M}\mathbf{V}_g\cdot\mathbf{k} + \left(\mathbf{I} - 2\frac{\mathbf{kk}}{k^2}\right)\cdot\nabla\mathbf{u}_b^T + \frac{\nu}{1+M}k^2\right)\hat{\mathbf{u}} \\ &+ \frac{\Gamma}{\langle n\rangle}\left(\mathbf{I} - \frac{\mathbf{kk}}{k^2}\right)\frac{M}{1+M}\mathbf{V}_g\hat{n}\end{aligned} \tag{4.24}$$

Although (4.24) is given in vectorial form, it is sufficient to solve for the velocity component along the gradient direction y only. The other component can be found from the continuity equation

$$k_x\hat{u}_x + k_y\hat{u}_y = 0 \tag{4.25}$$

Solutions to equations (4.23), (4.24) and (4.25) constitute the LSA result (LSA) and will be compared to the full numerical solutions of the Euler-Lagrange (EL), Two-Fluid (TF) and Anisotropic-Gaussian (AG) simulations.

4.4 Numerical strategies

4.4.1 Shear-periodicity and homogeneous shear treatment

When the confining scales are significantly larger than the length scales studied, homogeneous shear is a reasonable approximation of the local gradients. The unboundedness of the flow is of paramount importance and needs to be correctly accounted for. Artificial confinement by sliding top and bottom walls or Dirichlet conditions do not provide a good approximation to this flow. In fact, they would introduce additional scales that call for different solution forms than the rotating waves. These were first introduced by Thomson (1887), aka Lord Kelvin, in the study of the stability of single-phase planar channel flows. Lord Kelvin's idea was to express small disturbances as a series of rotating modes linearly combined with corrections localized near the walls to enforce the boundary conditions. His claim was that these corrections would hold a negligible amount of energy making the stability of the flow controlled by the rotating modes. It turned out that these corrections could not be proven to be localized and their energy dominated the flow. Nevertheless, the rotating waves, called Kelvin modes in single phase, are the foundation of the analyses of unbounded homogeneously sheared flows.

Numerical simulations that seek to study homogeneous shear require specially crafted algorithms. The oldest standing method consists in solving the governing equation on a deforming mesh. Introduced by Rogallo (1981), this methods retains the simplicity of periodic boundary conditions in all directions but this simplicity comes at a price. As the mesh deforms, the aspect ratio of the computational cells degrades over time. Below a certain threshold the computational solution is interpolated to a straightened mesh. This "remeshing" operation leads to a

sudden drop in kinetic energy in simulations of homogeneously sheared turbulence as well as discontinuous statistics. Brucker *et al.* (2007) estimate the loss to range from 5% at low shear rates to 40% at high shear rates. They propose a pseudo-spectral algorithm that avoids spatial remeshing by shifting the wavenumber space according to equation (4.19). Still, Sukheswalla *et al.* (2013) find that extensive use of numerical diffusion is required to relieve the Gibbs oscillations that arise from the fine vortical structures.

A third approach, described in (Kasbaoui *et al.*, 2017) and based on the earlier work of Gerz *et al.* (1989) and Baron (1982), solves the equations in physical space without remeshing. The key aspect is to enforce the so-called shear-periodic boundary conditions (see figure 4.3)

$$f(x, Ly, z) = f(x - \Gamma t L_y, 0, z) \tag{4.26}$$

where f is any quantity of interest like the velocity fluctuations $\mathbf{u}$, and L_y is the extent of the computational domain in the shear gradient direction y. In the methods of Rogallo (1981) and Brucker *et al.* (2007), the change of reference frame to the one of the deforming mesh allows the suppression of the distortion terms $\Gamma y(\partial f)/(\partial x)$. In the reference frame of the laboratory these terms are responsible for the turning of the waves. In this third approach (Gerz *et al.*, 1989; Kasbaoui *et al.*, 2017), these terms are added directly in physical space in a split step approach. Kasbaoui *et al.* (2017) show that this method is able to capture the rotation of the Kelvin modes by the shear while maintaining their normal structure intact. Most notably, this approach allows the stable simulations of single phase homogeneously sheared turbulence for long times until establishment of the universal self-similar regime seen in experiments (Tavoularis and Corrsin, 1981; Shen and Warhaft, 2000). This is the approach followed in the present study.

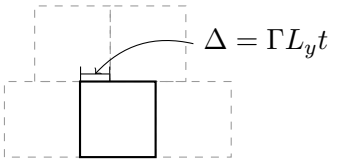

Figure 4.3: Shear-periodic boundary conditions

4.4.2 Numerical strategies for the Euler-Euler formulations

The appearance of clusters and void regions in the particle phase, call for special attention to the numerics used in Eulerian simulations. When clustering is significant, the volume fraction can drop significantly to near zero values in the neighboring depleted regions. Positivity-preserving, also called realizable, Euler-Euler methods maintain positive volume fraction even when the solution is nearly devoid of particles ($\phi \rightarrow 0$). Stability and mesh convergences of solvers for the dispersed phase are contingent on this property (Estivalezes and Villedieu, 1996; Desjardins *et al.*, 2008b).

The particle phase solver follows the Quadrature Based Method of Moments in (Fox, 2008; Vi *et al.*, 2015; Kong *et al.*, 2017). This is a realizable, second-order spatial discretization on a collocated mesh. The numerical strategy relies extensively on Lie operator splitting to ensure that every term in the governing equations is added in a realizable way. The distortion terms are treated in the same manner as in (Kasbaoui *et al.*, 2017).

At the beginning of the time step, we start by computing the drag term from the previous time step:

$$\mathbf{D}^n = \frac{\phi^n \mathbf{u}^n - (\phi \mathbf{v})^n}{\tau_p} \tag{4.27}$$

where $(\phi\mathbf{v})^n$ is the particle momentum at the previous step treated as a whole. Note that the fluid solver mesh is staggered whereas the particle mesh is collocated making interpolations of quantities from one mesh to the other necessary. At this point, we also compute the second order drag tensor if using AG. Next, the pure convection of particle volume fraction, momentum and energy is advanced with a third order Runge-Kutta. For the volume fraction field this reads

$$\widetilde{\phi} = \phi^n - dt\nabla\cdot(\phi\mathbf{v})^n \tag{4.28}$$

$$\widetilde{\widetilde{\phi}} = \frac{3}{4}\phi^n + \frac{1}{4}\left(\widetilde{\phi} - dt\nabla\cdot\widetilde{(\phi\mathbf{v})}\right) \tag{4.29}$$

$$\overline{\phi} = \frac{1}{3}\phi^n + \frac{2}{3}\left(\widetilde{\widetilde{\phi}} - dt\nabla\cdot\widetilde{\widetilde{(\phi\mathbf{v})}}\right) \tag{4.30}$$

where the numerical fluxes are computed with a second order kinetic flux (Vikas *et al.*, 2011). Combined with a minmod slope limiter, the numerical fluxes are both stable in the presence of shocks and realizable for first order forward in time integrations. The three stage Runge-Kutta extends this property to a realizable third order time accurate integration by using convex combinations of realizable states. The overall scheme preserves the volume fraction positivity and is shock capturing.

Further updates are needed to add the remaining forces. In the next step, the drag, gravity and the convection of homogeneous shear by the fluctuations are added. For the particle momentum this reads

$$\widehat{\phi\mathbf{v}} = \overline{\phi\mathbf{v}} - dt\left(\mathbf{D}^n + \mathbf{g}\phi^n - \Gamma(\phi v_y)^n\mathbf{e}_x\right) \tag{4.31}$$

This operation is also positivity-preserving. The last remaining terms are the distortion terms $\Gamma y\partial/(\partial x)$. These are added exactly using the characterstics method as in (Kasbaoui *et al.*, 2017)

$$(\phi\mathbf{v})^{n+1}(\mathbf{x}) = \widehat{\phi\mathbf{v}}\left(\mathbf{x} - \Delta t\Gamma y\mathbf{e}_x\right) \tag{4.32}$$

and the boundary conditions are applied with time $n + 1$.

The algorithm then solves for the fluid phase using the method explained in (Kasbaoui *et al.*, 2017) and with the drag term $-\mathbf{D}^n$ interpolated to the fluid mesh as a source term.

4.4.3 Numerical strategies for the Euler-Lagrange formulation

The Euler-Lagrange strategy follows the method of Capecelatro and Desjardins (2013b). The numerical method uses a volume-filtered approach that captures the particle modulation of the fluid without resolving the flow on the particle scale. The position and velocity of each Lagrangian particle (equation (4.8) and (4.9)) is advanced using a second-order Runge-Kutta scheme. Eulerian particle data such as the volume fraction field are computed from the Lagrangian data using a box kernel of width equal to the grid spacing Δx. The unperturbed fluid velocity at the particle location is computed using the method of Ireland and Desjardins (2017). This quantity is required for the correct calculation of the drag force and leads to correct predictions of the particle settling velocity. The method is fully conservative and yields grid-independent solutions in two-way coupled problems and has been verified against experiments (Capecelatro *et al.*, 2014; Capecelatro and Desjardins, 2013a).

The imposed homogeneous shear necessitates some additions. The shear term in equation (4.8) generally poses no computational challenges. Particles leaving from the top and bottom of the domain ($y = \pm L_y/2$) are reintroduced from the other side with translated x position and velocity. This procedure is the well known

Lees-Edwards boundary conditions (Lees and Edwards, 1972) and is the discrete analogue of the shear-periodic boundary conditions (4.26).

4.5 Linear regime: the preferential concentration instability

In this section, we simulate a homogeneously sheared particle-laden flow traversed by a small velocity perturbation. We seek to demonstrate the shear instability in a practical case that allows comparison with the linear stability analysis. The simulations are conducted with the EL, TF and AG methodologies. Comparisons with the LSA serve to validate the numerical strategies. Comparisons among the three methodologies are intended to assess the importance of the discrete nature of the particulate phase and the occurrence of particle trajectory crossing.

The flow parameters are shown in table 4.1. Glass beads of diameter $d_p = 150\,\mu$m and density $\rho_p = 2600\,\mathrm{kg{\cdot}m^{-3}}$ are suspended in air at standard temperature and pressure. The shear rate is $\Gamma = 0.5\,\mathrm{s}^{-1}$ and gravity is $g = 9.8\,\mathrm{m}\cdot\mathrm{s}^{-2}$. The Stokes number here, $St = 0.09$, falls in the range of small stokes numbers for which the expansion (4.20) is believed to be applicable. The Reynolds number is $Re = \rho_f V_g L_g/\mu_f = 1.05\,10^5$. Although the average volume fraction is small, $\langle\phi\rangle = 2.5\,10^{-4}$, the mass loading $M = 0.54$ is O(1) owing to the large ratio ρ_p/ρ_f of the density of glass beads to that of the gas. These parameters allow strong two-way coupling between the two phases via gravity and preferential concentration.

The choice of computational box size and resolution is guided by the analysis of the different wavelength perturbations in the LSA. According to the linear

Parameters	**Expression**	**Value**
Fluid density	ρ_f	$1.2\ \mathrm{kg \cdot m^{-3}}$
Fluid viscosity	μ	$1.8\,10^{-5}\ \mathrm{kg \cdot s^{-1} \cdot m^{-1}}$
Shear rate	Γ	$0.5\ \mathrm{s^{-1}}$
Particle density	ρ_p	$2600\ \mathrm{kg \cdot m^{-3}}$
Particle diameter	d_p	$150\ \mu\mathrm{m}$
Volume fraction	$\langle\phi\rangle$	$2.5\,10^{-4}$
Gravity	g	$9.8\ \mathrm{m \cdot s^{-2}}$
Settling Velocity	V_g	$1.7695\ \mathrm{m \cdot s^{-1}}$
Settling Distance	L_g	3.5388 m
Amplitude	$u_{y,0}/V_g$	$= A$
wavenumber	$k_{x,0}$	$= 2\pi/L_x$
	$k_{y,0}$	$= 2\pi/L_x$
Box size	$L_x = L_y$	$= L_g = V_g/\Gamma$
Grid	$n_x \times n_y$	512×512
Time step	Δt	$2\,10^{-4}$

Table 4.1: Simulation parameters for the standard case of $St = 0.09$ and $M = 0.5$

analysis, large scale perturbations have a typical wavelength comparable to the particle settling distance in one shear time $L_g = V_g/\Gamma$. On the other end, small scale perturbations of the size of the dissipation scale $L_\mu = \sqrt{\mu/(\rho_f\Gamma)}$ are rapidly suppressed. To resolve all scales, we set the 2D computational domain dimensions to $L_x = L_y = L_g$ and use 512 grid points in each direction to ensure an adequate resolution of the dissipative scales ($\Delta x/L_\mu \sim 1.2$).

A large scale sinusoidal perturbation with $k_x = 2\pi/L_g$ initiated in the oblique direction $x = y$ at $t = 0$ drives the particle and fluid initial velocities. The initial orientation, $k_{y,0}/k_x = 1$, allows the perturbation to sample the direction of strongest particle-fluid coupling ($k_y = 0$) during the turning of the wave and experience considerable growth. In Euler-Euler simulations, the initial volume fraction field is uniform. The particle velocity field is initialized based on expression (4.20). In Euler-Lagrange simulations, expression (4.20) is evaluated at the particle location to determine the Lagrangian particle velocities. Moreover, the particles

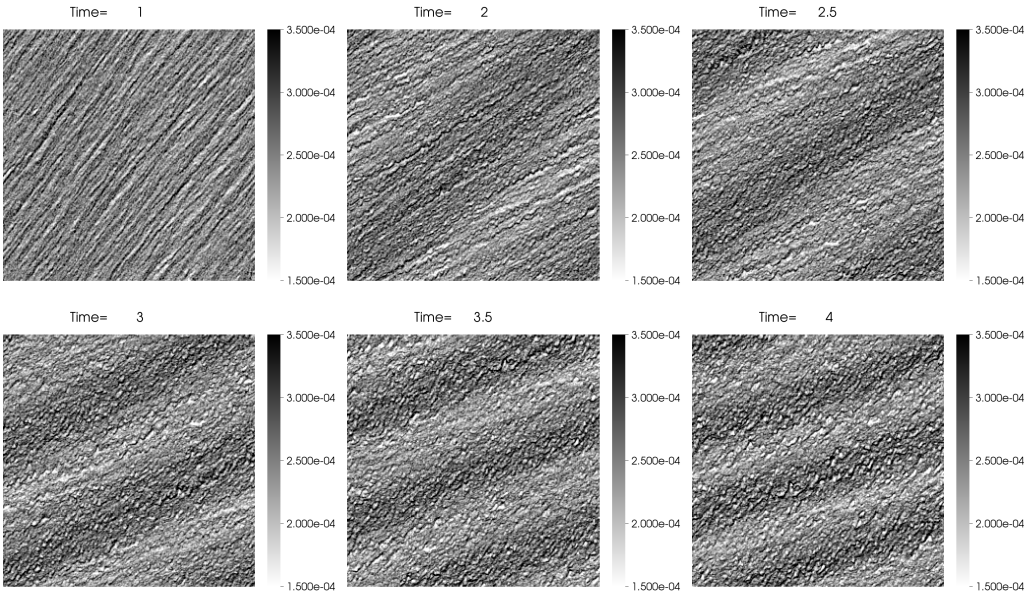

Figure 4.4: Snapshots of the volume fraction field in EL simulation with perturbation strength $A = 0.02$.

are seeded randomly in the domain. At the average volume fraction $\langle\phi\rangle = 2.5\,10^{-4}$ and for particles in table 4.1, the 2D simulation domain contains approximately $2.8\,10^6$ particles.

When the perturbation strength A, the ratio of the perturbation magnitude to the settling velocity, is sufficiently small, a linear evolution of the mode is expected. The linear stability analysis does not provide an indication on how small A needs to be to remain in the linear regime. However, one can expect non-linearities to manifest if the amplified perturbation was to reach a magnitude comparable to the base state. For the driving initial mode, $k_x^\star = L_g k_x/(2\pi) = 1$, the LSA predicts a total amplification $\phi_{rms}(k_x^\star = 1)/(A\langle\phi\rangle) \simeq 7$, where ϕ_{rms} is the volume fraction fluctuation r.m.s. Consequently, for $A \ll 0.14$ one can expect a linear evolution owing to the small total amplification, $\phi_{rms} \ll \langle\phi\rangle$, whereas, cases such that $A > 0.14$ can be expected to evolve non-linearly.

The case in table 4.1 is simulated with EL and TF methods for the initial

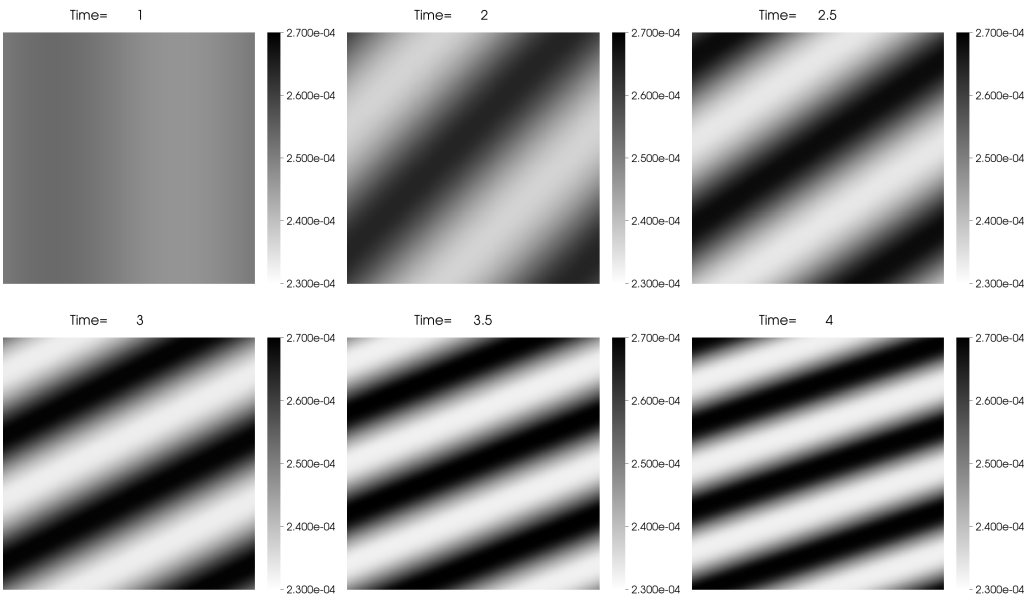

Figure 4.5: Snapshots of the volume fraction field in TF simulation with perturbation strength $A = 0.02$.

perturbation strength $A = 0.02$. Snapshots of EL and TF simulations (see figure 4.4 and 4.5 respectively) show the emergence of a sinusoidal perturbation in the volume fraction field. The turning of the perturbation is induced by the background base shear as explained in section 4.3.2 and depicted by the sketch on figure 4.2. The wavelength can be seen contracting owing to a compression of scales in the gradient direction.

The EL simulations show the existence of small scale perturbations in addition to the driving large scale mode. These perturbations are induced by the random distribution of the Lagrangian particles. They appear as streaky features in the volume fraction field at $\Gamma t = 1$ which then destabilize and form small bubbles depleted of particles. The streaky features could be interpreted as the preferential concentration instability happening at small scales. In fact, according to the LSA, the fastest growing modes are about ten times larger than the dissipation scale L_μ which explains the short wavelength of these streaky perturbations. Because the

TF data do not contain these short wavelength perturbations, direct comparisons with the EL data is difficult. Figure 4.6a shows the evolution of the domain-averaged root-mean-square volume fraction fluctuations, $\langle \phi_{rms} \rangle$, in EL and TF simulations. At $t = 0$, $\langle \phi_{rms} \rangle$ is already non-zero in EL simulations due to the random distribution of particles. The quantity $\langle \phi_{rms} \rangle$ encompasses the effects of modes at all scales resulting in the large deviation between the TF and EL evolutions seen in figure 4.6a.

For a meaningful comparison with the TF volume fraction, it is essential to separate the effects of the imposed perturbation from other fluctuations present in EL simulations. The procedure adopted here is to compute the Fourier spectrum of the volume fraction field ϕ in the sheared reference frame $x' = x - \Gamma t y$ and $y' = y$ and extract the imposed mode $k_x^\star = 1$. The complex amplitude associated with the Fourier mode k_x reads as

$$\langle \hat{\phi}(k_x, t) \rangle_{y'} = \frac{1}{L_y} \int_{y'} \left(\int_{x'} \phi(x' + \Gamma t y', y') e^{i 2\pi k_x x'} dx' \right) dy' \tag{4.33}$$

where $\langle \cdot \rangle_{y'}$ denotes the average over the direction $y' = y$. The larger sample pool yields better converging statistics. It is also important to realize that this averaging removes fluctuations in the transverse direction to the wave. Computing "frozen" Fourier modes in the sheared reference frame is equivalent to computing the rotating Fourier modes explained in section 4.3.2. Spectral interpolations are used to evaluate off grid points in $\phi(x' + \Gamma t y, y)$. The root mean square fluctuation associated with the mode k_x is

$$\begin{aligned} \langle \phi_{rms}(k_x, t) \rangle_{y'} &= \sqrt{\langle \left(\langle \hat{\phi}(k_x, t) \rangle_{y'} e^{i 2\pi k_x x'} + \langle \hat{\phi}(-k_x, t) \rangle_{y'} e^{-i 2\pi k_x x'} \right)^2 \rangle_{x'}} \\ &= \sqrt{2 \left(\mathrm{Re}\{ \langle \hat{\phi}(k_x, t) \rangle_{y'} \}^2 + \mathrm{Im}\{ \langle \hat{\phi}(k_x, t) \}^2 \rangle_{y'} \right)} \end{aligned} \tag{4.34}$$

Figure 4.6b shows the first three extracted modes from EL simulations. The

extracted mode $k_x^\star = 1$ follows closely the EE simulations for much of the integration time. Small departure beyond $\Gamma t \sim 3.5$ occurs concomitantly with the growth of the second mode and third modes $k_x = 2$ and 3. The initial random distribution of the particles helps seed modes. Although they start with significantly smaller amplitudes than k_x, these modes can grow comparatively faster. In this small perturbation case, their total amplification remains small for $\Gamma t \leqslant 4$.

The domain-averaged particle velocity fluctuations r.m.s are shown in figure 4.6c and 4.6d. The TF and EL simulations match well in this linear case. The simulations show a similar oscillatory behavior as the one predicted by the LSA. Notice that compressibility effects can be seen in the plot of v_x, since a solenoidal particle velocity field would imply the relation $v_x \sim -k_y/k_x v_y$ leading to $v_x = 0$ at the time k_y cancels, i.e., $\Gamma t = 1$. It is seen in 4.6d that vertical fluctuations $\langle v_{rms} \rangle$ persist even at long times. These fluctuations are in the downward direction, and lead to higher particle settling rates. In the literature of particle-laden turbulence, this is refereed to as preferential sweeping (Wang and Maxey, 1993; Yang and Lei, 1998; Good *et al.*, 2014; Aliseda *et al.*, 2002; Yang and Shy, 2005; Ireland *et al.*, 2016). The deviation of the EL curve from the TF one near $\Gamma t \sim 3.5$ proves that the long time persistent particle sweeping is enhanced by the small scale perturbations in EL simulations.

In both EL and TF simulations, the volume fraction and particle velocity fluctuations display similar time dependence to the LSA predictions, but a departure remains at long times. These differences are controlled by the Stokes number. Figure 4.7 shows how diminishing St leads to the convergence of TF and EL volume fraction to the LSA results. The lowering of St from $St = 0.18$ to $St = 0.01$ moves the TF curves upwards towards the LSA curve, which remains an upper limit. As

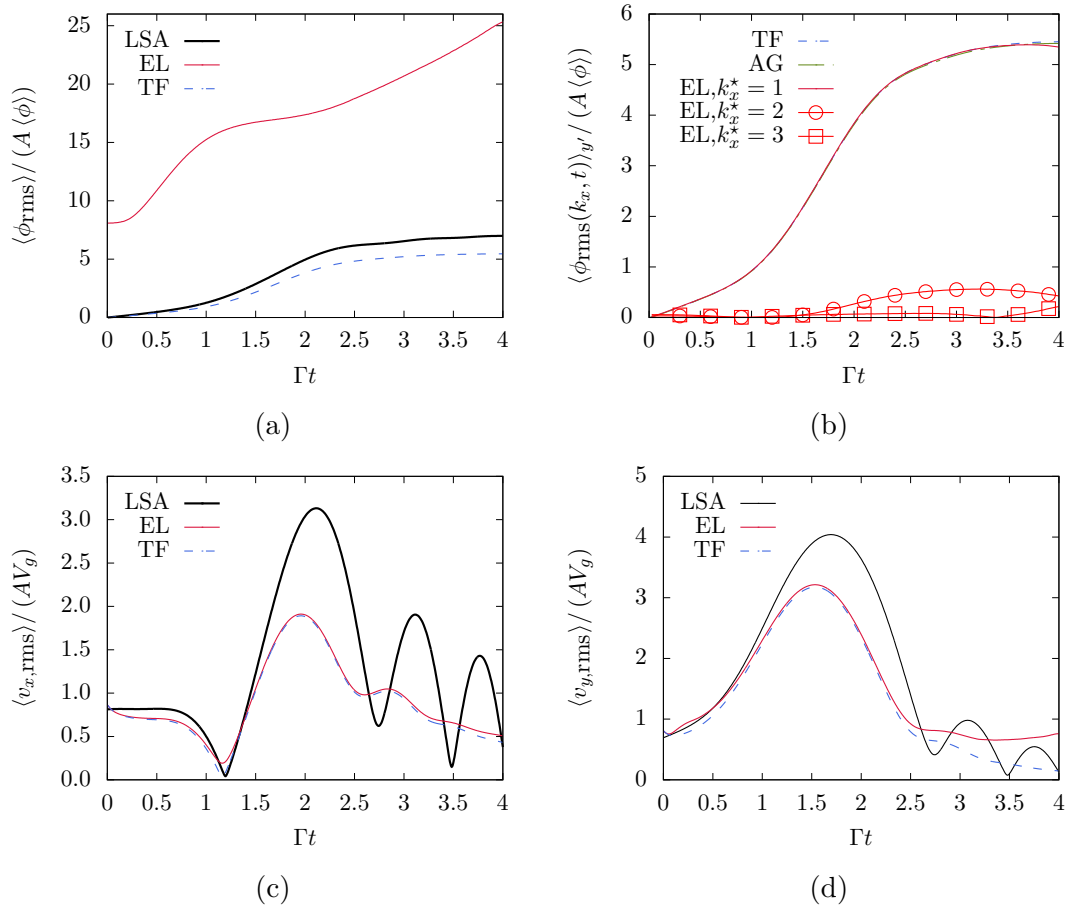

Figure 4.6: Time evolution of the fluctuations traversing the flow. Figure 4.6a shows the domain-averaged root-mean-square volume fraction fluctuations. The large deviation of the EL curve compared to the LSA and TF simulations is a consequence of the fluctuations introduced by the random distribution of the Lagrangian particles. Extracting the fluctuations associated with the mode $k_x^\star = k_x L_g/(2\pi) = 1$ in EL (figure 4.6b) shows a nearly identical evolution of to the TF and AG simulations. Fluctuations associated with the modes $k_x^\star = 2$ and 3 in EL simulations are also shown to remain small in this linear regime. The domain-averaged root-mean-square fluctuations of the horizontal (4.6c) and vertical (4.6d) particle velocities evolve similarly in EL and TF simulations and reproduce the same oscillatory behavior seen from the LSA. The flow parameters are as in table 4.1 and correspond to $\langle \phi \rangle = 2.5\,10^{-4}$, $M = 0.54$ and $St = 0.09$. The perturbation strength is $A = 0.02$.

explained in section , the small Stokes expansion (4.20) implies that the LSA is valid in the double limit of small perturbations ($A \ll 1$) and very small particle inertia ($St \ll 1$). Despite the significantly better agreement at $St = 0.01$, the volume fraction fluctuations remain higher for the larger Stokes numbers because the total amplification is proportional to the product StA. For the same reasons as in TF simulations, the lowering of St number from 0.18 to 0.04 moves the EL curves upwards towards the LSA one. However, the diminishing signal (proportional to St) results in the small scale perturbations, initiated by the random distribution of particles, gaining in relative strength. The destruction of the seeded large scale mode $k_x^\star = 1$, shows the difficulty of establishing comparisons with EL methods for very small Stokes number particles. Note that the variation of the Stokes number $St = \Gamma\tau_p$ was achieved by varying the shear rate, rather than the particle density ρ_p to keep the mass loading constant. One could also vary the particle diameter in order to change the Stokes number, however, at the same average volume fraction, smaller particles lead to a higher total count requiring more computational resources. We also vary the gravitational acceleration proportionally in order to maintain an identical box size $L_x = L_g = g\tau_p/\Gamma$. This ensures an equal count of particles per cell across all EL simulations and provides sufficient sampling for the computation of particle quantities.

Lastly, we address the results of AG in the linear regime. Figure 4.6b shows little difference with the TF method for the case with $A = 0.02$ and $St = 0.09$. As mentioned before, an anisotropic Gaussian number density pdf collapses onto a mono-kinetic pdf for very small St number yielding the TF governing equations. The near identical TF and AG evolutions in figure 4.6b show that particle-trajectory effects modeled by the AG distribution are absent in the linear regime. By reciprocity, AG also agrees with the EL simulations. Based on the quanti-

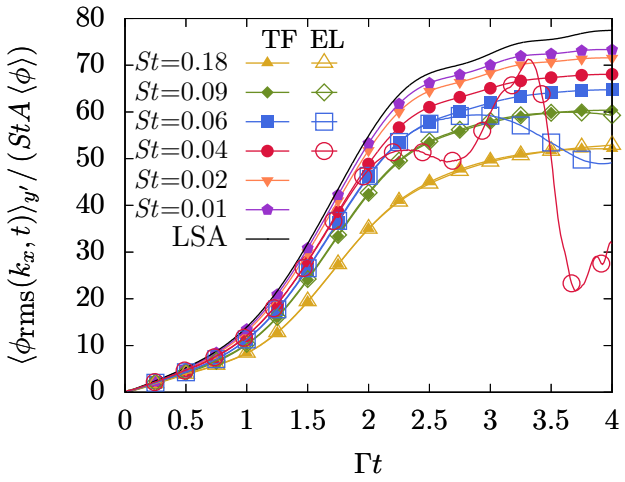

Figure 4.7: Effect of varying the Stokes number in EL and TF simulations.

tatively similar growth of the mode $k_x^\star = 1$ observed with all three simulation strategies, we conclude that particle-trajectory crossing is negligible for small inhomogeneities traversing a semi-dilute flow with small Stokes number particles. However, as we show in the next section, when non-linearities develop, severe out-of-equilibrium states take place leading to distinctly different evolutions for the three methods.

4.6 Non-linear regime: secondary Rayleigh-Taylor instability and caustics

Understanding the mechanisms leading to clustering in turbulent flows is often rendered difficult by the presence of multiple of length scales. Instead, we focus on clustering in the presence of a single perturbed velocity mode. Looking at the non-linear regime in this flow configuration, we propose to establish a route to clustering that unveils the principal mechanisms at play in two-way coupled semi-dilute flows. As we show below, these mechanisms are: the preferential concentration instability,

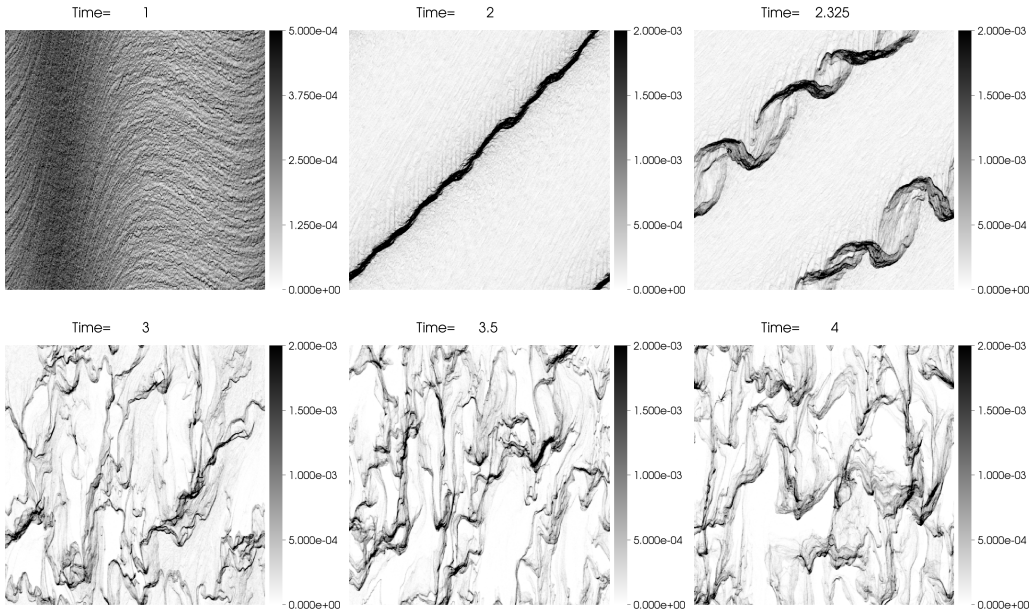

Figure 4.8: Snapshots of the volume fraction field in EL simulation for the large perturbation strength $A = 0.25$. A secondary transverse Rayleigh-Taylor instability breaks the sheet of particles formed by the primary preferential concentration. The final state displays sustained clustering.

particle-trajectory crossing, and the Rayleigh-Taylor instability.

4.6.1 Non-linearities in EL formulation

We start with the analysis of the non-linearities in EL simulations. The case in table 4.1 is run with an initial perturbation strength $A = 0.25$. At this level, a strong deviation from the linear evolution is guaranteed, since according to the LSA, the sinusoidal volume fraction perturbation would grow so much that the depleted regions, the troughs of the sinusoid, would have a non-physical negative volume fraction. Hence, it is expected that large void regions form and that the sinusoid deforms non-linearly.

Snapshots of the volume fraction field during $1 \leqslant \Gamma t \leqslant 4$ (see figure 4.8)

show the gradual evolution towards a state dominated by clusters similar to those seen in the grid turbulence experiments of Yang and Shy (2005) with copper beads ($\langle\phi\rangle = 5\,10^{-5}$, $M = 0.5$, $St = 0.36$). First, the preferential concentration instability causes the extreme accumulation of particles along the oblique direction of the rotating perturbation during $0 < \Gamma t < 2$. Nearly all of the particles are distributed on a sheet of small thickness. Despite the stronger non-linear amplification, this first stage is qualitatively understood from the LSA and the simulations in the linear regime. Shortly after, a transverse instability manifests around $\Gamma t = 2.1$ and is clearly visible on the snapshot at $\Gamma t = 2.325$. This secondary instability is of a Rayleigh-Taylor type as we explain below. It adds spatial dimensionality to the particle distribution by breaking the quasi-1D long band of particles formed by the preferential concentration instability. Notice that this secondary instability grows in a double helix shape: two modes in antiphase grow simultaneously. These modes grow on a time scale much smaller than the shear time Γ^{-1} and lead to the formation of clusters seen in the snapshots at $\Gamma t = 3$, 3.5 and 4.

Preferential concentration instability

Figure 4.9a shows the time evolution of the volume fraction fluctuation. One can see a clearly different evolution from the linear case in figure 4.6a. The volume fraction fluctuations grow linearly until $\Gamma t \sim 1.5$, after which a sharp peak is attained around $\Gamma t = 2$. The total volume fraction fluctuation then drops and eventually plateaus by the end of the simulation. Figure 4.9b shows that, in addition to the initialized mode $k_x^\star = 1$, the shorter wavelength modes $k_x^\star = 2$ and 3 are also strongly amplified. These modes exist initially because the random distribution of particles creates perturbations at all scales. In the non-linear regime, these modes grow nearly as large as the one seeded by the deterministic perturbation. The

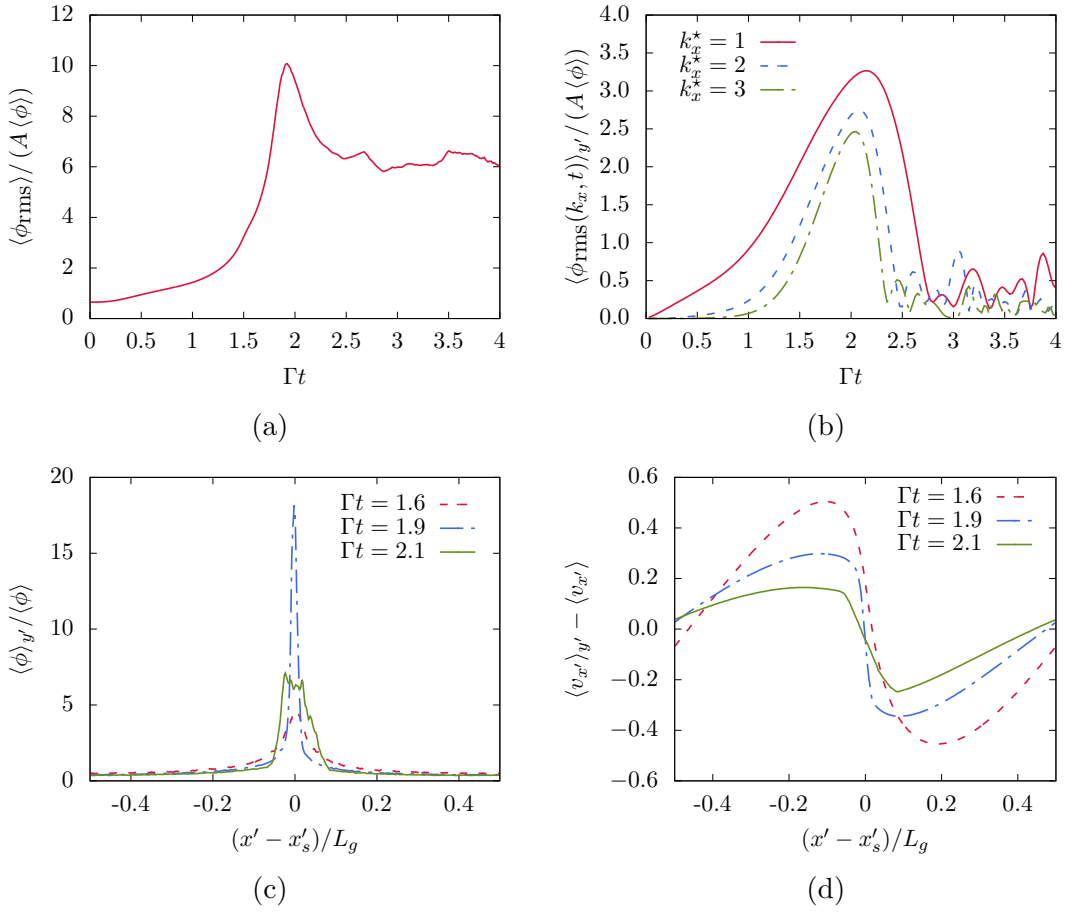

Figure 4.9: Evolution of the perturbation in the EL simulation. Figure 4.9a shows the domain-averaged fluctuations peak around $\Gamma t \sim 2$. Figure 4.9b shows significant growth of the unperturbed modes $k_x^\star = 2$ and 3. The collapse of these modes coincides with the appearance of the transverse secondary instability. Figures 4.9c and 4.9d show the volume fraction and wave-normal particle velocity as a function of the wave-normal coordinate $x' = \mathbf{k} \cdot \mathbf{x}/k$ centered on the high concentration band of particles. The steepening of the sinusoidal wave leads to a volume fraction shaped like an impulse ($\Gamma t = 1.6$ and 1.9). Particle trajectory crossing leads to the smoothening of the profiles at $\Gamma t = 2.1$.

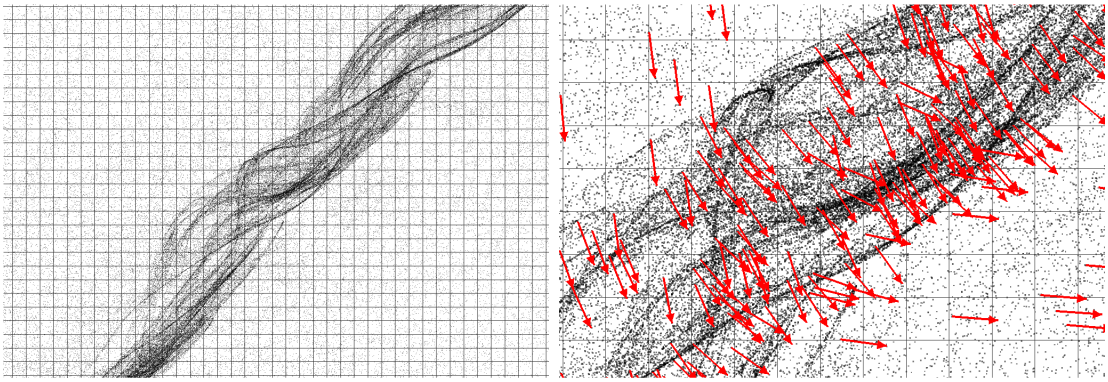

(a) (b)

Figure 4.10: Snapshots of the Lagrangian particles in a zoomed-in view around the high concentration band of particles at $\Gamma t = 2.05$. Particle trajectory crossing in EL simulations leads to: (4.10a) the formation of caustics, long intersecting filaments of particles, and (4.10b) particles within one grid cell with widely different velocity vectors. The arrows indicate the velocity directions of individual particles. The Lagrangian particles have been magnified three times for easier visualization.

plotted volume fraction averaged over the transverse direction $\langle \phi_{rms} \rangle_y$ associated with these modes collapses at about the time when the transverse perturbations appear, around $\Gamma t \sim 2.1$. Figure 4.9c shows the normalized volume fraction averaged over the transverse direction and plotted as a function of the wave-normal coordinate $x' = (\mathbf{k} \cdot \mathbf{x})/k$. The plots at the consecutive times $\Gamma t = 1.6, 1.9$ show the gradual concentration of the field into an impulse function reaching a peak nearly 18 times higher than the average volume fraction. Such high particle concentrations have also been observed in particle-laden turbulent simulations. Squires and Eaton (1991) report a volume fraction inside clusters reaching 25 times the average volume fraction in EL simulations of homogeneous isotropic turbulence with $St = 0.15$ particles.

Caustics and particle trajectory crossing

The two antiphase transverse modes forming the double helix (snapshot at $\Gamma t = 2.325$ in figure 4.8) originate from two streams of particles that cross at the high concentration sheet. To understand how this takes place, we report the Eulerian wave-normal particle velocity $v_{x'} = (\mathbf{k} \cdot \mathbf{v})/k$, where $\mathbf{v}$ is the Eulerian particle velocity computed from the Lagrangian data on the mesh. The figure shows clear steepening of the original sinuoidal wave. This non-linear process occurs as particles migrate to the location of the high concentration sheet. Particles from the two sides move in two opposing streams causing the slope of the centered wave-normal velocity to steepen and the volume fraction impulse to sharpen. When the two streams meet, around $\Gamma t = 2.1$, particle trajectory crossing takes place, i.e., the two streams inter-penetrate and continue moving in opposite directions. This has four consequences. First, the gradient of the wave-normal velocity $v_{x'}$ smoothens, as seen in figure 4.9d, due to the presence of particles with opposing velocities within one grid cell in the crossing zone. Second, the crossing of the streams leads to the spreading of the volume fraction impulse (see figure 4.9c). Third, particle trajectory crossing is known to manifest as caustics (Gustavsson *et al.*, 2012), long intersecting filaments of aligned particles. This can be seen in figure 4.10a in a zoomed-in view around the high concentration sheet. Fourth, the crossing of the particle streams along with transverse perturbations lead to particles within one gril cell having non-parallel velocity vectors (see figure 4.10b).

The dispersion of particles by caustics effectively puts an end to the non-linear amplification of the grid-resolved mean volume fraction variation due to preferential concentration. A quantitative measure of particle dispersion is given by the granular temperature defined as the variance of the velocities of particles within

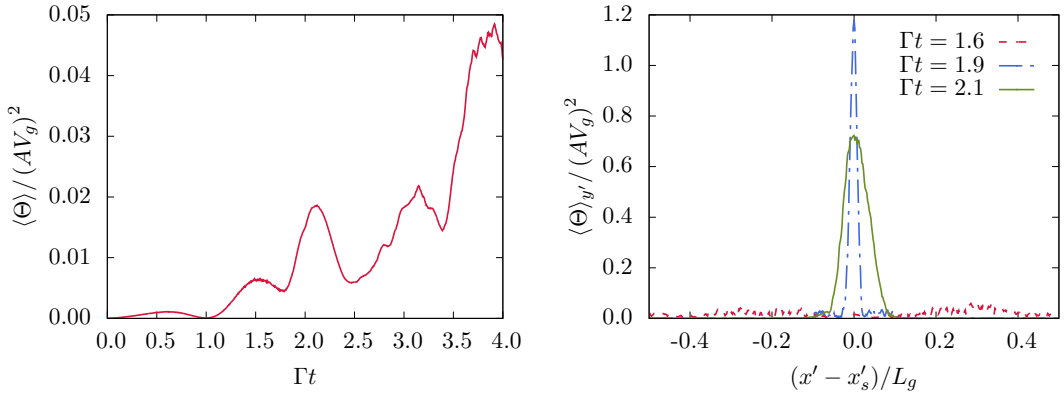

Figure 4.11: Granular temperature in the EL simulation. Figure 4.11a shows a peak of the domain-averaged granular temperature near the time caustics start appearing. Figure 4.11b shows the granular temperature peaks sharply at the location of the high concentration sheet of particles.

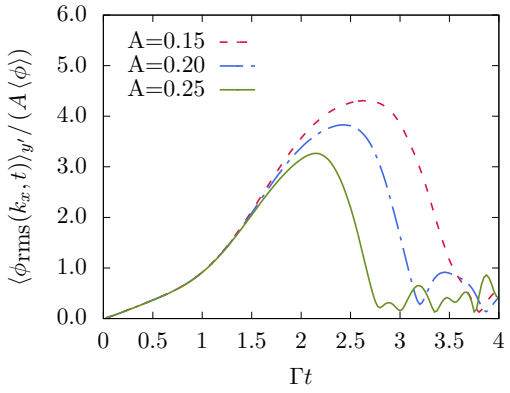

Figure 4.12: Evolution of mode $k_x^\star = 1$ for the initial perturbation strengths A =0.15, 0.20 and 0.25. The later decline of this mode for diminishing A show that the transverse perturbations are also delayed until a more favorable orientation and amplification are attained.

a grid cell. Figure 4.11a shows that the domain-averaged granular temperature $\langle\Theta\rangle$ reaches a peak around the same time $\langle\phi_{rms}\rangle$ peaks. Furthermore, figure 4.11b shows this peak is spatially located near the region of particle crossing.

Rayleigh-Taylor instability

The non-linear amplification of the preferential concentration instability triggers a transverse instability seen at $\Gamma t = 2.325$. The secondary instability is of a Rayleigh-Taylor type arising from the unstable vertical stacking of heavy (particle-rich) over light (particle-depleted) regions. This instability is of a hydrodynamic nature and a simpler formalism can be invoked to describe it. Using the expansion (4.20), one can show that a low order simplification of the governing equations of the particle-laden flow yields the equations for a variable density fluid

$$\rho_m \left(\frac{\partial \mathbf{u}_f}{\partial t} + \mathbf{u}_f \cdot \nabla \mathbf{u}_f \right) = -\nabla p + \mu \nabla^2 \mathbf{u}_f + (\rho_m - \rho_f)\, \mathbf{g} + O(\tau_p) \tag{4.35}$$

$$\nabla \cdot \mathbf{u}_f = 0 \tag{4.36}$$

$$\frac{\partial \rho_m}{\partial t} + \mathbf{u} \cdot \nabla \rho_m = O(\tau_p) \tag{4.37}$$

where $\rho_m = \rho_f + \rho_p \phi$ is the mixture density, and the preferential concentration terms are confined in the $O(\tau_p)$ terms. When completely neglecting the latter, the stability studies of unbounded variable density flows by Batchelor and Nitsche (1991) become of great relevance. Among the many base states they considered two of them are amenable to the configurations studied here: (1) sinusoidally varying density in the vertical direction, and (2) long horizontal sheet of high density. Despite the different base states, Batchelor and Nitsche (1991) show that the growth rates of the transverse modes scale similarly. Case (1) might describe a transverse Rayleigh-Taylor instability growing at the early stages of the evolution of the mode $k_x^\star = 1$, i.e., while it remains sinusoidal. We focus on case (2) since this is almost identical to the final stage of the non-linear preferential concentration instability, around $\Gamma t = 2$, when the secondary Rayleigh-Taylor instability becomes evident. In the present case, the long band of particles is inclined rather than horizontal. Nevertheless, the results of the analysis of Batchelor and Nitsche (1991)

can be used replacing the natural gravity by the effective wave-normal gravity $g_n = ||\mathbf{g} \cdot \mathbf{k}|| /k = gk_y/k$. To make use of the analysis, we will also assume a quasi-steady base state at $\Gamma t = 2$, meaning that the transverse perturbations grow on a time scale significantly smaller than Γ^{-1}. Batchelor and Nitsche (1991) also assume that the transverse modes evolve in an inviscid fashion and have a wavelength much larger than the thickness of the band. Given these assumptions, a transverse mode with a wavenumber α grows exponentially at the rate

$$\sigma = \left(\frac{\pi}{2}\right)^{1/4} \left(\alpha^3 l g_n^2\right)^{1/4} B^{1/2} \tag{4.38}$$

where l and B represent the width and height of the mixture density impulse: $\rho_m = \rho_f \left(1 + B \exp\left(-y^2/l^2\right)\right)$ and $B \simeq \rho_p/\rho_f \phi_{\max} - 1$. The ratio of time scales can be written in the following way

$$\frac{\sigma}{\Gamma} = \left(\frac{\pi}{2}\right)^{1/4} (\alpha l)^{3/4} \sqrt{\frac{L_g}{l} \frac{k_y}{k} \frac{B}{St}} \tag{4.39}$$

The dependence on the inverse of the Stokes number shows that for small Stokes particles a quasi-steady assumption ($\sigma/\Gamma \gg 1$) is valid. Expression (4.39) also shows that waves that achieve a more modest non-linear growth by the preferential concentration instability, i.e., lower B, will destabilize at an orientation closer to horizontal, i.e., larger k_y/k. This trend is confirmed in figure 4.12 representing the evolution of the mode $k_x^\star = 1$ for different initial strengths. The time at which this mode collapses indicates the time at which the transverse Rayleigh-Taylor instability appears. We see that for weaker initial strengths A (and thus lower B) the secondary instability is delayed, which allows the wave to further turn towards the horizontal.

The relation (4.39) can also be used to estimate the most likely transverse mode to grow. The scaling of the growth rate in $(\alpha l)^{3/4}$ suggests that shorter

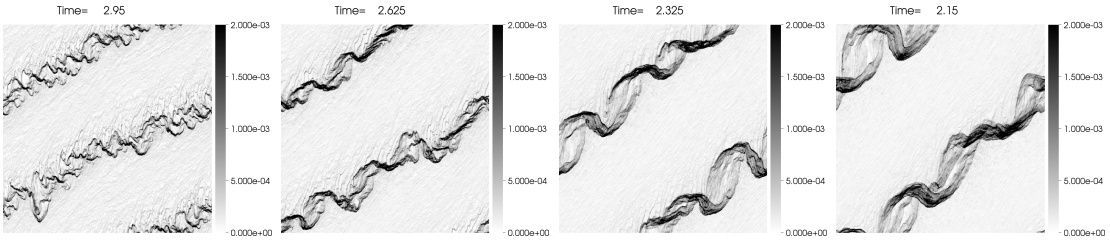

(a) $A = 0.15$ (b) $A = 0.20$ (c) $A = 0.25$ (d) $A = 0.30$

Figure 4.13: Effect of varying the initial perturbation strength A on the orientation and wavelength of the transverse mode.

wavelengths grow faster and the most likely mode to grow is such that $\alpha l \sim 1$. From figure 4.9c, we estimate $l \simeq 0.05 L_g$, $B \simeq 17M \simeq 9.18$ and $k_y/k \simeq 0.67$ at $t = 1.9$. This gives a transverse wavelength $\lambda_{RT} = 2\pi/\alpha \simeq 0.31 L_g$ growing at the fast rate $\sigma \simeq 41\Gamma$. The estimated wavelength appears in agreement with the one seen in the snapshot at $\Gamma t = 2.325$ in figure 4.8. The wavelength of the triggered mode in the transverse direction also depends on the strength of the initial perturbation driving the preferential concentration instability. Figure 4.13 shows that increasing the perturbation strength A from 0.15 to 0.30 leads to the selection of larger wavelengths, in addition to triggering the instability earlier. A rigorous quantitative description of the most likely transverse perturbation to grow requires an analysis beyond expression (4.39), which remains only qualitative at this point. Effects such as those of the shear, preferential concentration, caustics and viscosity will need to be taken in account.

4.6.2 Non-linearities in EE formulations

We now focus on analyzing the non-linear state with the TF and AG simulation methodologies. We run the simulations with the same perturbation strength $A = 0.25$ as in the EL case. Additionally, for a closer comparisons across the methods

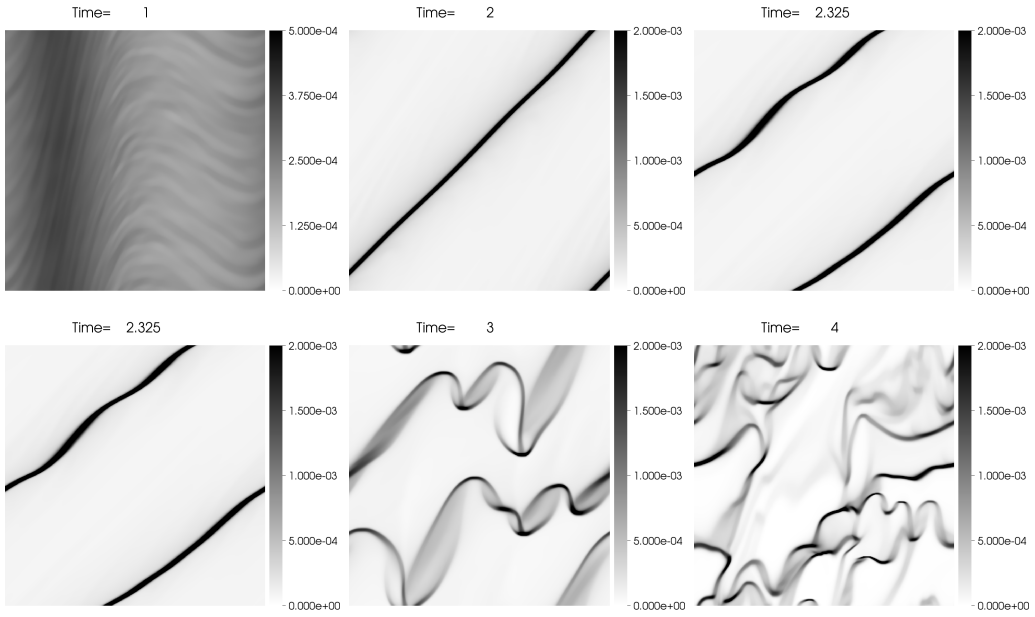

Figure 4.14: Snapshots of the volume fraction field in TF simulation at $A = 0.25$.

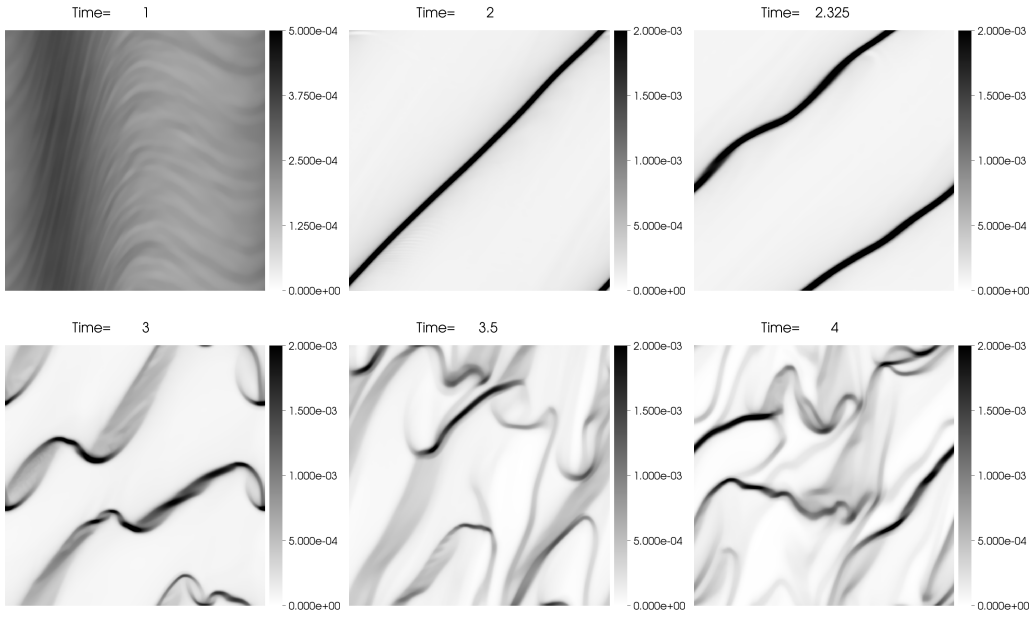

Figure 4.15: Snapshots of the volume fraction field in AG simulation at $A = 0.25$.

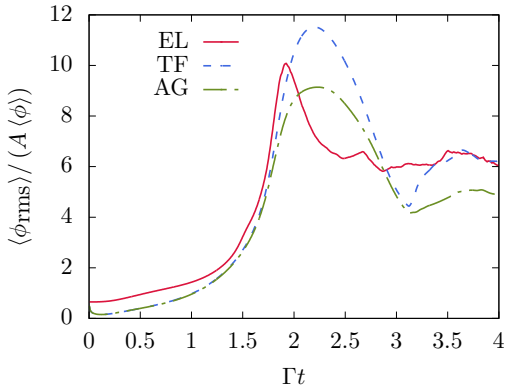

Figure 4.16: Evolution of the domain-averaged volume fraction fluctuations in the three simulation methods.

the initial volume fraction field in the two Eulerian methods is the same as the initial volume fraction field in EL simulations computed from randomly distributed particles. Snapshots of the simulations are shown in figures 4.14 and 4.15. Both simulation methods display the sharpening of the sinusoidal volume fraction into a highly concentrated sheet of particles that breaks up by the transverse Rayleigh-Taylor instability. It is however clear that the way and time at which the secondary instability appears and the final state at $\Gamma t = 4$ are different from EL. It is evident that in presence of strong clustering the three different simulation methods lead to different treatments of the void and high concentration regions. Since we have already described the physical processes in section 4.6.1, we will focus here on understanding the reasons behind the different evolutions.

The domain-averaged volume fraction fluctuations r.m.s for the three simulation methods are shown in figure 4.16. The fluctuations from TF and AG simulations peak at a later time than EL simulations. The TF simulation reaches a higher crest than in EL. The following decline is slower, and reaches a lower trough, although the end state has the same magnitude as in the Lagrangian methodology. In AG simulations, the fluctuations reach a lower maximum, the drop is slower

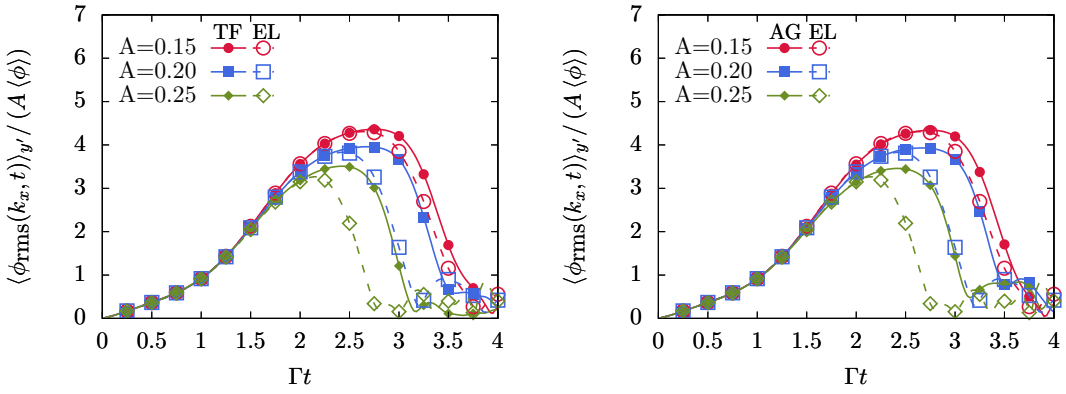

(a) (b)

Figure 4.17: Nonlinear evolution of mode $k_x^\star = 1$ in TF and EL simulations (figure 4.17a) and AG and EL simulations (figure 4.17a) for the perturbation strengths A =0.15, 0.20 and 0.25.

and the final plateau is below that of the EL simulation. This indicates that, by $\Gamma t = 4$, there are less fine scale features in AG than EL or TF simulations which can be visually verified from the provided snapshots. In the Euler-Euler simulations, many of the small scale features in the volume fraction field are suppressed by numerical diffusivity. This causes the fluctuations to drop quickly near $\Gamma t = 0$ in the Euler-Euler simulation and might explain the delay for these methods to reach a peak and the transverse perturbations to grow. Comparisons of the evolution of the extracted mode $k_x^\star = 1$ between TF and EL, and AG and EL, are shown in figure 4.17 for the initial strengths $A = 15$, 20 and 25. We see a nearly identical evolution for the three different methods until $\Gamma t = 2$. The collapse of the modes in TF and AG simulations, which is indicative of the appearance of the transverse Rayleigh-Taylor instability, is delayed compared to the EL simulations. This delay is larger for increasing perturbation strength.

A more appreciable difference in the methods concerns the way TF and AG handle the particle trajectory crossing observed in the EL simulations. The TF method used here is based on a mono-kinetic assumption that states all particle

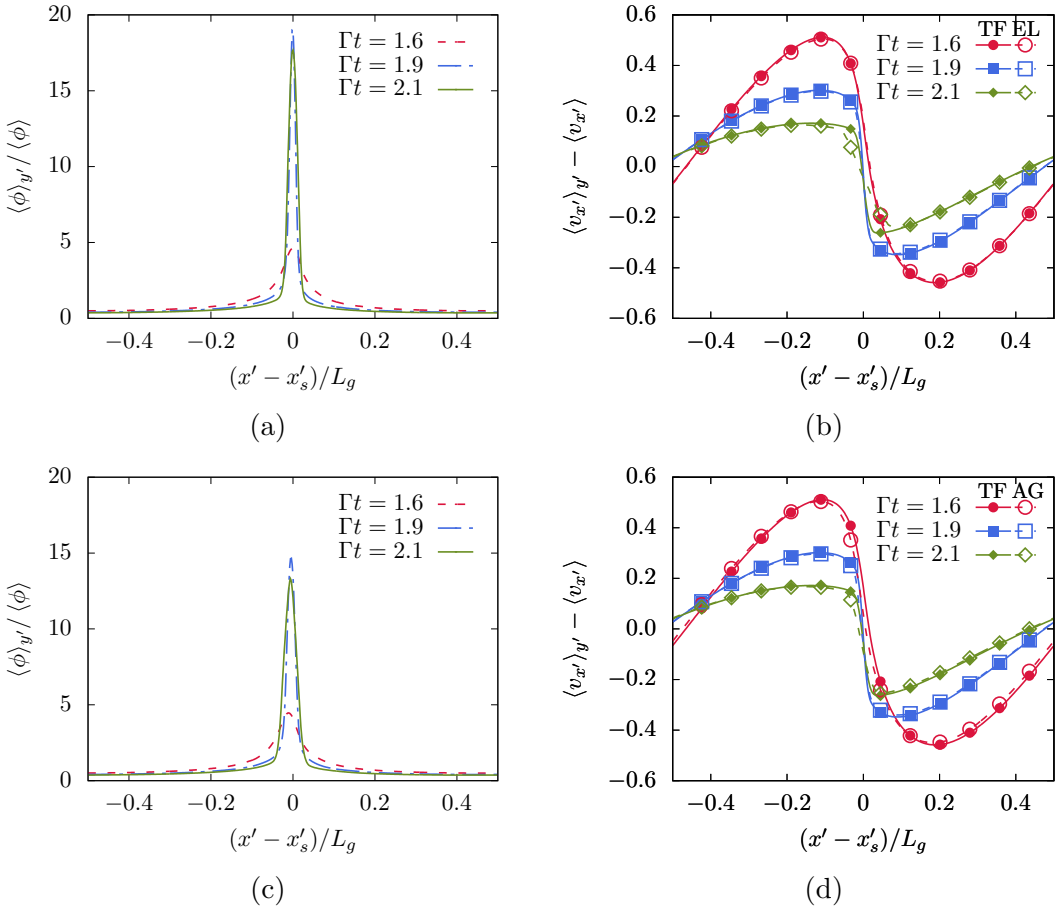

Figure 4.18: Volume fraction and wave-normal velocity as function of the centered wave-normal coordinate in TF (4.18a,4.18b) and AG (4.18c,4.18d) simulations. The inability of the TF method to resolve particle trajectory crossing leads to a higher volume fraction peak (4.18a) and steeper wave-normal velocity (4.18b) than in EL at $\Gamma t = 2.1$. The assumption of anisotropic Gaussian particle number density pdf leads to a smoother volume fraction field (4.18c) and lower gradient of the wave-normal velocity (4.18d) at $\Gamma t = 2.1$ than in TF.

velocity vectors are equal within one grid cell and as such, has no ability to capture the crossing. Figure 4.18b shows, the wave-normal velocity for the times $\Gamma t = 1.6$, 1.9 and 2.1 in TF and EL simulations. One can see that both methods collapse at the earlier two times, depicting the wave steepening pattern. However, the inability of the TF method to handle particle trajectory crossing leads to further steepening of the wave-normal gradient at the high concentration band and a sharper volume fraction impulse as seen in figure 4.18a. This depicts a shock in the TF methods.

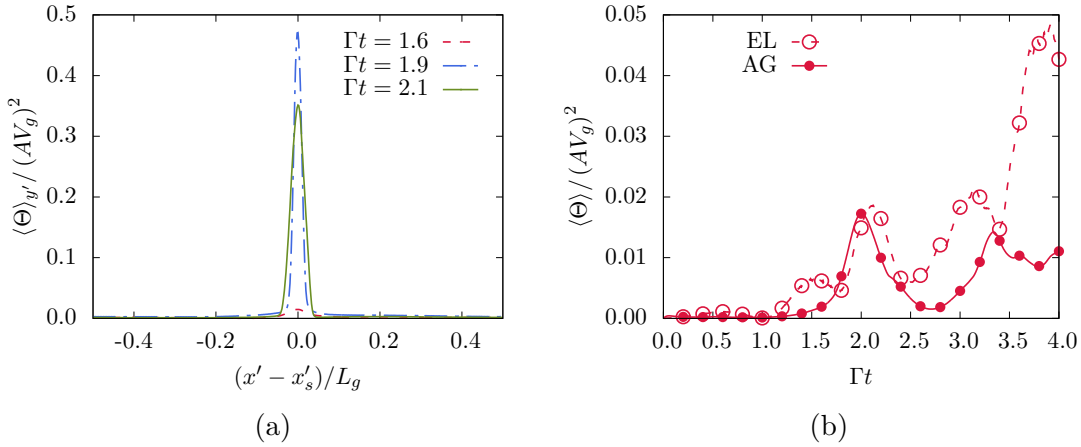

Figure 4.19: Granular temperature in AG simulations. Similarly to EL, graphs of the granular temperature in the wave-normal direction (4.19a) display a sharp peak at the particle sheet location, although lower to the one observed in EL. The domain-averaged granular temperature (4.19b) in AG and EL display qualitatively similar evolutions. The peak at $\Gamma t \sim 2$ due to the two particle streams crossing at the high concentration band is well reproduced in AG.

The width reached by the volume fraction discontinuity is controlled by numerical diffusion. Figure 4.18d shows that the AG method leads to a slightly less steep wave-normal velocity at $\Gamma t = 2.1$. This also comes with a more diffuse volume fraction across the particle sheet. A key element in smoothing the discontinuity in AG is the incorporation of a poly-kinetic sub-grid model for the particle number density pdf controlled by the particle pressure tensor. The trace of the latter, i.e., the granular temperature, is seen to reach a high peak at the particle sheet location in figure 4.19a. Despite differences in the magnitudes reached in AG and EL simulations, the trends are qualitatively similar. This similarity extends to the domain-averaged granular temperature in figure 4.19b.

4.7 Conclusion

An investigation of clustering in homogeneously sheared particle-laden flow in the two-way coupling regime reveals a "route to clustering" that involves three mechanisms leading to a state of significant clustering. Perturbations on the particle and fluid velocities induce inhomogeneities in the particle distribution by the preferential concentration mechanism. In presence of shear, these perturbations grow algebraically by a two-way mechanism that is promoted by preferential concentration and gravity. This first stage in the "route to clustering", leads to the accumulation of particles on fine sheets with a concentration about 18 times higher than the average. When the local volume fraction reaches high magnitudes ($> 10^{-3}$), particle trajectory crossing leads to a local dispersion of particles due to the formation of caustics. This also induces a spreading of the high concentration sheets. Finally, the turning of the sheets by the shear towards the horizontal leads to the appearance of a secondary Rayleigh-Taylor instability. The transverse perturbations breaks the particle sheet into smaller clusters. In the final stages of the simulations, these particle structures continue to sharpen and break repeatedly. In the absence of collisions, coalescence or aggregation, these structures traverse each other and only interact through their coupling with the fluid.

The simulations were conducted in the Euler-Lagrange and Euler-Euler formulations with a methodology that emulates the unboundedness of homogeneous shear. The use of the shear-periodic boundary conditions allows the forcing of fluctuations by the linear homogeneous shear without the introduction of confining scales, such as in mixing layers or wall driven shear. This allows the accurate description of the rotation of Fourier modes by the shear. The evolution of these modes in the linear regime was described in a prior study (Kasbaoui *et al.*, 2015)

using a Two-Fluid representation of the two phases. Full non-linear simulations with two Euler-Euler methods, the Two-Fluid and Anisotropic Gaussian methods, show agreement with Euler-Lagrange simulations and the linear stability analysis for small Stokes number particles, as long as the particle distribution inhomogeneities remain small.

In presence of strong clustering characterized by large void regions and highly concentrated particle structures, differences in the Euler Lagrange and Euler-Euler methods emerge. The Two-Fluid method relying on a mono-kinetic description of the local particle velocity pdf lead to the formation of discontinuities at the high concentration sheets. The volume fraction across these sheets takes the shape of an impulse. The particle velocity across the sheet steepens from a sinusoidal function to a nearly step function. Particle trajectory crossing in Euler-Lagrange simulations removes the discontinuity. The crossing of two streams of particle coming from both sides of the sheet of particles leads to the spreading of the volume fraction field around the sheet and smoother gradients. This poly-kinetic behavior is approximated in the Anisotropic Gaussian method which models the sub-grid particle number density pdf with an anistropic Gaussian distribution. In particular, the particle trajectory crossing at the particle sheet is reproduced with this Eulerian method. The granular temperature, a measure of particle trajectory crossing, is reproduced qualitatively.

CHAPTER 5

THE RAPID DISTORTION OF TWO-WAY COUPLED PARTICLE-LADEN TURBULENCE

5.1 Introduction

Rapid distortion theory (RDT) is a powerful analytical tool to describe the evolution of turbulence under strong shear. Significant advances have been achieved in single phase (see reviews of Savill (1987) and Hunt and Carruthers (1990)). However, the case of particle-laden turbulence has not been addressed until now. In this chapter, we extend the classic single phase RDT to strongly sheared turbulence loaded with heavy small particles.

Single phase rapid distortion theory has a long standing history. In a seminal paper, Pearson (1959) derived a closed form for the evolution of turbulent fluctuations due to uniform distortion. The theory relies on the analytical description of the evolution of the Fourier amplitudes of the velocity fluctuations. The closed form is made possible by the assumption that the non-linear inertial effects are negligible compared to the applied distortion. This generated significant interest particularly in the case of sheared turbulence Moffatt (1965); Townsend (1970). Further work by Rogers provided analytical expressions for the Reynolds stress tensor (Rogers, 1986; Rogers and Moin, 1987), and the mixing of a passive scalar field (Rogers, 1991).

The RDT is particularly suited for the analysis of homogeneously sheared turbulence (HST). In this flow the confining scales are assumed far removed and the energy containing large scales are assimilated to linear shear driving the turbu-

lence. Lee *et al.* (1990) show the pertinence of HST to the study of the near-wall region of a turbulent channel flow where the turbulence is subject to intense shear. Aside from its relevance to engineering flows, HST is a flow of fundamental interest. The work done by the mean shear produces turbulent kinetic energy and the shear deformation adds to the complexity of the flow structures. HST allows the analysis of the turbulence anisotropy due to shear without contamination by bounding walls. It also displays many of the features seen in wall bounded flows such as hairpin vortices (Rogers and Moin, 1987) and the sweep and ejection mechanisms (Pumir, 1996). Comparisons against direct numerical simulations in (Isaza *et al.*, 2009; Kasbaoui *et al.*, 2017) show that, where the shearing is strong enough, the RDT reproduces correctly a wide range of turbulence statistics in HST until $\Gamma t \sim 5$, where Γ is the large scale shear rate. This alleviates the need to run expensive simulations since the computation of the RDT integrals is far cheaper and provides a founding basis to the modeling of general turbulence (Isaza and Collins, 2009; Briard *et al.*, 2016; Hunt and Carruthers, 1990; Hunt *et al.*, 1991).

Beyond the single phase case, the interest in particle-laden turbulence is driven by its practical relevance. Flows containing dispersed particles suspended in a turbulent gas are abundant in nature and engineering. In environmental applications, substantial interest has been devoted to the dispersion of pollutants in the atmosphere (Shaw, 2003; Good *et al.*, 2014) and cloud formation (Gustavsson *et al.*, 2012; Falkovich *et al.*, 2002; Wilkinson *et al.*, 2006). Engineering applications that involve suspended particles include the pneumatic transport of solids, pulverized fuel combustors (Truelove, 1985), sprays (Fernando and Choi, 2007; Marmottant and Villermaux, 2004), fluidized beds and particle-laden jets (Longmire and Eaton, 1992). The suspended particles achieve various desired effects such as interphase heat and mass transfer, catalytic chemical reactions or combustion. The tendency

of particles to distribute inhomogeneously renders particle-laden turbulence significantly more complex than its single phase counterpart. In addition to the reasons listed for the single phase, particle-laden HST can be a gateway to the understanding of the interplay between the two phases and a means to understand how particles influence the turbulent kinetic energy budget.

Extending the RDT to particle-laden turbulence can be challenging owing to the strong interaction between the particulate and gaseous phases. Particles cluster in turbulence owing to their preferential sampling of the straining regions of the flow (Maxey, 1987; Squires and Eaton, 1991; Eaton and Fessler, 1994; Kasbaoui *et al.*, 2015; Sumbekova *et al.*, 2017). They also cause the anisotropic alteration of turbulence at small scales in the sedimentation direction (Elghobashi and Truesdell, 1992). This modulation, characterized by an order unity mass loading $M = \rho_p\langle\phi\rangle/\rho_f$, is strong for solid or liquid particles in a gas ($\rho_p/\rho_f \gg 1$) even at dilute volume fractions $\langle\phi\rangle \ll 1$. In this two-way coupled regime, the coupling between the two phases remains strong even under the simplifying assumption of fast shearing compared to the turbulence time scales in RDT. Whereas, in single phase, RDT explains the distortion of a frozen turbulence field, a two-way coupled RDT for particle-laden flows needs to capture the dynamic anisotropic modulation the two phases exert on each other as they are sheared. Single sinusoidal velocity perturbations to simple shear can produce large particle volume fraction variations even in a linearized treatment (Kasbaoui *et al.*, 2015) so that one may expect interesting results for the particle volume fraction when a range of scales exists as is the case in RDT of two-phase turbulence.

This chapter is organized as the following. Section 5.2 presents the governing equation for sheared particle-laden flows. To make the analysis tractable, we focus

on particles with small inertia for which the velocity field is given as an expansion in Stokes number. The derivation of the classical single phase RDT is presented in section 5.3. Two-phase results are derived in section 5.4. These results are analyzed in the limit of small total deformations in section 5.5.

5.2 Governing equations

An incompressible Newtonian gas of density ρ_f and viscosity μ_f is loaded with monodisperse particles of density ρ_p and diameter d_p at the average volume fraction $\langle\phi\rangle$. Small particles experience a hydrodynamic force equal to the Stokes drag and the gravitational force (Maxey and Riley, 1983)

$$\frac{d\mathbf{x}_p^i}{dt} = \mathbf{u}_p^i \tag{5.1}$$

$$\frac{d\mathbf{u}_p^i}{dt} = \frac{\mathbf{u}_f(\mathbf{x}_p^i, t) - \mathbf{u}_p^i}{\tau_p} + \mathbf{g} \tag{5.2}$$

where $\mathbf{x}_p^i$ and $\mathbf{u}_p^i$ are the Lagrangian position and velocity of particle "i", $\tau_p = \rho_p d_p^2/(18\mu_f)$ is the particle response time, $\mathbf{u}_f$ is the fluid velocity and $\mathbf{g}$ is the gravitational acceleration. Other hydrodynamic forces such as the Basset history force and the lift force can be neglected due to the large density ratio of solid particles or liquid droplets to the suspended in gas. Particle-particle interactions such as collisions, aggregation and coalescence are also negligible for dilute aerosols. The carrier gas satisfies the Navier-Stokes equations

$$\nabla \cdot \mathbf{u}_f = 0 \tag{5.3}$$

$$\rho_f \frac{\partial \mathbf{u}_f}{\partial t} + \rho_f \mathbf{u}_f \cdot \nabla \mathbf{u}_f = -\nabla p + \mu_f \nabla^2 \mathbf{u}_f + \rho_f \mathbf{g} + \rho_p \phi \frac{\mathbf{u}_p - \mathbf{u}_f}{\tau_p} \tag{5.4}$$

where $\mathbf{u}_p$ is the Eulerian particle velocity field.

In Euler-Lagrange approaches, individual particles are tracked using equations (5.1) and (5.2) and Eulerian quantities such as the local volume fraction ϕ and particle velocity field $\mathbf{u}_p$ are determined a posteriori. Euler-Euler approaches rely on solving partial differential equations for the Eulerian quantities directly and are preferred for analytical treatments. According to (Druzhinin, 1995), the particle evolution equations (5.1) and (5.2) lead to the following conservation equations for the particle mass and momentum

$$\rho_p \frac{\partial \phi}{\partial t} + \rho_p \nabla \cdot (\phi \mathbf{u}_p) = 0 \tag{5.5}$$

$$\rho_p \frac{\partial \phi \mathbf{u}_p}{\partial t} + \rho_p \nabla \cdot (\phi \mathbf{u}_p \mathbf{u}_p) = \rho_p \phi \mathbf{g} + \rho_p \phi \frac{\mathbf{u}_f - \mathbf{u}_p}{\tau_p} \tag{5.6}$$

While being conceptually and numerically simpler, this approach has been verified in many studies (Druzhinin, 1995; Zhang and Prosperetti, 1997; Druzhinin, 2001) to yield agreement with the Euler-Lagrange approach in semi-dilute particle-laden flows. This approach is also restricted to small and moderate Stokes numbers since particle-trajectory crossing effects, which are out-of-scope of this Euler-Euler formulation, become significant for high Stokes numbers.

It is seen from the two momentum equations (5.4) and (5.6) that the mass loading $M = \rho_p/\rho_f\langle\phi\rangle$ is a measure of the coupling between the phases. In the one-way regime, $M = 0$, perturbations in the gas velocity drive inhomogeneities in the particle phase but there is no feed back effect on the gas. This effectively takes place for volume fractions below 10^{-6}. In the semi-dilute regime where $10^{-5} < \langle\phi\rangle < 10^{-3}$, the particle feed back cannot be neglected due to the large density ratio $\rho_p/\rho_f = O(10^3)$.

In addition to the mass loading, the working regime of the particle-laden flow is determined by the Stokes number $St = \tau_p/\tau_f$ where τ_f is a characteristic fluid time scale. The Stokes number is a measure of the particle inertia. Particles

with $St = 0$ act like tracers, whereas particles with $St \to \infty$ have an uncorrelated ballistic motion. Particles with $St = O(1)$ have a motion correlated with the fluid but the non-vanishing slip velocity leads to strong clustering Squires and Eaton (1991); Eaton and Fessler (1994).

To further simplify the analysis, we constrain the study to particles with small but non-zero inertia. For such particles, it is possible to approximate the particle velocity field in terms of fluid quantities and gravity. The expansion in particle relaxation time truncated to first order (Maxey, 1987; Druzhinin, 1994; Ferry and Balachandar, 2001) reads

$$\mathbf{u}_p = \mathbf{u}_f + \mathbf{U}_g - \tau_p(\frac{\partial \mathbf{u}_f}{\partial t} + (\mathbf{u}_f + \mathbf{U}_g) \cdot \nabla \mathbf{u}_f) + O(\tau_p^2) \tag{5.7}$$

The studies of Ferry and Balachandar (2002) in turbulent channel flow and Ferry and Balachandar (2001); Rani and Balachandar (2003) in isotropic homogeneous turbulence show this approximation holds for $St_\eta = \tau_p/\tau_\eta < 0.3$ based on the Kolmogorov time scale. Shotorban (2009) performed two-way coupled simulations with (5.7) of decaying particle-laden homogeneous isotropic turbulence and showed kinetic energy and dissipation rate that match Euler-Lagrange simulations for $St_\eta < 0.25$. In homogeneously sheared turbulence, the existence of a second flow time scale, $\tau_f \Gamma^{-1}$, introduces a second stokes number based on the shear rate $St_\Gamma = \Gamma \tau_p$. Both Stokes numbers St_η and St_Γ need to be small in order for the expansion (5.7) to be applicable. The simulations of Kasbaoui *et al.* (2017) of sheared sedimenting particles in the two-way coupling regime show favorable comparisons with the full Eulerian equations for the shear-based Stokes number $St_\Gamma = \tau_p \Gamma \sim 0.01$. Hence, we will consider this expansion applicable for $St_\Gamma < 0.1$ and $St_\eta < 0.3$.

With the expansion (5.7) the complete governing equations take the following

form

$$\nabla \cdot \mathbf{u}_f = 0 \tag{5.8}$$

$$(\rho_f + \rho_p\phi)\left(\frac{\partial \mathbf{u}_f}{\partial t} + \mathbf{u}_f \cdot \nabla \mathbf{u}_f\right) = -\nabla p + \mu_f \nabla^2 \mathbf{u}_f + (\rho_f + \rho_p\phi)\,\mathbf{g} - \rho_p\phi \mathbf{U}_g \cdot \nabla \mathbf{u}_f \tag{5.9}$$

$$\frac{\partial \phi}{\partial t} + \left(\mathbf{u}_f + \mathbf{U}_g - \tau_p\left(\frac{\partial \mathbf{u}_f}{\partial t} + (\mathbf{u}_f + \mathbf{U}_g) \cdot \nabla \mathbf{u}_f\right)\right) \cdot \nabla \phi = \phi \nabla \mathbf{u}_f : \nabla \mathbf{u}_f \tag{5.10}$$

These equations resemble those of a variable density fluid of density $\rho_f + \rho_p\phi$ although differences exist. The most notable differences can be seen from the volume fraction equation (5.10), in which the right-hand side contains a source of volume fraction fluctuations due to preferential concentration. It can be shown that this term expresses as the difference between the second tensor invariants of the straining and rotation tensors. Hence, in regions where the straining exceeds the rotation, this term causes the exponential accumulation of particles. In the opposite scenario, this term acts as a sink. Moreover, the volume fraction field is convected at the particle velocity rather than that of the fluid.

When the flow is subject to a large scale homogeneous shear $\Gamma x_2 \mathbf{e}_1$, it is often useful to rewrite the previous equations for the fluctuating velocity $\mathbf{u}'_f = \mathbf{u}_f - \Gamma x_2 \mathbf{e}_1$

$$\nabla \cdot \mathbf{u}'_f = 0 \tag{5.11}$$

$$(\rho_f + \rho_p\phi)\left(\frac{\partial \mathbf{u}'_f}{\partial t} + \Gamma x_2 \frac{\partial \mathbf{u}'_f}{\partial x_1} + \mathbf{u}'_f \cdot \nabla \mathbf{u}'_f + \Gamma u'_{f,2}\mathbf{e}_1\right) = -\nabla p + \mu_f \nabla^2 \mathbf{u}'_f + (\rho_f + \rho_p\phi)\,\mathbf{g} - \rho_p\phi\left(\mathbf{U}_g \cdot \nabla \mathbf{u}'_f + \Gamma U_{g,2}\mathbf{e}_1\right) \tag{5.12}$$

$$\frac{\partial \phi}{\partial t} + \Gamma x_2 \frac{\partial \phi}{\partial x_1} + \mathbf{u}'_p \cdot \nabla \phi = \phi \nabla \mathbf{u}'_f : \nabla \mathbf{u}'_f + 2\phi\Gamma \frac{\partial u'_{f,2}}{\partial x_1} \tag{5.13}$$

where the convecting particle velocity field $\mathbf{u}'_p$ is given by

$$\mathbf{u}'_p = \mathbf{u}'_f + \mathbf{U}_g - \tau_p\left(\frac{\partial \mathbf{u}'_f}{\partial t} + \Gamma x_2 \frac{\partial \mathbf{u}'_f}{\partial x_1} + \left(\mathbf{u}'_f + \mathbf{U}_g\right) \cdot \nabla \mathbf{u}'_f + \Gamma\left(u_{f,2} + U_{g,2}\right)\mathbf{e}_1\right) \tag{5.14}$$

In this representation, the convection by homogeneous shear terms $\Gamma x_2 \partial/\partial x_1$ appear explicitly. These terms are also known as the distortion terms. In spectral space, they induce the turning of wave vector of the Fourier modes (Kasbaoui *et al.*, 2015; Thomson, 1887; Moffatt, 1965) towards a direction parallel to the velocity gradient. The distortion of turbulence leads to the elongation of vortex tubes (Rogers and Moin, 1987) and their alignment in direction nearly perpendicular to the velocity gradient Sukheswalla *et al.* (2013).

The RDT is applicable when the shearing is so strong that the distortion term in the momentum equation vastly exceeds in magnitude the non-linear convection. Formally, this is expressed as

$$\frac{\left|\left|\Gamma x_2 \partial \mathbf{u}'_f/\partial x_1\right|\right|}{\left|\left|\mathbf{u}'_f \cdot \nabla \mathbf{u}'_f\right|\right|} \sim \Gamma \tau_f = S^* \gg 1 \tag{5.15}$$

where $\tau_f = \langle u'_{f,i} u'_{f,i} \rangle / \epsilon$, is the large eddy turnover time and ϵ is the dissipation rate. It is clear that the RDT will be applicable in the limit of large shear numbers $S^* = \Gamma \langle u'_{f,i} u'_{f,i} \rangle / \epsilon$.

The expansion (5.7) for the particle velocity field adds additional constrains. It is important to maintain small Stokes number be it defined with the Kolmogorov time scale or the shear one. Consider particles such as the $St_\eta < 0.3$. Then the shear-based stokes number can be expressed as the following

$$St_\Gamma = \Gamma \tau_p = \Gamma \tau_f \frac{\tau_p}{\tau_\eta} \frac{\tau_\eta}{\tau_f} \sim \frac{S^* St_\eta}{\sqrt{Re_l}} \tag{5.16}$$

where $Re_l = \rho_f \epsilon l^2 / (\langle u'_{f,i} u'_{f,i} \rangle \mu_f)$ is the large scale Reynolds number, and l denotes the integral length scale (Pope, 2001). Thus, we see that for sufficiently large Reynolds number, the condition $St_\Gamma \ll 1$ is verified.

The assumption of rapid distortion allows linearization of the governing equations. We will also make a Boussinesq approximation. Note that velocity

fluctuations drive an order $1/S^*$ smaller volume fraction fluctuations and thus $\phi' = \phi - \langle\phi\rangle \ll 1$. The linearized equations read as

$$\nabla \cdot \mathbf{u}'_f = 0 \tag{5.17}$$

$$\frac{\partial \mathbf{u}'_f}{\partial t} + \Gamma x_2 \frac{\partial \mathbf{u}'_f}{\partial x_1} + \Gamma u'_{f,2}\mathbf{e}_1 = -\frac{1}{\rho_m}\nabla p' + \frac{\mu_f}{\rho_m}\nabla^2 \mathbf{u}'_f + \frac{\rho_p \phi'}{\rho_m}\mathbf{g} - \frac{\rho_p \langle\phi\rangle}{\rho_m}\mathbf{U}_g \cdot \nabla \mathbf{u}'_f \tag{5.18}$$

$$\frac{\partial \phi'}{\partial t} + \Gamma x_2 \frac{\partial \phi'}{\partial x_1} + \mathbf{U}_g \cdot \nabla \phi = 2\langle\phi\rangle \Gamma \frac{\partial u'_{f,2}}{\partial x_1} \tag{5.19}$$

where $p' = p + \rho_m \mathbf{g} \cdot \mathbf{x}$ is a reduced pressure and $\rho_m = \rho_f + \rho_p \langle\phi\rangle$ is an effective mixture density. Equations (5.17), (5.18) and (5.19) constitute the RDT governing equations in physical space. It is worthwhile to transform these equations to spectral space. Such representation allows the understanding of the distortion of turbulence in terms of its spectral content. Applying a Fourier transform to the RDT equations yields

$$\mathbf{k} \cdot \hat{\mathbf{u}}_f = 0 \tag{5.20}$$

$$\frac{\partial \hat{\mathbf{u}}_f}{\partial t} - \Gamma k_1 \frac{\partial \hat{\mathbf{u}}_f}{\partial k_2} + \Gamma \hat{u}_{f,2}\mathbf{e}_1 = -\frac{i\mathbf{k}}{\rho_m}\hat{p} + \frac{\mu_f}{\rho_m}k^2 \hat{\mathbf{u}}_f + \frac{\rho_p \hat{\phi}}{\rho_m}\mathbf{g} - \frac{\rho_p \langle\phi\rangle}{\rho_m} i\mathbf{U}_g \cdot \mathbf{k}\hat{\mathbf{u}}_f \tag{5.21}$$

$$\frac{\partial \hat{\phi}}{\partial t} - \Gamma k_1 \frac{\partial \hat{\phi}}{\partial k_2} + i\mathbf{U}_g \cdot \mathbf{k}\hat{\phi} = 2\langle\phi\rangle \Gamma i k_1 \hat{u}_{f,2} \tag{5.22}$$

where $\hat{\mathbf{u}}_f$ and $\hat{\phi}$ are the Fourier amplitudes associated to the mode of wavevector $\mathbf{k} = (k_1, k_2, k_3)$ and wavenumber $k = \sqrt{k_1^2 + k_2 + k_3}$

$$\hat{\mathbf{u}}_f(t, \mathbf{k}) = \frac{1}{(2\pi)^{3/2}} \int_{\mathbf{x}\in\mathbb{R}^3} \mathbf{u}'_f(t, \mathbf{x}) \exp\left(-i\mathbf{k} \cdot \mathbf{x}\right) d\mathbf{x} \tag{5.23}$$

$$\hat{\phi}(t, \mathbf{k}) = \frac{1}{(2\pi)^{3/2}} \int_{\mathbf{x}\in\mathbb{R}^3} \phi'(t, \mathbf{x}) \exp\left(-i\mathbf{k} \cdot \mathbf{x}\right) d\mathbf{x} \tag{5.24}$$

The solenoidal condition (5.20) ensures that the pressure acts solely in the wave normal direction $\mathbf{k}$. The forces driving the flow are obtained by projecting on the

wave parallel directions $\delta_{ij} - k_i k_j/k$ resulting in

$$\frac{\partial \hat{\mathbf{u}}_f}{\partial t} - \Gamma k_1 \frac{\partial \hat{\mathbf{u}}_f}{\partial k_2} + \Gamma \hat{u}_{f,2} \left(\mathbf{I} - 2\frac{\mathbf{kk}}{k} \right) \cdot \mathbf{e}_1 + \frac{\rho_p \langle \phi \rangle}{\rho_m} i \mathbf{U}_g \cdot \mathbf{k} \hat{\mathbf{u}}_f = \frac{\mu_f}{\rho_m} k^2 \hat{\mathbf{u}}_f + \frac{\rho_p \hat{\phi}}{\rho_m} \left(\mathbf{I} - \frac{\mathbf{kk}}{k} \right) \cdot \mathbf{g} \qquad (5.25)$$

In the previous equations, the distortion term appears as $\Gamma k_1 \partial/\partial k_2$ in the transformed equations. This term causes a transfer of energy in the Fourier space from the large scale modes to short modes parallel to the velocity gradient direction. A key step in the RDT derivation for rapidly sheared flows dates back to Lord Kelvin (Thomson, 1887). It consists in solving along the characteristic in spectral space $dk_2/dt = -k_1\Gamma$. This effectively means that Fourier modes turn towards a direction parallel to the velocity gradient. Note that, in single phase flows, a single rotating Fourier mode is a complete solution to the non-linear Navier Stokes equations (Craik and Criminale, 1986). This shows that these modes are fundamental solutions for homogeneously sheared flows. Finally, the complete set of equations for the rotating Fourier modes are

$$\frac{d\hat{\mathbf{u}}_f}{dt} + \Gamma \hat{u}_{f,2} \left(\mathbf{I} - 2\frac{\mathbf{kk}}{k} \right) \cdot \mathbf{e}_1 + \frac{\rho_p \langle \phi \rangle}{\rho_m} i \mathbf{U}_g \cdot \mathbf{k} \hat{\mathbf{u}}_f = \frac{\mu_f}{\rho_m} k^2 \hat{\mathbf{u}}_f + \frac{\rho_p \hat{\phi}}{\rho_m} \left(\mathbf{I} - \frac{\mathbf{kk}}{k} \right) \cdot \mathbf{g} \qquad (5.26)$$

$$\frac{d\hat{\phi}}{dt} + i \mathbf{U}_g \cdot \mathbf{k} \hat{\phi} = 2 \langle \phi \rangle \Gamma i k_1 \hat{u}_{f,2} \qquad (5.27)$$

$$\mathbf{k}(t) = (k_1, k_2, k_3) = (k_{1,0}, k_{2,0} - k_{1,0}\Gamma t, k_{3,0}) \qquad (5.28)$$

Defining the linear operator $\mathbf{X}(\mathbf{k}_0, t)$ solution to the equations above, any fluctuations $\mathbf{u}'_f(\mathbf{x}, t)$ and $\phi'(\mathbf{x}, t)$ can be computed from the spectral content at a time origin $t = 0$ (equations (5.23) and (5.24)), and the evolution equations (5.26), (5.27) and (5.28)

$$\chi(\mathbf{x}, t) = \int\int\int \left\{ \mathbf{X}(\mathbf{k}_0, t) \hat{\chi}_0 \exp\left(i \mathbf{k}(t) \cdot \mathbf{x} \right) \right\} d\mathbf{k}_0 \qquad (5.29)$$

where $\chi = \left(\mathbf{u}'_f, \phi'\right)^T$ are the physical space fluctuations and $\hat{\chi}_0 = \left(\hat{\mathbf{u}}_{f,0}, \hat{\phi}_0\right)^T$ are the Fourier amplitudes at the initial time.

5.3 Derivation of the single phase RDT

The purpose of the RDT is to find a solution operator $\mathbf{X}$ that maps the later turbulence spectrum to the initial one. When the particle volume fraction is null (and hence corresponding to the single phase flow scenario), the solution operator can be obtained analytically (Moffatt, 1965; Pearson, 1959; Townsend, 1970). In this section, we introduce some of the concepts necessary to the treatment of the particle-laden case and show how the classical single phase RDT result can be recovered for $\langle\phi\rangle = 0$.

First, we write the general two-phase equations (5.26) and (5.27) in the following matrix form

$$\frac{d\hat{\chi}}{dt} + \left(\mathbf{D} + \mathbf{V} + \mathbf{G} + \mathbf{C}\right)\hat{\chi} = 0 \tag{5.30}$$

$$\hat{\chi}(t=0) = \left(\hat{u}_{f,1}(0), \hat{u}_{f,2}(0), \hat{u}_{f,3}(0), \hat{\phi}(0)\right)^T = \hat{\chi}_0 \tag{5.31}$$

where $\mathbf{D}$, $\mathbf{V}$, $\mathbf{G}$, and $\mathbf{C}$ are the distortion, viscous diffusion, gravitational settling and coupling operators respectively

$$\mathbf{D}(\mathbf{k}_0, t) = \Gamma\frac{k_1}{k^2}\left(\begin{array}{ccc|c} 0 & \left(k_2^2 + k_3^2 - k_1^2\right)/k_1 & 0 & 0 \\ 0 & -2k_2 & 0 & 0 \\ 0 & -2k_3 & 0 & 0 \\ \hline 0 & 0 & 0 & 0 \end{array}\right) \tag{5.32}$$

$$\mathbf{V}(\mathbf{k}_0,t) = \frac{\mu_f k^2}{\rho_m}\left(\begin{array}{ccc|c} 1 & 0 & 0 & 0 \\ 0 & 1 & 0 & 0 \\ 0 & 0 & 1 & 0 \\ \hline 0 & 0 & 0 & 0 \end{array}\right) \tag{5.33}$$

$$\mathbf{G}(\mathbf{k}_0,t) = i(\mathbf{U}_g\cdot\mathbf{k})\left(\begin{array}{ccc|c} \frac{\rho_p\langle\phi\rangle}{\rho_m} & 0 & 0 & 0 \\ 0 & \frac{\rho_p\langle\phi\rangle}{\rho_m} & 0 & 0 \\ 0 & 0 & \frac{\rho_p\langle\phi\rangle}{\rho_m} & 0 \\ \hline 0 & 0 & 0 & 1 \end{array}\right) \tag{5.34}$$

$$\mathbf{C}(\mathbf{k}_0,t) = \left(\begin{array}{ccc|c} & & & -\frac{\rho_p}{\rho_m}\left(g_1-\frac{(\mathbf{g}\cdot\mathbf{k})k_1}{k^2}\right) \\ & 0 & & -\frac{\rho_p}{\rho_m}\left(g_2-\frac{(\mathbf{g}\cdot\mathbf{k})k_2}{k^2}\right) \\ & & & -\frac{\rho_p}{\rho_m}\left(g_3-\frac{(\mathbf{g}\cdot\mathbf{k})k_3}{k^2}\right) \\ \hline 0 & -i2\Gamma\langle\phi\rangle k_1 & 0 & 0 \end{array}\right) \tag{5.35}$$

The operators above are all time dependent since $k_2 = k_{2,0} - \Gamma k_1 t$ and $k = \sqrt{k_1^2+k_2^2+k_3^2}$ are time dependent. The distortion operators is responsible for the change of magnitude of the spectral modes due to the rotation of the wavevectors. The viscous dissipation operators applies on the fluid velocity only and causes the dissipation of momentum by viscosity. The gravitational settlings describes the momentum transport due to settling. The coupling operator captures the effects that each phase applies on the other one: the imbalance of fluid strain and rotation, i.e., preferential concentration, promotes the growth volume fraction perturbations, while variations in the particle distribution leads to varying gravitational loading on the fluid. Notice that unlike the other block diagonal operators, the coupling operator contains only off-diagonal components responsible for tying the dynamics of the fluid velocity and the particle volume fraction.

The time dependency of the operators renders the task of finding a solution

to (5.30) vastly more complicated than for constant operators. In the spirit of the general theory of linear functional equations (Bellman, 1997), we will focus on solving the differential system (5.30) for the variable time matrix $\mathbf{X}(t)$ with the initial condition $\mathbf{X}(t=0) = \mathbf{I}$.

$$\frac{d\mathbf{X}}{dt} + (\mathbf{D} + \mathbf{V} + \mathbf{G} + \mathbf{C})\,\mathbf{X} = 0 \tag{5.36}$$

$$\mathbf{X}(t=0) = \mathbf{I} \tag{5.37}$$

Finding the solution to the general problem $\mathbf{X}(t)$, leads to a specific solution $\hat{\chi}(t)$ that incorporates the initial conditions $\hat{\chi}_0$ following the simple multiplication rule $\hat{\chi}(t) = \mathbf{X}(t)\hat{\chi}_0$.

In the single phase setting ($\langle\phi\rangle = 0$), the coupling and gravitational settling operators are zero. Assuming an inviscid flow for now, the fluctuations associated with the initial mode $\mathbf{k}_0$ are completely determined by the distortion

$$\frac{d\mathbf{X}}{dt} + \mathbf{D}\mathbf{X} = 0 \tag{5.38}$$

Given the simple form of the operator $\mathbf{D}$ solving the system (5.38) can be done by hand, component by component, with the initial condition $\mathbf{X} = I$. Doing so, one arrives to a solution equal to the classical single phase RDT operator, $\mathbf{X} = \mathbf{A}$, where

$$\mathbf{A}(\mathbf{k}_0, t) = \begin{pmatrix} 1 & \frac{k_0^2}{k_1^2+k_3^2}\left(-\frac{k_3^2}{k_0^2}P + \frac{k_1^2}{k_0^2}Q\right) & 0 & 0 \\ 0 & \frac{k_0^2}{k^2} & 0 & 0 \\ 0 & \frac{k_1 k_3}{k_1^2+k_3^2}\,(P+Q) & 1 & 0 \\ 0 & 0 & 0 & 1 \end{pmatrix} \tag{5.39}$$

See appendix B for the functions P, Q. This form has been derived by Pearson (1959) although earlier results can be found in (Thomson, 1887).

The inclusion of viscous effects, although trivial, serves to illustrate how a full solution can be built by adding the effects of the operators one at a time. When

keeping the viscous dissipation operator, the equation we seek to solve, which supersedes (5.38), is

$$\frac{d\mathbf{X}}{dt} + (\mathbf{D} + \mathbf{V})\,\mathbf{X} = 0 \tag{5.40}$$

To find a solution to the viscous RDT equation above that extends the inviscid result, consider the new matrix $\mathbf{Y} = \mathbf{A}^{-1}\mathbf{X}$. Injecting this form in (5.40) yields an equation on $\mathbf{Y}$

$$\frac{d\mathbf{Y}}{dt} + \mathbf{A}^{-1}\mathbf{V}\mathbf{A}\mathbf{Y} = 0 \tag{5.41}$$

with the initial condition $\mathbf{Y}(0) = \mathbf{I}$. The inverse of the RDT matrix is simply $\mathbf{A}^{-1}(\mathbf{k}_0, t) = \mathbf{A}(\mathbf{k}(t), -t)$, which states that the distortion of the mode $\mathbf{k}(t)$ backwards in time recovers the mode $\mathbf{k}_0$. Because of the particular diagonal structure of $\mathbf{V}$, it commutes with the distortion operator $\mathbf{A}$, which leads to $\mathbf{A}^{-1}\mathbf{V}\mathbf{A} = \mathbf{V}$. This means, that the viscous dissipation acts in the same way in the laboratory reference frame and the distorted one.

Because $\mathbf{V}$ is a diagonal operator, the solution to (5.41) is found easily: $\mathbf{Y}(t) = \mathrm{diag}\,(e^{-\alpha_1}, e^{-\alpha_1}, e^{-\alpha_1}, 1)$ a diagonal matrix with $\alpha_1 = \frac{\mu_f}{\rho_m}\int_0^t k^2 dt' = \frac{\mu_f}{\rho_m}\,(k^2 - k_{1,0}k_{2,0}\Gamma t + (k_{1,0}\Gamma t)^2/3)$. Hence, we recover the classical single phase viscous RDT (Isaza and Collins, 2009; Kasbaoui *et al.*, 2017)

$$\mathbf{X}(\mathbf{k}_0, t) = \mathbf{A}\mathbf{Y} \tag{5.42}$$

$$= \begin{pmatrix} e^{-\alpha_1} & e^{-\alpha_1}\frac{k_0^2}{k_1^2+k_3^2}\left(-\frac{k_3^2}{k_0^2}P + \frac{k_1^2}{k_0^2}Q\right) & 0 & 0 \\ 0 & e^{-\alpha_1}\frac{k_0^2}{k^2} & 0 & 0 \\ 0 & e^{-\alpha_1}\frac{k_1 k_3}{k_1^2+k_3^2}\,(P+Q) & e^{-\alpha_1} & 0 \\ 0 & 0 & 0 & 1 \end{pmatrix} \tag{5.43}$$

The commutation property between operators greatly facilitates the task of building an exact full solution to (5.36) that adds one operator at a time. We have seen that leaving the distortion operator $\mathbf{D}$ and zeroing all three others leads

to a solution $\mathbf{X} = \mathbf{A}$. Then, when retaining the viscous dissipation operator $\mathbf{V}$ and zeroing all others, i.e., the system (5.41), leads to the solution $\mathbf{X} = \mathbf{Y}$. Finally, retaining both distortion and viscous dissipation operators and zeroing the other ones yields a solution that factors the solutions of the two sub-systems, i.e., $\mathbf{X} = \mathbf{AY}$. This is the case because $\mathbf{V}$ and $\mathbf{A}$ commute in (5.41). This divide and conquer approach is sometimes refereed to as operator splitting (Chorin, 1968). When the commutation property is lacking, more involved approaches are required and these can sometimes become intractable.

5.4 The particle-laden case

Similarly to the splitting approach shown for the viscous RDT, we seek to find a solution to the full particle-laden RDT equation (5.36) by including the effects of the remaining operators one at a time. First, we seek to take into account the effect of particle sedimentation, in addition to the distortion and viscous dissipation. To find a solution to the truncated system

$$\frac{d\mathbf{X}}{dt} + (\mathbf{D} + \mathbf{V} + \mathbf{G})\,\mathbf{X} = 0 \tag{5.44}$$

we introduce the matrix $\mathbf{Z} = \mathbf{Y}^{-1}\mathbf{A}^{-1}\mathbf{X}$. Equation (5.44) written for $\mathbf{Z}$ reads as

$$\frac{d\mathbf{Z}}{dt} + \mathbf{Y}^{-1}\mathbf{A}^{-1}\mathbf{GAYZ} = 0 \tag{5.45}$$

Here again the diagonal structure of $\mathbf{G}$ leads to $\mathbf{Y}^{-1}\mathbf{A}^{-1}\mathbf{GAY} = \mathbf{G}$. The solution to (5.45) is the diagonal matrix $\mathbf{Z} = \mathrm{diag}\left(e^{-\frac{M}{1+M}\alpha_2}, e^{-\frac{M}{1+M}\alpha_2}, e^{-\frac{M}{1+M}\alpha_2}, e^{-\alpha_2}\right)$ where $\alpha_2(t) = it\,(\mathbf{U_g}\cdot\mathbf{k} + U_{g,2}\Gamma t k_1/2)$.

We continue the splitting procedure to build the full particle-laden solution. We define the matrix $\mathbf{U} = \mathbf{Z}^{-1}\mathbf{Y}^{-1}\mathbf{A}^{-1}\mathbf{X}$. When including the coupling, this matrix

is subject to the equation

$$\frac{d\mathbf{U}}{dt} + \mathbf{Z}^{-1}\mathbf{Y}^{-1}\mathbf{A}^{-1}\mathbf{CAYZU} = 0 \tag{5.46}$$

The difficulty here comes from the fact that $\mathbf{C}$ and $\mathbf{A}$ do not commute. The shearing alters the coupling between the two phases but does not suppress it. Let us define the coupling operator in the transformed reference frame

$$\mathbf{C}' = \mathbf{Z}^{-1}\mathbf{Y}^{-1}\mathbf{A}^{-1}\mathbf{CAYZ} \tag{5.47}$$

$$= \begin{pmatrix} 0 & 0 & 0 & e^{\alpha_1+(\frac{M}{1+M}-1)\alpha_2}\left(c_{14} - a_{12}c_{24}/a_{22}\right) \\ 0 & 0 & 0 & e^{\alpha_1+(\frac{M}{1+M}-1)\alpha_2}\frac{c_{24}}{a_{22}} \\ 0 & 0 & 0 & e^{\alpha_1+(\frac{M}{1+M}-1)\alpha_2}\left(c_{34} - a_{32}c_{24}/a_{22}\right) \\ 0 & a_{22}c_{42}e^{-\alpha_1-(\frac{M}{1+M}-1)\alpha_2} & 0 & 0 \end{pmatrix} \tag{5.48}$$

where a_{ij} and c_{ij} are the components of the distortion and coupling operators respectively. Unfortunately, the sparsity of this operator does not lead to a simpler set of equations for the components u_{ij} of $\mathbf{U}$. The most significant sub-systems in (5.46) are the pairs (u_{42}, u_{22}) and (u_{44}, u_{24}), which satisfy

$$\frac{d}{dt}\begin{pmatrix} u_{4i} \\ u_{2i} \end{pmatrix} + \begin{pmatrix} 0 & c'_{42} \\ c'_{24} & 0 \end{pmatrix}\begin{pmatrix} u_{4i} \\ u_{2i} \end{pmatrix} = 0 \tag{5.49}$$

where c'_{ij} are the components of the operator $\mathbf{C}'$, $i = 2$ or 4 and the initial conditions are $(u_{42}, u_{22}) = (0, 1)$ and $(u_{44}, u_{24}) = (1, 0)$. Equation (5.49) boils the coupling problem to its essence: the preferential concentration driving volume fraction fluctuations (u_{4i}) are driven solely by the velocity gradient component in the gradient direction (u_{2i}) since only this component couples with the imposed shear flow to modulate the strain and rotation magnitudes. Because this is a 2-by-2 system, two independent solutions can exist. An initial volume fraction perturbation leads to the emergence of the solution u_{44}, while an initial momentum perturbation leads to u_{42}. Solving the coupled pair of equations (5.49), allows

the subsequent computation of the velocities in directions 1 and 3, i.e.,

$$\mathbf{U} = \begin{pmatrix} 1 & -\int c'_{14} u_{42} dt' & 0 & -\int c'_{14} u_{44} dt' \\ 0 & u_{22} & 0 & u_{24} \\ 0 & -\int c'_{34} u_{42} dt' & 1 & -\int c'_{34} u_{44} dt' \\ 0 & u_{42} & 0 & u_{44} \end{pmatrix} \tag{5.50}$$

It is worthwhile to express (5.49) as a scalar equation in order to extract physical insight. Using $du_{2i}/dt = c_{24} u_{4i}$ to combine the equations for u_{2i} and u_{4i} into a second order differential equation yields

$$\frac{d^2 u_{4i}}{dt^2} + \left(\frac{1}{k^2} \frac{dk^2}{dt} + \frac{k^2}{(1+M)\, Re} + i \left(\mathbf{U}_g \cdot \mathbf{k} \right) \right) \left(\frac{M}{1+M} - 1 \right) \frac{du_{4i}}{dt} - II_c u_{4i} = 0 \tag{5.51}$$

$$\begin{array}{c|c} u_{42}(0) = 0 & u_{44}(0) = 1 \\ \frac{du_{42}}{dt}(0) = -c'_{42}(0) = -c_{42}(0) & \frac{du_{44}}{dt}(0) = 0 \end{array} \tag{5.52}$$

where $II_c = c_{42} c_{24}$ is the second invariant of the coupling tensor. The ODE (5.51) shows that the variation of u_{42} and u_{44} is due to 4 effects: (1) the wave stretching (first term on the left multiplying the first order derivative) due to the turning and alteration of scales by the shear (2) the viscous dissipation (second term) (3) the difference in sedimentation speeds of the two phases (third term) and (4) the two-way coupling through preferential concentration and gravity (term multiplying the zero order derivative).

Equation (5.51) does not admit an analytical solution, although various techniques can be used to find an approximate solution for large wavenumber modes (Kasbaoui *et al.*, 2015). Unlike the single phase RDT, the particle-laden case is only semi-analytical. The full particle-laden RDT solution is formally given by $\hat{\chi}(t) = \mathbf{AYZU} \hat{\chi}_0$, but the last operator cannot be expressed in terms of simple functions.

Further simplifications can be made in the special case of vanishingly small mass loading ($M \ll 1$), i.e, in the one-way coupling regime. Flows in this regime are abundant in the atmosphere (Shaw, 2003) and the most prominent application may be cloud formation (Falkovich *et al.*, 2002; Ireland *et al.*, 2016). The super-dilute conditions, $\langle\phi\rangle < 10^{-6}$, lead to a mass loading of $O(10^{-3})$ for water droplets in clouds. In this regime, the particle feed back is negligible. The coupling operator reduces to $\mathbf{C} = -2i\Gamma\langle\phi\rangle k_1 \mathbf{e}_4\mathbf{e}_2$. The second invariant of the coupling operator cancels, and it is easy to see from (5.51) that $u_{44} = 1$ and

$$u_{42} = \int_0^t i2\Gamma\langle\phi\rangle \frac{k_0^2}{k^2} k_1 e^{-\alpha_2 - (\frac{M}{1+M}-1)\alpha_1} dt' \tag{5.53}$$

The remaining entries of operator $\mathbf{U}$ are zero.

5.5 Short time evolution

A difficulty in extending the RDT to particle-laden flows, is that building the operator $\mathbf{U}$ requires solving the second order differential equation (5.51). This equation results from the lack of commutativity of $\mathbf{C}$ with itself (at two different times) and with the operators $\mathbf{A}$, $\mathbf{Y}$, and $\mathbf{Z}$. Given the challenge in finding an exact solution valid at all times, we are interested in finding one that holds for the short total integration time Δt. The goal is to construct a numerical integrator capable of propagating the solution with a time step Δt. The key benefice to finding short time solutions is that effects due to the lack of commutativity can be negligible. This approach is often referred to as operator splitting (Chorin, 1968) and is commonly used in computational fluid dynamics.

To find a short time approximation to equation (5.49), we follow the theory for

linear functional equations, and introduce a two-by-two operator $\mathbf{V}$ such that

$$\frac{d}{dt}\mathbf{V} + \underbrace{\begin{pmatrix} 0 & c'_{42} \\ c'_{24} & 0 \end{pmatrix}}_{\mathbf{M}}\mathbf{V} = 0 \tag{5.54}$$

This reduced system, captures the difficulty of the problem of particle-laden RDT. The reduced operator $\mathbf{M}$ does not commute with itself at two different times. As we will see later, there is much to gain from expressing the reduced operator $\mathbf{M}$ as a combination of Pauli matrices (Bellman, 1997). The latter are the three matrices $\mathbf{\Sigma}_1$, $\mathbf{\Sigma}_2$ and $\mathbf{\Sigma}_3$ such that

$$\mathbf{\Sigma}_1 = \begin{pmatrix} 0 & 1 \\ 1 & 0 \end{pmatrix}, \quad \mathbf{\Sigma}_2 = \begin{pmatrix} 0 & -i \\ i & 0 \end{pmatrix}, \quad \mathbf{\Sigma}_3 = \begin{pmatrix} 1 & 0 \\ 0 & -1 \end{pmatrix} \tag{5.55}$$

various properties are known for these matrices. The reduced operator decomposes as $\mathbf{M} = (c'_{42} + c'_{24})\mathbf{\Sigma}_1/2 + i(c'_{42} - c'_{24})\mathbf{\Sigma}_2/2$.

In order to understand the difficulty arising from the lack of commutativity, we examine the Magnus solution to (5.54) (Magnus, 1954; Blanes *et al.*, 2009). This states that the solution $\mathbf{V}$ expresses as the (matrix-)exponential of an infinite series

$$\mathbf{V} = \exp\left(\sum_{i=1}^{\infty}\Omega_i\right) \tag{5.56}$$

$$\Omega_1 = \int_0^t \mathbf{M}(t_1)dt_1 \tag{5.57}$$

$$\Omega_2 = -\frac{1}{2}\int_0^t\int_0^{t_1}[\mathbf{M}(t_1), \mathbf{M}(t_2)]dt_2dt_1 \tag{5.58}$$

$$\dots \tag{5.59}$$

where $[\mathbf{A}, \mathbf{B}] = \mathbf{AB} - \mathbf{BA}$ is the commutator of the operators $\mathbf{A}$ and $\mathbf{B}$. The order $n \geqslant 2$ term in the Mangus series expresses as combination of n-fold integrals

and $n-1$ nested commutators. It becomes evident that the lack of commutativity retains these high order terms and renders analytical approaches difficult. Despite the elegance of this form, the series needs to be truncated for any explicit calculations. We truncate at first order

$$\begin{aligned} \mathbf{V} &\simeq \exp\left(\int_0^t \mathbf{M}(t')dt'\right) && (5.60)\\ &\simeq \exp\left(\int_0^t (c'_{42}+c'_{24})/2dt'\boldsymbol{\Sigma}_1 + i\int_0^t (c'_{42}-c'_{24})/2dt'\boldsymbol{\Sigma}_2\right) && (5.61)\end{aligned}$$

The matrix-exponential of a combination of Pauli matrices is computed easily using Sylvester's formula (Bellman, 1997), yielding the following

$$\mathbf{V} \simeq \begin{pmatrix} \cosh(q) & a\sinh(q)/q \\ b\sinh(q)/q & \cosh(q) \end{pmatrix} \tag{5.62}$$

$$\tag{5.63}$$

with $a = \int_0^t c'_{42}dt$, $b = \int_0^t c'_{24}dt'$ and $q = (ab)^{1/2}$. Furthermore, we assume that all functions are slowly varying over the range $0 < t < \Delta t$ and approximate them as constants. This allows one to express the quantities thus found in the closed form

$$a = \Delta t c'_{42} \tag{5.64}$$

$$b = \Delta t c'_{24} \tag{5.65}$$

$$q = \Delta t(II_c)^{1/2} = \Delta t(iM2\Gamma k_1\left(g_2 - (\mathbf{g}\cdot\mathbf{k})\,k_2/k^2\right))^{1/2} \tag{5.66}$$

The target functions u_{22}, u_{42}, u_{24} and u_{44} are from their respective initial conditions

$$\begin{aligned} u_{22} &= \cosh(q) && (5.67)\\ u_{42} &= a\sinh(q)/q = c'_{42}\sinh\left(\Delta t(II_c)^{1/2}\right)/(II_c)^{1/2} && (5.68)\\ u_{24} &= b\sinh(q)/q = c'_{24}\sinh\left(\Delta t(II_c)^{1/2}\right)/(II_c)^{1/2} && (5.69)\\ u_{44} &= \cosh(q) = \cosh(\Delta t(II_c)^{1/2}) && (5.70)\end{aligned}$$

The remaining components of the coupling solution $\mathbf{U}$ are found from (5.50). For example, $u_{14} = \Delta t c'_{14} \cosh(\Delta t (II_c)^{1/2})$ and $u_{12} = \Delta t c'_{14} c'_{42} \sinh\left(\Delta t (II_c)^{1/2}\right) / (II_c)^{1/2}$. Note that in the one-way coupling regime $M \to 0$, and consequently $II_c \to 0$. Taking this limit in (5.68) and (5.70) leads to $u_{44} \to 1$ and $u_{42} = \Delta t c'_{42}$. These are indeed the solutions in the one-way coupling limit addressed in the previous section.

The non-zero components of the complete particle-laden RDT operator valid for short times are

$$x_{11} = e^{-\alpha_1 - \frac{M}{1+M}\alpha_2} \tag{5.71}$$

$$x_{12} = -e^{-\alpha_1 - \frac{M}{1+M}\alpha_2} \frac{\Delta t c_{42} c_{14} \sinh\left(\Delta t (II_c)^{1/2}\right)}{(II_c)^{1/2}} \tag{5.72}$$

$$x_{22} = e^{-\alpha_1 - \frac{M}{1+M}\alpha_2} \frac{k_0}{k^2} \cosh(\Delta t (II_c)^{1/2}) \tag{5.73}$$

$$x_{32} = -e^{-\alpha_1 - \frac{M}{1+M}\alpha_2} \frac{\Delta t c_{42} c_{34} \sinh\left(\Delta t (II_c)^{1/2}\right)}{(II_c)^{1/2}} \tag{5.74}$$

$$x_{42} = e^{-\alpha_1 - \frac{M}{1+M}\alpha_2} c_{42} \frac{\sinh\left(\Delta t (II_c)^{1/2}\right)}{(II_c)^{1/2}} \tag{5.75}$$

$$x_{33} = e^{-\alpha_1 - \frac{M}{1+M}\alpha_2} \tag{5.76}$$

$$x_{14} = -e^{-\alpha_2} \Delta t c_{14} \cosh\left(\Delta t (II_c)^{1/2}\right) \tag{5.77}$$

$$x_{24} = e^{-\alpha_2} c_{24} \frac{\sinh\left(\Delta t (II_c)^{1/2}\right)}{(II_c)^{1/2}} \tag{5.78}$$

$$x_{34} = -e^{-\alpha_2} \Delta t c_{34} \cosh\left(\Delta t (II_c)^{1/2}\right) \tag{5.79}$$

$$x_{44} = e^{-\alpha_2} \cosh\left(\Delta t (II_c)^{1/2}\right) \tag{5.80}$$

As it has been done in (Kasbaoui *et al.*, 2017), various turbulence statistics can be computed by integrating over the whole spectral space using (5.29). To demonstrate how a solution can be propagated from initial state using the particle-

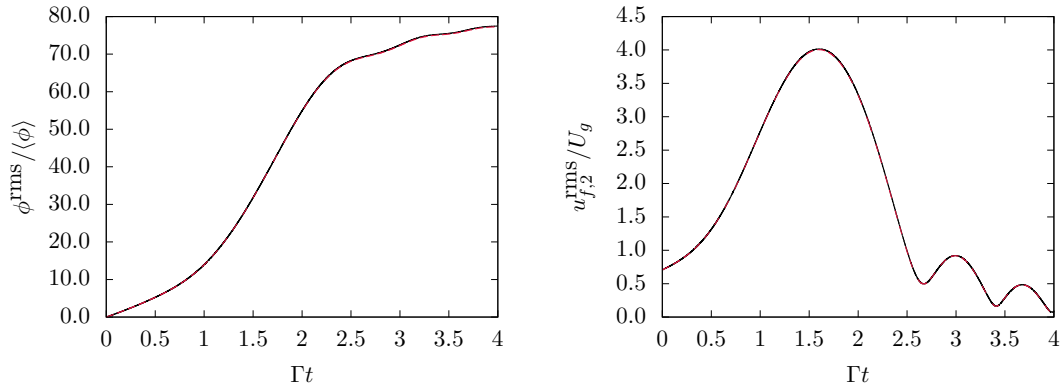

(a) (b)

Figure 5.1: Comparison of the fluctuating volume fraction (5.1a) and vertical fluid root-mean square (5.1b) obtained from direct integration (solid line) of the stiff equations (5.26) and (5.27) and the semi-analytical approach (dashed line) based on the Magnus series.

laden RDT (PL-RDT) operator above, we consider the following simple initial state

$$u_{f,1}(\mathbf{x}, t=0) = -U_g \cos\left(k_1(x+y)\right) \tag{5.81}$$

$$u_{f,2}(\mathbf{x}, t=0) = U_g \cos\left(k_1(x+y)\right) \tag{5.82}$$

$$u_{f,3}(\mathbf{x}, t=0) = 0 \tag{5.83}$$

$$\phi(\mathbf{x}, t=0) = \langle\phi\rangle \tag{5.84}$$

corresponding to $d_p = 150\,\mu$m particles, distributed at the average volume fraction $\langle\phi\rangle = 2.5\,10^{-4}$ in sheared air at the rate $\Gamma = 0.5\,\mathrm{s}^{-1}$. The particle sedimentation is driven by a gravitational acceleration in the direction $-\mathbf{e}_2$ equal to $g = 9.8\,\mathrm{m}\cdot\mathrm{s}^{-2}$. The wavenumber is $k_1 = 2\pi/L_g$, where $L_g = U_g/\Gamma$ is the distance settled by particles in one shear time.

Figure 5.1 shows the evolution of the fluctuations root-mean-square for the volume fraction and fluid fluctuating velocity in the gradient direction 2. The reference solution is obtained from (Kasbaoui *et al.*, 2015) by direct integration of the original set of stiff ordinary differential equations (5.26) and (5.27). The

plots trace the same curves regardless of the solution methodology employed. This validates the approach based on the truncated Magnus series. In addition, the computational cost is reduced by two orders of magnitude on the same machine. This is particularly useful for the integration of turbulence spectrum containing a wide range of modes.

5.6 Conclusion

In this chapter, we lay foundation to the analysis of homogeneously sheared particle-laden turbulence in the two-way coupled semi-dilute regime using the Rapid Distortion Theory. The analysis presented relies on the two assumptions: (1) particles have small inertia, and (2) the shearing happens on a time scale faster than the inertial turbulence time scales. The approach allows the description of the turbulence spectral content in a semi-analytical form. It is shown that in addition to the distortion by the shear, the Fourier modes are further altered due to the preferential concentration mechanism and the gravitational loading exerted by the particles.

The extension of RDT to particle-laden HST provides semi-analytical expressions for the turbulent velocity and volume fraction fluctuations. These forms can be used to compute the evolution of various turbulence statistics such as the turbulent kinetic energy and volume fraction auto-correlation. More importantly, these forms give access to the full spectrum of length scales enabling the identification of the most vigorous scales for turbulence modulation and clustering. Future work will consider these quantities and compare with Euler-Lagrange simulations of HST.

CHAPTER 6

CONCLUSION AND PERSPECTIVES

The clustering of inertial aerosols in the semi-dilute regime has been addressed in this work. It has been shown with a linear stability analysis that this process is kick-started by the preferential concentration mechanism, i.e., the tendency of inertial particles to be expelled from vertical regions, and is significantly enhanced by gravity and mean shear. The non-linear growth of the preferential concentration instability leads to the formation of fine sheets of particles. Numerical simulations in the Euler-Euler and Euler-Lagrange formulations, show that particle-trajectory crossing leads to the local dispersion of particles within the clusters which limits further accumulation. In addition, the turning of the particle sheets towards the horizontal by the shear allows a secondary Rayleigh-Taylor instability to break the particle structure into smaller clusters. An extension of the single-phase RDT captures the multi-scale modulation of turbulence by particles when the shearing happens at time scales significantly faster than the large eddy turnover time.

The continuation of this work involves gathering comprehensive statics on particle distribution, slip velocity, and the carrier turbulent gas from high fidelity Euler-Lagrange simulations. This data will serve to assess the ability of various Euler-Euler simulation methodologies to capture particle-trajectory crossing. Analyses of this sorts are greatly needed in order to design better performing Eulerian closures and arrive at simulation methodologies that significantly reduce the high computational cost of Euler-Lagrange simulations.

Continued work on particle-laden HST will reveal further insights on the modulation of turbulence by particles. The particle-laden RDT was built to capture the early development of this flow. However, the range of applicability of this

theory needs to be tested in highly resolved Euler-Lagrange simulations. These simulations will also serve to address the long time development of this flow. In single-phase HST, the reorganization of turbulence by non-linear inertial effects leads to the establishment of a self-similar regime independent of the initial conditions. Simulations of particle-laden HST can address the alteration of this universal self-similar regime by sedimenting particles.

APPENDIX A

INVISCID SOLUTION IN THE INNER REGION

Gradshteyn *et al.* (2000) provide asymptotic relationships for the behavior of the parabolic cylinder functions as $T \to \pm\infty$ and this facilitates the derivation of analytical relationships between the amplitudes of the upstream and downstream modes. To match the upstream outer region ($t \lesssim -1$) to the turning point, consider the asymptotic expansion of the parabolic cylinder functions for times such that $t \leqslant 0$ and $|T| \gg 1$:

$$\begin{aligned} D_{2M}[(1+i)T] &\simeq 2^M e^{-i\frac{3\pi}{2}M} e^{-i\frac{T^2}{2}} |T|^{2M} \\ &+ \frac{\sqrt{2\pi}}{\Gamma(-2M)} e^{-i\pi\frac{M}{2}} e^{-i\frac{\pi}{4}} \frac{1}{2^{1/2+M}} + \frac{e^{iT^2/2}}{|T|^{1+2M}} \qquad \text{(A.1)} \\ D_{2M}[-(1+i)T] &\simeq 2^M e^{i\frac{\pi}{2}M} e^{-i\frac{T^2}{2}} |T|^{2M} \qquad \text{(A.2)} \end{aligned}$$

Using these expansions, the inner solution for $t \leqslant 0$ and $|t| \gg 1/\sqrt{k_1}$ approaches:

$$\begin{aligned} \hat{n}(t) &\simeq \left(\frac{k_1}{1+M}\right)^M (\Lambda_+ e^{-i\frac{3\pi}{2}M} + \Lambda_- e^{i\frac{\pi}{2}M}) |t|^{2M} e^{-ik_1\frac{t^2}{2}} \\ &+ \Lambda_+ \frac{\sqrt{2\pi}}{\Gamma(-2M)} e^{-i\frac{\pi}{2}M} e^{-i\frac{\pi}{4}} \left(\frac{1+M}{k_1}\right)^{1/2+M} \frac{e^{-i\frac{M}{1+M}k_1\frac{t^2}{2}}}{|t|^{2M+1}} \qquad \text{(A.3)} \end{aligned}$$

Note that the asymptotic expressions for the upstream $\mathtt{N}$ and $\mathtt{M}$ modes when $|t| \ll 1$ are:

$$\begin{aligned} \hat{n}^{\mathtt{N}} &\sim |t|^{2M} e^{-ik_1\frac{t^2}{2}} \qquad \text{(A.4)} \\ \hat{n}^{\mathtt{M}} &\sim \frac{1}{|t|^{2M+1}} e^{-i\frac{M}{1+M}k_1\frac{t^2}{2}} \qquad \text{(A.5)} \end{aligned}$$

It is seen that the functional form of the parabolic cylinder functions is consistent with that of the $\mathtt{N}$ and $\mathtt{M}$ modes within the matching region $t < 0$ and $1/\sqrt{k_1} \ll |t| \ll 1$ provided that we relate the coefficients as:

$$\begin{cases} \overline{\Lambda}_{\mathtt{N}} = \left(\frac{k_1}{1+M}\right)^M (\Lambda_+ e^{-i\frac{3\pi}{2}M} + \Lambda_- e^{i\frac{\pi}{2}M}) \\ \overline{\Lambda}_{\mathtt{M}} = \Lambda_+ \frac{\sqrt{2\pi}}{\Gamma(-2M)} e^{-i\frac{\pi}{2}M} e^{-i\frac{\pi}{4}} \left(\frac{1+M}{k_1}\right)^{1/2+M} \end{cases} \qquad \text{(A.6)}$$

A similar matching of the inner solution with the downstream outer solution in the matching region $1 \gg t \gg 1/\sqrt{k_1}$ yields:

$$\begin{cases} \underline{\Lambda}_{\mathtt{N}} = & \left(\frac{k_1}{1+M}\right)^M \left(\Lambda_- e^{-i\frac{3\pi}{2}M} + \Lambda_+ e^{i\frac{\pi}{2}M}\right) \\ \underline{\Lambda}_{\mathtt{M}} = & \Lambda_- \frac{\sqrt{2\pi}}{\Gamma(-2M)} e^{-i\frac{\pi}{2}M} e^{-i\frac{\pi}{4}} \left(\frac{1+M}{k_1}\right)^{1/2+M} \end{cases} \tag{A.7}$$

The coefficients of the downstream modes can therefore be expressed in terms of the amplitudes of the upstream modes as:

$$\begin{cases} \underline{\Lambda}_{\mathtt{N}} = & -\frac{i\sqrt{i}}{M\Gamma(2M)}\sqrt{\frac{\pi}{2}} \left(\frac{k_1}{1+M}\right)^{1/2+2M} e^{-i\pi M}\overline{\Lambda}_{\mathtt{M}} + e^{-2\pi i M}\overline{\Lambda}_{\mathtt{N}} \\ \underline{\Lambda}_{\mathtt{M}} = & -e^{-2\pi i M}\overline{\Lambda}_{\mathtt{M}} - i\sqrt{i}\sqrt{\frac{2}{\pi}} 2M \sin(2M\pi)\Gamma(2M) e^{-i\pi M} \left(\frac{1+M}{k_1}\right)^{1/2+2M} \overline{\Lambda}_{\mathtt{N}} \end{cases} \tag{A.8}$$

APPENDIX B

THE RAPID DISTORTION MATRIX

In the context of Rapid Distortion Theory, a Fourier mode with the initial wavevector $\mathbf{k}(t=0) = \mathbf{k}_0 = (k_{x,0}, k_{y,0}, k_{z,0})$ is turned by the base homogeneous shear flow $\mathbf{u}_b$ according to

$$\frac{d\mathbf{k}}{dt} = \nabla \mathbf{u}_b \cdot \mathbf{k} \tag{B.1}$$

When shear gradient is in the y direction and the shear rate is Γ, $\mathbf{u}_b = y\Gamma \mathbf{e}_x$, the components x and z of the wavevector remain constant whereas

$$k_y = k_{y,0} - k_x \Gamma t \tag{B.2}$$

In addition to the change of orientation and wavelength incurred by the variation of $\mathbf{k}$, the amplitude of the Fourier mode evolves following

$$\hat{\mathbf{u}}(t) = \mathbf{A}(\mathbf{k}_0, t)\hat{\mathbf{u}}_0 e^{-\nu t\left(k^2 - k_{x,0}k_{y,0}\Gamma t + \frac{(k_{x,0}\Gamma t)^2}{3}\right)} \tag{B.3}$$

where $\mathbf{u}_0$ is the initial amplitude, ν is the kinematic viscosity and $\mathbf{A}$ is the RDT matrix

$$\mathbf{A}(\mathbf{k}_0, t) = \begin{pmatrix} 1 & \frac{k_0^2}{k_x^2+k_z^2}\left(-\frac{k_z^2}{k_0^2}P + \frac{k_x^2}{k_0^2}Q\right) & 0 \\ 0 & \frac{k_0^2}{k^2} & 0 \\ 0 & \frac{k_x k_z}{k_x^2+k_z^2}(P+Q) & 1 \end{pmatrix} \tag{B.4}$$

$$P = \frac{k_0^2}{k_x\sqrt{k_x^2+k_z^2}}(\arctan\alpha - \arctan\tau) \tag{B.5}$$

$$Q = \frac{\Gamma t\left(k_0^2 - 2k_{y,0}^2 + k_x k_{y,0}\Gamma t\right)}{k^2} \tag{B.6}$$

$$\alpha = \frac{k_{y,0}}{\sqrt{k_x^2+k_z^2}} \tag{B.7}$$

$$\tau = \frac{k_y}{\sqrt{k_x^2+k_z^2}} \tag{B.8}$$

BIBLIOGRAPHY

Adrian, R. J. and Moin, P. 1988. Stochastic estimation of organized turbulent structure: homogeneous shear flow. *Journal of Fluid Mechanics*, **190**, 531–559.

Akselvoll, K. 1995. *Large eddy simulation of turbulent confined coannular jets and turbulent flow over a backward facing step /.* Ph.D. thesis, Stanford University, Stanford, CA.

Al Taweel, A. M. and Landau, J. 1977. Turbulence modulation in two-phase jets. *International Journal of Multiphase Flow*, **3** (4), 341–351.

Alfaro, S. C. and Gomes, L. 2001. Modeling mineral aerosol production by wind erosion: Emission intensities and aerosol size distributions in source areas. *Journal of Geophysical Research: Atmospheres*, **106** (D16), 18075–18084.

Aliseda, A., Cartellier, A., Hainaux, F., and Lasheras, J. C. 2002. Effect of preferential concentration on the settling velocity of heavy particles in homogeneous isotropic turbulence. *Journal of Fluid Mechanics*, **468**, 77–105.

Anderson, K., Sundaresan, S., and Jackson, R. 1995. Instabilities and the formation of bubbles in fluidized beds. *Journal of Fluid Mechanics*, **303**, 327–366.

Baggett, J. S. and Trefethen, L. N. 1997. Low-Dimensional Models of Subcritical Transition to Turbulence. *Physics of Fluids*, **9**, 1043–1053.

Baron, F. 1982. *Macro-simulation tridimensionnelle d'ecoulements turbulents cisailles.* Ph.D. thesis. Google-Books-ID: 78yrtgAACAAJ.

Batchelor, G. K. 1988. A new theory of the instability of a uniform fluidized bed. *Journal of Fluid Mechanics*, **193**, 75–110.

Batchelor, G. K. and Nitsche, J. M. 1991. Instability of stationary unbounded stratified fluid. *Journal of Fluid Mechanics*, **227**, 357–391.

Bellman, R. 1997. *Introduction to Matrix Analysis, Second Edition*. Society for Industrial and Applied Mathematics.

Bender, C. M. and Orszag, S. A. 1999. *Advanced Mathematical Methods for Scientists and Engineers: Asymptotic Methods and Perturbation Theory*. Springer.

Biferale, L. and Procaccia, I. 2005. Anisotropy in turbulent flows and in turbulent transport. *Physics Reports*, **414** (23), 43–164.

Blanes, S., Casas, F., Oteo, J. A., and Ros, J. 2009. The Magnus expansion and some of its applications. *Physics Reports*, **470** (5-6), 151–238. ArXiv: 0810.5488.

Boivin, M., Simonin, O., and Squires, K. D. 1998. Direct numerical simulation of turbulence modulation by particles in isotropic turbulence. *Journal of Fluid Mechanics*, **375**, 235–263.

Boris, J., Luca, B., Gaetano, I., and Carlo Massimo, C. 2004. Anisotropic fluctuations in turbulent shear flows. *Physics of Fluids*, **16** (11), 4135–4142.

Briard, A., Gomez, T., Mons, V., and Sagaut, P. 2016. Decay and growth laws in homogeneous shear turbulence. *Journal of Turbulence*, **17** (7), 699–726.

Brucker, K. A., Isaza, J. C., Vaithianathan, T., and Collins, L. R. 2007. Efficient algorithm for simulating homogeneous turbulent shear flow without remeshing. *Journal of Computational Physics*, **225** (1), 20–32.

Capecelatro, J. and Desjardins, O. 2013a. EulerianLagrangian modeling of turbulent liquidsolid slurries in horizontal pipes. *International Journal of Multiphase Flow*, **55**, 64–79.

Capecelatro, J. and Desjardins, O. 2013b. An EulerLagrange strategy for simulating particle-laden flows. *Journal of Computational Physics*, **238**, 1–31.

Capecelatro, J., Desjardins, O., and Fox, R. O. 2015. On fluidparticle dynamics in fully developed cluster-induced turbulence. *Journal of Fluid Mechanics*, **780**, 578–635.

Capecelatro, J., Pepiot, P., and Desjardins, O. 2014. Numerical characterization and modeling of particle clustering in wall-bounded vertical risers. *Chemical Engineering Journal*, **245**, 295–310.

Casciola, C. M., Gualtieri, P., Jacob, B., and Piva, R. 2005. Scaling Properties in the Production Range of Shear Dominated Flows. *Physical Review Letters*, **95** (2), 024503.

Chorin, A. J. 1968. Numerical solution of the Navier-Stokes equations. *Mathematics of Computation*, **22** (104), 745–762.

Chung, D. and Matheou, G. 2012. Direct numerical simulation of stationary homogeneous stratified sheared turbulence. *Journal of Fluid Mechanics*, **696**, 434–467.

Craik, A. D. D. and Criminale, W. O. 1986. Evolution of Wavelike Disturbances in Shear Flows: A Class of Exact Solutions of the Navier-Stokes Equations. *Proceedings of the Royal Society of London. A. Mathematical and Physical Sciences*, **406** (1830), 13–26.

Dasgupta, S., Jackson, R., and Sundaresan, S. 1994. Turbulent gas-particle flow in vertical risers. *AIChE Journal*, **40** (2), 215–228.

Desjardins, O., Blanquart, G., Balarac, G., and Pitsch, H. 2008a. High order conservative finite difference scheme for variable density low Mach number turbulent flows. *Journal of Computational Physics*, **227** (15), 7125–7159.

Desjardins, O., Fox, R. O., and Villedieu, P. 2008b. A quadrature-based moment method for dilute fluid-particle flows. *Journal of Computational Physics*, **227** (4), 2514–2539.

Druzhinin, O. A. 1994. Concentration waves and flow modification in a particleladen circular vortex. *Physics of Fluids (1994-present)*, **6** (10), 3276–3284.

Druzhinin, O. A. 1995. On the two-way interaction in two-dimensional particle-laden flows: the accumulation of particles and flow modification. *Journal of Fluid Mechanics*, **297**, 49–76.

Druzhinin, O. A. 2001. The influence of particle inertia on the two-way coupling and modification of isotropic turbulence by microparticles. *Physics of Fluids*, **13** (12), 3738–3755.

Dukowicz, J. K. and Dvinsky, A. S. 1992. Approximate factorization as a high order splitting for the implicit incompressible flow equations. *Journal of Computational Physics*, **102** (2), 336–347.

Dyson, F. J. 1949. The Radiation Theories of Tomonaga, Schwinger, and Feynman. *Physical Review*, **75** (3), 486–502.

Eaton, J. K. and Fessler, J. R. 1994. Preferential concentration of particles by turbulence. *International Journal of Multiphase Flow*, **20, Supplement 1**, 169–209.

Elghobashi, S. and Truesdell, G. C. 1992. Direct simulation of particle dispersion in a decaying isotropic turbulence. *Journal of Fluid Mechanics*, **242**, 655–700.

Elghobashi, S. and Truesdell, G. C. 1993. On the twoway interaction between homogeneous turbulence and dispersed solid particles. I: Turbulence modification. *Physics of Fluids A: Fluid Dynamics*, **5** (7), 1790–1801.

Elghobashi, S. E. and AbouArab, T. W. 1983. A twoequation turbulence model for twophase flows. *Physics of Fluids (1958-1988)*, **26** (4), 931–938.

Estivalezes, J. L. and Villedieu, P. 1996. High-Order Positivity-Preserving Kinetic Schemes for the Compressible Euler Equations. *SIAM Journal on Numerical Analysis*, **33** (5), 2050–2067.

Falkovich, G., Fouxon, A., and Stepanov, M. G. 2002. Acceleration of rain initiation by cloud turbulence. *Nature*, **419** (6903), 151–154.

Ferchichi, M. and Tavoularis, S. 2000. Reynolds number effects on the fine structure of uniformly sheared turbulence. *Physics of Fluids (1994-present)*, **12** (11), 2942–2953.

Fernando, H. J. S. and Choi, Y.-J. 2007. Particle laden geophysical flows: from geophysical to sub-kolmogorov scales. In *Particle-Laden Flow*, ERCOFTAC Series. Springer, Dordrecht, pp. 407–421. DOI: 10.1007/978-1-4020-6218-6_32.

Ferrante, A. and Elghobashi, S. 2007. On the accuracy of the two-fluid formulation in direct numerical simulation of bubble-laden turbulent boundary layers. *Physics of Fluids (1994-present)*, **19** (4), 045105.

Ferry, J. and Balachandar, S. 2001. A fast Eulerian method for disperse two-phase flow. *International Journal of Multiphase Flow*, **27** (7), 1199–1226.

Ferry, J. and Balachandar, S. 2002. Equilibrium expansion for the Eulerian velocity of small particles. *Powder Technology*, **125** (23), 131–139.

Fox, R. O. 2008. A quadrature-based third-order moment method for dilute gas-particle flows. *Journal of Computational Physics*, **227** (12), 6313–6350.

Fvrier, P., Simonin, O., and Squires, K. D. 2005. Partitioning of particle velocities in gassolid turbulent flows into a continuous field and a spatially uncorrelated random distribution: theoretical formalism and numerical study. *Journal of Fluid Mechanics*, **533**, 1–46.

Garg, S. and Warhaft, Z. 1998. On the small scale structure of simple shear flow. *Physics of Fluids (1994-present)*, **10** (3), 662–673.

George, W. K. and Gibson, M. M. 1992. The self-preservation of homogeneous shear flow turbulence. *Experiments in Fluids*, **13** (4), 229–238.

Gerz, T., Schumann, U., and Elghobashi, S. E. 1989. Direct numerical simulation of stratified homogeneous turbulent shear flows. *Journal of Fluid Mechanics*, **200**, 563–594.

Gillandt, I., Fritsching, U., and Bauckhage, K. 2001. Measurement of phase interaction in dispersed gas/particle two-phase flow. *International Journal of Multiphase Flow*, **27** (8), 1313–1332.

Goldreich, P. and Tremaine, S. 1978. The excitation and evolution of density waves. *The Astrophysical Journal*, **222**, 850–858.

Good, G. H., Ireland, P. J., Bewley, G. P., Bodenschatz, E., Collins, L. R., and Warhaft, Z. 2014. Settling regimes of inertial particles in isotropic turbulence. *Journal of Fluid Mechanics*, **759**.

Gradshteyn, I. S., Ryzhik, I. M., Jeffrey, A., and Zwillinger, D. 2000. *Table of Integrals, Series, and Products, Sixth Edition*. Academic Press, 6th edition edition.

Gresho, P. M. 1990. On the theory of semi-implicit projection methods for viscous incompressible flow and its implementation via a finite element method that also introduces a nearly consistent mass matrix. Part 1: Theory. *International Journal for Numerical Methods in Fluids*, **11** (5), 587–620.

Gualtieri, P., Casciola, C. M., Benzi, R., Amati, G., and Piva, R. 2002. Scaling laws and intermittency in homogeneous shear flow. *Physics of Fluids*, **14** (2), 583–596.

Gualtieri, P., Casciola, C. M., Benzi, R., and Piva, R. 2007a. Preservation of statistical properties in large-eddy simulation of shear turbulence. *Journal of Fluid Mechanics*, **592**, 471–494.

Gualtieri, P., Casciola, C. M., Jacob, B., and Piva, R. 2007b. The residual anisotropy at small scales in high shear turbulence. *Physics of Fluids*, **19** (10), 101704.

Gustavsson, K., Meneguz, E., Reeks, M., and Mehlig, B. 2012. Inertial-particle dynamics in turbulent flows: caustics, concentration fluctuations and random uncorrelated motion. *New Journal of Physics*, **14** (11), 115017.

Hardalupas, Y., Taylor, A. M. K. P., and Whitelaw, J. H. 1989. Velocity and Particle-Flux Characteristics of Trubulent Particle-Laden Jets. *Proceedings of the Royal Society of London A: Mathematical, Physical and Engineering Sciences*, **426** (1870), 31–78.

Hinch, E. J. 1991. *Perturbation Methods*. Cambridge University Press.

Holt, S. E., Koseff, J. R., and Ferziger, J. H. 1992. A numerical study of the evolution and structure of homogeneous stably stratified sheared turbulence. *Journal of Fluid Mechanics*, **237**, 499–539.

Hunt, J. C. R. and Carruthers, D. J. 1990. Rapid distortion theory and the problems of turbulence. *Journal of Fluid Mechanics*, **212**, 497–532.

Hunt, J. C. R., Carruthers, D. J., and Fung, J. C. H. 1991. Rapid distortion theory as a means of exploring the structure of turbulence. In *New Perspectives in Turbulence*. Springer, New York, NY, pp. 55–103. DOI: 10.1007/978-1-4612-3156-1_2.

Ireland, P. J., Bragg, A. D., and Collins, L. R. 2016. The effect of Reynolds number on inertial particle dynamics in isotropic turbulence. Part 2. Simulations with gravitational effects. *Journal of Fluid Mechanics*, **796**, 659–711.

Ireland, P. J. and Desjardins, O. 2017. Improving particle drag predictions in EulerLagrange simulations with two-way coupling. *Journal of Computational Physics*, **338**, 405–430.

Isaza, J. C. and Collins, L. R. 2009. On the asymptotic behaviour of large-scale turbulence in homogeneous shear flow. *Journal of Fluid Mechanics*, **637**, 213–239.

Isaza, J. C. and Collins, L. R. 2011. Effect of the shear parameter on velocity-gradient statistics in homogeneous turbulent shear flow. *Journal of Fluid Mechanics*, **678**, 14–40.

Isaza, J. C., Warhaft, Z., Collins, L. R., and Research, I. C. f. T. 2009. Experimental investigation of the large-scale velocity statistics in homogeneous turbulent shear flow. *Physics of Fluids (1994-present)*, **21** (6), 065105.

Ishihara, T., Yoshida, K., and Kaneda, Y. 2002. Anisotropic Velocity Correlation Spectrum at Small Scales in a Homogeneous Turbulent Shear Flow. *Physical Review Letters*, **88** (15), 154501.

Jacobitz, F. G., Liechtenstein, L., Schneider, K., and Farge, M. 2008. On the structure and dynamics of sheared and rotating turbulence: Direct numerical simulation and wavelet-based coherent vortex extraction. *Physics of Fluids (1994-present)*, **20** (4), 045103.

Jacobitz, F. G., Schneider, K., Bos, W. J. T., and Farge, M. 2010. On the structure and dynamics of sheared and rotating turbulence: Anisotropy properties and geometrical scale-dependent statistics. *Physics of Fluids (1994-present)*, **22** (8), 085101.

Jacobitz, F. G., Schneider, K., Bos, W. J. T., and Farge, M. 2016. Structure of sheared and rotating turbulence: Multiscale statistics of Lagrangian and Eulerian accelerations and passive scalar dynamics. *Physical Review E*, **93** (1), 013113.

Jenny, P., Roekaerts, D., and Beishuizen, N. 2012. Modeling of turbulent dilute spray combustion. *Progress in Energy and Combustion Science*, **38** (6), 846–887.

Johnson, B. M. and Gammie, C. F. 2005. Linear Theory of Thin, Radially Stratified Disks. *The Astrophysical Journal*, **626** (2), 978.

Kaltenbach, H.-J., Gerz, T., and Schumann, U. 1994. Large-eddy simulation of homogeneous turbulence and diffusion in stably stratified shear flow. *Journal of Fluid Mechanics*, **280** (-1), 1.

Kasbaoui, M. H., Koch, D. L., Ravi, G. P., and Desjardins, O. 2017. An algorithm for solving the Navier-Stokes equations with shear-periodic boundary conditions and its application to homogeneously sheared turbulence. *Manuscript submitted for publication.*

Kasbaoui, M. H., Koch, D. L., Subramanian, G., and Desjardins, O. 2015. Preferential concentration driven instability of sheared gassolid suspensions. *Journal of Fluid Mechanics*, **770**, 85–123.

Kaufmann, A., Moreau, M., Simonin, O., and Helie, J. 2008. Comparison between Lagrangian and mesoscopic Eulerian modelling approaches for inertial particles suspended in decaying isotropic turbulence. *Journal of Computational Physics*, **227** (13), 6448–6472.

Kelvin, L. 1887. Stability of fluid motion: rectilinear motion of viscous fluid between two parallel plates. *Phil. Mag*, **24** (5), 188–196.

Kim, J. and Moin, P. 1985. Application of a fractional-step method to incompressible Navier-Stokes equations. *Journal of Computational Physics*, **59** (2), 308–323.

Koch, D. L. 1990. Kinetic theory for a monodisperse gassolid suspension. *Physics of Fluids A: Fluid Dynamics (1989-1993)*, **2** (10), 1711–1723.

Kong, B., Fox, R. O., Feng, H., Capecelatro, J., Patel, R., Desjardins, O., and Fox, R. O. 2017. Eulereuler anisotropic gaussian mesoscale simulation of homogeneous cluster-induced gasparticle turbulence. *AIChE Journal*, **63** (7), 2630–2643.

Lau, T. C. W. and Nathan, G. J. 2014. Influence of Stokes number on the

velocity and concentration distributions in particle-laden jets. *Journal of Fluid Mechanics*, **757**, 432–457.

Lee, M. J., Kim, J., and Moin, P. 1990. Structure of turbulence at high shear rate. *Journal of Fluid Mechanics*, **216**, 561–583.

Lees, A. W. and Edwards, S. F. 1972. The computer study of transport processes under extreme conditions. *Journal of Physics C: Solid State Physics*, **5** (15), 1921.

Levermore, C. D. and Morokoff, W. J. 1998. The Gaussian Moment Closure for Gas Dynamics. *SIAM Journal on Applied Mathematics*, **59** (1), 72–96.

Longmire, E. K. and Eaton, J. K. 1992. Structure of a particle-laden round jet. *Journal of Fluid Mechanics*, **236**, 217–257.

Lun, C. K. K., Savage, S. B., Jeffrey, D. J., and Chepurniy, N. 1984. Kinetic theories for granular flow: inelastic particles in Couette flow and slightly inelastic particles in a general flowfield. *Journal of Fluid Mechanics*, **140** (-1), 223.

Magnus, W. 1954. On the exponential solution of differential equations for a linear operator. *Communications on Pure and Applied Mathematics*, **7** (4), 649–673.

Marmottant, P. and Villermaux, E. 2004. On spray formation. *Journal of Fluid Mechanics*, **498**, 73–111.

Masi, E. and Simonin, O. 2014. Algebraic-Closure-Based Moment Method for Unsteady Eulerian Simulations of Non-Isothermal Particle-Laden Turbulent Flows at Moderate Stokes Numbers in Dilute Regime. *Flow, Turbulence and Combustion*, **92** (1-2), 121–145.

Maxey, M. R. 1982. Distortion of turbulence in flows with parallel streamlines. *Journal of Fluid Mechanics*, **124**, 261–282.

Maxey, M. R. 1987. The gravitational settling of aerosol particles in homogeneous turbulence and random flow fields. *Journal of Fluid Mechanics*, **174**, 441–465.

Maxey, M. R. and Riley, J. J. 1983. Equation of motion for a small rigid sphere in a nonuniform flow. *Physics of Fluids (1958-1988)*, **26** (4), 883–889.

McGraw, R. 1997. Description of Aerosol Dynamics by the Quadrature Method of Moments. *Aerosol Science and Technology*, **27** (2), 255–265.

Meyer, D. W. 2012. Modelling of turbulence modulation in particle- or droplet-laden flows. *Journal of Fluid Mechanics*, **706**, 251–273.

Modarress, D., Elghobashi, S., and TAN, H. 1984. Two-component LDA measurement in a two-phase turbulent jet. *AIAA Journal*, **22** (5), 624–630.

Moffatt, H. K. 1965. *The interaction of turbulance with rapid uniform shear*. Dept. of Aeronautics and Astronautics, Stanford University, Stanford.

Mostafa, A. A., Mongia, H. C., Mcdonel, V. G., and Samuelsen, G. S. 1989. Evolution of particle-laden jet flows - A theoretical and experimental study. *AIAA Journal*, **27** (2), 167–183.

Nishimura, K. and Hunt, J. C. R. 2000. Saltation and incipient suspension above a flat particle bed below a turbulent boundary layer. *Journal of Fluid Mechanics*, **417**, 77–102.

Orszag, S. A., Israeli, M., and Deville, M. O. 1986. Boundary conditions for incompressible flows. *Journal of Scientific Computing*, **1** (1), 75–111.

Pai, M. G. and Subramaniam, S. 2012. Two-way coupled stochastic model for dispersion of inertial particles in turbulence. *Journal of Fluid Mechanics*, **700**, 29–62.

Parthasarathy, R. N. and Faeth, G. M. 1990. Turbulence modulation in homogeneous dilute particle-laden flows. *Journal of Fluid Mechanics*, **220**, 485–514.

Pearson, J. R. A. 1959. The effect of uniform distortion on weak homogeneous turbulence. *Journal of Fluid Mechanics*, **5** (02), 274.

Pierce, C. D. 2001. *Progress-Variable Approach for Large-Eddy Simulation of Turbulent Combustion*. Ph.D. thesis, Stanford University, Stanford, CA.

Pierce, C. D. and Moin, P. 2004. Progress-variable approach for large-eddy simulation of non-premixed turbulent combustion. *Journal of Fluid Mechanics*, **504**, 73–97.

Poelma, C., Westerweel, J., and Ooms, G. 2007. Particlefluid interactions in grid-generated turbulence. *Journal of Fluid Mechanics*, **589**, 315–351.

Pope, S. B. 2001. Turbulent Flows. *Measurement Science and Technology*, **12** (11), 2020.

Prevost, F., Boree, J., Nuglisch, H. J., and Charnay, G. 1996. Measurements of fluid/particle correlated motion in the far field of an axisymmetric jet. *International Journal of Multiphase Flow*, **22** (4), 685–701.

Pumir, A. 1996. Turbulence in homogeneous shear flows. *Physics of Fluids*, **8** (11), 3112–3127.

Pumir, A. and Shraiman, B. I. 1995. Persistent Small Scale Anisotropy in Homogeneous Shear Flows. *Physical Review Letters*, **75** (17), 3114–3117.

Rani, S. L. and Balachandar, S. 2003. Evaluation of the equilibrium Eulerian approach for the evolution of particle concentration in isotropic turbulence. *International Journal of Multiphase Flow*, **29** (12), 1793–1816.

Ravichandran, S. and Govindarajan, R. 2015. Caustics and clustering in the vicinity of a vortex. *Physics of Fluids (1994-present)*, **27** (3), 033305.

Rogallo, R. S. 1981. Numerical experiments in homogeneous turbulence. *NASA STI/Recon Technical Report N*, **81**, 31508.

Rogers, M. M. 1986. *The Structure and Modeling of the Hydrodynamic and Passive Scalar Fields in Homogeneous Turbulent Shear Flow*. Ph.D., Stanford University, United States – California.

Rogers, M. M. 1991. The structure of a passive scalar field with a uniform mean gradient in rapidly sheared homogeneous turbulent flow. *Physics of Fluids A: Fluid Dynamics (1989-1993)*, **3** (1), 144–154.

Rogers, M. M. and Moin, P. 1987. The structure of the vorticity field in homogeneous turbulent flows. *Journal of Fluid Mechanics*, **176**, 33–66.

Rohr, J. J., Itsweire, E. C., Helland, K. N., and Atta, C. W. V. 1988. An investigation of the growth of turbulence in a uniform-mean-shear flow. *Journal of Fluid Mechanics*, **187**, 1–33.

Sabat, M., Vi\'{e}, A., Larat, A., and Massot, M. 2016. Fully Eulerian simulation of 3d turbulent particle laden flow based on the Anisotropic Gaussian Closure. Firenze, Italy.

Saffman, P. G. 1962. On the stability of laminar flow of a dusty gas. *Journal of Fluid Mechanics*, **13** (01), 120–128.

Salhi, A., Jacobitz, F. G., Schneider, K., and Cambon, C. 2014. Nonlinear dynamics and anisotropic structure of rotating sheared turbulence. *Physical Review E*, **89** (1), 013020.

Savill, A. M. 1987. Recent Developments in Rapid-Distortion Theory. *Annual Review of Fluid Mechanics*, **19** (1), 531–573.

Schmid, P. J. 2007. Nonmodal Stability Theory. *Annual Review of Fluid Mechanics*, **39** (1), 129–162.

Schmid, P. J. and Kytomaa, H. K. 1994. Transient and asymptotic stability of granular shear flow. *Journal of Fluid Mechanics*, **264**, 255–275.

Schumacher, J. 2001. Derivative moments in stationary homogeneous shear turbulence. *Journal of Fluid Mechanics*, **441**, 109–118.

Schumacher, J. 2004. Relation between shear parameter and Reynolds number in statistically stationary turbulent shear flows. *Physics of Fluids*, **16** (8), 3094–3102.

Schumacher, J. and Eckhardt, B. 2000. On statistically stationary homogeneous shear turbulence. *EPL (Europhysics Letters)*, **52** (6), 627.

Schumann, U. 1985. Algorithms for direct numerical simulation of shear-periodic turbulence. In Soubbaramayer and J. P. Boujot, editors, *Ninth International Conference on Numerical Methods in Fluid Dynamics*, number 218 in Lecture Notes in Physics. Springer Berlin Heidelberg, pp. 492–496.

Schumann, U. 1996. Direct and large eddy simulations of stratified homogeneous shear flows. *Dynamics of Atmospheres and Oceans*, **23**, 81–98.

Schumann, U., Elghobashi, S. E., and Gerz, T. 1986. Direct Simulation of Stably Stratified Turbulent Homogeneous Shear Flows. In U. Schumann and R. Friedrich, editors, *Direct and Large Eddy Simulation of Turbulence*. Vieweg+Teubner Verlag, Wiesbaden, pp. 245–264. DOI: 10.1007/978-3-663-00197-3_16.

Shaw, R. A. 2003. Particle-Turbulence Interactions in Atmospheric Clouds. *Annual Review of Fluid Mechanics*, **35** (1), 183–227.

Shen, X. and Warhaft, Z. 2000. The anisotropy of the small scale structure in high Reynolds number (R1000) turbulent shear flow. *Physics of Fluids (1994-present)*, **12** (11), 2976–2989.

Shotorban, B. 2009. Two-fluid approach for direct numerical simulation of particle-laden turbulent flows at small Stokes numbers. *Physical Review E*, **79** (5).

Shotorban, B. and Balachandar, S. 2006. Particle concentration in homogeneous shear turbulence simulated via Lagrangian and equilibrium Eulerian approaches. *Physics of Fluids (1994-present)*, **18** (6), 065105.

Shuen, J. S., Solomon, A. S. P., FAETH, G. M., and ZHANG, Q. F. 1985. Structure of particle-laden jets - Measurements and predictions. *AIAA Journal*, **23** (3), 396–404.

Simonin, O., Fvrier, P., and Laviville, J. 2002. On the spatial distribution of heavy-particle velocities in turbulent flow: from continuous field to particulate chaos. *Journal of Turbulence*, **3**, N40.

Squires, K. D. and Eaton, J. K. 1991. Preferential concentration of particles by turbulence. *Physics of Fluids A: Fluid Dynamics (1989-1993)*, **3** (5), 1169–1178.

Sukheswalla, P., Vaithianathan, T., and Collins, L. R. 2013. Simulation of homogeneous turbulent shear flows at higher Reynolds numbers: numerical challenges and a remedy. *Journal of Turbulence*, **14** (5), 60–97.

Sumbekova, S., Cartellier, A., Aliseda, A., and Bourgoin, M. 2017. Preferential concentration of inertial sub-Kolmogorov particles: The roles of mass loading of particles, Stokes numbers, and Reynolds numbers. *Physical Review Fluids*, **2** (2), 024302.

Tavoularis, S. 1985. Asymptotic laws for transversely homogeneous turbulent shear flows. *Physics of Fluids (1958-1988)*, **28** (3), 999–1001.

Tavoularis, S. and Corrsin, S. 1981. Experiments in nearly homogenous turbulent shear flow with a uniform mean temperature gradient. Part 1. *Journal of Fluid Mechanics*, **104**, 311–347.

Tavoularis, S. and Karnik, U. 1989. Further experiments on the evolution of turbulent stresses and scales in uniformly sheared turbulence. *Journal of Fluid Mechanics*, **204**, 457–478.

Temam, R. 1968. Une mthode d'approximation de la solution des quations de Navier-Stokes. *Bulletin de la Socit Mathmatique de France*, **96**, 115–152.

Thomson, W. 1887. XXXIV. Stability of motion (continued from the May, June, and August Numbers).Broad river flowing down an inclined plane bed. *Philosophical Magazine Series 5*, **24** (148), 272–278.

Tio, K.-K., GanCalvo, A. M., and Lasheras, J. C. 1993. The dynamics of

small, heavy, rigid spherical particles in a periodic Stuart vortex flow. *Physics of Fluids A: Fluid Dynamics*, **5** (7), 1679–1693.

Townsend, A. A. 1970. Entrainment and the structure of turbulent flow. *Journal of Fluid Mechanics*, **41** (1), 13–46.

Trefethen, L. 1997. Pseudospectra of Linear Operators. *SIAM Review*, **39** (3), 383–406.

Trefethen, L. N., Trefethen, A. E., Reddy, S. C., and Driscoll, T. A. 1993. Hydrodynamic Stability Without Eigenvalues. *Science*, **261** (5121), 578–584.

Truelove, J. S. 1985. The modelling of flow and combustion in swirled, pulverized-coal burners. *Symposium (International) on Combustion*, **20** (1), 523–530.

Vikas, V., Wang, Z. J., Passalacqua, A., and Fox, R. O. 2011. Realizable high-order finite-volume schemes for quadrature-based moment methods. *Journal of Computational Physics*, **230** (13), 5328–5352.

Vi, A., Doisneau, F., and Massot, M. 2015. On the Anisotropic Gaussian Velocity Closure for Inertial-Particle Laden Flows. *Communications in Computational Physics*, **17** (1), 1–46.

Vi, A., Pouransari, H., Zamansky, R., and Mani, A. 2016. Particle-laden flows forced by the disperse phase: Comparison between Lagrangian and Eulerian simulations. *International Journal of Multiphase Flow*, **79**, 144–158.

Wall, C., Pierce, C. D., and Moin, P. 2002. A Semi-implicit Method for Resolution of Acoustic Waves in Low Mach Number Flows. *Journal of Computational Physics*, **181** (2), 545–563.

Wang, C.-H., Jackson, R., and Sundaresan, S. 1996. Stability of bounded rapid shear flows of a granular material. *Journal of Fluid Mechanics*, **308**, 31–62.

Wang, L.-P. and Maxey, M. R. 1993. Settling velocity and concentration distribution of heavy particles in homogeneous isotropic turbulence. *Journal of Fluid Mechanics*, **256**, 27–68.

Wilkinson, M., Mehlig, B., and Bezuglyy, V. 2006. Caustic Activation of Rain Showers. *Physical Review Letters*, **97** (4), 048501.

Williams, F. A. 1958. Spray Combustion and Atomization. *The Physics of Fluids*, **1** (6), 541–545.

Yang, C. Y. and Lei, U. 1998. The role of the turbulent scales in the settling velocity of heavy particles in homogeneous isotropic turbulence. *Journal of Fluid Mechanics*, **371**, 179–205.

Yang, T. S. and Shy, S. S. 2005. Two-way interaction between solid particles and homogeneous air turbulence: particle settling rate and turbulence modification measurements. *Journal of Fluid Mechanics*, **526**, 171–216.

Zhang, D. Z. and Prosperetti, A. 1997. Momentum and energy equations for disperse two-phase flows and their closure for dilute suspensions. *International Journal of Multiphase Flow*, **23** (3), 425–453.